8-18-2020 1:30 PM

Rational design of cell configurations for high-performance Na-O2 batteries

Xiaoting Lin, *The University of Western Ontario*

Supervisor: Sun, Xueliang, *The University of Western Ontario*
A thesis submitted in partial fulfillment of the requirements for the Doctor of Philosophy degree
in Mechanical and Materials Engineering
© Xiaoting Lin 2020

Abstract

Na-O_2 batteries are considered as the promising candidates for electric vehicles due to their ultrahigh theoretical energy densities. However, state-of-the-art Na-O_2 batteries suffer from serious challenges including 1) pore clogging and insufficient O_2 transportation within the air electrode; 2) degradation of air electrode, 3) Na dendrite growth; and 4) Na corrosion induced by O_2/O_2^- crossover. This thesis, therefore, focuses on rational design of cell configurations to address these problems and understanding the insight mechanisms.

3D printing of "O_2 breathable" air electrodes for Na-O_2 batteries were first developed. The unique air electrode structure features non-competitive pathways for O_2, electrons, and Na^+, leading to high-capacity and long-life Na-O_2 batteries.

Except for air electrode, it is found that the Na anode also plays crucial roles in determining the Na-O_2 cell performance. To prevent the Na dendrite growth and Na degradation induced by O_2/O_2^- crossover, novel Na-O_2 batteries using carbon paper protected Na anode was first designed. Besides, hybrid solid-state Na-O_2 batteries based on solid-state electrolytes and protected Na anodes were successfully developed.

Furthermore, the cycling stability of Na@alucone anode was investigated. It is revealed that the chemical stability of Na protective layer against O_2^- is critical to the cycling stability of Na anode, and a universal approach was proposed to achieve high-performance Na-O_2 batteries.

A flame-resistant, dendrite-free and O_2/O_2^-- impermeable composite electrolyte was fabricated, both safety and electrochemical performance of Na-O_2 batteries can be enhanced significantly.

In summary, the discoveries in this thesis provide important guidance to achieve high-performance Na-O_2 batteries.

Keywords

Summary for Lay Audience

With the depletion of fossil fuels and increasing environmental concerns, development of green and sustainable energy-storage systems has never been more urgent. Rechargeable Na-O_2 batteries have aroused substantial attention due to their high theoretical energy densities, high energy efficiency, and abundance of sodium. However, state-of-the-art Na-O_2 batteries suffer from key challenges that hinder their practical application, such as 1) pore clogging and insufficient O_2 transportation within the air electrode, 2) degradation of air electrode, 3) Na dendrite growth and resultant cell short circuiting, and 4) Na corrosion induced by O_2/O_2^- crossover. The thesis mainly focuses on addressing the challenges of Na-O_2 batteries via rational design of cell configurations, as well as clarifying the underlying degradation mechanism of Na-O_2 cell performance.

Freestanding "O_2 breathable" air electrodes for Na-O_2 batteries were first fabricated using 3D printing technique. The designed air electrode has a stacked mesh structure with macroscale open pores and conductive filaments composed of reduced graphene oxide sheets. The unique air electrode structure features separated pathways for O_2, electrons, and electrolyte (Na$^+$), leading to high-capacity and long-life Na-O_2 batteries.

Except for air electrode, it is found that the Na anode also plays important roles in determining the Na-O_2 cell performance. Novel Na-O_2 batteries using electrically connected carbon paper and Na metal as protected Na anode were constructed, in order to improve the Na-O_2 cell performance. To address the issues of Na dendrite growth and O_2/O_2^- crossover comprehensively, hybrid solid-state Na-O_2 batteries based on solid-state electrolytes and protected Na anodes were successfully developed.

Furthermore, by investigating the electrochemical behavior of alucone protected Na (Na@alucone) anode in Na-O_2 batteries, it is revealed that the chemical instability of the Na protective layer against superoxide radical can be fatal to the Na-O_2 cell performance. More importantly, a universal strategy was proposed to eliminate superoxide crossover for efficient Na dendrite suppressing film.

A flame-resistant, dendrite-free and O_2/O_2^- impermeable composite electrolyte was developed to construct quasi-solid-state Na-O_2 battery. Benefiting from the merits of composite

electrolyte, both safety and electrochemical performance of Na-O$_2$ batteries can be improved significantly.

In summary, the strategies developed in this thesis provide important guidance to achieve high-performance superoxide-based Na-O$_2$ batteries.

Co-Authorship Statement

1.

Title: The application of carbon materials in nonaqueous Na-O$_2$ batteries

Authors: Xiaoting Lin, Qian Sun, Kieran Doyle Davis, Ruying Li, Xueliang Sun

The final version of this manuscript has been published in ***Carbon Energy,*** 2019; 1: 141-164. All the authors contributed to designing and modifying the manuscript.

2.

Title: 3D printing of freestanding "O$_2$ breathable" air electrodes for high-capacity and long-life Na-O$_2$ batteries

Authors: Xiaoting Lin, Jiwei Wang, Xuejie Gao, Sizhe Wang, Qian Sun, Jing Luo, Changtai Zhao, Yang Zhao, Xiaofei Yang, Changhong Wang, Ruying Li, Xueliang Sun

The final version of this manuscript has been published in ***Chemistry of Materials***, 2020; 32, 7, 3018-3027. X.L. and X.S. conceived and designed the experimental work with the help from J.W. and X.G. who printed the air electrodes; S.W. and X.Y. helped with the schematic diagram; C.W performed the XRD characterization, and Y.Z helped with the Na anode protection; X.L., Q.S., C.Z. and J.L. participated in the discussion of the data; R.L. helped with SEM and purchasing all the chemicals. X.S. supervised the overall project. All authors have given approval to the final version of the manuscript.

3.

Title: On the cycling performance of Na-O$_2$ cells: revealing the impact of the superoxide crossover toward the metallic Na electrode

Authors: Xiaoting Lin, Qian Sun, Hossein Yadegari, Xiaofei yang, Yang Zhao, Changhong Wang, Jianneng Liang, Alicia Koo, Ruying Li, Xueliang Sun

The final version of this manuscript has been published in ***Advanced Functional Materials***, *2018, 28, 1801904*; X.L. and Q.S. conceived and designed the experimental work with the help

from Y.Z. who proposed method for Na protection; X.L., Q.S., and H.Y. participated in analyzing the experimental results and preparing the manuscript; X.Y. helped with the schematic diagram; C.W and J.L. performed the XRD characterization; R. L helped with purchasing all the chemicals. X.S. supervised the overall project. All authors have given approval to the final version of the manuscript.

4.

Title: O_2/O_2^- crossover- and dendrite-free hybrid solid-state Na-O_2 batteries

Authors: Xiaoting Lin, Fei Sun, Qian Sun, Sizhe Wang, Jing Luo, Changtai Zhao, Xiaofei Yang, Yang Zhao, Changhong Wang, Ruying Li, Xueliang Sun

The final version of this manuscript has been published in ***Chemistry of Materials**, 2019, 31, 9024-9031*; X.L. and Q.S. designed the experimental work with the help from Y.Z. who proposed method for Na protection; S.W. and X.Y. helped with the schematic diagram; C.W. performed the XRD characterization; X.L., Q.S., C.Z., and J.L. participated in the discussion of the data; R. L helped with purchasing all the chemicals. X.S. supervised the overall project. All authors have given approval to the final version of the manuscript.

5.

Title: Probing blind point of the protected anodes in Na-O_2 batteries: their failure mechanism against superoxide crossover and resolving strategy

Authors: Xiaoting Lin, Yipeng Sun, Qian Sun, Yang Zhao, Jing Luo, Changtai Zhao, Xiaofei Yang, Changhong Wang, Hanyu Huo, Ruying Li, Xueliang Sun

The final version of this manuscript will be submitted to a high-impact journal. X.S. conceived the overall project; X.L. designed the experimental work with help from Q.S. and wrote this manuscript; Y.S. and Y.Z. helped with MLD process. Q.S. and X.L. proposed the reaction mechanism. J.L. polished the language; Q.S., C.Z, X.Y., and H.H. participated in the discussion of the data; C.W. performed the XRD characterization; R.L. helped with SEM and purchasing all the chemicals. All authors have given approval to the final version of the manuscript.

6.

Title: Flame-resistant, dendrite-free and O_2/O_2^-- impermeable composite electrolyte for quasi-solid-state Na-O_2 batteries

Authors: Xiaoting Lin, Changtai Zhao, Qian Sun, Xiaofei Yang, Jing Luo, Fei Sun, Jianneng Liang, Changhong Wang, Ruying Li, Xueliang Sun

The final version of this manuscript will be submitted to a high-impact journal. X.S. conceived the overall project; X.L. designed the experimental work with help from C.Z. and Q.S.; F.S. and J.L. helped with the electrolyte synthesis and X.Y helped with schematic diagram. J.L. polished the language; C.W. performed the XRD characterization; R.L. helped with SEM and purchasing all the chemicals. All authors have given approval to the final version of the manuscript.

7.

Title: Carbon nanomaterials for Na-O_2 batteries

Authors: Xiaoting Lin, Keegan Adair, and Xueliang Sun

The final version of this manuscript was published <u>as a book chapter</u> in "Carbon Nanomaterials for Electrochemical Energy Technologies" edited by Shuhui Sun, Xueliang Sun, Zhongwei Chen, Yuyu Liu, David P. Wilkinson, Jiujun Zhang, CRC publisher, ISBN-13: 978-1497846021 (2017). X.L. wrote the manuscript under Prof. Sun's supervision and guidance.

8.

Title: Carbon nanomaterials for Li-O_2 batteries

Authors: Xiaoting Lin, Keegan Adair, and Xueliang Sun

The final version of this manuscript was published <u>as a book chapter</u> in "Carbon Nanomaterials for Electrochemical Energy Technologies" edited by Shuhui Sun, Xueliang Sun, Zhongwei Chen, Yuyu Liu, David P. Wilkinson, Jiujun Zhang, CRC publisher, ISBN-13: 978-1497846021 (2017). X.L. wrote the manuscript under Prof. Sun's supervision and guidance.

Acknowledgments

This Ph.D. thesis work was accomplished in Prof. Xueliang (Andy) Sun's Nanomaterials and Energy Group at the University of Western Ontario (UWO), Canada. Herein, it is my tremendous pleasure to express my acknowledgments to everyone who has helped me and contributed to my work throughout the past four years.

I would first like to express my sincerest gratitude and respect to my supervisor Prof. Xueliang (Andy) Sun, a professor in Department of Mechanical and Materials Engineering at UWO, Canada Research Chair, Fellow of the Canadian Academy of Engineering and Fellow of the Royal Society of Canada. I am very grateful that Prof. Sun provided great opportunity and an incredible platform for me to work and gave me strong support for my research in the past four years. As my supervisor, Prof. Sun always encouraging me to think deeply about the fundamental scientific issues and guide me how to design strategies to address the problems. His prospective vision, careful guidance, as well as his personal charisma have greatly inspired me. I believe that all the experience, knowledge, and technical skills I gained here would make a profound impact in my future career and life.

I would like to extend my heartfelt gratitude to our lab manager Mrs. Ruying (Kathy) Li, for her strong support and countless help not only in my work, but also in my life. Without her help, my research could not be carried out smoothly. She has always been supporting and encouraging me with her loving heart, bring me endless warmth in the past four years. Words are not enough to express my gratitude towards her in my mind.

I must acknowledge my advisory committee members, Dr. Jun Yang and Dr. Takashi Kuboki, for their invaluable advice towards my Ph.D work. I would also like to thank the examiners of my thesis defense, Dr. Christian Kuss, a professor in Energy Material at University of Manitoba, Dr. Clara Wren, a professor in the Department of Chemistry at UWO, Dr. Liying Jiang, a professor in the Mechanical and Material Engineering department at UWO, and Dr. Eric Johlin, a professor in the Mechanical and Material Engineering department at UWO, for their careful examination on my thesis and helpful discussion and suggestions.

Next, I have been indebted to all current and former members in Dr. Sun's group at UWO. I would like to thank Dr. Qian Sun, Dr. Hossein Yadegari, and Dr. Changtai Zhao for their

invaluable advice and constructive comments on my research. I am grateful for the knowledge and skills that they have shared and consider myself lucky to have had the chance of learning from them. In addition, I would like to thank Dr. Xia Li, Dr. Yang Zhao, Dr. Biqiong Wang, Dr. Biwei Xiao, Dr. Fei Sun, Dr. Xiaofei Yang, Dr. Zhongxin Song, Mr. Jianneng Liang for their training on experimental apparatus, material synthesis, and professional software. I would also like to extend my appreciations to Miss. Jing Luo, Dr. Changhong Wang, Mr. Keegan Adair, Dr. Jiwei Wang, Miss Xuejie Gao, Dr. Sizhe Wang, Mr. Yipeng Sun, Mr. Junjie Li, Mr. Kieran Doyle Davis, Miss Alicia Koo, Dr. Yulong Liu, Dr. Xiaoyuan Zeng, Dr. Hanyu Huo for their help on discussing/editing my work. Last but not least, thanks to every other colleagues from the groups: Dr. Wei Xiao, Dr. Dawei Wang, Dr. Jianwen Liang, Mrs. Xiaona Li, Dr. Sixu Deng, Mr. Yao Yao, Dr. Weihan Li, Mrs. Minsi Li, Mr. Feipeng Zhao, Mrs. Shumin Zhang, Dr. Lei Zhang, Dr. Muhammad Iqbal, Dr. Li Hou, Dr. Fanpeng Kong, Miss. Mengxue He, Mr. Tiansheng Mu, Mr. Matthew Zheng; and all the former members who studied and worked in the group.

I would like to express my appreciation to two of my roommates, Miss. Zhe Li and Mrs. Shuang Chen, for their cares and accompany. I will never forget every day we spent together. Wish you all best in future.

Finally, I would like to express my gratitude to my parents Mr. Jingqing Lin, Mrs. Huanping Sun, my elder sister Mrs. Xiaofen Lin, and my little brother Mr. Jianwu Lin, for their love, encouragement, and support throughout the four years study and my life. I love you all!

Xiaoting Lin

University of Western Ontario

August 27th, 2020

Table of Contents

List of Figures

List of Appendices

List of Abbreviations

3D: three-dimensional

A

ALD: atomic layer deposition

B

BET: Brunauer-Emmett-Teller

B-OLC: boron-doped onion like carbon

C

CE: Coulombic efficiency

CNFs: carbon nanofiber

CNTs: carbon nanotubes

CP: carbon paper

CVD: chemical vapor deposition

D

DEGDME: diethylene glycol dimethyl ether

DFT: density functional theory

DMSO: dimethyl sulfoxide

DLC: diamond-like carbon

E

EG: ethylene glycol

EIS: electrochemical impedance spectroscopy

EVs: electric vehicles

F

FEC: fluoroethylene carbonate

FE-SEM: field emission scanning electron microscope

G

GO: graphene oxide

GNS: graphene nanosheets

H

HRTEM: high resolution transmission electron microscopy

HXMA: hard X-ray micro-analysis

L

LIBs: lithium ion batteries

LE: liquid electrolyte

M

MLD: molecular layer deposition

N

NCNTs: nitrogen doped carbon nanotubes

NCNT-CP: nitrogen doped CNT on carbon paper

NCFs: nitrogen doped carbon fibers

N-GNSs: nitrogen doped graphene nanosheets

NIBs: Na-ion batteries

NMBs: Na-metal batteries

O

OER: oxygen evolution reaction

ORR: oxygen reduction reaction

OMC: ordered mesoporous carbon

P

PCSs: porous carbon spheres

PDIC: phenylene diisocyanate

PVDF: poly(vinylidene fluoride)

R

rGO: reduced graphene oxide

S

SAED: selected area electron diffraction

SEM: scanning electron microscopy

SEI: solid electrolyte interphase

SSEs: solid-state electrolytes (SSEs)

T

TEM: transmission electron microscopy

TEGDME: tetraethylene glycol dimethyl ether

TMA: trimethylaluminum

TOF-SIMS: time-of-flight secondary ion mass spectrometry

V

VACNTs: vertically aligned carbon nanotubes

X

XAS: X-ray absorption spectroscopy

XPS: X-ray photoelectron spectroscopy

XRD: X-ray powder diffraction

<div align="center">

Chapter 1

</div>

1 Introduction

1.1 Superoxide-based Na-O$_2$ batteries

With the depletion of non-renewable fossil fuels and increasing environmental concerns, development of green and sustainable energy is of considerable significance.[1] The success of lithium-ion batteries (LIBs) has contributed to the advancement of portable electronic devices, while their limited energy density cannot satisfy the stringent demands of emerging electric vehicles (EVs).[2, 3] The development of high-energy-density battery technologies has never been more urgent.[4-6]

Non-aqueous Li-O$_2$ batteries have captured significant attention due to their high theoretical energy densities in the past few years.[7-9] However, the practical application of Li-O$_2$ batteries has been hindered by their high charge overpotential, which severely deteriorates the cell performance.[9-13] As an alternative to Li-O$_2$ battery, Na-O$_2$ battery do not suffer from the negative effects of high charge overpotential even with pure carbon cathodes, promising a high energy efficiency and clean chemistry.[14-16] The theoretical energy densities of Na-O$_2$ batteries are calculated to be 1105 and 1602 Wh kg^{-1} based on the formation of NaO$_2$ and Na$_2$O$_2$, respectively, which is 6-9 times higher than that of LIBs. With these advantages, as well as the low cost and natural abundance of sodium metal, Na-O$_2$ batteries show great application potential for EV transportation in the future.

Although the electrochemical formation of Na$_2$O$_2$ (mostly Na$_2$O$_2 \cdot$2H$_2$O) delivers higher theoretical energy density than that of NaO$_2$, peroxide-based Na-O$_2$ batteries exhibit a high charge overpotential like Li-O$_2$ cells. In sharp contrast, the electrochemical reduction of NaO$_2$ exhibits a low charge overpotential, and thus the concerns of electrolyte decomposition, cathode degradation, and contaminants formation at high voltages can be avoided. Compared to Na$_2$O$_2$, NaO$_2$ is identified as the only discharge product of Na-O$_2$ batteries with a dry non-aqueous electrolyte and ultrapure oxygen gas. Therefore, this thesis mainly focuses on enhancing the electrochemical performance of superoxide-based Na-O$_2$ batteries via addressing the challenges of this battery system.

1.2 Challenges of superoxide-based Na-O$_2$ batteries

Important progress related to the electrochemistry of Na-O$_2$ batteries has been achieved. However, the practical discharge capacities of Na-O$_2$ batteries are far from the theoretical value, and the cycling performance is poor. It is widely accepted that the inefficiency of the air electrode and Na anode are primarily responsible for the low capacity, poor safety, and limited cycle life of state-of-the-art Na-O$_2$ batteries. The major challenges and issues of the electrodes in superoxide-based Na-O$_2$ batteries can be summarized as follows:

1) Pore clogging and insufficient O$_2$ transportation within the air electrode

The discharge product of Na-O$_2$ battery (NaO$_2$) is insoluble in the organic electrolyte and will precipitate within the pores of the air electrode during the discharge process. Meanwhile, the limited solubility and low diffusivity of O$_2$ in the organic electrolyte results in the relative higher local charge density distribution on the air electrode near the O$_2$ reservoir. Consequently, the insoluble NaO$_2$ products will preferentially deposit at the air electrode that faces the oxygen reservoir. Such a distribution of the NaO$_2$ potentially clogs the pores at the oxygen side and further block the O$_2$ transport pathways, resulting in a premature cease of the discharge process and underutilization of the air electrodes.

2) Air electrodes degradation.

Carbon-based materials are widely used as the air electrodes in non-aqueous Na-O$_2$ batteries. However, the reactive NaO$_2$ can directly oxidize the carbon cathode, especially at high charge voltages. Further, the nucleophilic attack of O$_2^-$ intermediate towards the cathode binders also contribute to the air electrodes degradation. Noted that the singlet ^{1}O$_2$ that generated during the operation of Na-O$_2$ batteries is also a problematic species, which can result in carbon cathode corrosion and electrolyte decomposition. The side products are hard to decompose during the subsequent charging process and will gradually cover the active sites of the cathode. This phenomenon will lead to a gradual increase in the charge overpotential, capacity fading during cycling and limited cycle life.

3) Uncontrollable Na dendrite growth and cell short circuit

Uneven stripping/plating of Na metal can result in the formation of dendritic Na structures, which can penetrate through the solid-electrolyte interphase (SEI) film on the Na electrode. The repeated breakage and repair of the SEI layer induces continuous consumption of the organic electrolyte and Na metal anode, resulting in decreased Coulombic efficiency along with increased interfacial cell resistance. Premature Na-O_2 cell death can be expected after the electrolyte or Na metal is eventually exhausted. Moreover, the accumulation of sharp Na dendrites may penetrate through the separator, causing safety concerns over internal cell short circuits.

4) Na anode corrosion induced by O_2/O_2^- crossover

The electrochemical power source of Na-O_2 batteries is based on conversion reactions, in which solvated O_2 and superoxide (O_2^-) intermediates are involved. The conventional porous glass fiber separator cannot block the diffusion of O_2/O_2^- from the cathode to the Na anode. The O_2/O_2^- crossover in Na-O_2 batteries can induce severe passivation/parasitic reactions on the Na metal anode, resulting in severe Na corrosion. The gradual accumulation of side products on the Na surface could result in blockage of Na^+ migration, increased polarization, and eventually battery failure.

Therefore, effective strategies need to be developed in order to address the critical challenges of the Na-O_2 batteries before the practical application of this novel battery system.

1.3 Thesis objectives

The development of efficient air electrodes and highly stable Na anodes has been of great significance due to their crucial roles in determining the overall Na-O_2 cell performance. In order to improve the electrochemical performance of Na-O_2 batteries, the authors have devoted significant time to facilitate continuous O_2 transportation by designing an advanced air electrode, and to stabilize the Na metal anode by suppressing the Na dendrite growth and alleviating the Na corrosion induced by O_2/O_2^- crossover. The underlying degradation mechanism of Na-O_2 cell performance was also revealed. These studies can be separated into two major categories:

Part 1: Design of highly efficient air electrode

i). To prevent the pore clogging and underutilization of the air electrodes induced by the limited O_2 transportation, novel freestanding "O_2 breathable" air electrodes were designed by using 3D printing technique. The characterization on the discharge products, as well as the influence of air electrode structure on the capacity and cycle life of Na-O_2 batteries will be demonstrated.

Part 2: Different strategies for the stabilization of Na metal anode

ii). To reveal the crucial role of the Na anode in determining the Na-O_2 cell performance, a novel Na-O_2 battery using carbon paper (CP) protected Na anode was designed. The effect of O_2^- crossover on the Na-O_2 cell performance will be studied. Also, the effectiveness of CP interlayer in preventing Na dendrite growth, alleviating Na degradation, as well as enhancing the reversibility and cycling performance of Na-O_2 batteries will be investigated.

iii). To address the O_2/O_2^- crossover and Na dendrite growth issues comprehensively, hybrid solid-state (HSS) Na-O_2 batteries were designed. The electrochemical performance of HSS Na-O_2 batteries with solid-state electrolyte (SSE) shield and protected Na anode, as well as the underlying degradation mechanisms of Na metal anode in the presence of O_2 and/or O_2^- crossover will be investigated in detail.

iv). To enable high-performance Na-O_2 batteries, the MLD alucone layer protected Na anode (Na@alucone) was integrated with SSE to construct HSS Na-O_2 batteries. Electrochemical behaviors of Na-O_2 battery with a Na@alucone anode, as well as the understanding with scanning electron microscopy (SEM) and time-of-flight secondary ion mass spectrometry (TOF-SIMSs) study on cycled Na@alucone anodes will be investigated.

v). To address the safety issue and enhance the Na-O_2 battery performance, flame-resistant, dendrite-free and O_2/O_2^-- impermeable composite electrolyte was designed. The properties of composite electrolyte, as well as the electrochemical performance of resultant quasi-solid-state Na-O_2 batteries will be investigated.

1.4   Thesis organizations

This thesis consists of 9 chapters (two introductory chapters, one experimental and characterization details, five articles, and one conclusive chapter) and is organized according to the requirements on Integrated-Article form as outlined in the *Thesis Regulation Guide* by the School of Graduate and Postdoctoral Studies (SGPS) of the University of Western Ontario. Specially, it organizes according to the following sequence:

Chapter 1 gives a brief introduction of superoxide-based Na-O$_2$ batteries and their challenges. Furthermore, the research objectives and the thesis structure are also stated.

Chapter 2 reviews the recent development of non-aqueous Na-O$_2$ batteries. From the fundamental understanding on the electrochemistry of Na-O$_2$ battery system, the problems that may result in the cell performance deficiency, to the methods that researchers have adopted to address these problems.

Chapter 3 outlines experimental methods and analytical apparatus used in the work of this thesis.

Chapter 4 presents a study on the 3D printing of "O$_2$ breathable" air electrodes for Na-O$_2$ batteries. The underutilization of air electrodes and poor cycling performance caused by limited O$_2$ transportation within the air electrode was well addressed by introducing O$_2$ transport channels using 3D printing technique. In addition, the diameter of the O$_2$ transport channels in the air electrode is optimized based on the balance between electronic conductivity and the O$_2$ transportation. This is the first study related to fabricating free-standing "O$_2$ breathable" air electrodes for Na-O$_2$ batteries via 3D printing.

Chapter 5 systematically studies the electrochemical performance of Na-O$_2$ batteries using CP protected Na anodes. It was found that the presence of CP on the Na metal facilitates dense Na deposition without dendritic Na growth, preventing the cell from short-circuiting. The research work also verifies the O$_2$/O$_2^-$ crossover issue in Na-O$_2$ batteries and presents the effectiveness of CP in alleviating the Na degradation induced by O$_2$/O$_2^-$ crossover. The crucial role of the Na anode in determining the Na-O$_2$ battery performance is emphasized.

Chapter 6 reports a novel hybrid solid-state Na-O$_2$ battery based on NASICON-type SSE and a protected Na anode. The dense structure of the SSE can effectively suppress the O$_2$/O$_2^-$ crossover, which mitigated the Na degradation and reversible charge capacity loss. In addition, adding a 3D protection layer on the Na anode facilitated dendrite-free Na deposition within the conductive matrix. The nature of the SEI layer on the Na anode in relation to O$_2$/O$_2^-$ crossover is systematically analyzed in this chapter.

Chapter 7 investigates the electrochemical behaviors of the alucone protected Na anode during the Na-O$_2$ battery operation. It was found that the alucone protective layer is vulnerable to the superoxide attack and incapable of facilitating stable cycling of Na-O$_2$ batteries, in sharp contrast to its stable performance in Na-metal batteries (NMBs). The results indicate that the distinct behaviors of alucone protected Na anodes in NMBs and Na-O$_2$ batteries was reasonably related to the different working principles of two battery systems. The study also proposed an effective strategy to eliminate the implications of the unstable Na protective layer, promising a long cycle life of Na-O$_2$ batteries.

Chapter 8 reports a composite electrolyte consisting of a 3D porous SSE framework that is infused with a gel polymer electrolyte (PSSE/GPE) for Na-O$_2$ batteries. The flame-resistivity, dendrite-free and O$_2$/O$_2^-$ impermeable properties of the fabricated hybrid electrolyte, as well as the cycling stability of constructed quasi-solid-state Na-O$_2$ batteries are systematically investigated.

Chapter 9 summarizes the results and contributions of the thesis work. Furthermore, the author gives some personal opinions, perspectives, and suggestions regarding future research outlook on superoxide-based Na-O$_2$ batteries.

1.5   Reference

1. Liang, J.; Sun, Z.-H.; Li, F.; Cheng, H.-M., *Energy Storage Materials* 2016, 2, 76-106.

2. Feng, N.; He, P.; Zhou, H., *Advanced Energy Materials* 2016, 6, (9), 1502303.

3. Bruce, P. G.; Freunberger, S. A.; Hardwick, L. J.; Tarascon, J.-M., *Nature Materials* 2012, 11, (1), 19-29.

4. Shao, Y.; Ding, F.; Xiao, J.; Zhang, J.; Xu, W.; Park, S.; Zhang, J.-G.; Wang, Y.; Liu, J., *Advanced Functional Materials* 2013, 23, (8), 987-1004.

5. Yadegari, H.; Sun, Q.; Sun, X., *Advanced Materials* 2016, 28, (33), 7065-7093.

6. Yang, X.; Li, X.; Adair, K.; Zhang, H.; Sun, X., *Electrochemical Energy Reviews* 2018, 1, (3), 239-293.

7. Oh, S. H.; Nazar, L. F., *Advanced Energy Materials* 2012, 2, (7), 903-910.

8. Lee, D. U.; Xu, P.; Cano, Z. P.; Kashkooli, A. G.; Park, M. G.; Chen, Z., *Journal of Materials Chemistry A* 2016, 4, (19), 7107-7134.

9. Amanchukwu, C. V.; Harding, J. R.; Shao-Horn, Y.; Hammond, P. T., ; *Chemistry of Materials* 2015, 27, (2), 550-561.

10. Liu, Y.; Wang, L.; Cao, L.; Shang, C.; Wang, Z.; Wang, H.; He, L.; Yang, J.; Cheng, H.; Li, J.; Lu, Z., *Materials Chemistry Frontiers* 2017, 1, (12), 2495-2510.

11. Yao, X.; Dong, Q.; Cheng, Q.; Wang, D., *Angewandte Chemie International Edition* 2016, 55, (38), 11344-11353.

12. Ma, Z.; Yuan, X.; Li, L.; Ma, Z.-F.; Wilkinson, D. P.; Zhang, L.; Zhang, J., *Energy & Environmental Science* 2015, 8, (8), 2144-2198.

13. Zhao, G.; Mo, R.; Wang, B.; Zhang, L.; Sun, K., *Chemistry of Materials* 2014, 26, (8), 2551-2556.

14. Hartmann, P.; Bender, C. L.; Vračar, M.; Dürr, A. K.; Garsuch, A.; Janek, J.; Adelhelm, P., *Nature Materials* 2013, 12, (3), 228-232.

15. Hartmann, P.; Bender, C. L.; Sann, J.; Durr, A. K.; Jansen, M.; Janek, J.; Adelhelm, P., *Physical Chemistry Chemical Physics* 2013, 15, (28), 11661-11672.

16. Bing, S.; Katja, K.; Xiuqiang, X.; Paul, M.; Zhangquan, P.; Guoxiu, W., *Advanced Materials* 2017, 29, (48), 1606816.

Chapter 2

2   Literature review

In this chapter, a comprehensive and detailed literature review of the non-aqueous $Na-O_2$ batteries is presented. From the fundamental understanding on the electrochemistry of $Na-O_2$ battery system, the main problems that may result in the decay of $Na-O_2$ cell performance, to the strategies that researchers have adopted to address these problems.

2.1 Introduction

The depletion of fossil fuels and its undesirable environmental consequences have quickly become a dilemma faced by the world.[1-3] In order to solve the issue of ever-growing emissions and save resources for future generations, several secondary energy-storage systems have been developed.[4-11] Rechargeable lithium-ion batteries (LIBs) have dominated the portable electronics market since their first commercialization by Sony in 1991. However, the specific capacity of the LIBs has been limited to a low value of 140~200 mAh g^{-1}, which is insufficient and unable to keep pace with the requirements of next-generation electric vehicles (EVs).

With this perspective, metal-O_2 batteries with high theoretical energy densities have attracted extensive research attention.[12-16] Unlike traditional LIBs, metal-O_2 batteries are designed with open systems that enable the uptake of oxygen gas from the surrounding environment. In principle, the unique cell design ensures that the reactants do not occupy the valuable volumetric and gravimetric space of the battery, which allows for an infinite supply of O_2 from nature.[6, 13, 17] Among various metal-O_2 batteries, non-aqueous Li-O_2 battery system has attracted enormous research attention owing to its high theoretical energy density, which is significantly higher than that of commercial LIBs and can compete with those of gasoline energy systems.[18, 19] However, the practical application of Li-O_2 batteries have been hindered by their high charge overpotential, which result in a low round-trip energy efficiency and limited cycle life.[20]

At first, research on non-aqueous Na-O_2 batteries was largely motivated by the low cost, non-toxicity and abundance of sodium compared to lithium. In addition, Na-O_2 batteries can achieve energy densities of up to 1105 and 1602 Wh kg^{-1} with the discharge products of NaO_2 and Na_2O_2, respectively, which is second only to that of the Li-O_2 battery system. Compared to Li-O_2 batteries, Na-O_2 cells exhibit lower charging overpotential that ensures a higher energy efficiency and clearer chemistry.[20, 21] Furthermore, the negative effect of high charge overpotential, such as electrolyte decomposition, air electrode degradation, and detrimental contaminants formation at high voltages, can be significantly avoided. With these advantages, Na-O_2 cells are considered as promising energy storage devices for next-generation EV transportation.

Although Na-O$_2$ batteries are still at their initial stage of development, impressive breakthroughs have been achieved.[17, 22] Along with the extensive efforts towards exploring the electrochemistry of Na-O$_2$ batteries, much attention has been devoted to improving the Na-O$_2$ battery performance by designing advanced electrodes since their efficiencies play crucial roles in determining the overall cell performance.[23-26] Therefore, in this review, we intend to introduce the recent advancements towards improving the performance of non-aqueous Na-O$_2$ batteries via rational design of the electrodes. Firstly, the reaction mechanism of non-aqueous Na-O$_2$ batteries and the key issues that may result in the cell performance deficiency will be systematically introduced. Recent reported literatures related to air electrodes and Na anode design will be sequentially presented in the following sections. Finally, the remaining challenges and future perspectives for the development of Na-O$_2$ batteries are proposed.

2.2   Principle of a non-aqueous Na-O$_2$ battery

2.2.1   Electrochemistry of a non-aqueous Na-O$_2$ battery

A typical non-aqueous Na-O$_2$ battery is composed of a sodium metal anode, a carbon cathode and a separator filled with Na$^+$ conducting organic electrolyte. A schematic illustration of a typical non-aqueous Na-O$_2$ cell configuration is shown in **Figure 2.1**.
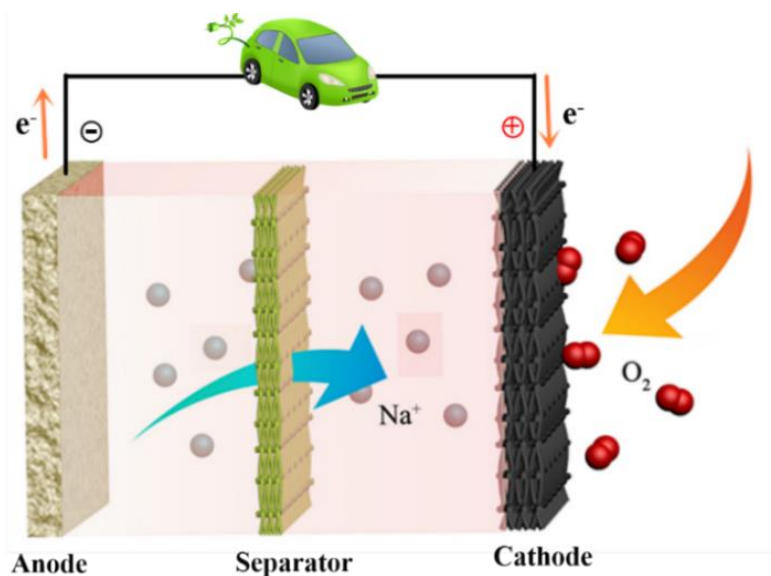
Figure 2.1 Schematic illustration of a non-aqueous Na-O$_2$ cell configuration.

Different to the reversible intercalation of Na^+ between the cathode and the anode in Na-ion batteries (NIBs), the energy in Na-O$_2$ batteries is stored and released based on conversion reactions. During the discharge process, sodium metal is oxidized to sodium ions (Na^+), which migrate towards the cathode through the organic electrolyte. At the same time, the O$_2$ is reduced on the cathode surface to form reduced oxygen species (O_2^- or O_2^{2-}), which will combine with migrated Na^+ to form metal oxides as the discharge products. During the charging process, the reactions will proceed in the reverse direction with Na metal plating on the anode and O$_2$ evolving at the cathode. While unlike the formation of Li$_2$O$_2$ as the major discharge product in Li-O$_2$ batteries, there are two discharge products (NaO$_2$ and Na$_2$O$_2$) produced in Na-O$_2$ battery system.[27, 28] The associated reaction equations can be briefly presented as follows:

Negative electrode: $Na \rightarrow Na^+ + e^-$ (1)

Positive electrode: $O_2 + e^- \rightarrow O_2^-$ (2)

Or $O_2 + 2e^- \rightarrow O_2^{2-}$ (3)

Overall: $Na + O_2 \rightarrow NaO_2 \quad E^0 = 2.27V$ (4)

Or $2Na + O_2 \rightarrow Na_2O_2 \quad E^0 = 2.33V$ (5)

In Na-O$_2$ batteries, the oxygen reduction reaction (ORR) can proceed via a one-electron pathway or a two-electron transfer process with the formation of NaO$_2$ or Na$_2$O$_2$, respectively. The formation of Na$_2$O$_2$ delivers higher theoretical energy density (1605 Wh kg^{-1}) compared with that of NaO$_2$ (1108 Wh kg^{-1}).[29] However, peroxide-based (mostly Na$_2$O$_2$·2H$_2$O) Na-O$_2$ batteries suffer from the high charge overpotential (> 1V), which is comparable to that of Li-O$_2$ cells.[17, 30, 31] In contrast, the NaO$_2$ can be electrochemically decomposed at a low voltage, avoiding the severe electrolyte decomposition and air electrode degradation at high voltages. Since the Na-O$_2$ cell performance is greatly affected by the nature of discharge products, controlling the formation of desired discharge product is crucial for achieving high-performance Na-O$_2$ batteries. Although both NaO$_2$ and Na$_2$O$_2$ have been predicted as the main discharge products of Na-O$_2$ batteries by using theoretical

computational techniques, it is still very difficult to identify which product is favorably produced based solely on thermodynamic data.[32, 33]

Experimentally, important progress has been made in terms of electrochemistry of Na-O$_2$ batteries under certain conditions. Also, some of the physicochemical factors that affect the reaction pathway of Na-O$_2$ batteries have been investigated. Firstly, the nature of the electrolyte has a profound effect on the electrochemistry of Na-O$_2$ batteries. As stated in previous report, distinct to the formation of NaO$_2$ via solution-mediated route in the solvents with a high donor number, low donor number solvents incapable of forming an ion pair with O$_2^-$ intermediates, and consequently contribute to the formation of Na$_2$O$_2$ on the Au electrode surface via further reduction of O$_2^-$ intermediate.[34] Moreover, the chemical stability of electrolytes against the O$_2^-$ attack is crucial for Na-O$_2$ cell performance. Formation of Na$_2$O$_2$·2H$_2$O due to the degradation of NaO$_2$ in the organic electrolyte has also been reported, and electrolyte solvents with high acid dissociation constants are considered beneficial to the formation of NaO$_2$.[35, 36] Therefore, gaining control of the mechanistic direction of discharge process (NaO$_2$ or Na$_2$O$_2$) with different electrolytes may enhance the ability to tailor the energy density of Na-O$_2$ batteries.

Except for electrolyte, surface chemistry and electrocatalytic activity of cathodes also play substantial roles in the electrochemical reaction paths. The discharge product of commercial H2315 carbon paper (CP) has been widely reported to be NaO$_2$ cubes.[20, 37] While after introducing Pd catalysts on the CP cathode, two-electron electrochemical process occur with the formation of Na$_2$O$_2$·2H$_2$O as the discharge product.[29] In our recent study, we found that the presence of oxygen functional groups (-COOH, -OH et al.) in CP cathodes can also facilitate the growth of peroxide-based discharge products through a surface-mediated path.[38] Aside from the composition and formation mechanism of discharge products, the morphology of NaO$_2$ also can be tuned by changing the properties of solvents and air electrodes.[39-41] Previous studies reported that trace H$_2$O additives in the electrolyte can be beneficial for the cell discharge capacity by promoting the solution-mediated growth of large NaO$_2$ cubes.[42, 43] However, it should be noted that excess water in the electrolyte tends to react with NaO$_2$ to produce Na$_2$O$_2$·2H$_2$O and NaOH during the

cell operation.[44] Moreover, the high content of humidity in the O_2 gas atmosphere also contributes to the formation of hydroxide and results in poor Na-O_2 cell performance.[45, 46]

In fact, the formation of peroxide-based (Na_2O_2, $Na_2O_2 \cdot 2H_2O$) discharge products in Na-O_2 batteries is highly related to the presence of O_2^- intermediates and their further reduction via chemical or electrochemical pathways. The minor difference in operating parameters of Na-O_2 batteries helps to explain the origin of discharge products diversity in different groups. While compared to Na_2O_2, the NaO_2 is identified as the only discharge product of non-aqueous Na-O_2 batteries using dry ether-based electrolyte and ultrapure O_2 gas.

2.2.2   Challenges of a non-aqueous Na-O_2 battery

Although Na-O_2 batteries have shown great potential as promising alternatives to LIBs due to their high theoretical energy density, several key challenges still need to be addressed before its commercialization.
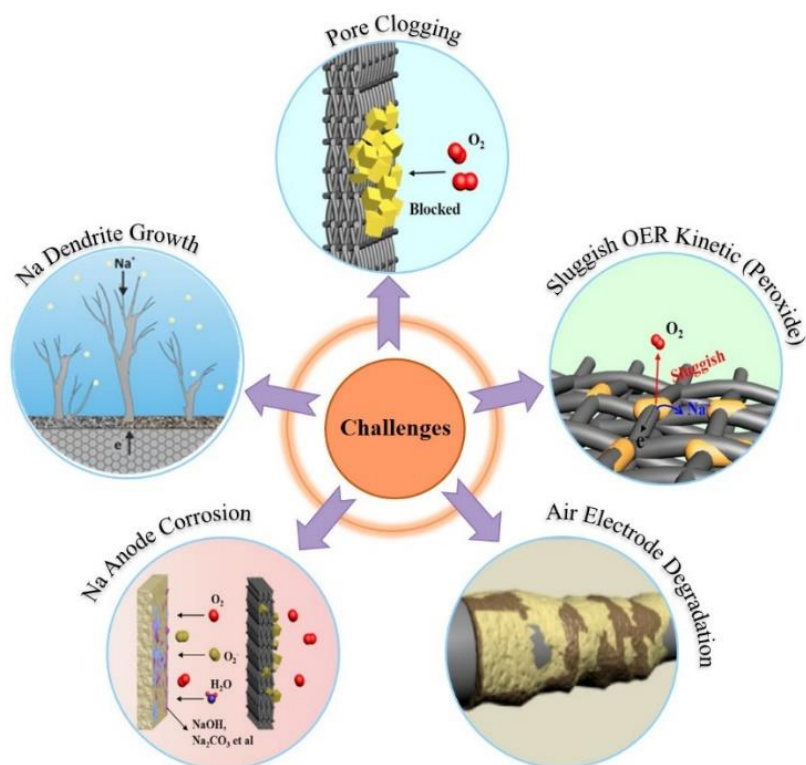
Figure 2.2 The key issues of electrodes in non-aqueous Na-O_2 batteries. [23, 47]

The operating atmosphere (humidity and gas contaminations) is an important factor that affects the nature of discharge products and the Na-O_2 cell performance.[46] Recent studies have also reported organic electrolytes that cannot tolerate the attack of oxygen species (O_2^-, $^1O_2$ et al.) suffer from the decomposition problem and generate unfavorable side products, which is harmful to the reversible charge capacity and cycle life of Na-O_2 batteries.[17] However, it is widely accepted that the inefficiency of the air electrode and Na metal anode are primarily responsible for the low capacity, poor safety and limited cycle life of state-of-the-art Na-O_2 batteries. The main challenges facing the development of air electrodes and Na anodes in non-aqueous Na-O_2 batteries are highlighted as follows (**Figure 2.2**):

(a) **Pore clogging of the air electrodes**. The dominant discharge product of non-aqueous Na-O_2 batteries (insulating Na_2O_2, NaO_2) are insoluble in the organic electrolyte, which will deposit on the surface or within the pores of the air electrode during the discharge process. Moreover, the limited solubility and low diffusivity of O_2 in the electrolyte results in the relative higher O_2 concentration on the air electrode facing the O_2 reservoir. Consequently, the discharge products will preferentially deposit in the air electrode region with sufficient exposure to O_2.[48] The accumulation of discharge products potentially clog the air electrode pores at the oxygen side and restrict O_2 access to the interior air electrode, resulting in the premature termination of discharge process and underutilization of air electrodes. [20, 49] Therefore, the achievable discharge capacity is much lower than the theoretical value.[49]

(b) **Sluggish electrochemical oxidation kinetics of Na_2O_2**. With the formation of NaO_2, the Na-O_2 batteries can be recharged with a low charge overpotential even with the pure carbon cathodes.[20] However, when it comes to Na_2O_2 (mostly $Na_2O_2 \cdot 2H_2O$), sluggish electrochemical oxidation kinetics with high charge overpotential can be observed on carbon-based air electrodes.[29] On one hand, the high charge overpotential lowers the round-trip energy efficiency by requiring greater power to recharge than can be recovered during the discharge process. On the other hand, the high charge potential will trigger severe electrolyte decomposition and carbon corrosion at high voltages, resulting in fast decay of the Na-O_2 battery performance.[23]

(c) **Air electrodes degradation.** Carbon material is widely used as the air electrode in Na-O_2 batteries. However, the discharge products (Na_2O_2, NaO_2) are problematic species towards the carbon cathode itself. Direct oxidation of carbon cathodes at high voltage has been reported (> 3.0V), with the formation of various insulating side products on the cathode surface. The undesired decomposition of cathode binders induced by hydrogen abstraction of O_2^- partially contributes to the air electrode degradation.[41] Moreover, carbonate-based side products can be formed on the outer shell of NaO_2 cubes due to the instability of organic electrolyte against the NaO_2.[24, 50] All of these side products are hard to decompose during the subsequent charging process, and will gradually cover the active sites of the carbon cathode. This leads to a gradual increase in the charge overpotential, capacity fading during cycling and limited cycle life.

(d) **Uncontrollable Na dendrite growth.** Na metal reacts easily with the surrounding electrolyte solvents, resulting in the formation of a solid electrolyte interphase (SEI) layer. Nonuniform stripping/plating of Na metal during long-term cycling can result in the formation of dendritic Na structures, which can penetrate the SEI layer. On one hand, the repeated breakage and repair of the SEI layer induces continuous consumption of the organic electrolyte and Na metal, resulting in decreased Coulombic efficiency along with increased interfacial resistance due to the accumulation of side products on the Na anode surface.[51] Premature cell death can be expected after the electrolyte or Na metal is eventually exhausted. On the other hand, the accumulation of sharp Na dendrites may penetrate through the separator, causing safety concerns over internal short circuits.[47, 52]

(e) **Na anode corrosion caused by contaminants crossover.** The electrochemical power source of Na-O_2 batteries is based on conversion reactions, in which solvated O_2 and O_2^- intermediate are involved. The dissolved O_2/O_2^- tends to migrate toward the Na metal, resulting in severe passivation/parasitic reactions on the Na metal anode.[49, 52, 53] The gradual accumulation of side products, such as NaOH, Na_2CO_3, and organic products, on the Na surface could impede Na^+ transportation, resulting in increased polarization and premature cell death. More recently, the generation of singlet oxygen species ($^1O_2$) has been reported,[54] and parasitic chemistry involving migrated $^1O_2$ at the

Na anode may also cause problems. Besides oxygen species (O_2, O_2^-, $^1O_2$), the Na anode can react with H_2O from electrolyte decomposition (or air) and further aggravate the Na degradation.[36, 43]

Based on above-mentioned challenges, multiple and combined strategies have been reported to break through the bottlenecks of Na-O_2 batteries: 1) designation of a conducting air electrode with hierarchical porous structure to alleviate the pore clogging and facilitate continuous O_2 transportation. 2) construction of air electrodes with high electrocatalytic activities to improve the oxygen evolution reaction (OER) kinetics. 3) application of 3D Na anodes or artificial layer protected Na anodes to suppress Na dendrite growth; 4) introduction of contaminants crossover impediments to alleviate/mitigate Na anode corrosion. According to these reported literatures, the following segments will introduce and summarize recent progress on air electrode design and Na metal anode protection for achieving high-performance non-aqueous Na-O_2 batteries.

2.3   Development of novel air electrodes

Since the discharge products of Na-O_2 batteries are electronically insulating and insoluble in organic electrolytes, many important properties should be considered when designing a highly efficient air electrode. For example, the air electrodes should have a high electronic conductivity to facilitate electron transportation, enough pore volume for discharge products accommodation, and optimized pore structure for rapid Na^+/O_2 mass transportation. Good mechanical strength to tolerate the volume expansion during the formation and decomposition of discharge products is also required. In this regard, carbon materials have been widely used to construct efficient air electrodes for Na-O_2 cells due to their good electrical conductivity, versatile porous nanostructure, high chemical stability and low cost.

A large number of hierarchical porous carbon-based air electrodes have been developed to alleviate the pore clogging problem and facilitate continuous O_2 transportation.[55, 56] Additionally, air electrode optimization through heteroatoms doping and catalyst attachment has also been developed to enhance the OER kinetics in peroxide-based Na-O_2 batteries.[57-59] The main focus of this section is the efficacy of various carbon-based

cathodes with unique architecture and chemical properties. The relationships between the cell performance and air electrode properties will also be discussed.

2.3.1   Pristine carbon materials

A room-temperature rechargeable Na-O_2 battery was first reported by Fu and co-workers by using a diamond-like carbon (DLC) thin film as the air electrode in 2012.[60] The DLC thin film cathode can deliver an initial discharge capacity of 1884 mAh g^{-1} at 1/10 C rate, where Na_2O_2 and Na_2CO_3 were detected as the discharge products of the constructed cell using a carbonate-based electrolyte. Kwak et al. synthesized the ordered mesoporous carbon (OMC) and evaluated it as a nanostructured conductive matrix to accommodate the nonconductive discharge products in Na-O_2 batteries.[61] The high surface area and pore volume of OMC endows the Na-O_2 battery to deliver an initial discharge capacity of 7987 mAh g^{-1} at 100 mA g^{-1}, which is significantly higher than the 4864 mAh g^{-1} capacity of a super P electrode.

In order to give a more holistic view on the rechargeability and reaction kinetics of Na-O_2 batteries, a series of carbon cathodes with specifically designed surface area and porous structure were synthesized by our group using a heat-treatment procedure (**Figure 2.3a**).[62] The results indicate that the cell discharge capacity has a linear relationship with the cathode specific surface area since a higher surface area provides more active sites to facilitate ORR and enable insoluble discharge product deposition (**Figure 2.3b**). Moreover, the morphology and chemical composition of discharge products is highly dependent on surface area and pore size of the carbon cathode, which is determined by the discharge reaction kinetics of Na-O_2 batteries (**Figure 2.3c** and **d**). The importance of cathode properties in determining the Na-O_2 cell performance was also highlighted by Bender et al..[33] Discharge capacities of Na-O_2 batteries with different types of carbon cathodes varied from 300 to 4000 mAh g^{-1} under the same experimental conditions, although NaO_2 cubes was identified as the only discharge product in all cells. Further investigations indicate that the capacity difference can be attributed to the different microstructure of the cathodes, which can greatly affect the size and morphology of the NaO_2 discharge product. More recently, to maximize the potential of the air electrode, Sun et al. prepared hierarchical porous carbon spheres (PCSs) through a facile chemical vapor deposition (CVD) method.

The typical TEM and SEM images of PCSs are shown in **Figure 2.3e-g**.[55] The air electrodes made of PCSs exhibited hierarchical porous structures that facilitated oxygen diffusion and electrolyte impregnation to the inner part of the air electrodes, contributing to the high capacity and rate capability of Na-O$_2$ batteries. More importantly, the discharge product, NaO$_2$, showed a film-like morphology, which can be easily decomposed in comparison with micrometer-sized NaO$_2$ cubes, contributing to the high reversibility of Na-O$_2$ batteries (**Figure 2.3h** and **i**).
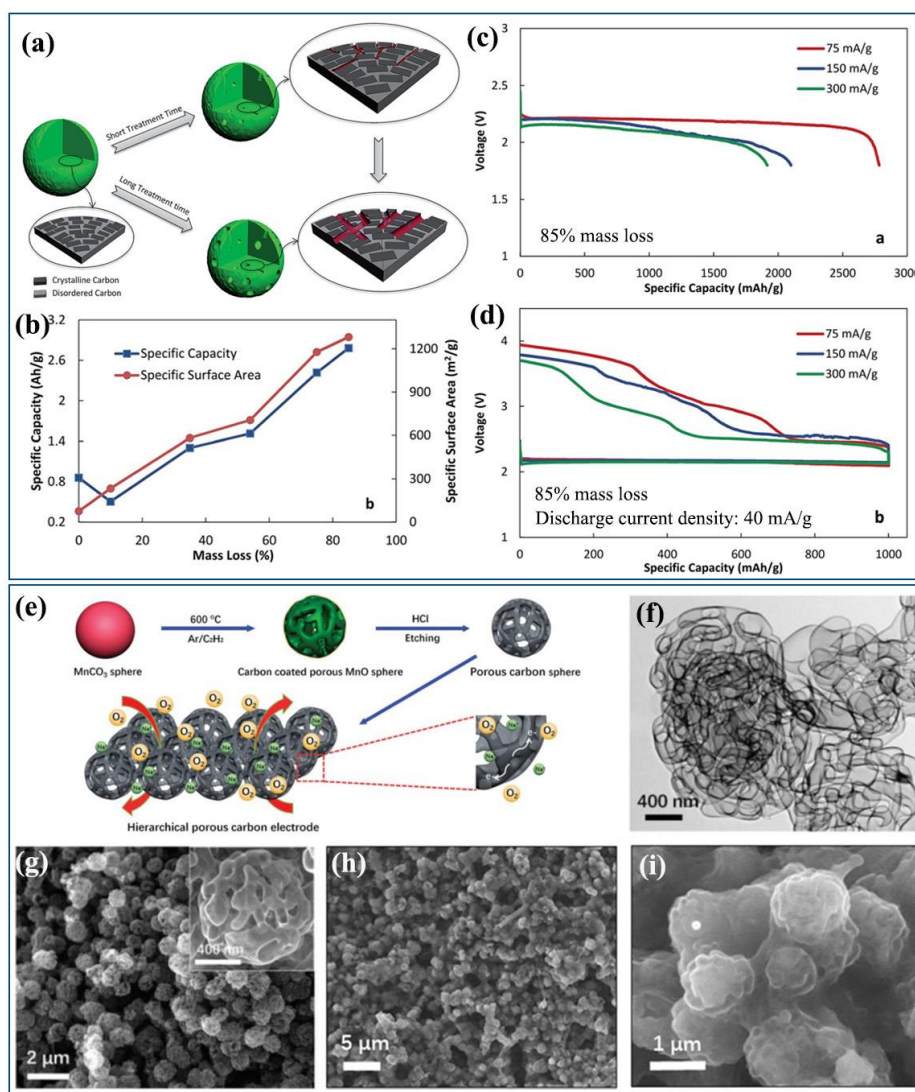
Figure 2.3 (a) Schematic diagram of the electrodes during the heat-treatment process, (b) plot of specific capacities and specific surface area of the cathode materials of the cells as a function of mass loss; (c, d) Discharge/charge curves of Na-O$_2$ cell using NH$_3$-treated

carbon materials with 85% mass loss as the cathode at different current densities.[62] (e) Schematic illustration of the synthesis processes for PCSs cathode material, The inset in (g) is a high magnification SEM image of PCSs. (f) TEM and (g) SEM images of as-prepared PCSs. (h, i) SEM images of discharged PCS electrode.[55]

One dimensional carbon nanotubes (CNTs) have also been employed as the oxygen diffusion electrode material in Na-O_2 batteries due to their high void volume between one-dimensional structures. A vertically aligned carbon nanotubes (VACNTs) electrode was reported by Zhao et al..[63] Benefiting from the reversible formation and decomposition of NaO$_2$ with a low charge overpotential, the energy efficiency of Na-O_2 cell with VACNTs electrodes is as high as 90 %. Furthermore, a high discharge capacity of 4200 mAh g^{-1} was delivered at 67 mA g^{-1} and 130 cycles can be achieved with a limited capacity of 750 mAh g^{-1}, which could be attributed to the high surface area and the interconnected, well-developed pore structure of the VACNTs electrodes. While it is also noteworthy that the optimal atmospheric conditions (static Ar/O_2 (80/20 vol %)) also contributed to the good cell performance by suppressing the side reactions involving H$_2$O. In another study, Jian et al. used a floating catalyst CVD method to prepare CNT paper composed of interpenetrating CNTs [64]. The resultant CNT paper was directly employed as the air electrode without adding any binders and additives, and a high initial discharge capacity of 7530 mAh g^{-1} was delivered at 500 mA g^{-1}. The main crystalline discharge product of constructed Na-O_2 cell is identified to be Na$_2$O$_2$·2H$_2$O through X-ray diffraction characterization.

As a typical two-dimensional material, graphene has attracted substantial attention in energy storage research.[65] Liu and colleagues, for the first time, employed graphene nanosheets (GNS) in Na-O_2 batteries in 2013.[66] Na-O_2 battery with a GNS electrode showed an excellent electrochemical performance with a high discharge capacity of 9268 mAh g^{-1}, which is superior to the 2030 mAh g^{-1} of normal carbon film cathodes tested at the same current density of 300 mA g^{-1}. Although Na$_2$O$_2$ rather than NaO$_2$ was identified as the discharge product under the effect of electrolyte composition, oxygen partial pressure and air electrode properties, GNS demonstrated its enormous potential in the application in Na-O_2 batteries. Graphene possesses high surface area and enough active

sites, which is beneficial for the ORR process of Na-O_2 batteries. However, the GNS tend to restack due to Var der Waals or capillary forces, which would decrease the active area and limit the effective diffusion of O_2 within the cathodes.[67] By controlling the freezing temperature of reduced graphene aerogels, reduced graphene oxide (rGO) air electrodes with different porosities were successfully developed by Vitoriano and co-workers.[68] They found that the air electrode porosity plays a key role in Na-O_2 cell performance by influencing the oxygen supply. Benefiting from the effective oxygen diffusion and ORR/OER reaction kinetics, rGO-based electrodes with meso-macroporosity and a narrow macropore size arrangement exhibit the best performance among all cathodes (6.61 mAh cm^{-2}). This work further indicates that tuning cathode porosity is an effective strategy to facilitate the oxygen diffusion and eliminate the diffusional/kinetic limitations towards ORR and OER during Na-O_2 cell operation, especially at high rates.

Three-dimensional (3D) carbon paper (CP) gas diffusion layer, which possesses pores on the scale of dozens of micrometers, is another good candidate of the air electrode in Na-O_2 batteries. Using CP as the air electrode in Na-O_2 batteries was first reported by Hartmann and co-workers.[20] A high initial discharge capacity of 3.3 mAh was delivered at 120 µA cm^{-2}, much higher than that of the Li-O_2 cell counterpart using the same cathode (**Figure 2.4a**). More importantly, the charge overpotential of Na-O_2 batteries is significantly lower than that of Li-O_2 batteries (**Figure 2.4b**). These results indicate the distinct reaction mechanisms between Li-O_2 and Na-O_2 battery systems, and the reversible formation/decomposition of NaO_2 cubes via one-electron transfer in Na-O_2 batteries is verified (**Figure 2.4c** and **d**). Moving forward, CP has been widely used as the air electrode to investigate the cell electrochemistry, as well as the physicochemical factors that affect the electrochemical behavior of Na-O_2 batteries.[37, 39, 42, 49, 69, 70]. While noting that both current density and O_2 pressure have a large effect on the spatial deposition of NaO_2 through the CP cathode, the maximum capacity is limited by insufficient O_2 supply as a result of CP cathode pore clogging at low current densities and high O_2 pressure (**Figure 2.4e**).[69-71] Therefore, to alleviate the pore clogging effect and enable continuous O_2 diffusion, air electrodes with non-competitive and continuous pathways for oxygen and electrolyte (Na$^+$) can be developed in the future studies.[72, 73]
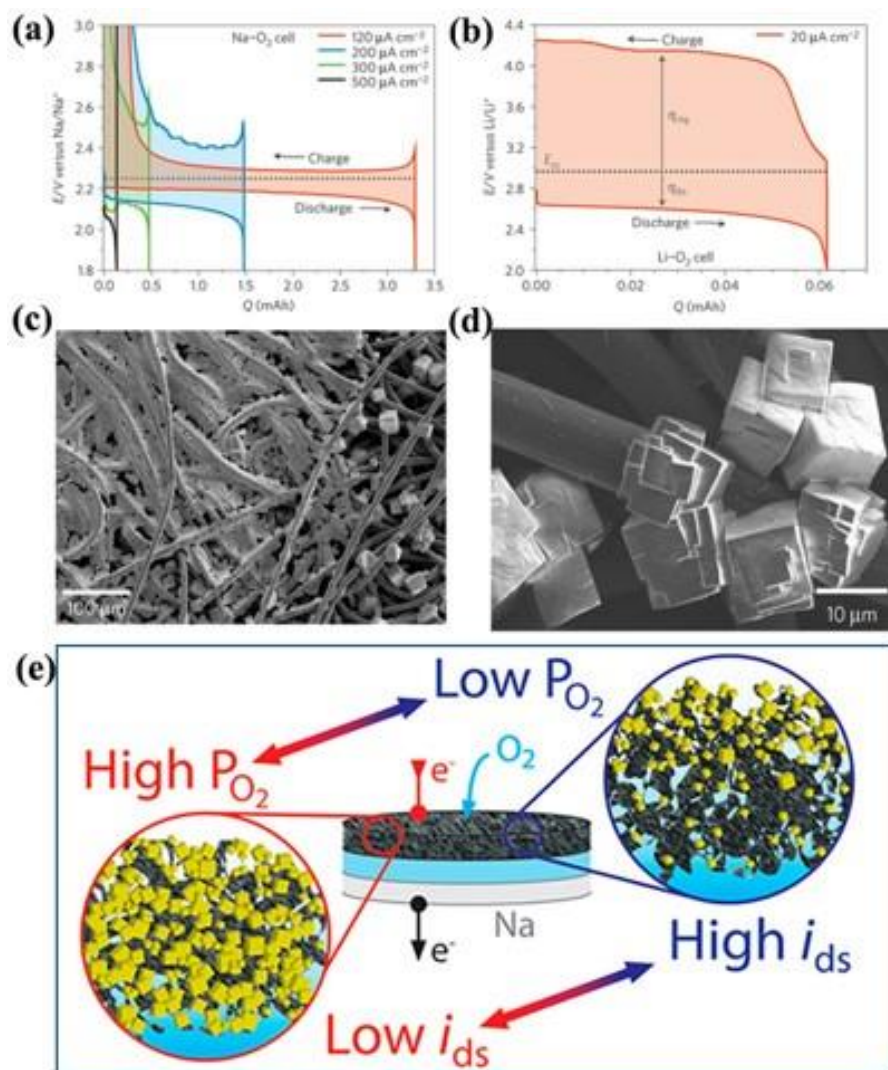
Figure 2.4 (a) Discharge-charge curves of Na-O_2 cells with CP cathodes at various current densities, (b) Discharge-charge voltage profile of a Li-O_2 cell with CP cathode for comparison. (c, d) SEM images of CP cathode after discharge to 2 mAh at 80 µA cm^{-2}.[20] (e) Schematic illustration of the effect of current density and oxygen pressure on the spatial deposition of NaO$_2$ through the cathode.[69]

2.3.2   Heteroatoms doped carbon materials

The microstructure of the air electrode is critical, since the overall cell capacity is highly dependent on the amount of insoluble discharge products that can be accommodated within the porous electrode structure. The chemical properties of the air electrode also play an important role in affecting the overall cell performance, especially for the peroxide-based

Na-O$_2$ batteries.[29] To tackle the sluggish OER kinetics of peroxide-based Na-O$_2$ batteries, air electrode optimization is essential. Doping foreign atoms, such as N, S, O and P, into the carbon cathode structure is an effective strategy to tailor the electronic structure, chemical nature, as well as the electrocatalytic activity of the cathodes.[74, 75] Moreover, the heteroatom-doped catalytic sites are at the atomic level, which contribute to a high catalytic site density on the electrode at a low doping quantity. Therefore, heteroatoms doped carbon materials have been reported as effective air electrodes in Na-O$_2$ battery system.
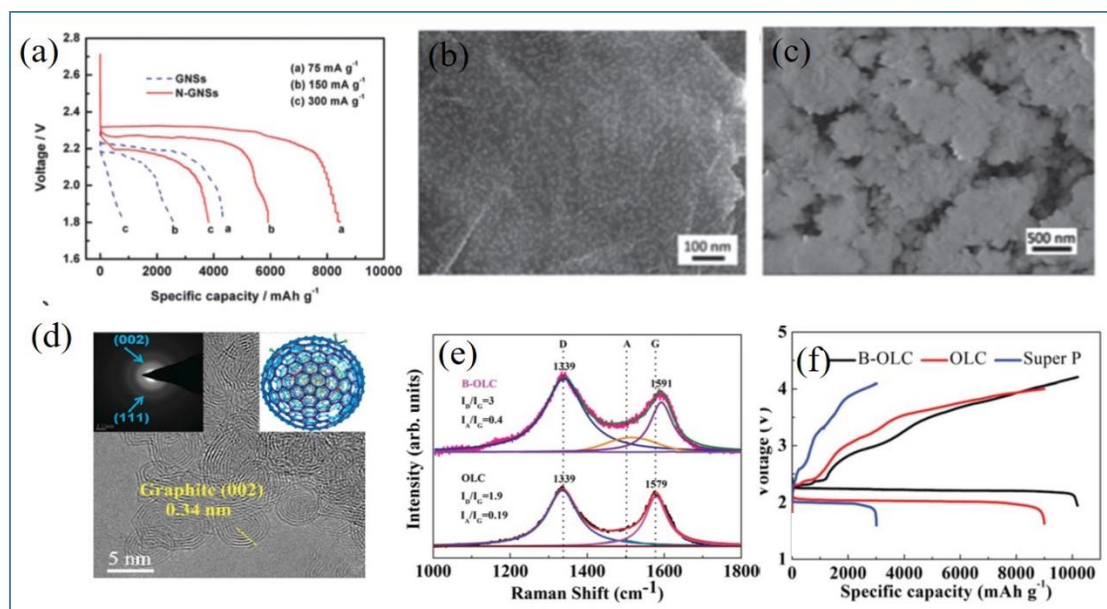
Figure 2.5 (a) The discharge curves of GNS and N-GNS electrodes, SEM images of N-GNS electrodes after (b) discharged for 12h and (c) fully discharged.[77] (d) HRTEM image and SAED pattern (inset) of B-OLC, (e) Raman spectra of B-OLC and OLC, (f) Discharge/charge curves of B-OLC, OLC and Super P electrodes in Na-O$_2$ batteries at 0.15 mA cm^{-2}.[58]

As a typical example, N-doped graphene nanosheets (N-GNSs) were fabricated and used as the cathode material in sodium-air batteries by our group in 2013.[57] We found that the N-GNSs demonstrated significantly improved electrocatalytic activity towards ORR; and the discharge capacity of N-GNSs is two times higher than that of the pristine counterpart (**Figure 2.5a**). The electrochemical enhancement can be related to the charge delocalization in the GNSs structure due to the N doping, resulting in a high positive charge

density of neighboring carbon. The charged carbon can act as the active sites with a strong O_2 adsorption to facilitate the uniform nucleation of discharge products (**Figure 2.5b** and **c**). This is consistent with the theoretical calculation on the catalytic role of defective sites in graphene, which indicated the effectiveness of N-doping in facilitating nucleation of Li_2O_2 cluster in Li-O_2 batteries.[76] Self-stacked N-doped CNT (NCNT) as the air electrodes for Na-O_2 batteries have also been investigated; which exhibit higher rate performance and extended cycle life at high current densities in comparison with CNT electrode.[59] The outstanding catalytic activity of the N-doped sites in NCNT contributed to the high cycling stability of cell. It should also be noted that the enhanced electrochemical performance can be partially attributed to the robust network of aligned NCNTs, which enables rapid oxygen and Na^+ transport while accommodating the discharge product.

Free-standing air electrodes composed of N-doped graphene aerogels on Ni foam (3D N-GA) were successfully synthesized by Zhang et al. using hydrothermal method.[78] Due to the unique properties of interconnected architecture with excellent conductivity, high surface area, and ideal pore size distribution, Na-O_2 batteries with a 3D N-GAs@Ni air electrode delivered a high discharge capacity of 10950 mAh g^{-1} at 100 mA g^{-1}. While only 9230 mAh g^{-1} can be achieved for GAs@Ni at the same current density. With further investigation on the morphology of the discharged air electrode, they revealed that the N-doping of graphene plays an important role in facilitating the uniform deposition of Na_2O_2 discharge product at the nanoscale, as well as the reduction of Na_2O_2 with lower overpotential. Other than an interconnected porous architecture and positive effect of N-doping, the binder-free property of 3D N-GAs@Ni electrode also contributed to the good performance of Na-O_2 cell by avoiding the side reactions involving polymeric binders. For the same purpose, free-standing 3D nanostructured air electrodes composed of vertically grown N-doped CNT on CP (NCNT-CP) were developed and used as the air electrode in Na-O_2 batteries.[23] The NCNT-CP air electrode could deliver a high discharge capacity of over 11 mAh cm^{-2}, which is about 17 times higher than that of bare CP at 0.1 mA cm^{-2}. The increase in discharge capacity is related to the continuous O_2/Na^+ transportation through the micrometer pores of the CP structure and the increase of surface area by introducing NCNT on CP skeleton.[59] By using synchrotron-based X-ray absorption spectroscopy, the electrochemical and chemical mechanism of the Na-O_2 cell with NCNT-

CP cathode was further investigated. Na_2O_2 and NaO_2 are identified as the main discharge products of the $Na-O_2$ cell, however the formation of carbonate-based side products and its gradual accumulation on the air electrode surface diminishes the cell life and should not be ignored in future studies.

Other than N-doping, theoretical and experimental studies showed that incorporating boron atoms into the carbon lattice can also be a good catalytic substrate to facilitate the oxidation of peroxide-based discharge products.[79, 80] As reported by Shu and co-workers, the boron-doped onion like carbon (B-OLC) was synthesized by a simple thermal method and then applied as the cathode for non-aqueous $Na-O_2$ batteries (**Figure 2.5 d-f**).[58] Similar to N-doped carbon, adsorption of O_2 on B-doped carbon is easier due to the distinct electronegativity between oxygen and boron, which is a prerequisite for the subsequent reaction. The resulting B-OLC cathodes exhibit outstanding electrochemical performance with high specific capacity (10200 mAh g^{-1}), good rate capability and cycling stability, which is superior to that of Super P and OLC electrodes. The cell performance improvements could be reasonably ascribed to the synergistic effect of the unique porous structure of B-OLC and its improved catalytic activity after boron doping.

2.3.3   Carbon materials loaded with solid catalysts

Apart from the heteroatoms-doped carbon cathodes discussed in the previous section, metals and/or metal oxides have also been used as the catalysts to decrease the charge overpotential and enhance the overall performance of (peroxide-based) $Na-O_2$ batteries. The reported metal and/or metal oxide as catalysts mainly include noble metals and/or their oxides, transitional metals and/or their oxides, perovskite-related oxides and their combinations. Considering that metal-based catalysts possess relatively high density, which will cause the compromise on the key advantages of cathode in high capacity and energy density, anchoring the nanometer- or micrometer-sized solid catalysts onto the porous carbon framework may simultaneously enhance the ORR/OER kinetics and increase the specific energy of the $Na-O_2$ battery. In this section, we will summarize the recent progress in fabricating highly efficient air electrodes that incorporate carbon materials with solid catalysts to address the sluggish kinetics of peroxide oxidation in $Na-O_2$ batteries.
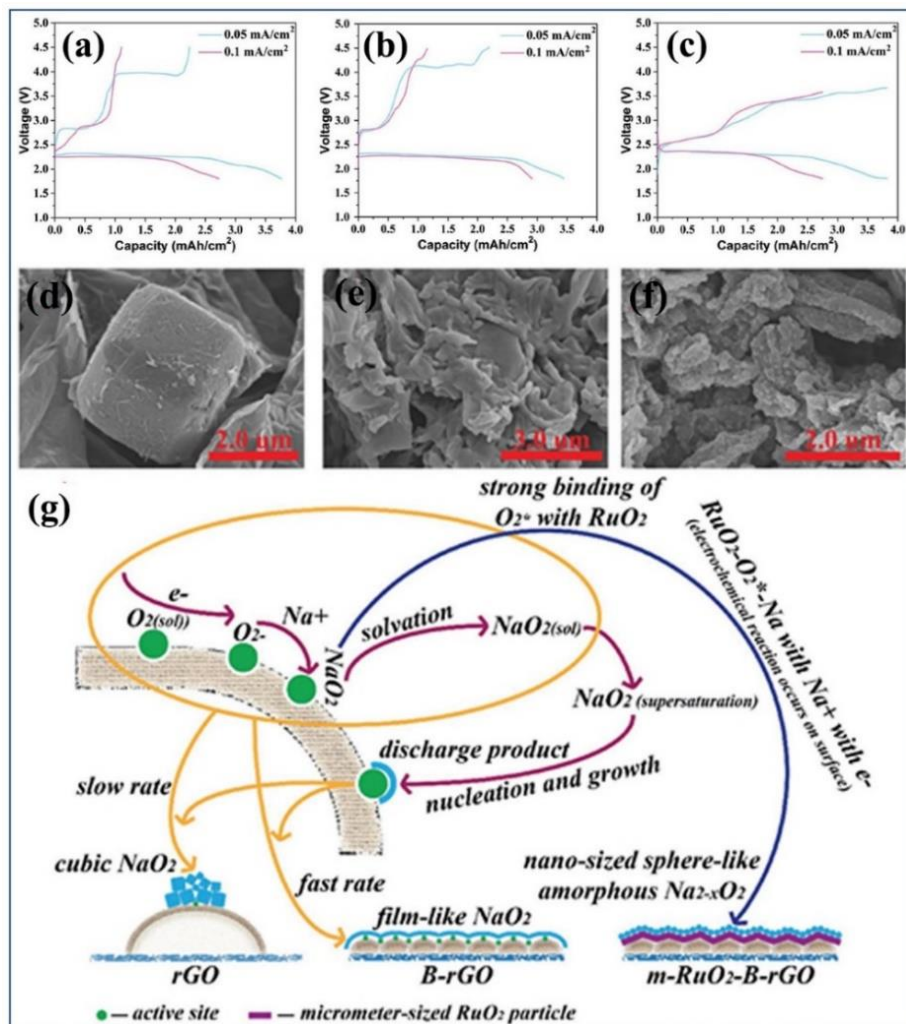
Figure 2.6 Deep discharge/charge curves of Na-O$_2$ batteries with a) rGO, b) B-rGO, c) m-RuO$_2$-B-rGO cathodes at 0.05 and 0.1 mA cm^{-2} in the voltage range of 1.8-4.5 V versus Na$^+$/Na, SEM images of discharged (d) rGO, (e) B-rGO, and (f) m-RuO$_2$-B-rGO cathodes at 0.05 mA cm^{-2}. (g) Schematic illustration of the proposed mechanism accounting for the different morphology of discharge products on different electrodes. [81]

Graphene nanosheets (GNS) loaded with homogeneous dispersed Pt nanoparticles (Pt@GNS) were successfully developed by Yang and co-workers via a hydrothermal method.[82] The Pt nanoparticles not only acts as additional oxygen adsorption sites that benefit the capacity increase, but it also prevents discharge product aggregation by regulating the uniform deposition of discharge products. As a result, significant enhanced ORR and OER kinetics were achieved, as well as improved cell capacity and cycling

stability under the shallow cycling mode. The Ag nanoparticle decorated rGO (Ag-rGO) as a bifunctional oxygen electrode for ORR and OER was investigated by Kumar and co-workers. However, different to the formation of Na_2CO_3 on the discharged Pt@GNS electrode, NaO_2, Na_2O_2 and Na_2O were identified as the discharge products of Na-O_2 cells assembled with Ag-rGO cathodes.[83] Pd nanoparticles as the catalyst for the cathode was reported by Amine et al. recently, and a peroxide-based Na-O_2 battery with low overpotential and high discharge capacity was successfully developed.[29] Kang and colleagues used ruthenium decorated CNTs (CNT/Ru) as the solid catalyst to enhance the ORR/OER kinetics of Na-O_2 batteries, and high energy efficiency can be achieved due to the formation of deficient sodium peroxide ($Na_{2-x}O_2$) as a main discharge product.[84]

In fact, the composition and morphology of the discharge products are highly affected by the surface chemistry and microstructure of the air electrodes. In recent research work, Ren and coworkers found that the characteristics of the air electrode plays an important role in determining the nature of the discharge products and accordingly Na-O_2 cell performance, as depicted in **Figure 2.6**.[85] Micrometer-sized NaO_2 and nano-sized film-like NaO_2 are the main discharge products of rGO and B-doped rGO cathodes, respectively. While with further decoration of micrometer-sized RuO_2 on the surface of B-rGO (m-RuO_2-B-rGO), nano-sized spherical amorphous Na-deficient $Na_{2-x}O_2$ was formed due to the high affinity of RuO_2 for oxygen. More importantly, the amorphous $Na_{2-x}O_2$ phase in discharged m-RuO_2-B-rGO cathodes has good electrical contact with the RuO_2 particles, and thus can be decomposed completely under 3.1V. This ultimately contributes to a significant enhancement of cycle life compared with other cathodes.

More recently, transition metal-based catalysts have aroused great interest to enhance the catalytic activity of the cathode in Na-O_2 battery systems. For example, our group synthesized Co_3O_4 decorated CNTs (CNT@Co_3O_4) via atomic layer deposition (ALD), and then employed as the cathode for Na-O_2 batteries (**Figure 2.7a** and **b**).[56] Synchrotron-based X-ray analysis revealed that the well dispersed Co_3O_4 catalyst on CNTs could serve as functionalized active sites, promote the electrochemical decomposition of sodium peroxide, superoxide, and carbonates. High-spin Co_3O_4 as the electrocatalyst for Na-O_2 batteries was reported by Mai and co-workers, and the formation of NaO_2 nanowires

induced by high-spin Co_3O_4 catalyst significantly boosts the electrochemical performance of Na-O_2 batteries (**Figure 2.7c** and **d**).[86] In another study, free-standing C@NiCo$_2$O$_4$ air electrode composed of vertical NiCo$_2$O$_4$ nanoneedle arrays on CP have been delicately fabricated by Liu et al. through a hydrothermal method.[87] The porous CP skeleton enables fast electron transport and oxygen diffusion, while the NiCo$_2$O$_4$ nanoneedles provide adequate active sites and sufficient space for discharge product accommodation (**Figure 2.7e** and **f**). A high discharge capacity of 6500 mAh g^{-1} at 50 mA g^{-1}, and stable cycling of 120 cycles can be achieved due to the reversible formation/decomposition of film-like Na$_2$O$_2$ in Na-O_2 batteries with C@NiCo$_2$O$_4$ electrodes.
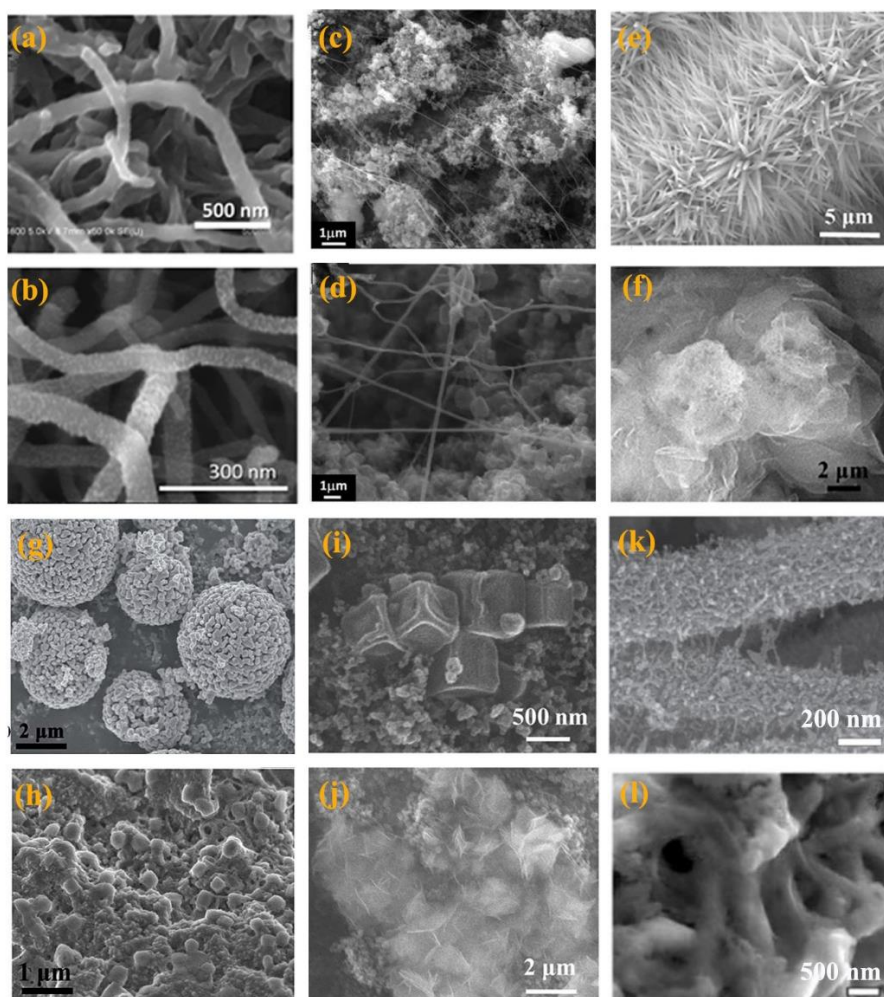
Figure 2.7 SEM images of (a) pristine and (b) discharged CNT@Co$_3$O$_4$ electrode at 300 mA g^{-1}.[56] (c, d) SEM images of NaO$_2$ nanowires (discharge product of Na-O_2 batteries) beside the high-spin Co$_3$O$_4$ electrocatalyst.[86] SEM images of (e) pristine and (f) discharged

C@NiCo$_2$O$_4$-NAs electrode with a limited capacity of 6500 mAh g^{-1}.[87] SEM images of (g) pristine CaMnO$_3$ and (h) discharged CaMnO$_3$/C electrodes.[88] SEM images of (i) pristine and (j) discharged h-Co$_3$O$_4$@MnCo$_2$O$_{4.5}$ electrodes with a capacity limitation of 1000 mAh g^{-1}.[89] SEM image of (k) pristine and (l) discharged RuO$_2$/Mn$_2$O$_3$/CNF electrode at 0.05 mA cm^{-2}.[90]

In addition to transitional metal oxides, several other metal-based catalysts have also been studied as cathode catalysts in Na-O$_2$ batteries and exhibited promising catalytic activity towards both ORR and OER. For example, the introduction of the CoB cathode catalyst successfully endowed Na-O$_2$ batteries with a low charge overpotential, good rate capability and cycling stability.[91] Chen and co-workers reported the perovskite CaMnO$_3$ microsphere as an efficient electrocatalyst for rechargeable Na-O$_2$ batteries (**Figure 2.7g** and **h**).[88] Pyrochlore-type oxide as a cathode catalyst has also been reported in Na-O$_2$ batteries.[92] Moreover, Jiang et al. found that the Na-O$_2$ cell performance is highly related to the electronic structure and specific surface area of Pyrochlore-type oxide, and the La$_2$Co$_2$O$_7$ catalyst enables a high-performance Na-O$_2$ battery with ultrahigh discharge capacity (20184.2 mAh g^{-1}) and long cycle life (over 167 cycles).[92]

Due to the limited catalytic activity of single-component oxide catalyst towards ORR/OER, the design of efficient bifunctional electrocatalysts is highly desired. With this regards, Liu and colleagues constructed heterogeneously structured CoO/CoP nanosheets which combine the advantages of the high OER activity of CoP and the high ORR activity of CoO.[93] More importantly, the catalytic activity of the designed CoO/CoP nanosheets exceeds that of the parent CoO or CoP due to the interpenetration of O-P on the CoO/CoP interface. Hierarchical Co$_3$O$_4$@MnCo$_2$O$_{4.5}$ nanocubes (hCo$_3$O$_4$@ MnCo$_2$O$_{4.5}$ Ns) cathode catalyst with a yolk-shell structure was successfully fabricated by Liu et al. by using the metal-organic framework template (**Figure 2.7i** and **j**).[89] In another study reported by Yilmaz and co-workers, 3D RuO$_2$/Mn$_2$O$_3$/CNF as bifunctional electrocatalysts towards ORR and OER were prepared, as shown in **Figure 2.7k** and **l**.[90] Taking the benefit of RuO$_2$ and Mn$_2$O$_3$ synergy, the RuO$_2$/Mn$_2$O$_3$/CNF electrode exhibits much higher specific capacity and catalytic activity compared to its CNF, Mn$_2$O$_3$/CNF and RuO$_2$/CNF counterparts. The incorporation of heterogeneous catalysts to simultaneously boost the

ORR and OER activities of Na-O$_2$ batteries was also reported by our group.[94] The NCNT@CP air electrode was decorated with mesoporous Mn$_3$O$_4$ as an ORR catalyst and ALD deposited Pd nanoclusters as OER catalysts. We found that the catalytic activity is related to the dynamic interaction between the catalyst and discharge products. By monitoring the electronic state of the solid catalyst during ORR and OER processes, we further revealed that the synergistic effect between Mn$_3$O$_4$ and Pd catalyst originates from the electron exchange between the noble metal and the metal oxide.

Although the electrochemical performance and cycling life of Na-O$_2$ batteries have been improved, the research on the carbon-based air electrode in Na-O$_2$ batteries is still limited and the achievable electrochemical performance is still unsatisfied. Due to the similar working principles, the research results obtained from the Li-O$_2$ battery system may provide guidance for the future research of Na-O$_2$ batteries.

2.4   Strategies for efficient use of sodium metal anode

Unlike the intense research on understanding the Na-O$_2$ cell electrochemistry and air electrode design, the study on the role of the Na anode in determining the overall cell performance has been less focused. In the Na-O$_2$ batteries, sodium metal is the ultimate choice as the anode material due to its high theoretical specific capacity (1166 mAh g^{-1}) and low redox potential (-2.714V *vs.* standard hydrogen electrode). However, the Na dendrite growth and Na corrosion are identified as two major issues of Na-O$_2$ batteries, which severely degrade the cell performance.

Manufacturing a robust SEI layer by surface engineering is an effective strategy for the stabilization of Na metal in Na-O$_2$ batteries.[95] As reported by Zhou and co-workers, electrolyte additives (fluoroethylene carbonate) can be used to passivate the Na surface by forming a stable fluoride-rich film, which contributes to the dendrite-free anode and significantly improved cycling stability of Na-O$_2$ batteries.[53] There are also reports of protecting the Na anode by direct formation of an artificial protective layer via ALD/MLD technique or solution-based method in NIBs. However, the feasibility of these protected Na anodes in Na-O$_2$ batteries need further investigation due to its unique working principles.[96-98] Designing high-modulus separators/membranes are presumably effective in

suppressing Na dendrite growth and alleviating Na degradation in Na-O$_2$ batteries.[99] However, the stabilization of Na metal anode in Na-O$_2$ batteries has been seriously neglected. So far, few studies have reported to stabilize the Na metal and achieve long-term cycling of Na-O$_2$ batteries.

Among various strategies that can help achieve stable cycling of Na metal, carbon materials have shown the greatest potential for large-scale fabrication and application in the future due to its unique properties [100-103]: 1) Carbon materials with high surface area and porosity can construct a 3D host or interlayer for Na metal, which can lower the local current density for uniform Na deposition. Simultaneously, the infinite volume expansion of Na metal during continuous stripping/plating can also be well addressed; 2) The "Na-philic" functional groups/nanomaterials on the carbon surface help increase sodium affinity, which facilitates homogeneous Na nucleation with a low overpotential; 3) Carbon films with high mechanical flexibility and chemical stability can act as a protective layer for stabilizing the SEI layer, which not only suppresses the Na dendrite growth, but also alleviates the Na corrosion; 4) Carbon materials are relatively light and cost effective, and at the same time, the thickness and porosity of the 3D carbon networks can be easily controlled.

Therefore, this section summarizes the recent progresses that use carbon-based materials to address the issues of Na anodes and highlights the advantages and roles of carbon materials in Na protection for Na-O$_2$ batteries. Furthermore, the potential carbon materials that can be used in protecting Na metal in the further study of Na-O$_2$ batteries are also discussed.

2.4.1   Carbon hosted sodium anode

Based on "Sand's time" theory and experimental results from Janek et al, current density has a determining effect on the morphology of Na deposits.[47, 104] Therefore, the rational design of 3D carbon hosts for metallic Na is an effective strategy to alleviate the dendrite growth by decreasing the electrode current density. By designing Na metal anodes for Na-O$_2$ batteries, the 3D carbon host should be pre-stored with Na to supply the Na source. Compared with electrodeposition, which is complex and time-consuming, utilizing a thermal infusion strategy with molten Na infused into a 3D Na-philic substrate is much

more promising. Luo and colleagues used rGO as a host to fabricate a processable and moldable composite Na metal anode (Na@rGO) for Na batteries, as shown in **Figure 2.8a**.[105] Interestingly, by controlling the thickness of the densely stacked GO film, the Na@rGO anode thickness can be determined; in fact, it was found to be 20 times the thickness of the GO film. Moreover, the shape of the Na@rGO composite anode can also be engineered by tailoring the precursor GO films with desired shapes. With only 4.5 wt. % of GO, the mechanical properties and corrosion stability of Na@rGO composite anode significantly improved without sacrificing much capacity of the Na anode. Consequently, the dendrite-free Na anode with enhanced cycling performance can be achieved in Na symmetric cells using both ether and carbonate electrolytes. As a proof of concept, the electrochemical performance of Na-O$_2$ cells using Na@rGO anode was further investigated. As a result, Na-O$_2$ cells exhibit a lower discharge/charge overpotential and improved cycling stability compared with that of the cell with bare Na anode.
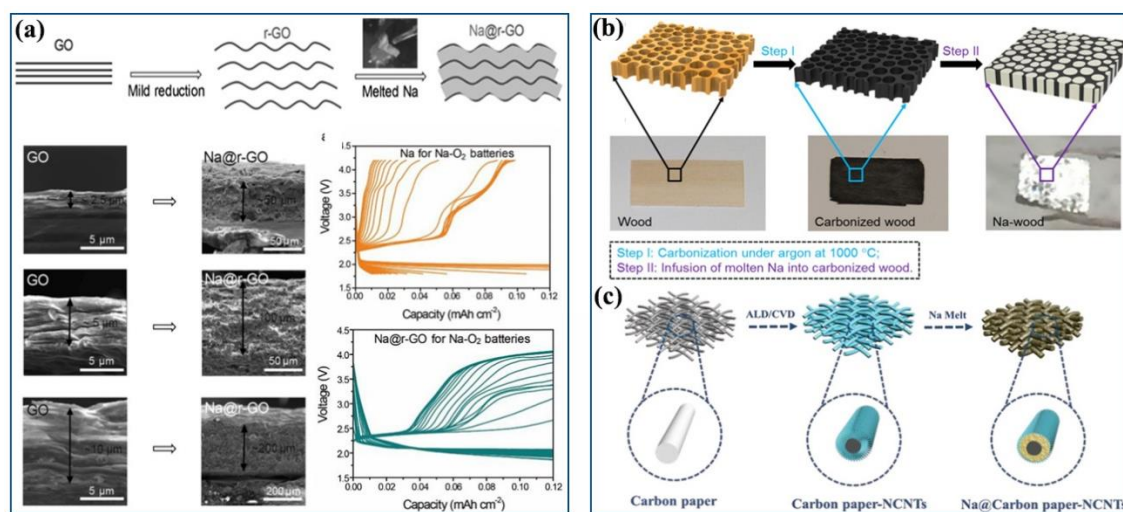
Figure 2.8 (a) Schematic representation of the preparation of Na@r-GO composites, and the cycling performance of Na-O$_2$ batteries with Na and Na@r-GO anode from 1st and 20th cycle.[105] (b) Encapsulation of metallic Na into carbonized wood by a spontaneous and instantaneous infusion.[106] (c) Schematic diagram of the fabrication procedure of Na@CP-NCNTs.[107]

In another work reported by Hu et al., carbonized wood with channels were used as a 3D host for fabricating Na-wood composite anodes using a thermal infusion process (**Figure 2.8b**).[106] The hierarchical structure of carbonized wood can be well maintained after

encapsulation of metallic Na, which offers a large surface area for homogeneous Na deposition by lowering the effective current density. Benefiting from its unique structure, the Na-wood composite electrode exhibited stable cycling performance for over 250 cycles at 1 mA cm^{-2} with capacity of 0.5 and 1.0 mA cm^{-2}, respectively. Comparatively, the Na symmetric cell with a bare Na electrode only runs for less than 90 cycles and 50 cycles under the same testing conditions. Recently, the rational design of the Na@CP-NCNT composite electrode with 3D CP-NCNT framework host was reported by Sun and co-workers. The schematic presentation of the electrode fabrication process is shown in **Figure 2.8c**.[107] Interestingly, the cross-conductive network of CP and NCNT can facilitate the uniform Na deposition by decreasing the local current density. On the other hand, the "Na-phobic" property of CP changes to "Na-philic" after introducing NCNT on the CP skeleton. More importantly, the constructed Na symmetric cell using Na@CP-NCNTs electrode exhibited improved cycling stability compared to the bare Na electrode at high current densities of 3 and 5 mA cm^{-2}. Although the electrochemical performance of the Na@CP-NCNTs electrode did not characterize in the Na-O$_2$ batteries, the design of the 3D host with the "Na-philic" property provided some guidance in fabricating advanced Na anodes in the future study of Na-O$_2$ batteries.

Aside from pre-store the Na metal into 3D host with thermal infusion method, significant improved cycling performance of Na anode was also demonstrated by introducing commercial CP as the interlayer between the Na metal and separator.[108] The positive effect of CP was attributed to its high surface area for decreasing current density. More importantly, this method is straightforward, cost-effective and timesaving, which is beneficial for the practical application of Na metal batteries. However, uniform deposition of Na metal is hardly achieved at high current density with a high Na capacity. Decorating the carbon materials with functional groups is an effective strategy to increase the affinity of substrate for sodium. As reported by Wang and colleagues, who introduced a nitrogen and sulfur co-doped CNT (NSCNT) interlayer on the Na metal anode in Na-O$_2$ batteries (**Figure 2.9a**).[109] The N and S-containing functional groups on the CNT induce the NSCNT to be "Na-philic", which can regulate the initial Na nucleation and enables uniform deposition of Na on the interlayer. The large surface area and good electronic conductivity of NSCNT are also beneficial for dendrite-free Na anodes even at a high current density.

In addition to Na ion regulation, the 3D porous NSCNT structure can buffer the infinite volume change of Na during continuous plating/stripping processes. Consequently, the assembled Na-O$_2$ battery using Na/NSCNT anodes show very stable cycling performance for over 90 cycles, while the cycling of Na-O$_2$ cell using a bare Na anode was interrupted by short-circuiting at the 53rd cycle due to the Na dendrite penetration.
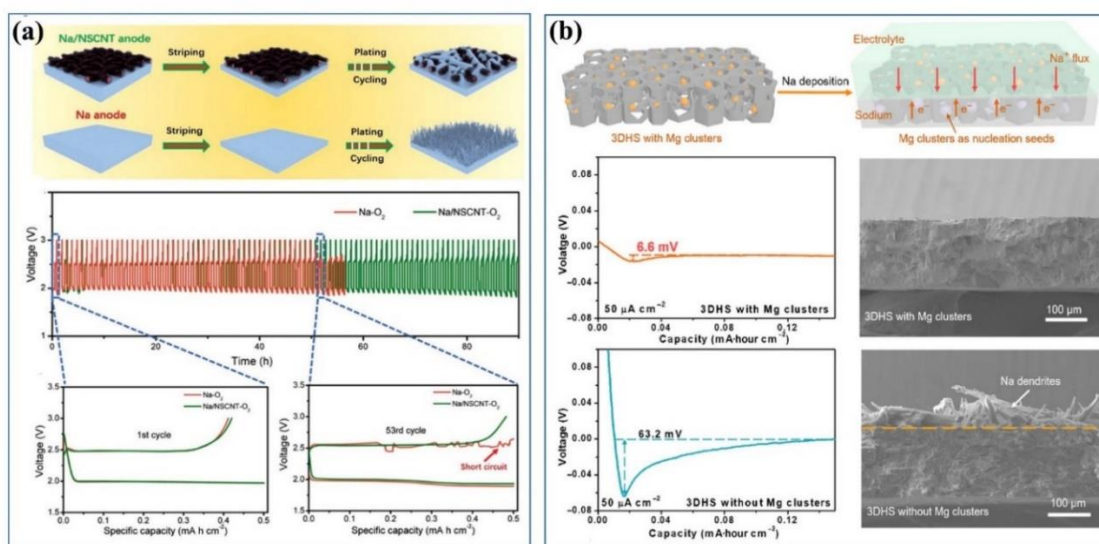
Figure 2.9 (a) Schematic illustration of the Na striping/plating on Na metal anode and Na/NSCNT anode, and the cycling performance of Na-O$_2$ batteries with Na anodes and Na/NSCNT anodes at 1 mA cm^{-2} with a cut-off capacity of 0.5 mA cm^{-2}.[109] (b) Controllable nucleation and growth of Na in the 3DHS film with Mg clusters at 50 µA cm^{-2}.[110]

It is worth noting that the uniform Na deposition also can be achieved through introducing heterogeneous nucleation seeds other than functional groups/defects. In the research of Na metal anode, Yang and colleagues investigated the nucleation behavior of Na on different metals.[110] They found that the Na can be controllably deposited onto the main group II metal substrates such as Be, Mg and Ba since they have definite solubility in sodium. The formation of a solid solution surface layer enables guidance on the Na growth in the parallel direction of metal substrates, as well as significantly reduced Na nucleation barrier. Another impressive work has been reported by Tang and co-workers, who introduced a layer of Au to realize stable Na deposition by alloying. With the formation of a "sodiophilic" Au-Na alloy layer on Cu substrate, the Na could be uniformly deposited with

low overpotential.[111] The 3D carbon framework is effective in suppressing the Na dendrite, and heterogeneous nucleation seeds are beneficial for regulating Na deposition and realizing spatial control over Na nucleation. It is expected that homogeneously dispersing sodiophilic nanoseeds onto the skeleton of 3D carbon-based substrates can direct the deposition of Na within the 3D structure, resolving the issues of Na dendrite growth in Na-O_2 batteries (**Figure 2.9c**). Furthermore, the difference in the Na nucleation barrier between different materials suggests an effective way to construct sodiophilic-sodiophobic gradient interlayers, which can alleviate the preferentially nucleation of Na on the top surface of a conductive interlayer at a high current density [112]. This ensures long-term cycling of dendrite-free Na anodes in high-energy-density Na-O_2 batteries.

2.4.2   Artificial layer protected sodium anode

Modification of the Na metal anode with a protective interlayer shows great potential in suppressing Na dendrite growth and alleviating Na corrosion in Na-O_2 batteries. In our recent work, a Na-O_2 battery using electrically connected CP with Na metal as a protected anode was successfully developed.[49] Interestingly, we found that the function of CP is beyond that of a conductive 3D current collector to prevent the Na dendrite growth; the CP also acts as a protective layer to alleviate the Na degradation during cycling. More specifically, the electrochemical potential of the CP gains a pseudo-equal potential when in contact with Na metal, and the side reactions induced by O_2/O_2^- crossover preferentially occur on the CP instead of the Na surface (**Figure 2.10a**). Consequently, the cycling stability of constructed Na-O_2 batteries can be significantly improved compared with that of the cell using a bare Na anode. This strategy has been demonstrated to be effective in alleviating Na degradation, while the Na corrosion induced by contaminants crossover cannot be avoided during long-term cycling due to the porous structure of CP, which provides abundant contaminant diffusion paths.

In fact, carbon films with a relatively dense structure are more desired in order to alleviate the Na corrosion in Na-O_2 batteries. Free-standing graphene films have been reported as an artificial protection layer on the Na metal surface to stabilize the SEI layer as well as physically blocking the Na dendrite growth. This makes these films ideal for suppressing side reactions induced by contaminants crossover on the Na metal surface (**Figure**

2.10b).[113] On one hand, the contaminants can only diffuse through the interlayer ionic channels of the graphene layers rather than migrate freely from the cathode to the Na metal surface. On the other hand, the high surface area of graphene layer is hardly covered by the side products, ensuring a significantly improved cycle life of Na metal anode in the presence of contaminant crossover. A similar strategy has been reported in Li-S batteries, where an integrated anode composed of a compacted graphite film and Li metal was developed by Huang and co-workers.[114] Lithiated graphite placed in front of the Li metal can not only effectively stabilize the SEI layer on Li surface, but also simultaneously retard the etching of Li metal by migrated polysulfides. This achieves dendrite-free Li anodes and enhanced cycling performance of the Li-S batteries. Amorphous carbon also has the potential to be used as a protective layer on the Na metal anode. A monolayer of interconnected amorphous hollow carbon spheres coating, developed by Cui and colleagues, acts as a stable interfacial layer on Li metal (**Figure 2.10c**).[115] Due to the conductivity difference between carbon spheres and current collectors, Li metal deposition takes place on the Cu current collector, and a stable, conformal SEI layer forms on the carbon nanospheres. The SEI layer formed on the interconnected carbon surface is not only effective in inhibiting dendrite Li growth but also can be helps to prevent the penetration of solvent molecules and contaminants. These benefits show great feasibility in preventing Na degradation Na-O$_2$ battery system.
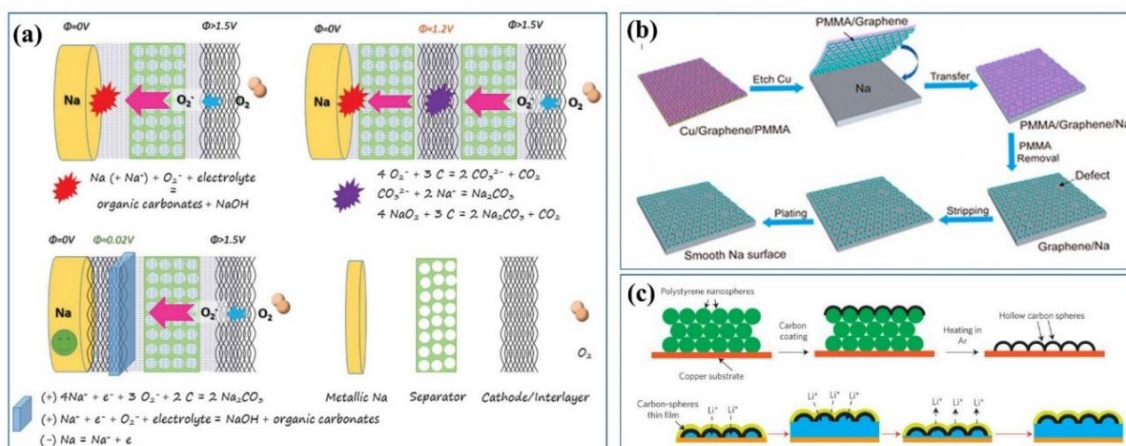
Figure 2.10 (a) Illustration of protective effect of CP protective layer towards Na corrosion induced by superoxide radical crossover.[49] (b) Illustration of preparation and

stripping/plating behavior of graphene-coated Na anode.[113] (c) Fabrication process for the hollow carbon nanosphere-modified Cu electrode, and modifying the Cu substrate with a hollow carbon nanosphere layer creates a scaffold for stabilizing the SEI layer.[115]

As discussed above, developing a protective carbon layer coating on the Na metal anode is an effective strategy to alleviate the Na corrosion caused by contaminants crossover. At the same time, such carbon layer also acts as a physical barrier to suppress the dendrite growth. More importantly, fabricating a protective layer on the Na metal anode is a universal and effective approach to effectively restrict the O_2/O_2^- from reaching the Na surface. It can be expected that a longer cycle life of Na-O_2 batteries can be achieved using a more effective protective layer on Na metal anode. Although the study on suppressing the Na dendrite growth and Na degradation is relatively scarce in Na-O_2 batteries, earlier research towards Na protection in symmetric cells provides some guidance for the rational design of carbon materials for stabilizing the Na metal anode in Na-O_2 batteries.[51]

2.5 Conclusion and perspective

Non-aqueous Na-O_2 batteries have attracted enormous attention in the past few years owing to their high energy density, low cost and environmental friendliness. As discussed above, much effort has been made in exploring the cell chemistry and fabricating advanced electrodes in order to improve the electrochemical performance of Na-O_2 batteries. However, Na-O_2 battery technology is still at an immature stage and electrochemistry of the Na-O_2 battery is still elusive and controversial. The slight difference in the experimental parameters, such as the microstructure and surface chemistry of air electrodes, the composition and concentration of organic electrolyte, as well as the atmospheric conditions, would affect the nature of discharge products and the Na-O_2 cell performance. A fundamental understanding on the working mechanism and impact factors is crucial for the development of high-performance Na-O_2 batteries. Theoretical calculations and various in-situ/in-operando characterizations may help in searching for the underlying mechanism of this system.

As a key component in Na-O_2 battery, the development of highly efficient air cathodes has been of significance due to its crucial role in determining the overall cell performance. As

discussed, rational microstructure design through tailoring porous structure can effectively increase the specific capacity and cycle life of the batteries. The application of heteroatoms-doped air electrodes, as well as the attachment of solid catalysts on carbon cathodes can facilitate peroxides oxidation with a lower charge overpotential, and thus the side reactions involving a carbonaceous cathode at high voltage can be wisely avoided. It should be noted that in order to screen a suitable catalyst in Na-O$_2$ batteries, we should not only focus on the effectiveness of the catalyst in facilitating peroxides decomposition, but the parasitic reactions promoted by the catalysts should also not be neglected. Additionally, to mitigate the side reactions induced by polymer binders' decomposition, the binder-free air electrode design is desirable to improve the stability of Na-O$_2$ batteries.

In fact, the most outstanding advantage of Na-O$_2$ batteries comes from its high theoretical energy density, which is a result of high capacity of not only cathode materials but also the Na metal anode. Safety issues caused by Na dendrite growth, as well as the Na degradation induced by O$_2$/O$_2^-$ crossover severely limit the cycling stability of Na metal. Carbon materials have been proved to be effective to promote the practical application of Na metal and Na-O$_2$ batteries due to their multifunctional roles, such as acting as a stable Na host, lowering the local current density, stabilizing the SEI layer, and blocking the contaminants crossover. However, the research on Na protection in Na-O$_2$ battery systems has been severely overlooked; designing highly stable Na anodes for practical use in Na-O$_2$ batteries is urgently needed. Therefore, it is necessary to understand the mechanism underlying the Na dendrite growth in Na-O$_2$ batteries, and the optimization of the organic electrolyte to construct robust and stable SEI layer on the Na metal anode should also be considered.

So far, the Na-O$_2$ batteries are still in its initial stages of development. Further enhancements of the cell performance still need technology breakthroughs in mechanism study and electrodes designing. Since Na-O$_2$ and Li-O$_2$ battery systems exhibit similar working principles, the previous research on Li-O$_2$ battery systems would be helpful for providing guidance for the future research direction of Na-O$_2$ batteries. We believe that with more and more efforts being devoted, the practical application of Na-O$_2$ batteries can be expected in the foreseen future.

2.6 Reference

1. Youn, D. H.; Heller, A.; Mullins, C. B., *Chemistry of Materials* 2016, 28, (5), 1343-1347.

2. Youn, D. H.; Patterson, N. A.; Park, H.; Heller, A.; Mullins, C. B., *ACS Applied Materials & Interfaces* 2016, 8, (41), 27788-27794.

3. Wu, H.; Mou, J.; Zhou, L.; Zheng, Q.; Jiang, N.; Lin, D., *Electrochimica Acta* 2016, 212, 1021-1030.

4. Kreuer, K.-D.; Portale, G., *Advanced Functional Materials* 2013, 23, (43), 5390-5397.

5. Tan, Z. a.; Li, S.; Wang, F.; Qian, D.; Lin, J.; Hou, J.; Li, Y., *Scientific Reports* 2014, 4, 4691.

6. Bruce, P. G.; Freunberger, S. A.; Hardwick, L. J.; Tarascon, J.-M., *Nat Mater* 2012, 11, (1), 19-29.

7. Yang, Z.; Nie, H.; Chen, X. a.; Chen, X.; Huang, S., *Journal of Power Sources* 2013, 236, 238-249.

8. Sharaf, O. Z.; Orhan, M. F., *Renewable and Sustainable Energy Reviews* 2014, 32, 810-853.

9. McCloskey, B. D.; Bethune, D. S.; Shelby, R. M.; Mori, T.; Scheffler, R.; Speidel, A.; Sherwood, M.; Luntz, A. C., *The Journal of Physical Chemistry Letters* 2012, 3, (20), 3043-3047.

10. Ding, J.; Wang, H.; Li, Z.; Kohandehghan, A.; Cui, K.; Xu, Z.; Zahiri, B.; Tan, X.; Lotfabad, E. M.; Olsen, B. C.; Mitlin, D., *ACS Nano* 2013, 7, (12), 11004-11015.

11. Larcher, D.; Tarascon, J. M., *Nat Chem* 2015, 7, (1), 19-29.

12. Pei, P.; Wang, K.; Ma, Z., *Applied Energy* 2014, 128, 315-324.

13. McKerracher, R. D.; Ponce de Leon, C.; Wills, R. G. A.; Shah, A. A.; Walsh, F. C., *ChemPlusChem* 2015, 80, (2), 323-335.

14. Egan, D. R.; Ponce de León, C.; Wood, R. J. K.; Jones, R. L.; Stokes, K. R.; Walsh, F. C., *Journal of Power Sources* 2013, 236, 293-310.

15. Zhang, T.; Tao, Z.; Chen, J., *Materials Horizons* 2014, 1, (2), 196-206.

16. Li, Y.; Dai, H., *Chemical Society Reviews* 2014, 43, (15), 5257-5275.

17. Yadegari, H.; Sun, Q.; Sun, X., *Advanced Materials* 2016, 28, (33), 7065-7093.

18. Rahman, M. A.; Wang, X.; Wen, C., *Journal of Applied Electrochemistry* 2014, 44, (1), 5-22.

19. Shao, Y.; Ding, F.; Xiao, J.; Zhang, J.; Xu, W.; Park, S.; Zhang, J.-G.; Wang, Y.; Liu, J., *Advanced Functional Materials* 2013, 23, (8), 987-1004.

20. Hartmann, P.; Bender, C. L.; Vračar, M.; Dürr, A. K.; Garsuch, A.; Janek, J.; Adelhelm, P., *Nat Mater* 2013, 12, (3), 228-232.

21. McCloskey, B. D.; Garcia, J. M.; Luntz, A. C., *The Journal of Physical Chemistry Letters* 2014, 5, (7), 1230-1235.

22. Yadegari, H.; Sun, X., *Accounts of Chemical Research* 2018, 51, (6), 1532-1540.

23. Yadegari, H.; Banis, M. N.; Xiao, B.; Sun, Q.; Li, X.; Lushington, A.; Wang, B.; Li, R.; Sham, T.-K.; Cui, X.; Sun, X., *Chemistry of Materials* 2015, 27, (8), 3040-3047.

24. Yadegari, H.; Norouzi Banis, M.; Lin, X.; Koo, A.; Li, R.; Sun, X., *Chemistry of Materials* 2018, 30, (15), 5156-5160.

25. Lee, B.; Seo, D.-H.; Lim, H.-D.; Park, I.; Park, K.-Y.; Kim, J.; Kang, K., *Chemistry of Materials* 2014, 26, (2), 1048-1055.

26. Lee, B.; Kim, J.; Yoon, G.; Lim, H.-D.; Choi, I.-S.; Kang, K., *Chemistry of Materials* 2015, 27, (24), 8406-8413.

27. Yang, S.; Siegel, D. J., *Chemistry of Materials* 2015, 27, (11), 3852-3860.

28. Younesi, R.; Hahlin, M.; Björefors, F.; Johansson, P.; Edström, K., *Chemistry of Materials* 2013, 25, (1), 77-84.

29. Ma, L.; Zhang, D.; Lei, Y.; Yuan, Y.; Wu, T.; Lu, J.; Amine, K., *ACS Energy Letters* 2018, 3, (2), 276-277.

30. Zhao, S.; Qin, B.; Chan, K.-Y.; Li, C.-Y. V.; Li, F., *Batteries & Supercaps* 2019, 2, 725-742.

31. Bender, C. L.; Schröder, D.; Pinedo, R.; Adelhelm, P.; Janek, J., *Angewandte Chemie International Edition* 2016, 55, (15), 4640-4649.

32. Kang, S.; Mo, Y.; Ong, S. P.; Ceder, G., *Nano Letters* 2014, 14, (2), 1016-1020.

33. Bender, C. L.; Hartmann, P.; Vracar, M.; Adelhelm, P.; Janek, J., *Advanced Energy Materials* 2014, 4, 1301863.

34. Aldous, I. M.; Hardwick, L. J., *Angewandte Chemie* 2016, 128, (29), 8394-8397.

35. Zhao, N.; Guo, X., *The Journal of Physical Chemistry C* 2015, 119, (45), 25319-25326.

36. Kim, J.; Lim, H.-D.; Gwon, H.; Kang, K., *Physical Chemistry Chemical Physics* 2013, 15, (10), 3623-3629.

37. Hartmann, P.; Bender, C. L.; Sann, J.; Durr, A. K.; Jansen, M.; Janek, J.; Adelhelm, P., *Physical Chemistry Chemical Physics* 2013, 15, (28), 11661-11672.

38. Yadegari, H.; Franko, C. J.; Banis, M. N.; Sun, Q.; Li, R.; Goward, G. R.; Sun, X., *The Journal of Physical Chemistry Letters* 2017, 8, (19), 4794-4800.

39. Lutz, L.; Yin, W.; Grimaud, A.; Alves Dalla Corte, D.; Tang, M.; Johnson, L.; Azaceta, E.; Sarou-Kanian, V.; Naylor, A. J.; Hamad, S.; Anta, J. A.; Salager, E.; Tena-Zaera, R.; Bruce, P. G.; Tarascon, J. M., *The Journal of Physical Chemistry C* 2016, 120, (36), 20068-20076.

40. Lutz, L.; Corte, D. A. D.; Chen, Y.; Batuk, D.; Johnson, L. R.; Abakumov, A.; Yate, L.; Azaceta, E.; Bruce, P. G.; Tarascon, J.-M.; Grimaud, A., *Advanced Energy Materials* 2018, 8, (4), 1701581.

41. Sun, B.; Kretschmer, K.; Xie, X.; Munroe, P.; Peng, Z.; Wang, G., *Advanced Materials* 2017, 29, (48), 1606816.

42. Xia, C.; Black, R.; Fernandes, R.; Adams, B.; Nazar, L. F., *Nat Chem* 2015, 7, (6), 496-501.

43. Abate, I. I.; Thompson, L. E.; Kim, H.-C.; Aetukuri, N. B., *The Journal of Physical Chemistry Letters* 2016, 7, (12), 2164-2169.

44. Pinedo, R.; Weber, D. A.; Bergner, B.; Schröder, D.; Adelhelm, P.; Janek, J., *The Journal of Physical Chemistry C* 2016, 120, (16), 8472-8481.

45. Bi, X.; Wang, R.; Ma, L.; Zhang, D.; Amine, K.; Lu, J., *Small Methods* 2017, 1, (7), 1700102.

46. Sun, Q.; Yadegari, H.; Banis, M. N.; Liu, J.; Xiao, B.; Li, X.; Langford, C.; Li, R.; Sun, X., *The Journal of Physical Chemistry C* 2015, 119, (24), 13433-13441.

47. Medenbach, L.; Bender, C. L.; Haas, R.; Mogwitz, B.; Pompe, C.; Adelhelm, P.; Schröder, D.; Janek, J., *Energy Technology* 2017, 5, (12), 2265-2274.

48. Ortiz-Vitoriano, N.; Batcho, T. P.; Kwabi, D. G.; Han, B.; Pour, N.; Yao, K. P. C.; Thompson, C. V.; Shao-Horn, Y., *The Journal of Physical Chemistry Letters* 2015, 6, (13), 2636-2643.

49. Xiaoting, L.; Qian, S.; Hossein, Y.; Xiaofei, Y.; Yang, Z.; Changhong, W.; Jianneng, L.; Alicia, K.; Ruying, L.; Xueliang, S., O *Advanced Functional Materials* 2018, 28, 1801904.

50. Sun, Q.; Liu, J.; Xiao, B.; Wang, B.; Banis, M.; Yadegari, H.; Adair, K. R.; Li, R.; Sun, X., *Advanced Functional Materials* 2019, 29, 1808332.

51. Zhao, Y.; Adair, K. R.; Sun, X., *Energy & Environmental Science* 2018, 11, (10), 2673-2695.

52. Bi, X.; Ren, X.; Huang, Z.; Yu, M.; Kreidler, E.; Wu, Y., *Chemical Communications* 2015, 51, (36), 7665-7668.

53. Wu, S.; Qiao, Y.; Jiang, K.; He, Y.; Guo, S.; Zhou, H., *Advanced Functional Materials*, 2018, 28, 1706374.

54. Lukas, S.; Nika, M.; Bettina, S.; Martin, W.; Christian, S.; M., B. S.; A., F. S., *Angewandte Chemie International Edition* 2017, 56, (49), 15728-15732.

55. Bing, S.; Katja, K.; Xiuqiang, X.; Paul, M.; Zhangquan, P.; Guoxiu, W., *Advanced Materials* 2017, 29, (48), 1606816.

56. Sun, Q.; Liu, J.; Li, X.; Wang, B.; Yadegari, H.; Lushington, A.; Banis, M. N.; Zhao, Y.; Xiao, W.; Chen, N.; Wang, J.; Sham, T.-K.; Sun, X., *Advanced Functional Materials* 2017, 27, (16), 1606662.

57. Li, Y.; Yadegari, H.; Li, X.; Banis, M. N.; Li, R.; Sun, X., *Chemical Communications* 2013, 49, (100), 11731-11733.

58. Shu, C.; Lin, Y.; Zhang, B.; Abd Hamid, S. B.; Su, D., *Journal of Materials Chemistry A* 2016, 4, (17), 6610-6619.

59. Sun, Q.; Yadegari, H.; Banis, M. N.; Liu, J.; Xiao, B.; Wang, B.; Lawes, S.; Li, X.; Li, R.; Sun, X., *Nano Energy* 2015, 12, 698-708.

60. Sun, Q.; Yang, Y.; Fu, Z.-W., *Electrochemistry Communications* 2012, 16, (1), 22-25.

61. Kwak, W.-J.; Chen, Z.; Yoon, C. S.; Lee, J.-K.; Amine, K.; Sun, Y.-K., *Nano Energy* 2015, 12, 123-130.

62. Yadegari, H.; Li, Y.; Banis, M. N.; Li, X.; Wang, B.; Sun, Q.; Li, R.; Sham, T.-K.; Cui, X.; Sun, X., *Energy & Environmental Science* 2014, 7, (11), 3747-3757.

63. Zhao, N.; Li, C.; Guo, X., *Physical Chemistry Chemical Physics* 2014, 16, (29), 15646-15652.

64. Jian, Z.; Chen, Y.; Li, F.; Zhang, T.; Liu, C.; Zhou, H., *Journal of Power Sources* 2014, 251, 466-469.

65. Dong, Y.; Wu, Z.-S.; Ren, W.; Cheng, H.-M.; Bao, X., *Science Bulletin* 2017, 62, (10), 724-740.

66. Liu, W.; Sun, Q.; Yang, Y.; Xie, J.-Y.; Fu, Z.-W., *Chemical Communications* 2013, 49, (19), 1951-1953.

67. Pumera, M., *Energy & Environmental Science* 2011, 4, (3), 668-674.

68. Enterría, M.; Botas, C.; Gómez-Urbano, J. L.; Acebedo, B.; López del Amo, J. M.; Carriazo, D.; Rojo, T.; Ortiz-Vitoriano, N., *Journal of Materials Chemistry A* 2018, 6, (42), 20778-20787.

69. Nichols, J. E.; Knudsen, K. B.; McCloskey, B. D., *The Journal of Physical Chemistry C* 2018, 122, 13462-13472.

70. Schröder, D.; Bender, C. L.; Osenberg, M.; Hilger, A.; Manke, I.; Janek, J., *Scientific Reports* 2016, 6, 24288.

71. Nichols, J. E.; McCloskey, B. D., *The Journal of Physical Chemistry C* 2017, 121, (1), 85-96.

72. Xu, S.; Yao, Y.; Guo, Y.; Zeng, X.; Lacey, S. D.; Song, H.; Chen, C.; Li, Y.; Dai, J.; Wang, Y.; Chen, Y.; Liu, B.; Fu, K.; Amine, K.; Lu, J.; Hu, L., *Advanced Materials* 2018, 30, (4), 1704907.

73. Chen, C.; Xu, S.; Kuang, Y.; Gan, W.; Song, J.; Chen, G.; Pastel, G.; Liu, B.; Li, Y.; Huang, H.; Hu, L., *Advanced Energy Materials* 2019, 9, (9), 1802964.

74. Duan, J.; Chen, S.; Jaroniec, M.; Qiao, S. Z., *ACS Catalysis* 2015, 5, (9), 5207-5234.

75. Li, L.; Liu, S.; Manthiram, A., *Nano Energy* 2015, 12, 852-860.

76. Yun, K.-H.; Hwang, Y.; Chung, Y.-C., *Journal of Power Sources* 2015, 277, 222-227.

77. Li, Y.; Yadegari, H.; Li, X.; Banis, M. N.; Li, R.; Sun, X., *Chemical Communications* 2013, 49, (100), 11731-11733.

78. Zhang, S.; Wen, Z.; Jin, J.; Zhang, T.; Yang, J.; Chen, C., *Journal of Materials Chemistry A* 2016, 4, (19), 7238-7244.

79. Tang, Y.-B.; Yin, L.-C.; Yang, Y.; Bo, X.-H.; Cao, Y.-L.; Wang, H.-E.; Zhang, W.-J.; Bello, I.; Lee, S.-T.; Cheng, H.-M.; Lee, C.-S., *ACS Nano* 2012, 6, (3), 1970-1978.

80. Ren, X.; Zhu, J.; Du, F.; Liu, J.; Zhang, W., *The Journal of Physical Chemistry C* 2014, 118, (39), 22412-22418.

81. Wu, F.; Xing, Y.; Lai, J.; Zhang, X.; Ye, Y.; Qian, J.; Li, L.; Chen, R., *Advanced Functional Materials* 2017, 27, (30), 1700632.

82. Zhang, S.; Wen, Z.; Rui, K.; Shen, C.; Lu, Y.; Yang, J., *Journal of Materials Chemistry A* 2015, 3, (6), 2568-2571.

83. Kumar, S.; Kishore, B.; Munichandraiah, N., *RSC Advances* 2016, 6, (68), 63477-63479.

84. Kang, J.-H.; Kwak, W.-J.; Aurbach, D.; Sun, Y.-K., *Journal of Materials Chemistry A* 2017, 5, (39), 20678-20686.

85. Wu, F.; Xing, Y.; Lai, J.; Zhang, X.; Ye, Y.; Qian, J.; Li, L.; Chen, R., *Advanced Functional Materials* 2017, 27, (30), 1700632.

86. Khajehbashi, S. M. B.; Xu, L.; Zhang, G.; Tan, S.; Zhao, Y.; Wang, L.-S.; Li, J.; Luo, W.; Peng, D.-L.; Mai, L., *Nano Letters* 2018, 18, (6), 3934-3942.

87. Liu, Y.; Chi, X.; Han, Q.; Du, Y.; Yang, J.; Liu, Y., *Journal of Alloys and Compounds* 2019, 772, 693-702.

88. Hu, Y.; Han, X.; Zhao, Q.; Du, J.; Cheng, F.; Chen, J., *Journal of Materials Chemistry A* 2015, 3, (7), 3320-3324.

89. Liu, Y.; Chi, X.; Han, Q.; Du, Y.; Huang, J.; Lin, X.; Liu, Y., *Nanoscale* 2019, 11, 5285-5294.

90. Mohammad Fathi, T.; Bhushan, P.; Cevriye, K.; Tamer, U.; Eda, Y., *Nanotechnology* 2018, 29, 475401.

91. Ma, J.-l.; Li, N.; Zhang, Q.; Zhang, X.-b.; Wang, J.; Li, K.; Hao, X.-f.; Yan, J.-m., *Energy & Environmental Science* 2018, 11-2833-2838.

92. Li, N.; Yin, Y.; Jiang, Q., *ACS Catalysis* 2017, 7, (11), 7688-7694.

93. Wang, J.; Gao, R.; Zheng, L.; Chen, Z.; Wu, Z.; Sun, L.; Hu, Z.; Liu, X., *ACS Catalysis* 2018, 8953-8960.

94. Yadegari, H.; Norouzi Banis, M.; Lushington, A.; Sun, Q.; Li, R.; Sham, T.-K.; Sun, X., *Energy & Environmental Science* 2017, 10, (1), 286-295.

95. Lutz, L.; Alves Dalla Corte, D.; Tang, M.; Salager, E.; Deschamps, M.; Grimaud, A.; Johnson, L.; Bruce, P. G.; Tarascon, J.-M., *Chemistry of Materials* 2017, 29, (14), 6066-6075.

96. Zhao, Y.; Liang, J.; Sun, Q.; Goncharova, Lyudmila V.; Wang, J.; Wang, C.; Adair, K. R.; Li, X.; Zhao, F.; Sun, Y.; Li, R.; Sun, X., *Journal of Materials Chemistry A* 2019, 7, (8), 4119-4125.

97. Zhao, Y.; Goncharova, L. V.; Zhang, Q.; Kaghazchi, P.; Sun, Q.; Lushington, A.; Wang, B.; Li, R.; Sun, X., *Nano Letters* 2017, 17, (9), 5653-5659.

98. Zhao, Y.; V., G. L.; Andrew, L.; Sun, Q.; Yadegari, H.; Wang, B.; Xiao, W.; Li, R.; Sun, X., *Advanced Materials* 2017, 29, (18), 1606663.

99. Yang, H.; Sun, J.; Wang, H.; Liang, J.; Li, H., *Chemical Communications* 2018, 54, (32), 4057-4060.

100. Lu, Y.; Zhang, Q.; Han, M.; Chen, J., *Chemical Communications* 2017, 53, (96), 12910-12913.

101. Wang, Z.; Li, M.; Ruan, C.; Liu, C.; Zhang, C.; Xu, C.; Edström, K.; Strømme, M.; Nyholm, L., *The Journal of Physical Chemistry C* 2018, 122, (41), 23352-23363.

102. Zhang, Q.; Lu, Y.; Zhou, M.; Liang, J.; Tao, Z.; Chen, J., *Inorganic Chemistry Frontiers* 2018, 5, (4), 864-869.

103. Liu, S.; Tang, S.; Zhang, X.; Wang, A.; Yang, Q.-H.; Luo, J., *Nano Letters* 2017.

104. Rosso, M.; Gobron, T.; Brissot, C.; Chazalviel, J. N.; Lascaud, S., *Journal of Power Sources* 2001, 97-98, 804-806.

105. Wang, A.; Hu, X.; Tang, H.; Zhang, C.; Liu, S.; Yang, Y.-W.; Yang, Q.-H.; Luo, J., *Angewandte Chemie* 2017, 129, (39), 12083-12088.

106. Luo, W.; Zhang, Y.; Xu, S.; Dai, J.; Hitz, E.; Li, Y.; Yang, C.; Chen, C.; Liu, B.; Hu, L., *Nano Letters* 2017, 17, (6), 3792-3797.

107. Zhao, Y.; Yang, X.; Kuo, L. Y.; Kaghazchi, P.; Sun, Q.; Liang, J.; Wang, B.; Lushington, A.; Li, R.; Zhang, H.; Sun, X., *Small* 2018, (14), 1703717.

108. Li, P.; Xu, T.; Ding, P.; Deng, J.; Zha, C.; Wu, Y.; Wang, Y.; Li, Y., *Energy Storage Materials* 2018, 15, 8-13.

109. Bing, S.; Peng, L.; Jinqiang, Z.; Dan, W.; Paul, M.; Chengyin, W.; L., N. P. H.; Guoxiu, W., *Advanced Materials* 2018, 30, 1801334.

110. Zhu, M.; Li, S.; Li, B.; Gong, Y.; Du, Z.; Yang, S., *Science Advances* 2019, 5, (4), 6264.

111. Tang, S.; Qiu, Z.; Wang, X.-Y.; Gu, Y.; Zhang, X.-G.; Wang, W.-W.; Yan, J.-W.; Zheng, M.-S.; Dong, Q.-F.; Mao, B.-W., *Nano Energy*, 2018, 48, 101-106.

112. Zhang, H.; Liao, X.; Guan, Y.; Xiang, Y.; Li, M.; Zhang, W.; Zhu, X.; Ming, H.; Lu, L.; Qiu, J.; Huang, Y.; Cao, G.; Yang, Y.; Mai, L.; Zhao, Y.; Zhang, H., *Nature Communications* 2018, 9, (1), 3729.

113. Wang, H.; Wang, C.; Matios, E.; Li, W., *Nano Letters* 2017, 17, (11), 6808-6815.

114. Huang, C.; Xiao, J.; Shao, Y.; Zheng, J.; Bennett, W. D.; Lu, D.; Saraf, L. V.; Engelhard, M.; Ji, L.; Zhang, J.; Li, X.; Graff, G. L.; Liu, J., *Nature Communications* 2014, 5, 3015.

115. Zheng, G.; Lee, S. W.; Liang, Z.; Lee, H.-W.; Yan, K.; Yao, H.; Wang, H.; Li, W.; Chu, S.; Cui, Y., *Nat Nano* 2014, 9, (8), 618-623.

Chapter 3

3 Experimental Apparatus and Characterization Techniques

In this chapter, the materials synthesis, as well as the working principles of various physical and electrochemical characterization techniques are stated here.

3.1 Experimental apparatus

3.1.1 Fabrication of 3D printed air electrodes

The air electrodes were prepared using an extrusion-based 3D printer (**Figure 3.1**). Firstly, the starting material graphene oxide (GO) sheets were prepared by the modified Hummer's method. Then, the GO dispersion was washed with distilled water until the pH reached 7.0, and then collected by centrifugation to achieve a ~15.0 mg mL^{-1} GO ink. No binder was used for the printing ink preparation. Next, the ink was loaded into a 3 mL syringe and extruded through a 300 µm diameter nozzle. The air electrodes were printed into a grid structure with an overall diameter of 10 mm at a print motion speed of 8 mm s^{-1}. After removing the ink solvent of H_2O by freeze drying for 24 h, the dried GO structure underwent a thermal annealing process at 800°C in an Ar/H_2 atmosphere to obtain the 3D reduced graphene oxide (rGO) Na-O_2 air electrodes.
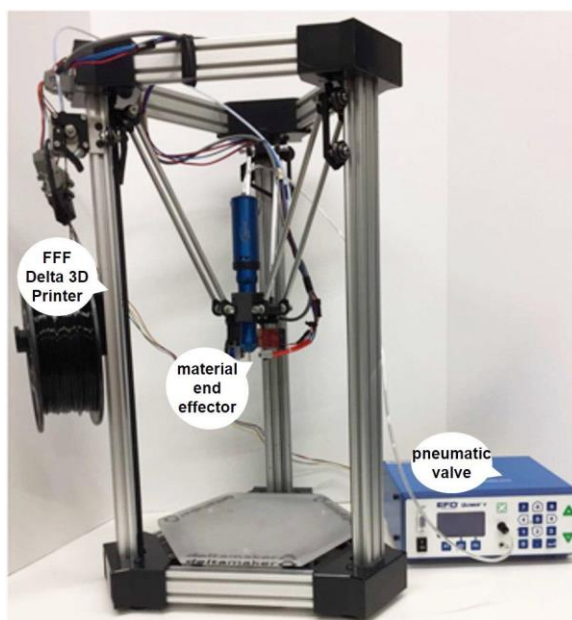
Figure 3.1 The fused filament fabrication (FFF) 3D printer.

3.1.2 Synthesis of Na$_{3.25}$Zr$_2$Si$_{2.25}$P$_{0.75}$O$_{12}$ solid-state electrolyte

The NASICON-type Na$_{3.25}$Zr$_2$Si$_{2.25}$P$_{0.75}$O$_{12}$ solid-state electrolyte (SSE) was synthesized via sol-gel method (**Figure 3.2**). Firstly, stoichiometric amounts of tetraethylorthosilicate (Si(OC$_2$H$_5$)$_4$, Sigma-Aldrich, 98%) and zirconium (IV) propoxide solution (Zr(OC$_4$H$_9$)$_4$,

Sigma-Aldrich, 99.99%) were sequentially dissolved in ethanol. Then, acetic acid and deionized water were added into the mixture dropwise, and the mixture sol was kept at 67°C under vigorous stirring for 10 h. Then, the sodium nitrate (Sigma-Aldrich, 99.0%) and ammonium dihydrogen phosphate (Prolabo, 99.9%) were, respectively, dissolved in water, and the solution was successively added into the hot mixture of silica and zirconia. In the next step, the solution was slowly evaporated at 67°C to produce the precursor powder with stirring, which was then heated at 500°C for 1 h under the O_2 atmosphere to burn out the organics. After this, the obtained powder was annealed at 1050°C for 10 h and then uniaxially pressed into pellets, which were sintered at 1300°C for 12 h in the air atmosphere.
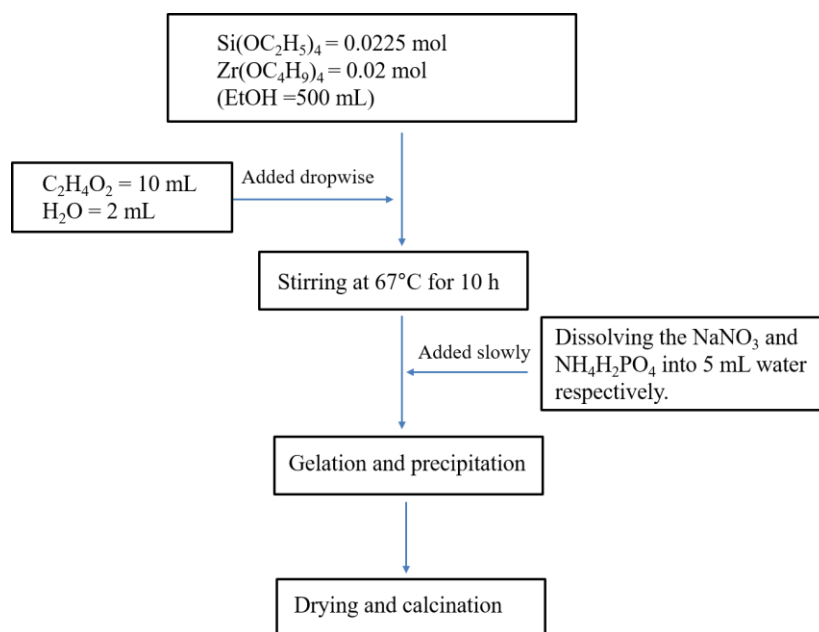
Figure 3.2 The flowchart for the synthesis of $Na_{3.25}Zr_2Si_{2.25}P_{0.75}O_{12}$ SSE.

3.1.3 Molecular layer deposition of alucone or polyurea on Na anode

Molecular layer deposition (MLD) alucone and polyurea coating on air-sensitive Na metal anode was carried out with the Gemstar-8 MLD system, which is directly connected to the Ar-filled glove box (**Figure 3.3**). The MLD process is based on surface reactions where the vapor-phase of precursors are alternatively pulsed into the reaction chamber and react in a self-limiting manner. The self-limiting surface reactions enable the precise control over

the thickness of conformal films on high aspect ratio substrates. Typically, the reactants of MLD are bifunctional monomers for stepwise condensation polymerization and can yield organic-inorganic or complete organic films.

The MLD-alucone thin film was deposited on fresh Na metal with two half reactions between trimethylaluminum (TMA) and ethylene glycol (EG) at 90°C. Firstly, the Na anode is exposed to TMA, and CH_4 is released as the byproduct. In the next step, the resulting surface reacts with the pulsed EG precursor, and again releases CH_4 as the byproduct. The MLD alucone process uses a 0.01s/40s/0.01s/70s TMA pulse/purge/EG pulse/purge sequence. In this thesis, 50 MLD alucone cycle coatings were carried out on Na foils. The MLD-polyurea was performed on fresh Na foil by alternatively introducing ethylenediamine (ED) and phenylene diisocyanate (PDIC) as the precursors at 90°C. A complete MLD polyurea cycle was described as ED pulse/purge/PDIC pulse/purge for period of 0.1s/30s/1s/50s. 50 cycles of polyurea was performed on Na foil in this work.

Figure 3.3 The Gemstar-8 ALD/MLD system connected with Ar-filled glove box (Arradiance, USA).

3.2 Characterization techniques

The physical and chemical properties of the materials, such as morphology, microstructure, composition, surface chemistry, surface area, et al., were determined by using various

characterization techniques. For instance, scanning electron spectroscopy (SEM), X-ray diffraction (XRD), Raman spectroscopy, X-ray photoelectron spectroscopy (XPS), time-of-flight secondary ion mass spectrometry (ToF-SIMS) etc. To investigate the electrochemical properties of the as-prepared Na electrode, galvanostatic cycling performance of coin cells at different current densities was evaluated using the Land testing system. The galvanostatic discharge-charge tests on Swagelok-type Na-O$_2$ batteries were carried out using the Arbin BT-2000 battery testing system.

3.2.1 Physical characterizations

The morphologies of the materials were characterized by a Hitachi S-4800 SEM equipped with energy dispersive spectroscopy (EDS), as shown in **Figure 3.4**. The SEM utilizes a beam of focused electrons as an electron probe that is scanned across the surface of a specimen. The beam's interactions with the sample results in the emission of electrons and photons as the electrons penetrate the surface. The emitted particles are collected using an appropriate detector to yield information about the sample surface. In this thesis, the SEM was operated at an acceleration voltage of 5KV in order to observe the sample morphologies.
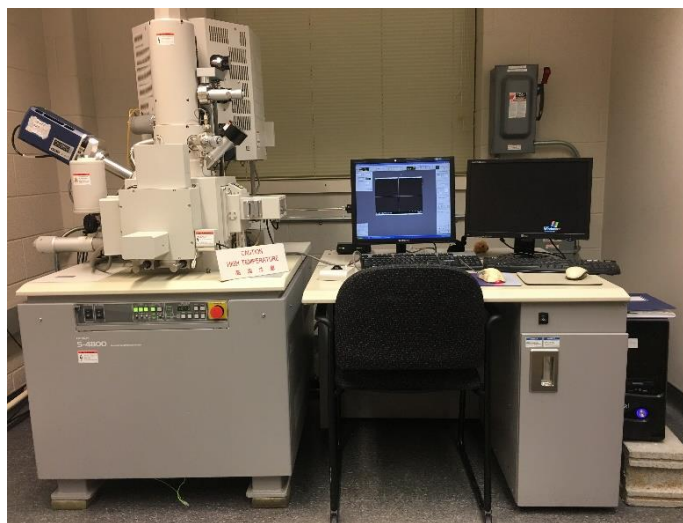
Figure 3.4 The Hitachi S-4800 scanning electron microscopy.

XRD is a powerful non-destructive technique to identify the structure of materials, especially crystalline ones. XRD peaks are produced by constructive interference of a

monochromatic beam of X-rays scattered at specific angles from each set of lattice planes in a sample. The peak intensities are determined by the atomic positions within the lattice planes. Consequently, the XRD pattern is the fingerprint of periodic atomic arrangements in a given material. In this thesis, the XRD patterns of the samples were collected on a Bruker D8 Advanced diffractometer using Cu Kα radiation at 40 kV and 40 mA, the digital photo of the XRD equipment is shown in **Figure 3.5**. For air-sensitive samples, a special leak-tight XRD sample holder was employed to prevent the exposure of air during sample testing.

Figure 3.5 The Bruker D8 Advance XRD with Cu-Kα radiation.

Raman spectroscopy is a technique to understand the vibration of chemical bonds through detecting the inelastic scattering of incident monochromatic light. The interaction of the incident light and the molecular vibrations results in light energy shifts and provides fingerprint information of the molecules. In this thesis, the Raman spectra were collected on a HORIBA Scientific LabRAM Raman spectrometer equipped with a 532.03 nm laser, the digital photo of the Raman spectrometer is shown in **Figure 3.6**.

Figure 3.6 Digital photo of HORIBA Scientific LabRAM HR Raman spectrometer system.

In this thesis, the specific surface area and pore volume of the 3D printed air electrodes were determined by N_2 adsorption/desorption isotherms conducted via Folio Mocromeritics TriStar 3020 surface Area and Pore Size Analyzer (**Figure 3.7**). The surface area of the electrode was used by the Brunauer, Emmett, and Teller (BET) model, and the porous structure was determined by the Barrett, Joyner, and Halenda (BJH) model.
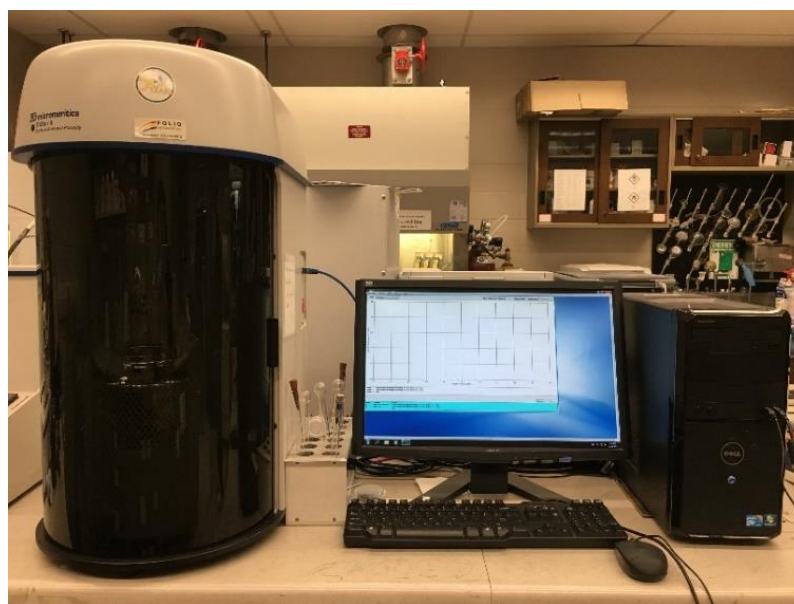
Figure 3.7 A Micromeritics Brunauer-Emmett-Teller surface area analyzer.

XPS is a tool to understand the chemical information of elements through detecting the amounts of escaped electrons from the sample surface at a certain excitation energy. In this thesis, the XPS spectra were collected using monochromatic Al Kα radiation, and all the spectra were calibrated by referencing the binding energy of a C-C bond at 284.8 eV.

ToF-SIMS is a powerful surface analysis technique. In this thesis, ToF-SIMS uses a pulsed Cs ion beam to dislodge chemical species on the cycled Na@alucone electrode surface. The secondary ions and ion clusters are removed from the surface of the samples. A time-of-flight analyzer is used to measure the exact mass of the emitted secondary ions and ion clusters, and then the identity of an element and molecular fragment can be determined based on the mass and intensity of the SIMS peak. A three-dimensional arrangement of the substance also can be revealed with depth profiling data.

3.2.2   Electrochemical characterizations

The stripping/plating stability of Na anode in Na symmetric cells (CR2032 coin cell) was evaluated using a Land 2001A battery test system at room temperature (**Figure 3.8**). A certain constant discharge/charge current was applied to the coin cells during the repeated stripping and plating process, then the electrochemical behavior of cells was recorded.

Figure 3.8 Land 2001A Battery Test System.

The electrochemical performance of Na-O$_2$ batteries was evaluated with Swagelok-type cells. As shown in **Figure 3.9**, the Swagelok-type Na-O$_2$ batteries are composed of plastic and metal Swagelok units combined with a stainless-steel mesh current collector, a cathode, a glass fiber separator, and a Na metal anode. The cathode side was exposed to O$_2$, while the opposite side is blocked. The galvanostatic discharge-charge tests on Swagelok-type Na-O$_2$ batteries were carried out using the Arbin BT-2000 battery testing system at room temperature (**Figure 3.10**). The capacity, discharge/charge overpotential and cycling stability of Na-O$_2$ cells at different current densities can be obtained. It is noted that both coin cells and Swagelok-type Na-O$_2$ cells were assembled in Ar-filled glove box with the oxygen and water contents below 0.1 ppm.
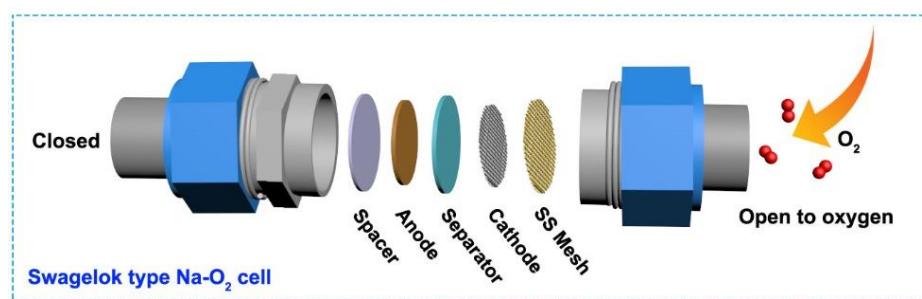
Figure 3.9 The configuration of Swagelok-type Na-O$_2$ cell.

Figure 3.10 Arbin BT-2000 battery testing system.

Chapter 4

4 3D printing of freestanding "O$_2$ breathable" air electrodes for high-capacity and long-life Na-O$_2$ batteries

Superoxide-based Na-O$_2$ batteries have been considered as one of the most promising candidates for next-generation energy storage systems due to their high theoretical energy density and energy efficiency. However, to fully realize the advantages of Na-O$_2$ batteries, the underutilization of air electrodes and poor cycling performance caused by limited O$_2$ transport within the air electrodes should be well addressed. 3D printing is a powerful technique in fabricating electrodes with special designs for various energy storage systems. 3D-printed electrodes have advantages of controllable 3D geometry/structure and tunable layers, which promises efficient mass (O$_2$/Na$^+$) and electron transport.

In this chapter, 3D printing of reduced graphene oxide (rGO)-based air electrodes with hierarchical porous structure were firstly demonstrated as "O$_2$ breathable" for the Na-O$_2$ batteries. The unique cathode structure features noncompetitive and continuous pathways for O$_2$, Na$^+$ ions and, electrons. The macro pores provide smooth passages to facilitate O$_2$ access across the whole electrode, while the micropores between rGO sheets serve as electrolyte reservoirs and accommodate NaO$_2$. The efficiently packed rGO sheets ensure good electronic conductivity within the 3D architecture. Benefiting from the separated pathways for the three phases, Na-O$_2$ batteries with high specific capacities and long cycling stability are achieved. In addition, the refined balance between electronic conductivity and O$_2$ transport was demonstrated.

4.1 Introduction

The depletion of fossil fuels and undesirable environmental consequences have dramatically promoted an extensive research for new energy storage systems, including Li-S and metal-O_2 batteries.[1-5] Among them, rechargeable Na-O_2 batteries have attracted significant attentions due to their high theoretical energy density, high energy efficiency, and environmental benignity.[6-8] The low cost and abundance of the Na element are additional advantages of the Na-O_2 battery system with respect to energy storage for next-generation electric vehicles. However, the practical discharge capacities of Na-O_2 batteries are still far from the theoretical value, and their cycling performance is poor. Chemical and electrochemical instabilities of cell components are partially responsible for the poor cell performance.[9-11] Electrolytes and polymer binders are readily attacked by the highly nucleophilic anion O_2^- or singlet oxygen species $^1O_2$ to generate unfavourable side products, which is harmful to the reversible charge capacity and overall cell performance.[12, 13] In addition, Na metal degradation caused by contaminants (O_2, O_2^-, and H_2O) and Na dendrite growth are two main reasons for the premature cell death that cannot be neglected.[14-19] Nonetheless, it is widely accepted that the properties of the air electrodes where the oxygen reduction reaction (ORR) and oxygen evolution reaction (OER) take place are primarily affecting the electrochemical performance of Na-O_2 batteries.

Unlike Li-O_2 batteries in which the cathodes have minor effects on the growth of toroidal Li_2O_2, which is reported as the only discharge product, the composition and morphologies of the discharge products in Na-O_2 batteries are highly dependent on the nature of the air electrodes. As reported by Wang et al., $Na_2O_2·2H_2O$ and NaOH were identified as major discharge products of Na-O_2 batteries with a CoO/CoP electrocatalyst.[20] Ma and co-workers constructed air electrodes with a porous CoB catalyst that produced both NaO_2 and Na_2O_2 during the discharge process of the Na-O_2 batteries.[21] Different to the formation of micrometre-sized NaO_2 on the carbon paper (CP) cathode through a solution-mediated path, Lutz et al. found that the introduction of Au on CP resulted in the formation of NaO_2 flakes through a surface-mediated route, accompanied by a significant decrease in capacity.[22] Compared with Na_2O_2, $Na_2O_2·2H_2O$, NaOH, and Na_2CO_3, micron-sized NaO_2 is more desired as a low overpotential and good capacity retention are hardly achieved

simultaneously once other products are produced. Therefore, the fabrication of air electrodes with favourable surface chemistries for reversible formation and decomposition of cubic NaO_2 is crucial to achieve high-performance Na-O_2 batteries.

In addition to the cathode surface properties, a rationally designed architecture could be important for fully utilizing the air electrode.[23-25] Due to the transport limitation of O_2 within the organic electrolytes, the NaO_2 particles predominantly deposited in the electrode region with sufficient exposure to O_2. The accumulation of NaO_2 particles on the oxygen side of cathode can clog the electrode surface that restricts O_2 access in the interior air electrode, resulting in the premature termination of the discharge process and underutilization of the air electrodes.[25-27] Even the H23 CP cathode with large pores on the scale of tens of microns shows no exception, with a Na-O_2 battery capacity of only ~50% of the theoretical value.[6] Nichols et al. verified that the discharge capacity of Na-O_2 batteries can be improved by increasing the oxygen partial pressure as it changed the concentration gradient for faster oxygen diffusion in the organic electrolyte.[26] By fabricating self-stacked nitrogen-doped carbon nanotube air electrode, Sun et al. further highlighted the importance of rapid O_2 and Na^+ transportation within the air electrode.[24] However, the studies of the fabrication of engineered air electrodes with effective O_2 transport channels are relatively scare, and limited O_2 mass transportation within the air electrode is still a substantial challenge, especially the thick cathodes.[28, 29] Additive manufacturing, also known as a 3D printing technique, has attracted an enormous amount of attention in the energy storage field due to its feasibility in fabricating a complex 3D architecture.[30-34] Among various printing materials, graphene oxide (GO) has shown unique viscoelastic properties and printing capabilities when dispersed in H_2O with a high concentration.[35] Moreover, the electrical conductivity of the GO can be retrieved after thermal reduction, with the formation of rGO electrode. Since highly concentrated GO ink can be directly printed into fine filaments, 3D periodic rGO-based air electrodes with the desired architecture and thickness can be well patterned through careful control of printing parameters.

Herein, we first fabricate a novel "O_2 breathable" air electrode by 3D printing for high-performance superoxide-based Na-O_2 batteries. The 3D printed air electrode has a stacked

mesh structure with macroscale open pores and interconnected conductive filaments that composed of rGO sheets. The vertical open channels across the electrode facilitate continuous O_2 access, promising a full utilization of the active sites on the air electrode. Additionally, the micropores among the rGO sheets provide sufficient space for electrolyte permeation and NaO_2 accommodation. The efficiently packed rGO sheets also ensure sufficient electronic conductivity within the 3D architecture. Consequently, a high specific capacity of 13484.6 mAh g^{-1} (9.1 mAh cm^{-2}) can be achieved at 0.2 A g^{-1}. Unprecedentedly stable performance is achieved over 120 cycles with a cutoff capacity of 500 mAh g^{-1} at 0.5 A g^{-1}. The diameter of the O_2 channels in the air electrode is optimized on the basis of the balance between electronic conductivity and the O_2 transportation. This work clearly elucidates the importance of the rational design of the air electrode structure for realizing high-performance Na-O_2 batteries. The emerging 3D printing technique combined with a freeze-drying procedure is demonstrated to be a powerful tool for fabricating effective air electrodes with hierarchical pores.

4.2   Experimental section

Graphene oxide (GO) ink preparation and air electrode preparation. GO sheets were prepared by the modified Hummer's method according to the previous report.[7] Then, the GO dispersion was washed with distilled water until the pH reached 7.0 and then collected by centrifugation to achieve an ~15.0 mg mL^{-1} GO ink. No binder was used for the printing ink preparation. Next, the ink was loaded into a 3 mL syringe and extruded through a 300 μm diameter nozzle. The 3D printed air electrodes with no open pores (3DP-NP), small open pores (3DP-SP), and large open pores (3DP-LP) were printed with an overall diameter of 10 mm at a print motion speed of 8 mm s^{-1}, and the diameter of the pores was controlled by changing the distances between the adjacent filaments. The printed GO-based patterns were freeze-dried for 24 h and subsequently thermally reduced at 800°C in a H_2/Ar atmosphere for 2 h to obtain the rGO-based air electrodes.

Battery assembly and electrochemical measurements. The electrochemical performance of Na-O_2 batteries was evaluated with Swagelok-type cells.[18] The Na-O_2 cell were assembled with a CP (Fuel Cell Store, H23) interlayer protected Na anode, a glass fibre separator, and a 3D printed air electrode. The configuration of the Na-O_2 batteries is shown

in **Figure S4.1**. The electrolyte was 1 M sodium triflate ($NaSO_3CF_3$) dissolved in diethylene glycol dimethyl ether (DEGDME, reagent grade $\geq$ 98%, Aldrich). The same amount of electrolyte (100 μL per cell) was added in the control. The electrolyte preparation and battery assembly were carried out in an Ar-filled glove box with the oxygen and water contents of < 0.1 ppm. The Na-O_2 cells were operated under static O_2 with the pressure of 1.5 atm in a homemade testing box. Each Na-O_2 cell was stabilized for 1h at room temperature before being tested. The galvanostatic discharge-charge tests were carried out using an Arbin BT-2000 battery testing system. Noted that the DEGDME was dried by freshly activated molecular sieves (4 Å, Aldrich) for two weeks, and $NaSO_3CF_3$ salt was dried under vacuum at 80 °C for one week before use.

Material characterization. The morphologies and structures of air electrodes, as well as the discharge product, were characterized by a Hitachi S-4800 scanning electron microscope (SEM) and transmission electron microscopy (TEM, JEOL 2100F). X-ray diffraction (XRD) (Bruker D8 Advance) with Cu-Ka radiation was used for structural characterization, and the data were collected from 30º to 70º in 2θ at a scanning rate of 1º min^{-1}. The Raman spectra were recorded on a HORIBA Scientific LabRAM Raman spectrometer equipped with a 532.03 nm laser. X-ray photoemission spectra (XPS) was carried out by a Kratos Axis Ultra Al-α spectrometer operated at 14 kV. The surface area and pore volume of three air electrodes were studied by N_2 adsorption/desorption using the Brunauer-Emmett-Teller (BET) method. In this study, the discharged/charged electrodes were washed with fresh DEGDME to remove any residual $NaSO_3CF_3$ salt and then thoroughly dried in a vacuum chamber before SEM, XRD and Raman measurements. Leak-tight XRD and Raman sample holders were used to prevent the exposure of air during sample testing.

4.3 Results and discussion

The fabrication of the free-standing "O_2 breathable" Na-O_2 battery cathode is schematically illustrated in **Figure 4.1**. A homogeneous GO ink was prepared with the desired rheological properties. Then, the stacked mesh structure of GO was printed layer by layer through a nozzle ($\varnothing$ = 300 μm). After the ink solvent of H_2O had been removed by freeze-drying for

24 h, the dried GO structure underwent a thermal annealing process at 800°C in an Ar/H$_2$ atmosphere to yield the 3D rGO Na-O$_2$ cathodes. For comparison, the 3DP-NP, 3DP-SP, and 3DP-LP air electrodes were prepared via an identical procedure except for the different spacing between adjacent filaments. It should be noted that the introduction of macro open pores into the air electrode is difficult to realize by the traditional electrode fabrication methods.[36] Additionally, different to the dip-casting method, no polymer binder was involved during the preparation of 3D-printed air electrodes because the highly concentrated GO ink provides the prerequisite viscosity to bind the GO nanosheets together. The binder-free feature of the 3D-printed air electrodes is not only favorable for increasing the electrode energy density but also can eliminate the binder-related parasitic reactions induced by the nucleophilic attack of O$_2^-$ towards binders in Na-O$_2$ batteries.[37-40]
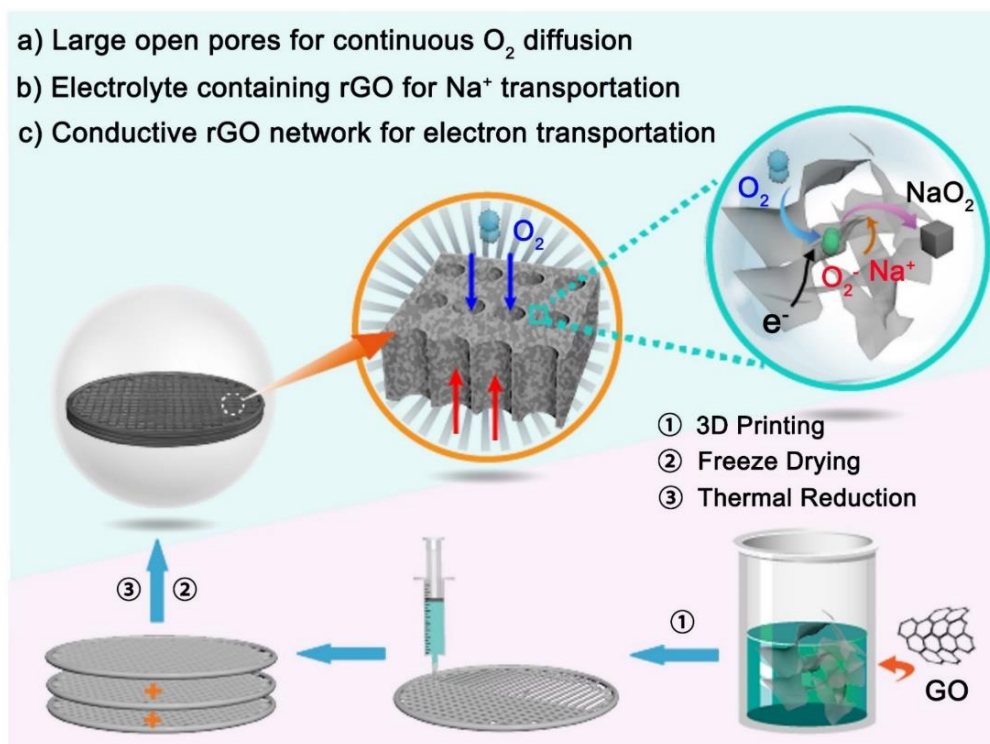
Figure 4.1 Schematic illustration of the 3D-printed "O$_2$ breathable" air electrodes for Na-O$_2$ batteries.

Raman characterization was conducted to investigate the structure changes of GO during the reduction process. As shown in **Figure S4.2**, GO showed broad D (1350 cm^{-1}) and G (1587 cm^{-1}) bands before the thermal treatment, which is a typical Raman spectrum of

GO.[41-43] After the thermal reduction, the peaks became sharper and the full width at half-maximum for both D and G bands decreased, suggesting a higher graphitization degree of the rGO air electrode. Additionally, the increase in the intensity ratio (I_D/I_G) from 0.93 of GO to 1.05 of rGO can be attributed to the presence of unrepaired defects that remained on rGO after the removal of oxygen-containing functional groups. The removal of oxygen-containing functional groups after reduction can be further confirmed by the remarkable increase in the atomic C/O ratio in the normalized wide-scan survey XPS spectra of rGO (**Figure S4.3**). On the basis of the deconvoluted XPS spectra of the C 1s and O 1s regions, the oxygen-containing functional groups, including C=O, COH, and COOH groups, can be partially removed during the thermal reduction process. It is noteworthy that thermal annealing not only can improve the electrode electrical conductivity (**Figure S4.4**), but also is favorable for minimizing the undesired reactions catalyzed by oxygen-containing functional groups at the air electrodes during the ORR process of Na-O$_2$ batteries.[44]

The microstructure of the as-prepared rGO air electrodes was characterized by SEM, as shown in **Figure 4.2**. Top-view SEM images of 3DP-SP and 3DP-LP cathodes show the stacked mesh structure with macroscale open channels for O$_2$ passage and conductive filaments (~300 µm) of rGO sheets. The diameter of the open channels for 3DP-SP and 3DP-LP electrodes are approximately 350 and 520 µm, respectively; no obvious gap was observed between adjacent filaments for the 3DP-NP electrode (**Figure 4.2a-c**). Despite the different macroscopic channels introduced by 3D printing, similar honeycomb porous microstructures were constructed in three air electrodes (**Figure 2d-f**). The presence of microscale pores in the air electrodes can be attributed to the removal of ice template during the freeze-drying procedure. The ice-templating mechanism can force the GO sheets to align along the growing boundaries of the ice crystals, and thus, the restack of the GO sheets under the effect of van der Waals or capillary force can be prevented.[35, 41, 45] The nitrogen adsorption/desorption isotherm of 3DP-NP, 3DP-SP, and 3DP-LP in **Figure S5** indicate the presence of both macropores (pore diameter > 50nm) and the mesopores (2 nm < pore diameter < 50 nm), and three electrodes possess similar BET surface area of 342.8, 362.6, and 369.6 m^2 g^{-1}, respectively. The resultant mesopores contributed to the high degree of exposure of active sites on cathodes for ORR and OER and, at the same time, micrometer-sized pores that are favorable for accommodating insoluble NaO$_2$.

Additionally, it is worth noting that the hierarchical structures of air electrodes were robust after freeze-drying and thermal reduction (**Figure S6** and inset in **Figure 2a-c**), even though no polymer binder was used, which is urgently desired for Na-O$_2$ batteries.
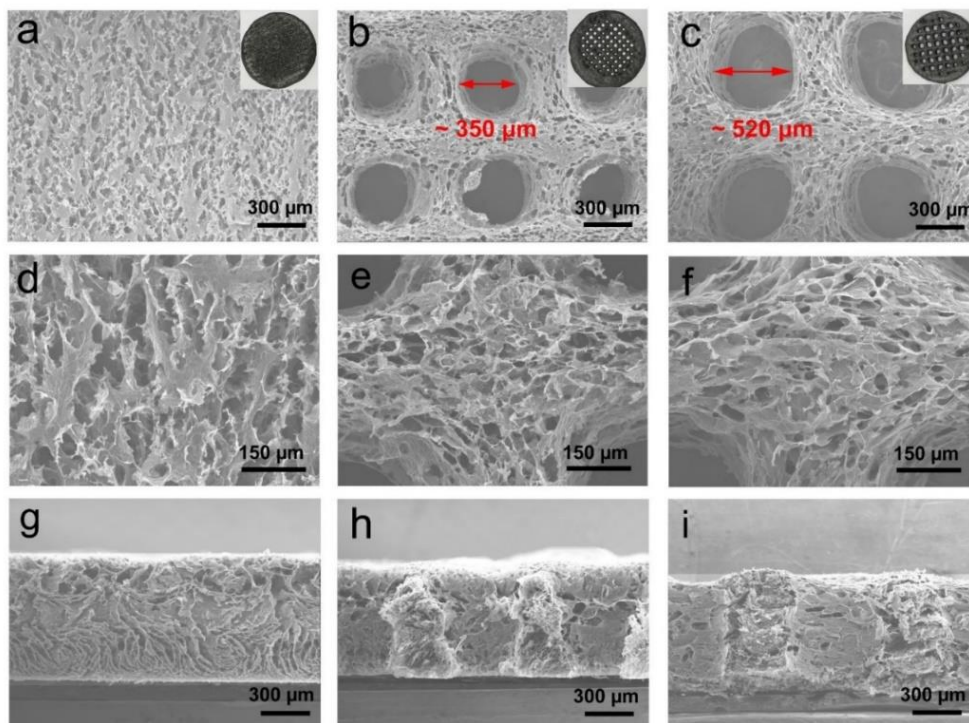
Figure 4.2 Top-view SEM images of (a, d) 3DP-NP, (b, e) 3DP-SP, and (c, f) 3DP-LP air electrodes at different magnifications (insets in a-c are optical images of the 3D printed electrodes); Cross-sectional SEM images of (g) 3DP-NP, (h) 3DP-SP, and (i) 3DP-LP cathodes.

The cross-sectional SEM images of three different air electrodes (**Figure 2g-i**) displayed a similar thickness of ~ 600 µm, which are thicker than the electrodes fabricated by conventional casting method.[36] The comparable electrode thickness can minimize the effect of electronic transmission efficiency on the performance of Na-O$_2$ batteries among the three air electrodes. Excellent affinity without obvious boundaries was observed between the adjacent printing layers in the three air electrodes. The structural unity and highly interconnected 2D rGO sheets with diameter of ~ 5 µm ensured efficient electronic conduction throughout the electrode (**Figure S7** and **S8**), and at the same time, infusion of liquid organic electrolyte in this structure yielded smooth Na$^+$ transport pathways. The

macro open channels in 3DP-SP and 3DP-LP electrodes that penetrated across the thickness of the air electrodes are beneficial for sufficient O_2 access during the ORR and OER processes. Meanwhile, the micro spacings are also distributed throughout the depth of the rGO filaments, providing a benefit for the full utilization of an air electrode during the discharge and charge process (**Figure S9**). Intuitively, the favorable hierarchical porous electrode with an interconnected conductive network and efficient O_2 transportation channels can reduce the internal cell resistance, ensure the high availability of the active sites, and thus improve the overall performance of Na-O_2 batteries.
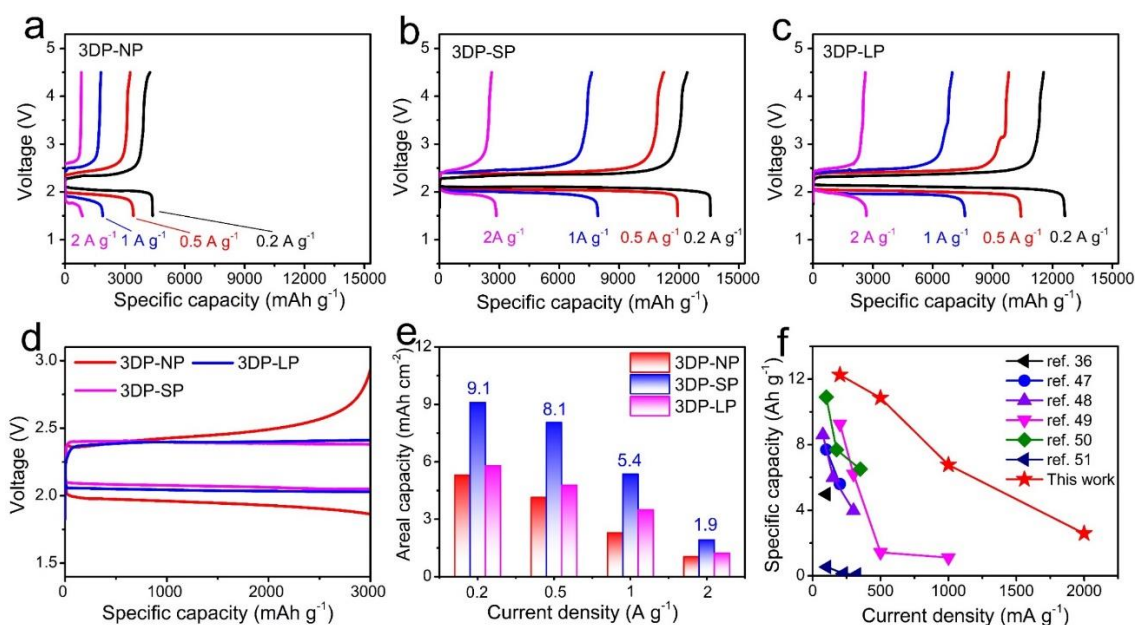
Figure 4.3 Initial discharge-charge profiles of (a) 3DP-NP, (b) 3DP-SP, and (c) 3DP-LP cathodes at the current densities of 0.2, 0.5, 1, and 2 A g^{-1}. (d) Initial discharge-charge profiles of the 3DP-NP, 3DP-SP and 3DP-LP cathodes that extracted from figure 3a-c at the current density of 0.5 A g^{-1}. (e) Areal specific capacity of Na-O_2 cells with three different cathodes. (f) Comparison on the rate performance of the 3DP-SP cathode in the present work with other reported rGO-based cathodes.

Electrochemical performance of Na-O_2 batteries with three different air electrodes was tested in the voltage range of 1.5-4.5 V at different current densities. Note that the electrically connected CP interlayer with Na metal as the protected Na anode is employed when assembling the Na-O_2 cells, to prevent Na dendrite growth and alleviate Na anode

degradation.[17, 18, 46] As shown in **Figure 4.3a-c**, the Na-O$_2$ batteries with different air electrodes exhibited similar discharge and charge voltage profiles except for the total specific capacities, which indicated no obvious difference in reaction mechanism during their ORR and OER processes. At different current densities of 0.2, 0.5, 1, and 2 A g^{-1}, the 3DP-SP air electrodes delivered initial discharge capacities of 13484.6, 11935.3, 7939.6, and 2841.4 mAh g^{-1}, respectively, whereas the 3DP-NP electrodes exhibited significantly decreased discharge capacities of 4385.6, 3425.8, 1890.5 and 865.9 mAh g^{-1}, respectively. Because the three air electrodes possess similar mesopores and micrometer pores, the absence or presence of large open pores on air electrodes should be responsible for the distinct discharge capacities of Na-O$_2$ batteries. While it is noticable that the discharge capacities of the 3DP-LP air electrode were slightly lower than those of the 3DP-SP electrode (**Figure 4.3b** and **c**). The initial discharge-charge profiles of the Na-O$_2$ batteries based on three air electrodes at 0.5 A g^{-1} was extracted from **Figure 4.3a-c** with a cutoff capacity of 3000 mAh g^{-1}. As shown in **Figure 4.3d**, the degrees of voltage polarization of the 3DP-SP and 3DP-LP air electrodes were significantly smaller than that of 3DP-NP air electrode, consequently yielding higher round-trip energy efficiencies. While 3DP-LP air electrode exhibited an overpotential slightly larger than that of the 3DP-SP electrode at 0.5 A g^{-1}, this difference was more obvious at a higher current density of 1 A g^{-1} (**Figure S4.10**), indicating that the different sizes of open channels had an influence on the internal resistance of the electrodes.

Compared to the 3DP-NP electrode, the enhancement of discharge capacities as well as the ORR/OER kinetics of the 3DP-SP and the 3DP-LP air electrodes can be attributed to their efficient O$_2$ transport across the electrode from the macro open channels. However, the increase in open pore size results in a higher porosity and less conductive pathways in the 3DP-LP air electrode than in the 3DP-SP electrode, which was adverse to the electronic conduction within the electrode[43] and thus led to the relative higher discharge/charge overpotential of the 3DP-LP air electrode. In addition, even though the O$_2$-breathing electrodes have been highly utilized, the high porosity of 3DP-LP cathodes could eventually limit the areal discharge capacity due to low carbon loading and insufficient active surface area. Overall, the 3DP-SP electrodes, which had maximized the active rGO surface with appropriate O$_2$-breathing capability, exhibited the highest areal capacities

among three designs of air electrodes at all current densities (**Figure 4.3e**). Specifically, the 3DP-SP electrode achieved a high areal capacity of 9.1 mAh cm^{-2} at 0.2 A g^{-1}, whereas the 3DP-NP and 3DP-LP air electrodes only delivered 5.3 and 5.8 mAh cm^{-2}, respectively. Compared to the reported rGO-based cathode for non-aqueous Na-O$_2$ batteries,[36, 47-51] the 3DP-SP air electrode demonstrates substantial superiority in specific capacities at all current rates (**Figure 4.3f**), benefiting from the well designed O$_2$ breathing channels and sufficient active surface. It is also noteworthy that the short-circuiting issue can be completely eliminated due to the employment of CP interlayer, which can facilitate Na deposition within its 3D structure, contributing to the high reversibility of Na-O$_2$ batteries (**Figure S4.11**).
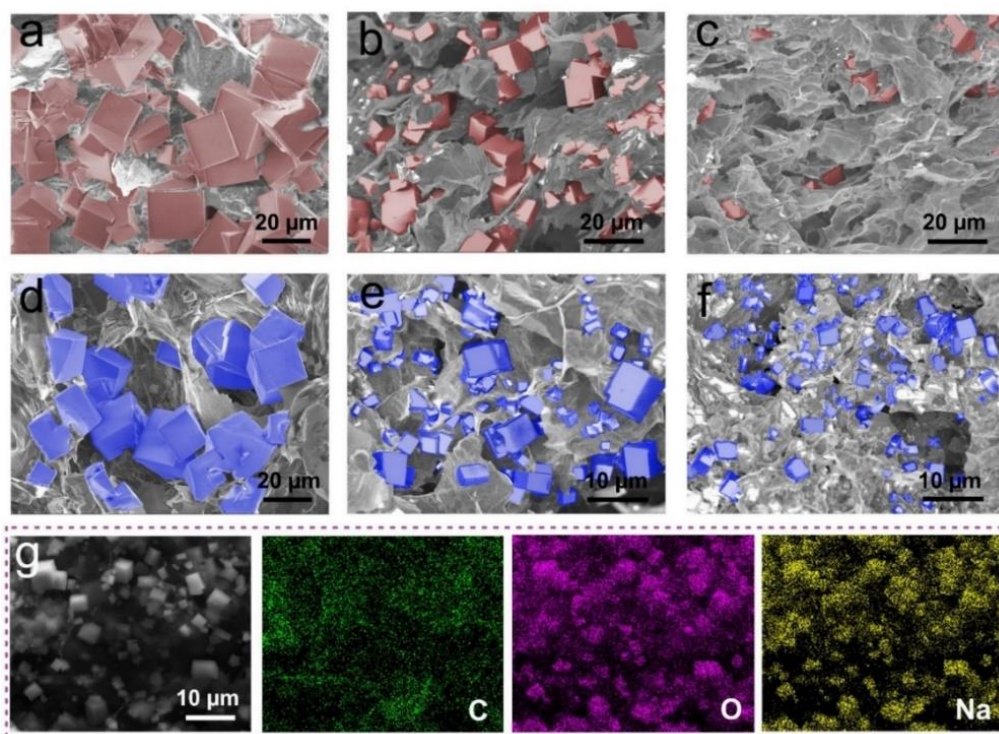
Figure 4.4 SEM images of (a-c) fully discharged 3DP-NP cathode and (d-f) partially discharged 3DP-SP cathode at 0.2 A g^{-1} with focuses on the O$_2$ accessible surface (a, d), cross-section close to the side of O$_2$ flow (b, e), and cross-section near the separator side (c, f). (g) SEM image and the corresponding EDX elemental mappings of the discharged 3DP-SP cathode. The discharge capacities of both 3DP-NP and 3DP-SP cathodes are 4613 mAh g^{-1}.

To further understand the different discharge capacities between 3DP-NP and 3DP-SP air electrodes, two typical electrodes were disassembled for morphological investigations after discharging at 0.2 A g^{-1}. Panels a-c of **Figure 4.4** depict the microstructures of the fully discharged 3DP-NP electrode and discharge products determined by SEM. It can be clearly observed that the outer surface (the side facing O$_2$ flow) of the air electrode was covered by numerous NaO$_2$ cubes with dimensions of > 20 μm. Such large cubic discharge products are similar to those observed on CP cathodes in our previous report.[18] The cross-sectional SEM images indicated a spatial variation in the distribution and size of NaO$_2$ cubes across the 3DP-NP electrode. Medium sized NaO$_2$ cubes with an average dimension of ~15 μm were dispersed in fitting pores of the electrode close to O$_2$ flow (**Figure 4.4b**), while the amount of NaO$_2$ cubes substantially decreased toward the separator side, indicating incomplete utilization of the 3DP-NP air electrode. The decreasing degree of deposition of NaO$_2$ from the O$_2$ accessible side to the separator side was consistently observed across the 3DP-NP electrode (**Figure S4.12**). Few NaO$_2$ were observed in the regions approaching the separator. In contrast, with the same discharge capacity, the discharge product NaO$_2$ deposited across the depth of the entire 3DP-SP air electrode (**Figure S4.13**). SEM images in **Figure 4.4d-f** clearly show the uniform and widespread occurance of cubic NaO$_2$ deposits across the depth of the 3DP-SP air electrode, but with decreasing dimensions. The small cubic deposits (≤ 5 μm) on the 3DP-SP air electrode toward the separator side were confirmed to be NaO$_2$ by energy dispersive X-ray spectroscopy (EDX) elemental mapping images in **Figure 4.4g**. Unlike the pore clogging behaviors in the 3DP-NP electrode, the dissolved Na$^+$-O$_2^-$ can be continuously deposited onto the existing small NaO$_2$ cubes upon further discharging due to the efficient O$_2$ access. This also explains the high discharge capacity achieved by the 3DP-SP air electrodes.

On the basis of the SEM observations, we can relate the distinct NaO$_2$ distributions to the different O$_2$ accessibilities across the two air electrodes. Due to the easy access of O$_2$ and fast electronic conductivity, the NaO$_2$ cubes were preferentially formed on the outer surface of both 3DP-NP and 3DP-SP electrodes in large size (20 μm) (**Figure 4.4a** and **d**). However, due to the pore clogging effect, the accumulation of the discharge product impeded O$_2$ transfer within the 3DP-NP air electrode for further discharge. As a result, active sites away from the surface were not fully utilized. In the case of the 3DP-SP air

electrode, the vertical open pores in the electrode act as the O_2 transport channels, ensuring continuous O_2 access during the proceeding discharge process. Hence, full utilization of active sites on the electrode as well as high discharge capacity can be achieved. A similar result also can be observed for the 3DP-LP air electrode due to the positive effect of the open O_2 channels (**Figure S4.14**).
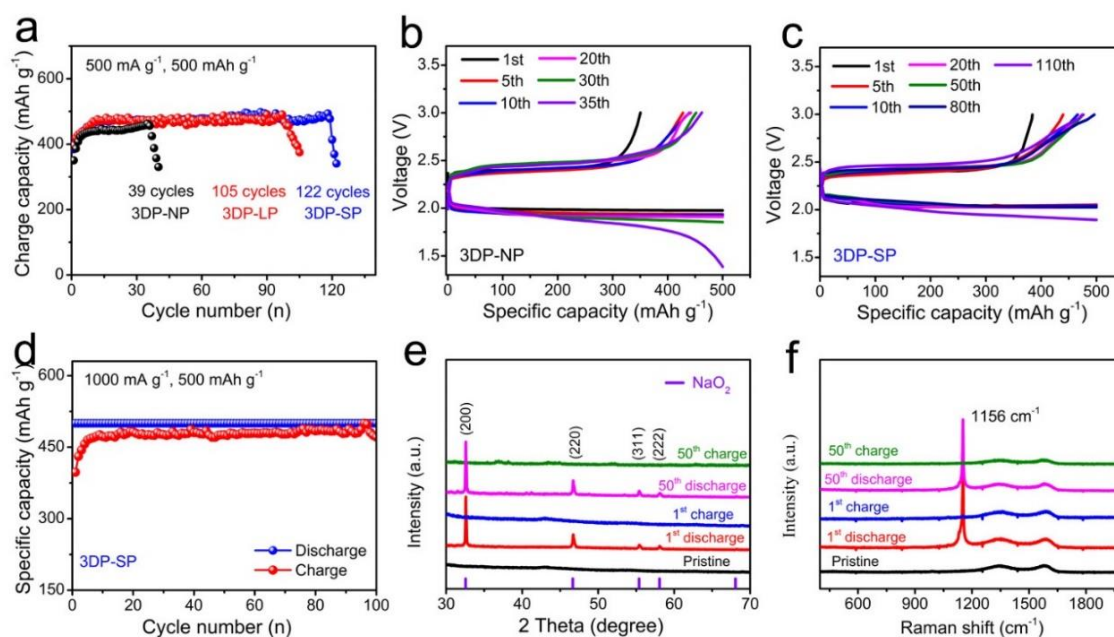
Figure 4.5 (a) Cycling performance of Na-O_2 batteries using 3DP-NP, 3DP-SP, and 3DP-LP cathodes with a limited discharge capacity of 500 mAh g^{-1} at 500 mA g^{-1}; corresponding discharge/charge profiles of (b) 3DP-NP and (c) 3DP-SP air electrodes at different cycles. (d) The cycling performance of 3DP-SP electrode at 1000 mA g^{-1} with a limited discharge capacity of 500 mAh g^{-1}. (e) XRD patterns and (f) Raman spectra of 3DP-SP electrodes at different discharge/charge states upon cycling at 500 mA g^{-1} by curtailing the discharge capacity to 500 mAh g^{-1}.

The cycling performance of Na-O_2 batteries using 3DP-NP, 3DP-SP, and 3DP-LP electrodes is shown in **Figure 4.5a**. At 0.5 A g^{-1} with a limited capacity of 500 mAh g^{-1}, the 3DP-SP cell exhibited the longest cycle life of the three of 122 cycles, which substantially surpassed the 39 cycles of the 3DP-NP cell and 105 cycles of the 3DP-LP cell. Notably, the discharge-charge profiles of 3DP-SP cell were highly stable during cycling, and the terminal discharge voltage was still > 2.0 V at 80 cycles. In a manner consistent

with the rate profiles in **Figure 4.3a-c**, the 3DP-NP cell exhibited a discharge/charge overpotential that was larger than that of the 3DP-SP and the 3DP-LP cells (**Figure 4.5b, c** and **S4.15**). As the thickness of the three air electrodes were comparable, O_2 accessibility and electronic conductivity rather than ionic resistance were responsible for the different cycle lives. Even with a limiting discharge capacity of 500 mAh g^{-1} at a higher current density of 1000 mA g^{-1}, a Na-O_2 battery based on the 3DP-SP cathode also achieved excellent cycling stability over 100 cycles (**Figure 4.5d** and **S4.16**). These result again highlight the rational design of the air electrode that significantly enhanced the electrochemical performance of Na-O_2 batteries.

Figure 4.5e shows the XRD patterns of the 3DP-SP air electrode at different discharge-charge cycles to evaluate the reversibility of the electrochemical products. Regardless of the 1st or the 50th discharge state, the characteristic peaks of crystalline NaO_2 can be observed clearly. Both the positions and intensities of the reflections are in good agreement with the previous reports.[27, 52] The disappearance of the NaO_2 characteristic peaks at the 1st and the 50th charge states indicated the high reversibility of NaO_2, as also evidenced by the absence of cubic particles on the SEM image of the recharged air electrode (**Figure S4.17**). While noted that small peaks of $Na_2O_2 \cdot 2H_2O$ appearing at $2\theta \approx 37.1º$, 40.6º and 41.2º after 50 cycles, which can be ascribe to the reaction between NaO_2 and water that from gas or an electrolyte during cycling.[53, 54] The highly reversible formation and decomposition of NaO_2 on the 3DP-SP electrode were further confirmed by Raman analyses (**Figure 4.5f**). The Raman spectra of the discharged 3DP-SP air electrodes exhibited strong signals of NaO_2 at 1156 cm^{-1} that disappeared after charge. The XRD and Raman results complementarily proved that the high discharge and charge capacities of the 3DP-SP air electrode were indeed resulted from the desirable formation and decomposition of NaO_2.

Different to the peroxide based Na-O_2 batteries that require a high charge voltage (> 3.5 V) like Li-O_2 batteries, the electrochemical reduction of NaO_2 exhibits a low charge overpotential. Therefore, the concerns about electrolyte decomposition and singlet $^1O_2$ generation during charging at high voltages were avoided.[13] Additionally, the binder-free feature of the 3D-printed air electrodes eliminated possibly undesirable side reactions that

could be induced by proton abstraction of O_2^- from the binder polymer backbone. However, it should be noted that the formation of NaO_2 via the solution-mediated path result in a large amount of the dissolved O_2^- intermediate in the organic electrolyte. Therefore, the degradation of the air electrode induced by the O_2^- radical cannot be avoided, and the active sites on the air electrode surface will be gradually covered by the film-like side products, especially after long-term cycling (**Figure S4.18**). Additionally, the dissolved O_2^- intermediate tends to migrates from the cathode to the Na anode, which not only induce severe Na anode corrosion but also result in reversible charge capacity loss and inferior Coulombic efficiency (< 100%) (**Figure 4.5b, c**).[15, 18] Note that the incomplete decomposition of NaO_2 also contribute to the limitted Coulombic efficiency of Na-O_2 batteries. Except for the issues mentions above, the structure changes of the air electrode during cycling may also responsible for the limited cycle life. Since the discharge product of Na-O_2 batteries is cubic NaO_2, and the NaO_2 size can be 1-50 µm. With the repeated formation and decomposition of NaO_2 during cycling, the pore structure of the air electrode may change or even cause slight pore structure collapse, which is adverse to the stable cycling of Na-O_2 batteries. Additionally, the Na-O_2 battery is an open system, so the effect of organic electrolyte evaporation as well as the electrolyte decomposition/consumption also cannot be neglected. All these factors inevitably attenuate the cycle life of Na-O_2 batteries.

In fact, the electrochemical performance of the Na-O_2 batteries is also comprehensively affected by the mass transport of O_2/Na^+ and the electronic conductivity within the cathode. The highly microporous structure of the 3DP-NP enabled thoroughout permeation of electrolyte in the electrode with high active surface area, which benefited rapid access of Na^+. However, the electrolyte flooding conversely limited O_2 transport. The accumulation of insoluble discharge products on the open surface of the air electrode had blocked the passage of O_2 to the inner electrode for complete discharge. Hence, the 3DP-NP cathode exhibited poor rate capability and low capacity. With respect to the 3DP-LP cathode, the entire air electrode was accessible to both the organic electrolyte and O_2 due to microporous framework and additional O_2 pathways. The sufficient O_2 and Na^+ access to the active surface led to a discharge capacity that was higher than that of the 3DP-NP air electrode; however, the total active rGO surface and electronic pathways were limited in the 3DP-LP

cathode when the O_2 open channels were too large, causing drawbacks to the Na-O_2 cell performance. The impressive performance of the 3DP-SP cathode was attributed to the fine balance between efficient ionic/electronic conductions and enhancement of O_2 diffusion kinetics within the electrode. The appropriate proportion of O_2 pathways in the electrode facilitated continuous ORR in the air electrode, alleviating the concern of rate-limiting O_2 transport that had been demonstrated by the 3DP-NP cathode. Moreover, the effective areal mass loading of the 3DP-SP cathode was much higher than that of the 3DP-LP electrode, providing a significant improvement in electronic conduction and active surface area. It should be noted that the optimized electrode in this work was the 3DP-SP electrode, but the optimal size and proportion of open O_2 channels may vary depending on the 3D printing materials, resolution, thickness, and drying methods for the electrodes. Upon development of 3D printing techniques that shall be printable for thicker electrodes with smaller O_2 open channels, further enhancements in areal capacity and rate capability for Na-O_2 batteries are expected.

4.4   Conclusion

In summary, we designed and fabricated a freestanding "O_2 breathable" air electrode with micro open pores by a 3D printing technique for high-performance Na-O_2 batteries. Unlike the uniform microporous 3DP-NP air electrode, the built-in O_2 pathways in the "O_2 breathable" cathode facilitated sufficient O_2 access even in the inner cathode, preventing surface clogging by discharge products and premature cease of discharge. Moreover, an appropriate proportion between rGO active frameworks and O_2 open channels in the 3DP-SP electrode (compared to the 3DP-LP electrode with large O_2 channels and less active rGO loading) endowed the cathode with an effective balance between electronic conductivity and O_2 access. In terms of synergistic results, the 3DP-SP air electrode achieved high utilization and a remarkable capacity of 13484.6 mAh g^{-1} (9.1 mAh cm^{-2}) at 0.2 A g^{-1}. Stable cycling performance was demonstrated over 120 cycles with a cutoff capacity of 500 mAh g^{-1} at 0.5 A g^{-1}, which is among the value of top-class superoxide Na-O_2 batteries. The ingenious application of 3D printing to demonstrate the importance of air electrode design with sufficient O_2/Na^+ transportation and excellent electronic conductivity shall inspire the development of high-performance Na-O_2 batteries.

4.5 Acknowledgments

4.6 Reference

1. Black, R.; Adams, B.; Nazar, L. F., *Advanced Energy Materials* 2012, 2, (7), 801-815.

2. Yang, X.; Li, X.; Adair, K.; Zhang, H.; Sun, X., *Electrochemical Energy Reviews* 2018, 1, (3), 239-293.

3. Yadegari, H.; Sun, Q.; Sun, X., *Advanced Materials* 2016, 28, (33), 7065-7093.

4. Lee, J.-S.; Tai Kim, S.; Cao, R.; Choi, N.-S.; Liu, M.; Lee, K. T.; Cho, J., *Advanced Energy Materials* 2011, 1, (1), 34-50.

5. Bruce, P. G.; Freunberger, S. A.; Hardwick, L. J.; Tarascon, J.-M., *ature Materials* 2011, 11, 19.

6. Hartmann, P.; Bender, C. L.; Vračar, M.; Dürr, A. K.; Garsuch, A.; Janek, J.; Adelhelm, P., *Nat Mater* 2013, 12, (3), 228-232.

7. Zhao, C.; Yu, C.; Liu, S.; Yang, J.; Fan, X.; Huang, H.; Qiu, J., *Advanced Functional Materials* 2015, 25, (44), 6913-6920.

8. Bi, X.; Wang, R.; Amine, K.; Lu, J., *Small Methods* 2019, (3), 1800247.

9. Sun, Q.; Lin, X.; Yadegari, H.; Xiao, W.; Zhao, Y.; Adair, K. R.; Li, R.; Sun, X., *Journal of Materials Chemistry A* 2018, 6, (4), 1473-1484.

10. Zhao, N.; Guo, X., *The Journal of Physical Chemistry C* 2015, 119, (45), 25319-25326.

11. Yadegari, H.; Norouzi Banis, M.; Lin, X.; Koo, A.; Li, R.; Sun, X., *Chemistry of Materials* 2018, 30, (15), 5156-5160.

12. Yadegari, H.; Banis, M. N.; Xiao, B.; Sun, Q.; Li, X.; Lushington, A.; Wang, B.; Li, R.; Sham, T.-K.; Cui, X.; Sun, X., *Chemistry of Materials* 2015, 27, (8), 3040-3047.

13. Lukas, S.; Nika, M.; Bettina, S.; Martin, W.; Christian, S.; M., B. S.; A., F. S., *Angewandte Chemie International Edition* 2017, 56, (49), 15728-15732.

14. Bi, X.; Ren, X.; Huang, Z.; Yu, M.; Kreidler, E.; Wu, Y., *Chemical Communications* 2015, 51, (36), 7665-7668.

15. Liu, C.; Carboni, M.; Brant, W. R.; Pan, R.; Hedman, J.; Zhu, J.; Gustafsson, T.; Younesi, R., *ACS Applied Materials & Interfaces* 2018, 10, 16, 13534-13541.

16. Sun, Q.; Yadegari, H.; Banis, M. N.; Liu, J.; Xiao, B.; Li, X.; Langford, C.; Li, R.; Sun, X., *The Journal of Physical Chemistry C* 2015, 119, (24), 13433-13441.

17. Bing, S.; Peng, L.; Jinqiang, Z.; Dan, W.; Paul, M.; Chengyin, W.; L., N. P. H.; Guoxiu, W., *Advanced Materials* 2018, (30), 1801334.

18. Xiaoting, L.; Qian, S.; Hossein, Y.; Xiaofei, Y.; Yang, Z.; Changhong, W.; Jianneng, L.; Alicia, K.; Ruying, L.; Xueliang, S., *Advanced Functional Materials* 2018, (28), 1801904.

19. Lin, X.; Sun, F.; Sun, Q.; Wang, S.; Luo, J.; Zhao, C.; Yang, X.; Zhao, Y.; Wang, C.; Li, R.; Sun, X., *Chemistry of Materials* 2019, 31, (21), 9024-9031.

20. Wang, J.; Gao, R.; Zheng, L.; Chen, Z.; Wu, Z.; Sun, L.; Hu, Z.; Liu, X., *ACS Catalysis* 2018, 8953-8960.

21. Ma, J.-l.; Li, N.; Zhang, Q.; Zhang, X.-b.; Wang, J.; Li, K.; Hao, X.-f.; Yan, J.-m., *Energy & Environmental Science* 2018, 11, 2833-2838.

22. Lutz, L.; Corte, D. A. D.; Chen, Y.; Batuk, D.; Johnson, L. R.; Abakumov, A.; Yate, L.; Azaceta, E.; Bruce, P. G.; Tarascon, J.-M.; Grimaud, A., *Advanced Energy Materials* 2018, 8, (4), 1701581.

23. Bender, C. L.; Hartmann, P.; Vračar, M.; Adelhelm, P.; Janek, J., *Advanced Energy Materials* 2014, 4, (12), 1301863.

24. Sun, Q.; Yadegari, H.; Banis, M. N.; Liu, J.; Xiao, B.; Wang, B.; Lawes, S.; Li, X.; Li, R.; Sun, X., *Nano Energy* 2015, 12, 698-708.

25. Sun, B.; Kretschmer, K.; Xie, X.; Munroe, P.; Peng, Z.; Wang, G., *Advanced Materials* 2017, 29, (48), 1606816.

26. Nichols, J. E.; Knudsen, K. B.; McCloskey, B. D., *The Journal of Physical Chemistry C* 2018, 122, 13462-13472.

27. Hartmann, P.; Bender, C. L.; Sann, J.; Durr, A. K.; Jansen, M.; Janek, J.; Adelhelm, P., *Physical Chemistry Chemical Physics* 2013, 15, (28), 11661-11672.

28. Chen, C.; Xu, S.; Kuang, Y.; Gan, W.; Song, J.; Chen, G.; Pastel, G.; Liu, B.; Li, Y.; Huang, H.; Hu, L., *Advanced Energy Materials* 2019, 9, (9), 1802964.

29. Xu, S.; Yao, Y.; Guo, Y.; Zeng, X.; Lacey, S. D.; Song, H.; Chen, C.; Li, Y.; Dai, J.; Wang, Y.; Chen, Y.; Liu, B.; Fu, K.; Amine, K.; Lu, J.; Hu, L., *Advanced Materials* 2018, 30, (4), 1704907.

30. Lyu, Z.; Lim, G. J. H.; Guo, R.; Kou, Z.; Wang, T.; Guan, C.; Ding, J.; Chen, W.; Wang, J., *Advanced Functional Materials* 2019, 29, (1), 1806658.

31. Qiao, Y.; Liu, Y.; Chen, C.; Xie, H.; Yao, Y.; He, S.; Ping, W.; Liu, B.; Hu, L., *Advanced Functional Materials* 2018, 28, (51), 1805899.

32. Lacey, S. D.; Kirsch, D. J.; Li, Y.; Morgenstern, J. T.; Zarket, B. C.; Yao, Y.; Dai, J.; Garcia, L. Q.; Liu, B.; Gao, T.; Xu, S.; Raghavan, S. R.; Connell, J. W.; Lin, Y.; Hu, L., *Advanced Materials* 2018, 30, (12), 1705651.

33. Gao, X.; Sun, Q.; Yang, X.; Liang, J.; Koo, A.; Li, W.; Liang, J.; Wang, J.; Li, R.; Holness, F. B.; Price, A. D.; Yang, S.; Sham, T.-K.; Sun, X., *Nano Energy* 2019, 56, 595-603.

34. Lacey, S. D.; Kirsch, D. J.; Li, Y.; Morgenstern, J. T.; Zarket, B. C.; Yao, Y.; Dai, J.; Garcia, L. Q.; Liu, B.; Gao, T.; Xu, S.; Raghavan, S. R.; Connell, J. W.; Lin, Y.; Hu, L., *Advanced Materials* 2018, 30, (12), 1705651.

35. Fu, K.; Yao, Y.; Dai, J.; Hu, L., *Advanced Materials* 2017, 29, (9), 1603486.

36. Enterría, M.; Botas, C.; Gómez-Urbano, J. L.; Acebedo, B.; López del Amo, J. M.; Carriazo, D.; Rojo, T.; Ortiz-Vitoriano, N., *Journal of Materials Chemistry A* 2018, 6, (42), 20778-20787.

37. Yang, Y.; Li, J.; Chen, D.; Zhao, J., *ACS Applied Materials & Interfaces* 2016, 8, (40), 26730-26739.

38. Yang, Y.; Huang, J.; Zeng, J.; Xiong, J.; Zhao, J., *ACS Applied Materials & Interfaces* 2017, 9, (38), 32801-32811.

39. Ma, J.-L.; Meng, F.-L.; Xu, D.; Zhang, X.-B., *Energy Storage Materials* 2017, 6, 1-8.

40. Jian, Z.; Chen, Y.; Li, F.; Zhang, T.; Liu, C.; Zhou, H., *Journal of Power Sources* 2014, 251, 466-469.

41. Zhang, Q.; Zhang, F.; Medarametla, S. P.; Li, H.; Zhou, C.; Lin, D., *Small* 2016, 12, (13), 1702-1708.

42. Wei, X.; Li, D.; Jiang, W.; Gu, Z.; Wang, X.; Zhang, Z.; Sun, Z., *Scientific Reports* 2015, 5, 11181.

43. Zhu, C.; Han, T. Y.-J.; Duoss, E. B.; Golobic, A. M.; Kuntz, J. D.; Spadaccini, C. M.; Worsley, M. A., *Nat. Commun.* 2015, 6, 6962.

44. Yadegari, H.; Franko, C. J.; Banis, M. N.; Sun, Q.; Li, R.; Goward, G. R.; Sun, X., *The Journal of Physical Chemistry Letters* 2017, 8, (19), 4794-4800.

45. Li, W.; Li, Y.; Su, M.; An, B.; Liu, J.; Su, D.; Li, L.; Li, F. *Journal of Materials Chemistry A* 2017, 5, (31), 16281-16288.

46. Li, P.; Xu, T.; Ding, P.; Deng, J.; Zha, C.; Wu, Y.; Wang, Y.; Li, Y., *Energy Storage Materials* 2018, 15, 8-13.

47. Wu, F.; Xing, Y.; Lai, J.; Zhang, X.; Ye, Y.; Qian, J.; Li, L.; Chen, R., *Advanced Functional Materials* 2017, 27, (30), 1700632.

48. Li, Y.; Yadegari, H.; Li, X.; Banis, M. N.; Li, R.; Sun, X., *Chemical Communications* 2013, 49, (100), 11731-11733.

49. Liu, W.; Sun, Q.; Yang, Y.; Xie, J.-Y.; Fu, Z.-W., *Chemical Communications* 2013, 49, (19), 1951-1953.

50. Zhang, S.; Wen, Z.; Jin, J.; Zhang, T.; Yang, J.; Chen, C., *Journal of Materials Chemistry A* 2016, 4, (19), 7238-7244.

51. Kumar, S.; Kishore, B.; Munichandraiah, N., *RSC Advances* 2016, 6, (68), 63477-63479.

52. Carter, G. F.; Templeton, D. H., *Journal of the American Chemical Society* 1953, 75, (21), 5247-5249.

53. Landa-Medrano, I.; Pinedo, R.; Bi, X.; Ruiz de Larramendi, I.; Lezama, L.; Janek, J.; Amine, K.; Lu, J.; Rojo, T., *ACS Applied Materials & Interfaces* 2016, 8, (31), 20120-20127.

54. Sayed, S. Y.; Yao, K. P. C.; Kwabi, D. G.; Batcho, T. P.; Amanchukwu, C. V.; Feng, S.; Thompson, C. V.; Shao-Horn, Y., *Chemical Communications* 2016, 52, (62), 9691-9694.

4.7   Supporting information
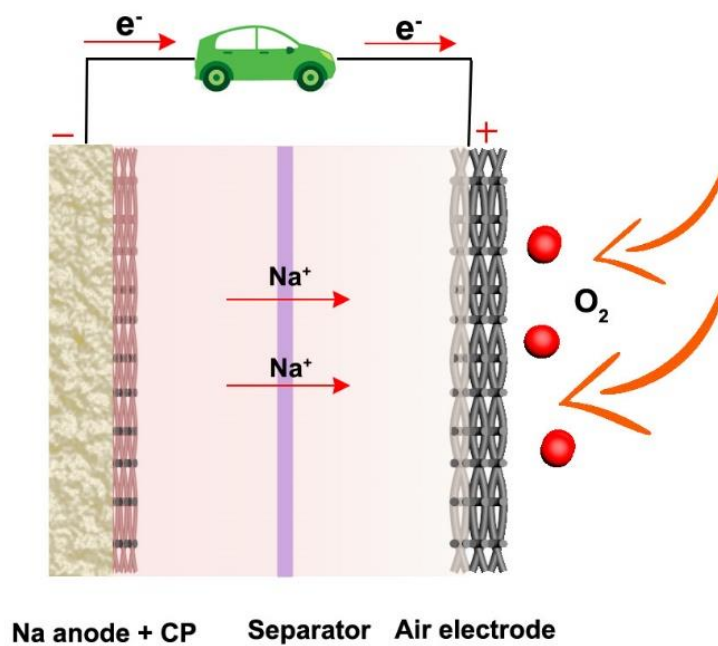
Figure S4.1 Schematic illustration of a Na-O$_2$ battery with carbon paper protected Na anode.
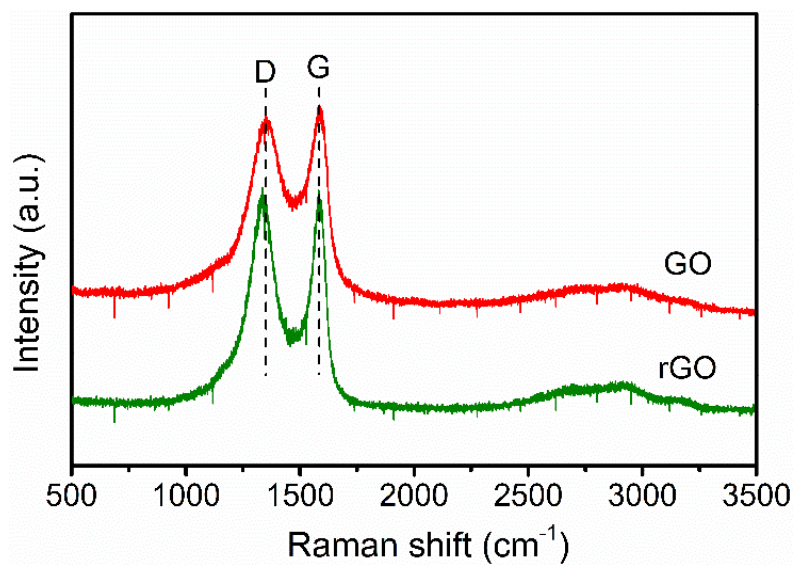
Figure S4.2 The Raman spectra of 3D printed GO and rGO electrodes.
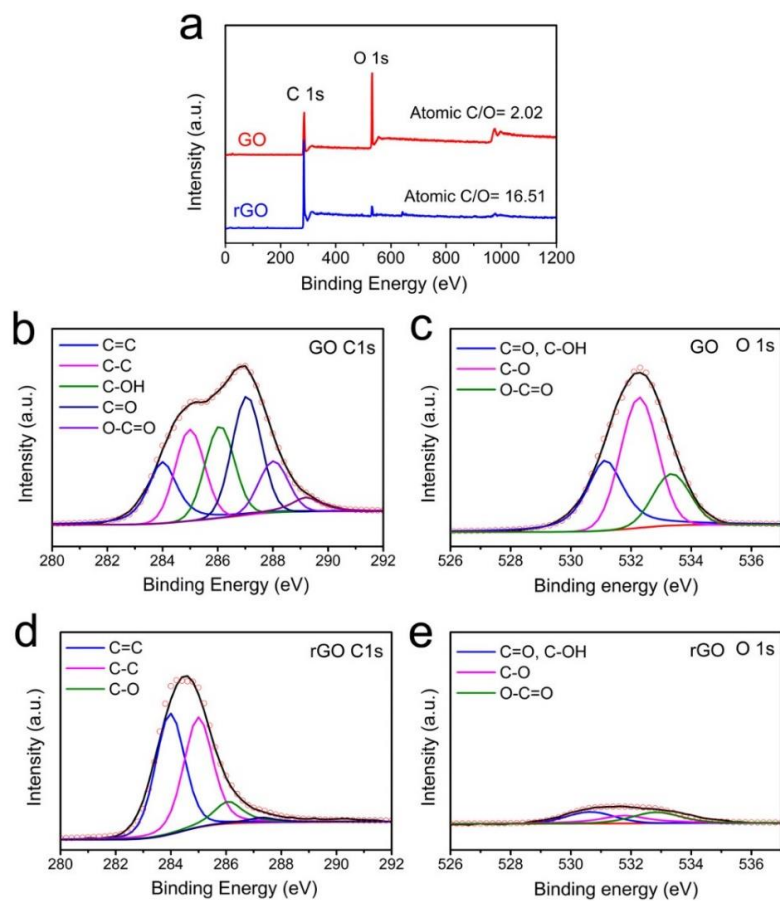
Figure S4.3 (a) Normalized wide-scan survey XPS spectra for GO and rGO. (b-e) C 1s and O 1s spectra of GO and rGO.
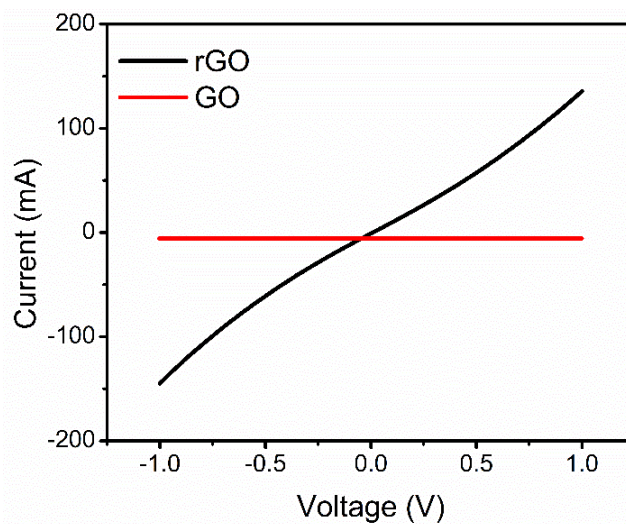
Figure S4.4 Current-voltage (I-V) curves of GO and rGO.
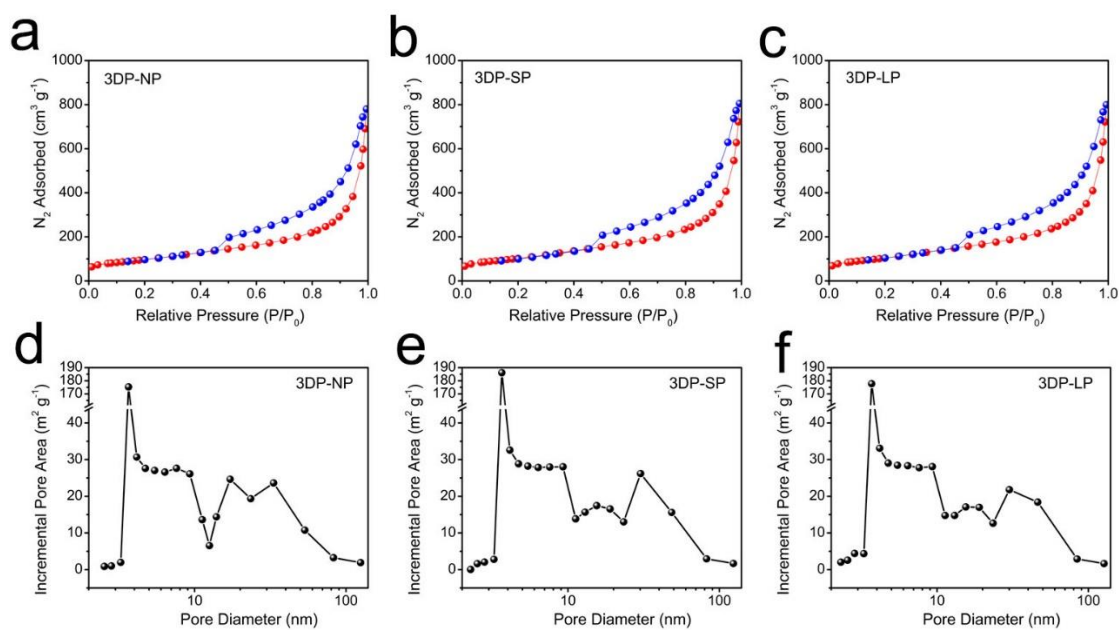
Figure S4.5 Nitrogen adsorption/desorption isotherm of the (a) 3DP-NP, (b) 3DP-SP, and (c) 3DP-LP cathode; Pore size distribution plot of the (d) 3DP-NP, (e) 3DP-SP, and (f) 3DP-LP cathodes.
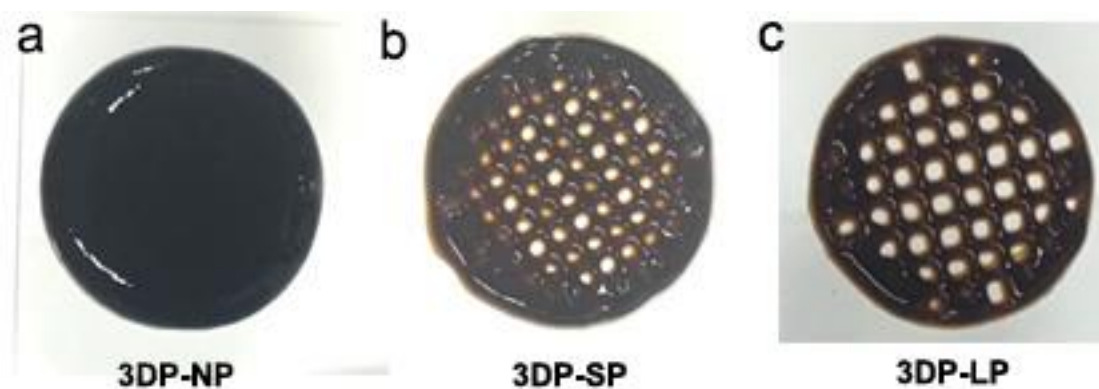
Figure S4.6 The optical images of the printed electrode before freeze-drying and thermal reduction.
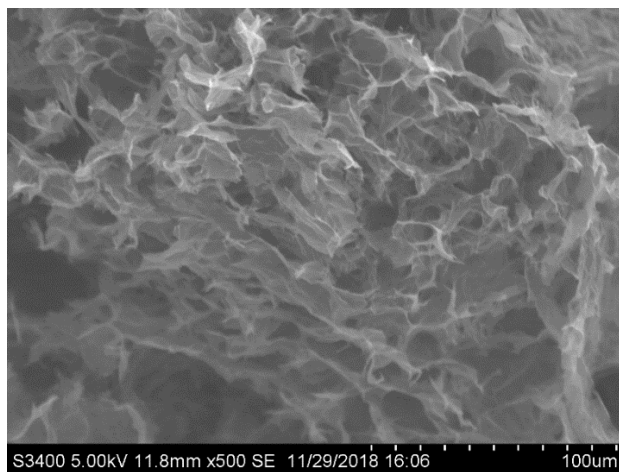
Figure S4.7 The high magnification SEM image of the 3DP-SP electrode with highly interconnected rGO sheets.
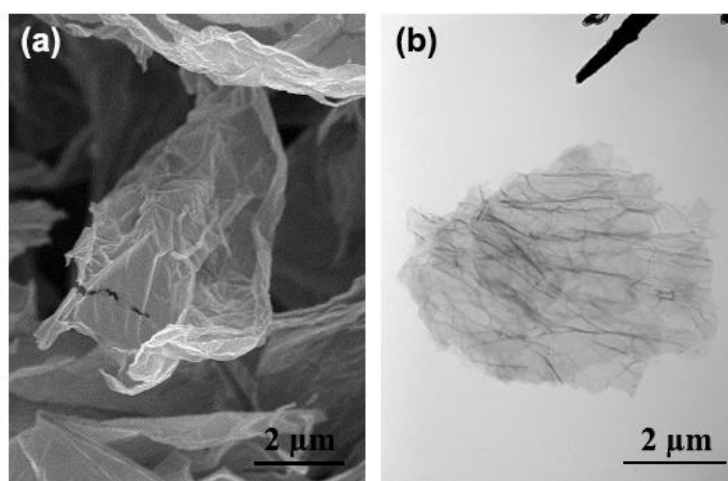
Figure S4.8 The (a) SEM and (b) TEM images of the rGO.
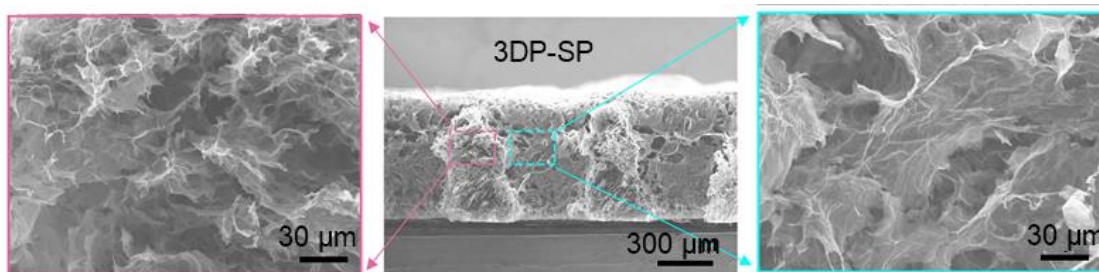
Figure S4.9 The cross-sectional SEM images of the 3DP-SP air electrode at different magnifications.
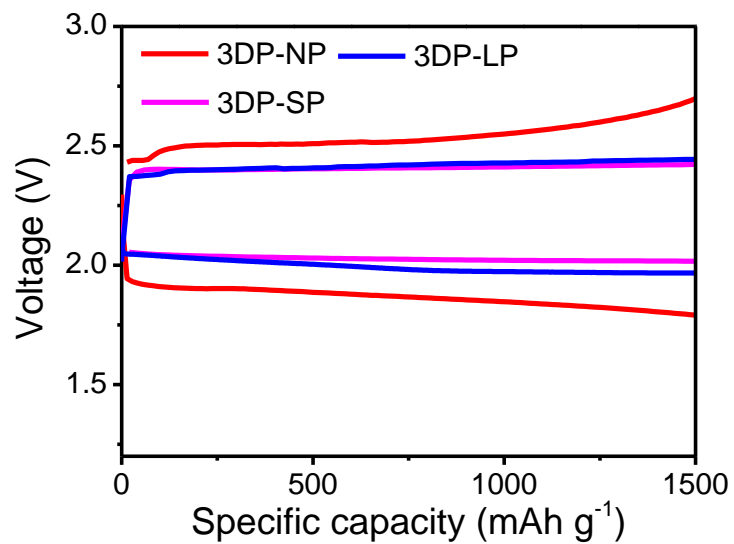
Figure S4.10 The discharge/charge profiles of the 3DP-NP, 3DP-SP and 3DP-LP air electrodes with a cutoff capacity of 1500 mAh g^{-1} at 1A g^{-1}.
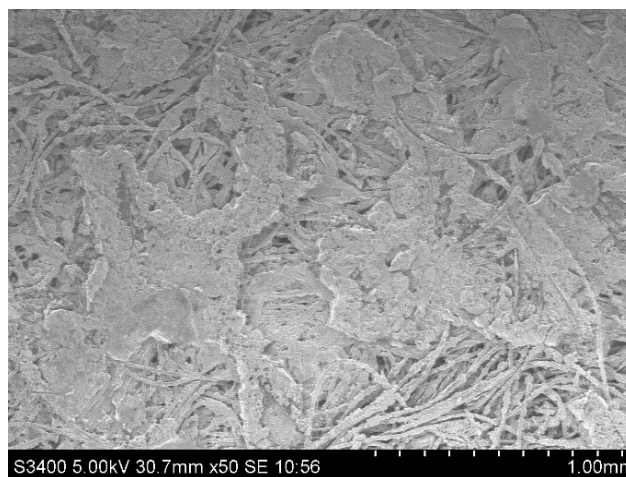
Figure S4.11 The SEM image of bulk Na side of carbon paper interlayer after the Na-O$_2$ cell is fully charged at 0.2 A g^{-1}.
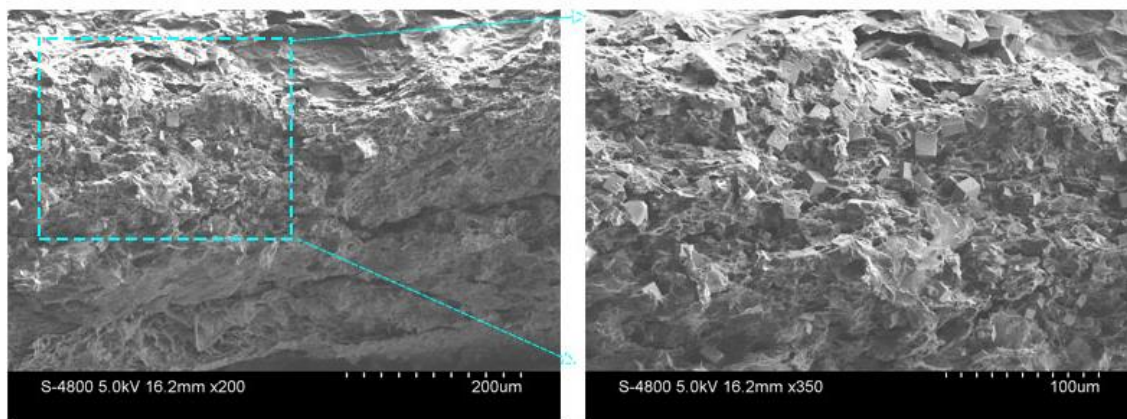
Figure S4.12 The cross-sectional SEM images of fully discharge 3DP-NP air electrode at 200 mA g^{-1}, and the discharge capacity is 4613 mAh g^{-1}.
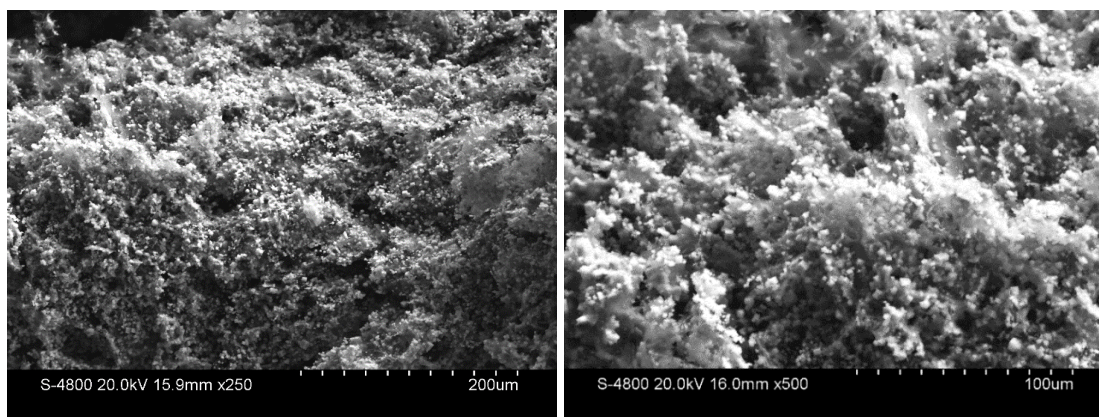
Figure S4.13 The cross-sectional SEM images of discharged 3DP-SP air electrode with a discharge capacity of 4613 mAh g^{-1} at 200 mA g^{-1}.
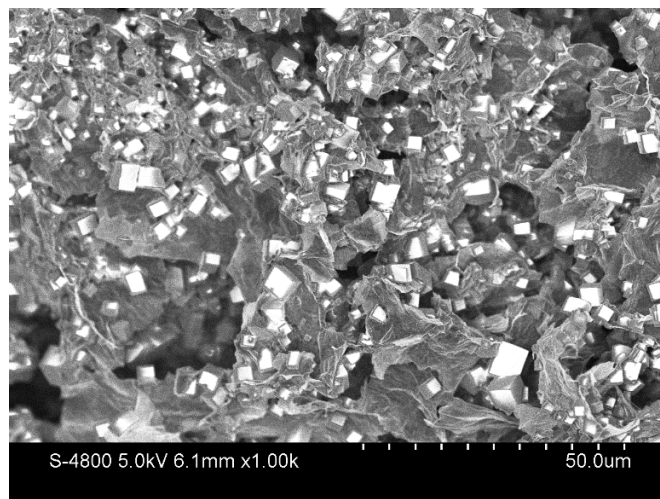
Figure S4.14 The cross-sectional SEM image of discharged 3DP-LP air electrode with a discharge capacity of 4613 mAh g^{-1} at 200 mA g^{-1}.
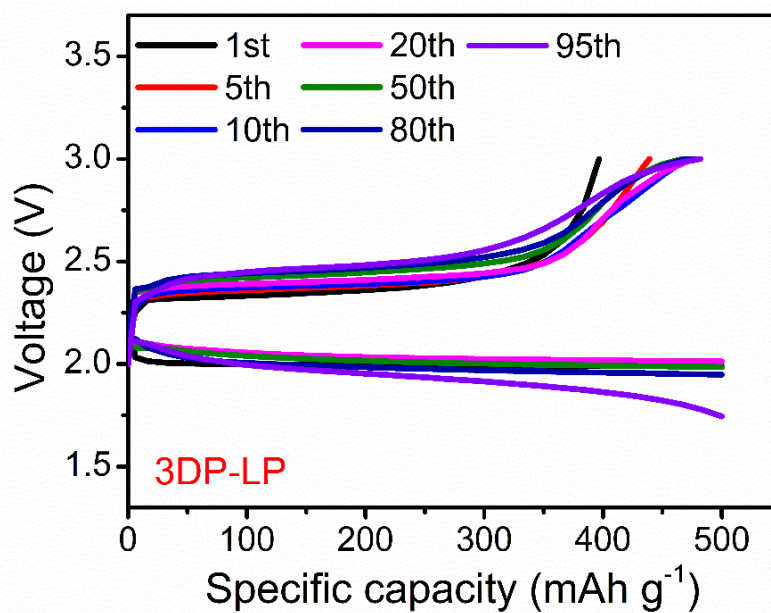
Figure S4.15 The discharge/charge profiles of 3DP-LP air electrodes at different cycles.
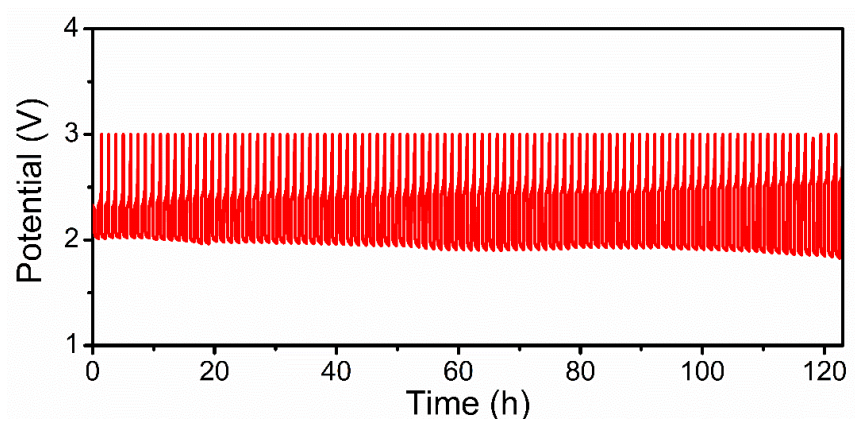
Figure S4.16 The cycling performance of Na-O$_2$ cell with 3DP-SP electrode at 1000 mA g^{-1} with a limited discharge capacity of 500 mAh g^{-1}.
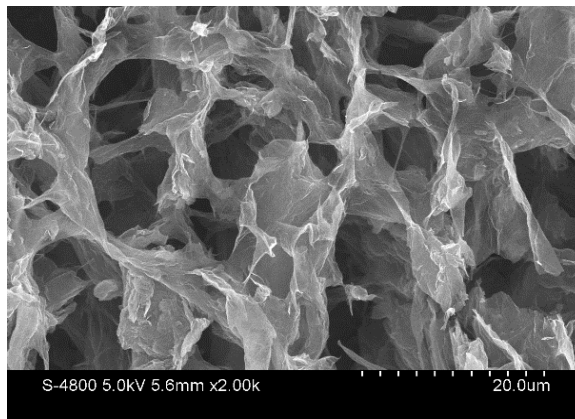
Figure S4.17 The morphology of the recharged 3DP-SP cathode at 500 mA g^{-1} with a capacity of 500 mAh g^{-1}.
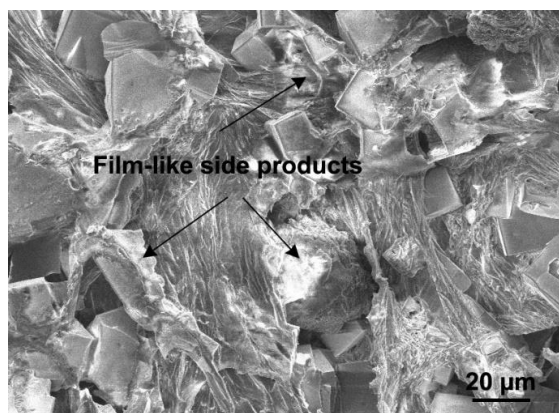
Figure S4.18 The SEM image of discharged 3DP-SP air electrode after 100 cycles.

Chapter 5

5 On the cycling performance of Na-O$_2$ cells: Revealing the impact of the superoxide crossover toward the metallic Na electrode

Na metal is used as the exclusive anode in most of the researches of Na-O$_2$ batteries. However, there have been a few papers showing that Na-O$_2$ batteries with metallic Na anode suffer from short-circuiting issue induced by dendrite growth, resulting in premature cell death and safety concerns. Compared with tremendous efforts that devoted to designing advanced air electrodes, research on the anode of Na-O$_2$ batteries has been severely overlooked. As a key component of Na-O$_2$ batteries, the effect of metallic Na anode on Na-O$_2$ cell performance should be investigated in detail.

In this chapter, a novel Na-O$_2$ battery using electrically connected carbon paper (CP) with Na metal as a protected anode is presented. The superoxide (O$_2^-$) crossover was found to be responsible for the limited Coulombic efficiency and detrimental Na corrosion in Na-O$_2$ batteries. Interestingly, the CP protected Na anode shows promising results for solving the cell short circuit via decreasing the local current density imposed to the Na anode. At the same time, the CP maintains a pseudo-equal potential with the Na metal and works as an artificial protective layer to suppress the detrimental side reactions induced by migrated O$_2^-$/O$_2$ on the Na electrode. Consequently, the Na-O$_2$ cells with CP protected Na anode exhibited two times higher discharge capacities and cycling stability compared with the cells using bare Na. These results indicate the crucial role of the Na anode in determining the overall cell performance, and a rational design of anode can dramatically contribute to develop advanced Na-O$_2$ batteries with longer lifespans and better cycling performance.

5.1 Introduction

Metal-oxygen batteries have recently attracted an extensive amount of attention as one of the most promising power sources for next generation electric vehicles and large-scale stationary electricity storage due to their ultrahigh theoretical energy densities.[1-4] In the past few decades, remarkable scientific advances have been made in elucidating the electrochemistry of various metal-oxygen batteries.[5, 6] Despite the fact that the rechargeable Li-O$_2$ batteries deliver a much higher energy density compared to other metal-oxygen battery systems, future development of Li-O$_2$ batteries have been hindered by scientific challenges, especially the high charge overpotential.[7-9] As an alternative of Li-O$_2$ battery, superoxide-based Na-O$_2$ batteries are more promising for future applications in terms of good reversibility, high round-trip energy efficiency, and clean chemistry.[10-13] However, the poor cycling performance is still one of the major challenges faced by state-of-the-art Na-O$_2$ batteries, and this critical problem will need to be properly addressed before it can be used in practical applications.

It is well accepted that the characteristics of the air electrodes, such as pore volume, pore size distribution, and surface area are key to achieving high performance Na-O$_2$ batteries.[14-17] Meanwhile, the presence of aprotic additives, the selection of organic electrolyte, conducting salts, binder, and even humidity have a profound effect on the Na-O$_2$ (or Na-air) cell performance.[18-22] In this regard, much effort has been devoted to investigating the underlying mechanisms at the cathode side of Na-O$_2$ batteries. In contrast, as another key component of Na-O$_2$ batteries, the effect of metallic Na anode on the Na-O$_2$ cell performance has been seldom studied in detail.[23-25] Up to now, there have been a number of papers showing that Na-O$_2$ batteries with metallic Na anode may suffer from short-circuiting issue induced by Na dendrite growth, leading to premature cell death and safety concerns. Nonetheless, it is still widely presumed that the air electrode plays the most important role in the electrochemical performance of Na-O$_2$ batteries. Therefore, very few researches in the field of Na-O$_2$ battery have focused on the anode side.

The observation of Na dendrite growth in Na-O$_2$ battery was firstly reported by Guo and coworkers.[23] The origin of Na dendrite growth in Na-O$_2$ battery system has also been reported and studied by Janek's group, where a ceramic Na$^+$ conductor was used to

suppress the dendrite growth in their reports.[25-28] In another study, they replaced the Na metal anode with a sodiated carbon anode, achieving improved cycling life and energy efficiency.[29] Nonetheless, from a practical perspective, the low capacity of current carbon anode for sodium batteries may still be insufficient to match the large capacity of air electrode. The importance of addressing challenges with regards to the Na anode were further confirmed with the application of sodium ion selective membranes in the research of Bi et al..[24] However, this study on the understanding of the role and mechanism of the negative electrode in Na-O$_2$ batteries is still relatively scarce.

Compared with Li-O$_2$ cells, the dissolved Na$^+$-O$_2^-$ in the Na-O$_2$ cells is more stable than its Li counterpart,[30] and a solution-based mechanism for the formation of NaO$_2$ have been widely reported.[31-33] Therefore, the crossing over of O$_2^-$ towards negative electrode may be expected to be more severe in Na-O$_2$ cells. Previous studies have shown that the crossing over of O$_2$ from cathode can lead to ether-based electrolyte decomposition on the anode, which leads to serious side reactions on the anode surface.[34-37] Undoubtedly, accumulation of contaminants on the Na surface results in suppressed Na$^+$ transportation and thus restricts the battery performance by imposing large charge/mass transfer overpotential during discharge and charge reactions. However, to the best of our knowledge, the crossing over of O$_2^-$ radical is rarely studied and its effect on Na-O$_2$ battery performance is yet poorly understood.

In this paper, an electrically connected CP and Na metal is fabricated and used as the protected Na anode in Na-O$_2$ batteries (**Figure. S5.1**). Interestingly, the adoption of this protected Na anode can dramatically improve the electrochemical performance and increase the cycling life of Na-O$_2$ batteries by shielding O$_2^-$/O$_2$ crossover to suppress the detrimental side reactions on the Na anode surface. Moreover, the resultant configuration also shows promising results for solving the short-circuiting issue by decreasing the local current density imposed to the anode. The presented results in this study indicate that the negative Na electrode in Na-O$_2$ cells greatly affects the overall performance of the battery and thus should be attracting further research attention in the future studies.

5.2 Experimental section

Materials and electrodes preparation. The CP (Freudenberg H2315, thickness of 210 µm, porosity of ≈80%), purchased from Fuel Cell Store, was utilized as the cathode and interlayer in the Na-O_2 batteries without further treatment. The surface area of the CP was lower than 1 m^2 g^{-1}. DEGDME (reagent grade ≥ 98%, Aldrich) was dried over freshly activated molecular sieves (4 Å, Aldrich) for at least one month before use. Sodium triflate ($NaSO_3CF_3$, Aldrich) was dried under vacuum at 80 °C for 3 days.

Battery assembly and electrochemical measurements. The electrochemical performance of Na-O_2 batteries was evaluated with Swagelok-type cells. Briefly, the Na-O_2 cell using Na foil as the anode, glass fiber (GF) as the separator, and CP as the air electrode. The CP and Na metal foil were cut into circular pieces with a geometric surface area of 0.7125 cm^{-2}. The electrolyte was 0.5 M $NaSO_3CF_3$ dissolved in DEGDME, and same amount of electrolyte was applied for comparison in each cell (100 µL). Different from conventional Na-O_2 batteries, the Na-O_2 cells with protected Na anode were assembled with CP interlayer sandwiched between Na foil and GF separator, and the cell configuration is shown in **Figure S5.1**. The electrolyte preparation and battery assembly were carried out in an argon-filled glove box with the oxygen and water contents below 0.1 ppm. The cells were operated under static O_2 with the pressure of 1.5 atm in a homemade testing box, and each cell was stabilized for 20 min at room temperature before electrochemical tests. The galvanostatic discharge/charge tests were carried out using Arbin BT-2000 battery testing system at room temperature. Electrochemical impedance spectroscopy measurements were carried out with electrochemical station.

Material characterization. The morphologies and structures of discharge product were characterized by Hitachi S-4800 field emission scanning electron microscope (SEM), and the morphological studies of the Na anode and separator were performed using a Hitachi 3400N environmental SEM. The Bruker D8 Advance X-ray diffraction (XRD) with Cu-Ka radiation was used for structural characterization, and the data were collected from 30° to 70° in 2θ at a scanning rate of 1° min^{-1}. The Raman spectra were collected on a HORIBA Scientific LabRAM Raman spectrometer equipped with a 532.03 nm laser. In this study, the disassembly of the Na-O_2 batteries was carried out in an Ar-filled glove box. The

discharged/charged electrodes and separator were washed by fresh DEGDME to remove residual $NaSO_3CF_3$ salt and then rigorously dried in the vacuum chamber before SEM, XRD, and Raman measurements. Leak-tight XRD and Raman sample holders were used to prevent the exposure of air during sample testing. X-ray photoemission spectra (XPS) was carried out by a Kratos Axis Ultra Al-α spectrometer operated at 14 kV.

5.3   Results and discussion

5.3.1 Electrochemical behaviors of Na-O$_2$ batteries with bare Na and protected Na anode

In our previous studies, we have already shown that the electrochemical behaviors and discharge products can be highly dependent on the configuration of the Na-O$_2$ batteries and the choice of the air electrodes.[17, 38, 39] In this study, we have chosen a commercial CP (H2315) as the air electrode, which has been widely used in different groups and the corresponding discharge product has been reported to be sodium superoxide (NaO$_2$).[11, 19, 40] In order to examine the effect of anode on the Na-O$_2$ cell performance, the electrochemical behaviors of Na-O$_2$ cells with and without protected Na were investigated at different current densities (**Figure 5.1**).

It can be clearly observed that the initial discharge capacities of the Na-O$_2$ cells increase significantly after introducing a CP protected Na electrode (**Figure 5.1**). Initial discharge capacities of 5.52, 5.08, 3.56, and 1.66 mAh cm^{-2} are achieved for Na-O$_2$ cells with protected Na at 0.1, 0.2, 0.5, and 1.0 mA cm^{-2}, respectively. In comparison, only less than 50% of the initial discharge capacities are delivered for the cells with bare Na anode at the same current densities (**Figure S5.2a**). Moreover, the Na-O$_2$ cells with protected Na anode exhibit lower discharge overpotentials than that of the cells with bare Na anode at all current densities (**Figure S5.2b**). To rule out any other possible beneficial contribution other than from the use of protected Na, all the other components of the cells including the air electrode and the cell electrolyte are kept the same. Therefore, it is evident that the significant increase of the initial discharge capacities can be solely related to the employment of protected Na anode.
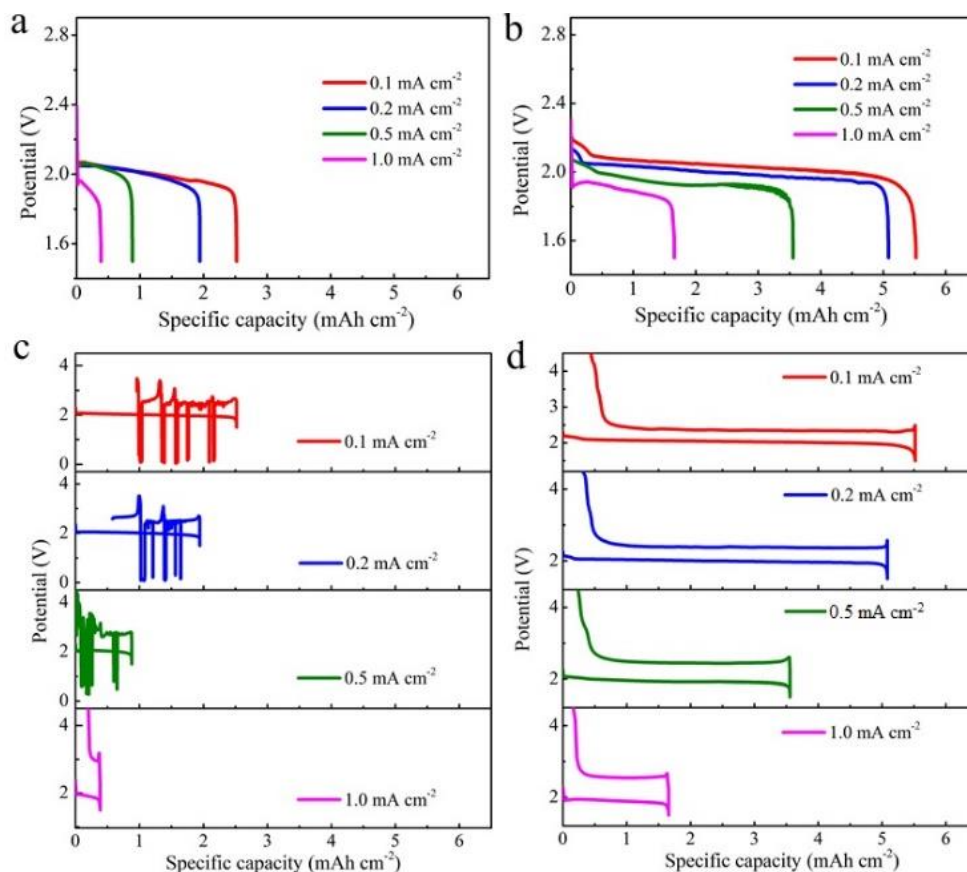
Figure 5.1 The initial discharge profiles of Na-O$_2$ cells with (a) bare Na anode and (b) protected Na anode at different current densities. The initial discharge/charge profiles of Na-O$_2$ cells with (c) bare Na anode and (d) protected Na anode in the potential range of 1.5-4.5 V versus Na/Na$^+$ at different current densities.

The discharge products of Na-O$_2$ batteries with bare Na and protected Na anode were characterized by XRD at the current density of 0.1 mA cm^{-2}. As shown in **Figure 5.2a** and **b**, the diffraction peak positions of two discharged cathodes are consistent with that of NaO$_2$, and no other side products can be observed. Meanwhile, the intensity of the NaO$_2$ peak on cathode obtained from the cell with protected Na anode is much stronger than that of the cell with bare Na (**Figure S5.3**), indicating a larger amount of NaO$_2$ is produced in the cell with protected Na. This result agrees well with the larger discharge capacities of cell with protected Na than that of the cell with bare Na at the same current density of 0.1 mA cm^{-2}. The formation of NaO$_2$ on the discharged cathode was further confirmed by the Raman signal at 1156 cm^{-1}, consistent with the previous report by Hartmann et al. (**Figure**

S5.4).[11] Note that no Raman peaks of NaOH, Na_2CO_3 or other side products can be observed from the discharged air electrode in the cell with protected Na. Those results indicate that the application of CP on metallic Na anode does not change the nature of the discharge product, and NaO_2 is identified as the only discharge product in Na-O_2 battery with protected Na. In addition, the discharged air electrodes in the cells using bare Na and protected Na anode were also investigated using SEM, as shown in **Figure 5.2c-f**. Cubic shaped NaO_2 almost completely fill the pores on the oxygen side of the air electrode for the cell with protected Na. This contrasts with the cell assembled with bare Na where the electrochemical reaction terminates before the pores on the oxygen side of cathode become blocked or active electrode surface becomes completely covered.
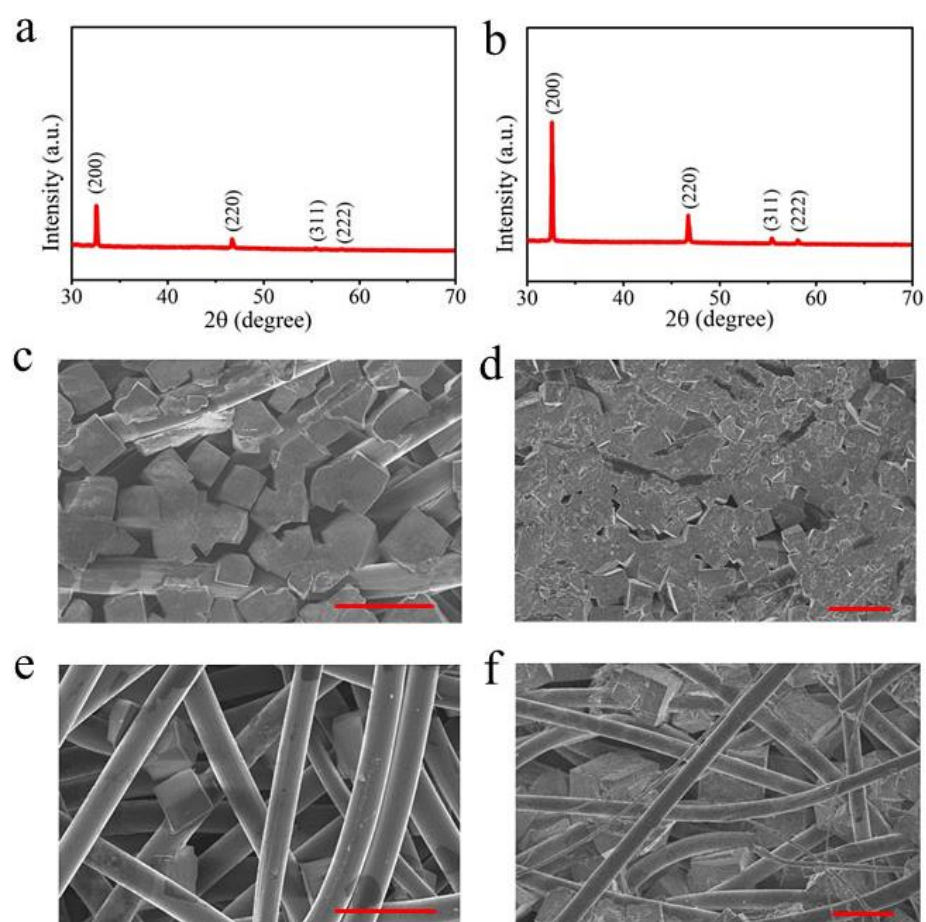
Figure 5.2 The (a, b) XRD patterns and (c-f) SEM images of fully discharged air electrodes in Na-O_2 cells with bare Na and protected Na anode at 0.1 mA cm^{-2}; (c, d) oxygen side and (e, f) separator side of discharged air electrodes (scale bars = 20 µm).

According to previous reports, the precipitation of insoluble discharge products within the pores of the cathode may prevent the continuous O_2 transportation into the interior of the cathode.[41, 42] Thus, it is not possible for the pores on the separator side of the air electrode to be fully deposited when the oxygen diffusion channels on the oxygen side have already been blocked. A similar phenomenon was observed on both sides of the air electrode in the case of the Na-O_2 cell with protected Na, indicating that the ending of discharge process for this cell is most likely due to the blocking of further oxygen diffusion caused by NaO_2 accumulation (**Figure 5.2d** and **f**). However, it is very interesting to find that the discharge process of the Na-O_2 battery with bare Na terminates before the cathode is fully blocked by discharge products (**Figure 5.2c** and **e**). Those results suggest an underlying protective effect of the CP when electrically connected with Na metal during the discharge process, and the puzzle of this protective effect will be discussed in Section 5.3.3 of this study.

Aside from the distinct initial discharge capacities, the charging behavior of Na-O_2 cells with bare Na and protected Na anode are also notably different, regardless of the formation of the same discharge product in both cells. The voltage of the cell with bare Na suddenly and repeatedly drops to almost 0 V after a charge capacity of ~ 0.35 mAh cm^{-2}, even at a low current density of 0.1 mA cm^{-2} (**Figure 5.1c**). This phenomenon is typical for the internal short-circuiting of the battery due to the growth and penetration of Na dendrites, which has also been observed in previous studies on Na-O_2 batteries.[43] The recovery of the battery voltage is assumed to be the "melting and breaking down" of Na dendrite reaching the air electrode, shortly resolving the short-circuit until another dendrite reaches the air electrode. As a result, the discharge product of the Na-O_2 cell with bare Na will not be thoroughly decomposed (**Figure S5.5a**). Additionally, the short-circuiting of the cells is more severe at higher current densities of 0.2 and 0.5 mA cm^{-2} as the first voltage drop occurs at lower charge capacities, which is caused by the accelerated Na dendrite growth at higher rates.[43-45] In contrast, the short-circuiting issue was completely addressed in the cells with protected Na, which showed a very smooth plateau at ~2.33V during the charge process. This value is very close to the theoretical value (2.27 V) for the electrochemical decomposition of NaO_2 to form Na^+, O_2 and an electron. Good reversibility of the Na-O_2 cells was further confirmed by XRD spectroscopy as the diffraction peaks of NaO_2 completely disappeared without forming any additional peaks after recharging (**Figure**

S5.5b). Moreover, it is necessary to emphasize that the Na-O$_2$ cells with protected Na displayed Coulombic efficiencies of more than 90%, even at a high current density of 1.0 mA cm^{-2}. To the best of our knowledge, these results compete some of the best cell performances using the same air electrode compared to other studies using similar current densities.[11, 19, 46, 47]

5.3.2 The direct evidence on the suppressing effect of protected Na anode on dendrite growth
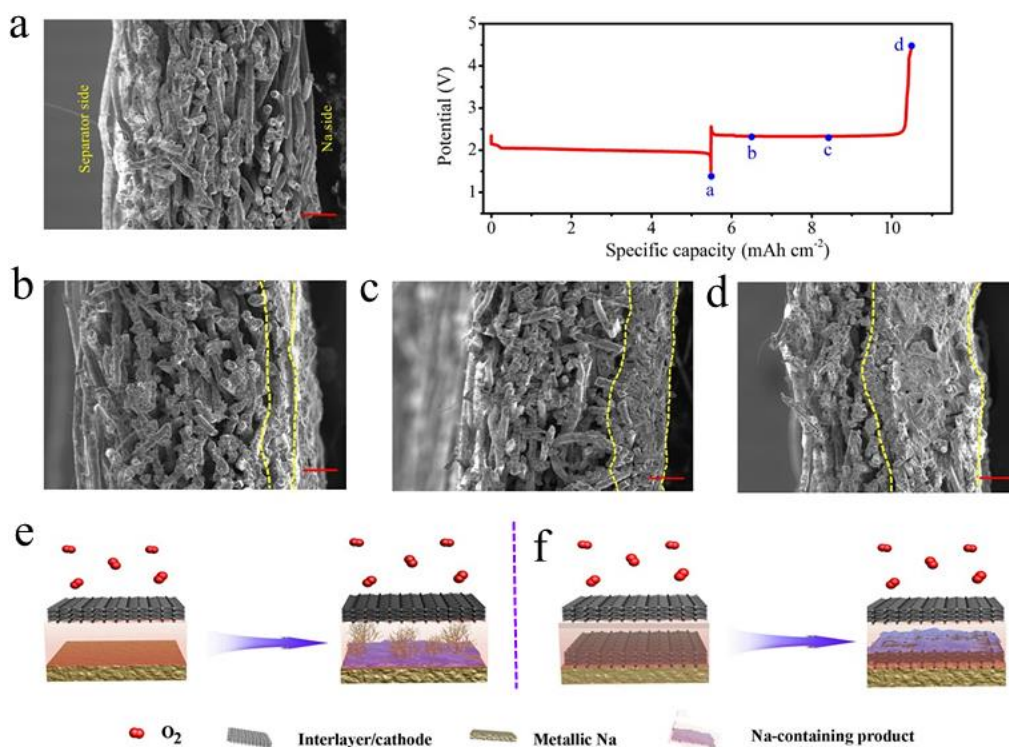
Figure 5.3 The cross-sectional SEM images of CP with different amount of Na deposits. (a) 0 mAh cm^{-2}, (b) 1 mAh cm^{-2}, (c) 3 mAh cm^{-2}, and (d) ≈5 mAh cm^{-2} (scale bars = 50 μm), the distance between two dotted yellow line showing the thickness of deposited Na during charging process; schematic diagrams of sodium deposition in cells with (e) bare Na and (f) protected Na.

To observe direct evidence that the short circuiting of Na-O$_2$ battery using bare Na anode is induced by the Na dendrite growth, we have disassembled the recharged cells for optical and SEM observations. As shown in **Figure S5.6a-c**, large numbers of dendritic spots can

be observed on the bulk Na surface after the cell with bare Na anode short-circuited during the charging process (~0.35 mAh cm^{-2}). In addition, the layered-structure of a pristine separator is no longer observed due to the growth of Na dendrites filling the porous structure of glass fiber (GF), leading to a stacked structure without obvious interlayer spacing (**Figure S5.6d-f** and **Figure S5.7**). These results are consistent with previous studies on the effect of Na dendrite on Na-O$_2$ batteries.[23-25] In contrast, the separator in the Na-O$_2$ cell with protected Na anode maintained its clean surface and clear layered-structure after the cell was fully recharged at 0.1 mA cm^{-2} (**Figure S5.8a** and **b**). Furthermore, CP interlayer were examined by optical and SEM imaging, and the metal luster morphology of the bulk Na side of the CP indicates that a large amount of Na deposit is confined inside the matrix (**Figure S5.8c-f**).

To clarify the deposition behavior of Na in the cell with a CP protected Na, the morphologies of the CP at different electrochemical states were investigated by SEM (**Figure 5.3a-d**). Interestingly, when the Na-O$_2$ cell with protected Na anode was fully discharged, the surface of the CP facing the Na side seems cleaner than that facing the separator side (**Figure 5.3a**). Further examining the surface of the CP revealed a greater accumulation of deposits on the separator side of the CP, which is almost fully covered by amorphous film-like products (**Figure S5.9a** and **b**). Raman characterization was conducted to identify the chemical nature of the deposits on the CP surface, where Na$_2$CO$_3$ and NaOH were identified as the main phase of the side products (**Figure S5.9c**). It is known that alkali metal is inherently unstable when in contact with organic electrolyte due to the low redox potential, leading to the formation of solid electrolyte interphase (SEI) layer on the alkali metal surface. CH$_3$OLi, CH$_3$Li and polymeric layers are the main decomposition products of an ether-based electrolyte on Li surface in Li-ion batteries (LIBs).[48] While in Li-O$_2$ batteries, different electrolyte decomposition reactions can be observed compared with that in LIBs, and the formation of LiOH and carbonates on the Li anode is predominantly due to the oxygen crossover effect.[34, 49] Similar electrolyte decomposition mechanism has also been reported in K-O$_2$ batteries in the presence of O$_2$ crossover.[13] Since more side products were observed on the CP that facing the separator side compared to the Na side in our case, which is identical to the migration direction of O$_2$ and O$_2^-$ from the air electrode toward the Na electrode. Therefore, the Na$_2$CO$_3$ and

NaOH on the CP interlayer could be formed through the reaction between O_2^- and electrolyte/CP, as well as the decomposition of the electrolyte in the presence of O_2 crossover.

In the subsequent charging process, Na was preferentially nucleated on the bulk Na side of the CP rather than the other side when plating 1 mAh cm^{-2} of Na, as shown in the area outlined with two dotted yellow lines (**Figure 5.3b**). This is perhaps caused by the initial nucleation of Na on the bulk Na surface due to the lower nucleation barrier, compared with that on the CP structure. On the other hand, the presence of nonconductive Na_2CO_3 and NaOH on the separator side of the CP may also contribute to the preferential deposition of Na on the other side. Further increasing the Na deposition capacity to 3mAh cm^{-2}, the voids on the Na side of the CP were gradually filled with deposited Na to a thickness of ~30μm (**Figure 5.3c**). When the cell with protected Na was fully charged with ~5.0 mAh cm^{-2} of Na deposit, about half of the inner space in the CP was filled by deposited Na, as shown in **Figure 5.3d**. Note that more side products (NaOH, Na_2CO_3 et al.) can be observed on the separator side of CP interlayer compared with that at discharge state, indicating the occurrence of same side reactions on the CP interlayer during both discharge and charge process (**Figure S5.9d** and **e**).

In the Na-O_2 cell with protected Na, the presence of a CP on the Na metal facilitates dense Na deposition without dendritic Na growth, and thus prevents the cell from short-circuiting. This could be related to the decreased current density in the presence of a 3D conductive network during the Na plating process. Combining the electrochemical properties of the cells with different configurations, it can be concluded that the difference in charging behavior between the cells with and without protected Na can be related to the presence of conductive CP interlayer.

Recent studies have reported that $NaPF_6$ is capable of forming a uniform and compact SEI layer on the Na electrode in diglyme, while the SEI formed using other electrolyte salts, including $NaSO_3CF_3$, $NaN(SO_2CF_3)_2$ and $NaClO_4$, is less uniform and compact in nature.[50, 51] This causes more Na to be exposed to undesirable side reactions with electrolytes, and at the same time, the rough surface of metallic Na would result in uneven charge

distribution and subsequent Na dendrite growth during the charging process. The low shear modulus of SEI layer formed on the Na surface is easier to be puncture with Na dendrites, short-circuit will occur after the Na dendrites penetrate the separator. Schematic of Na deposition on the anode of cells with bare Na and protected Na anode are shown in **Figure 5.3e** and **f**.

5.3.3 Understanding the superoxide radical crossover in Na-O_2 batteries with protected Na anode

However, the mystery of why the Na-O_2 battery with protected Na can also significantly increase its discharge capacity and Coulombic efficiencies compared to that of the cells with bare Na remains. In order to rule out the possible impact from merely the Na dendrite growth, capacity-limited cycling of the Na-O_2 cells with bare Na and protected Na were further investigated. The cut-off capacity of the cells is 0.1 mAh cm^{-2}, which is much lower than the above-mentioned initial short-circuit capacities (ISCCs) of the batteries and thus the effect of Na dendrite formation and growth can be minimized.
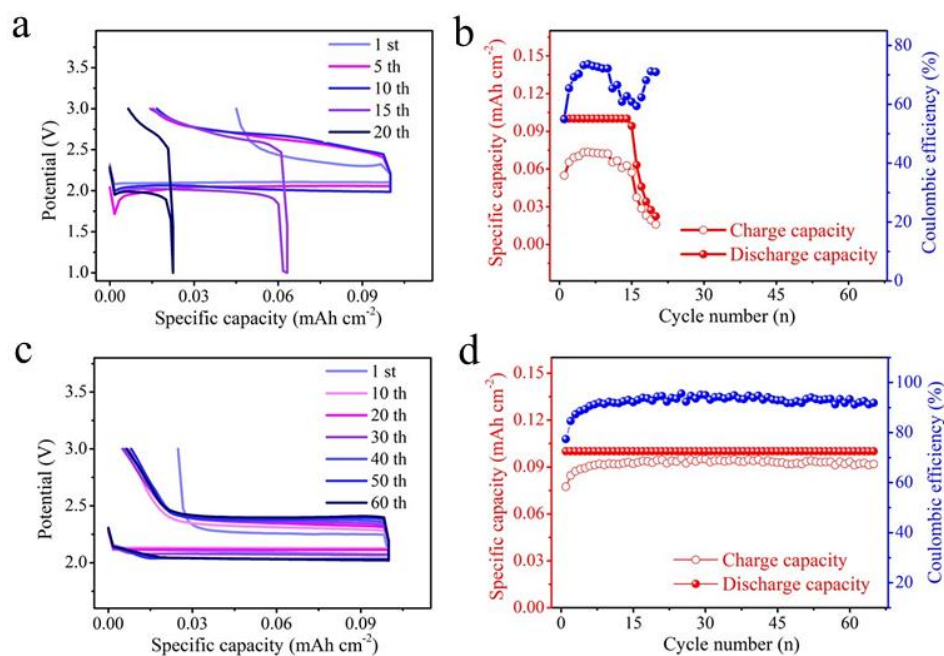
Figure 5.4 The selected charge/discharge curves of Na-O_2 cells with (a) bare Na and (c) protected Na anode. The cycling properties and Coulombic efficiency of Na-O_2 cells with (b) bare Na and (d) protected Na anode.

Long-term cycling stability of the Na-O$_2$ cells were investigated at 0.1 mA cm^{-2} with a fixed discharge capacity of 0.1 mAh cm^{-2} (**Figure 5.4**). Interestingly, as shown in **Figure 5.4a** and **b**, a stable discharge plateau at ~2.0V only remains for 14 cycles in the case of Na-O$_2$ cell with bare Na. The cell then starts to fail to deliver the defined discharge capacity and the cell shows an accelerated degradation afterward. At the 20th cycle, the cell maintains only ~20% of its initial capacity. In sharp contrast, the cell with protected Na can stably run for over 65 cycles with a high Coulombic efficiency of ~90%, which is much higher than that (~70%) of the cell with a bare Na anode (**Figure 5.4c** and **d**). Although the Na-O$_2$ cell with protected Na exhibits an overpotential gap of 0.16V in the initial cycle that increases gradually to 0.36V in 60th cycle, the decomposition potential of NaO$_2$ has been consistently much lower than that of the cell with bare Na anode. There is no doubt that the lower charge transfer resistance of the cell with protected Na partially contributes to the better electrochemical performance, compared with that of the cell with bare Na anode (**Figure S5.10**). However, it should also be noted that the cell with bare Na exhibited a much higher charge overpotential after the first cycle. The obvious increase of charge overpotential can be related to the increased resistance of the Na electrode caused by an accumulation of side products. While in the case of the cell with protected Na, a relatively slower increase in the charge overpotential can be observed, which may attribute to the alleviation of side reactions accumulation on the Na surface. Those results clearly indicate that the CP at the anode side has played another protective role during the cycling process of Na-O$_2$ batteries.

To reveal the nature of this protective effect, two different Na-O$_2$ cell configurations with the same Na anode, electrolyte, and air electrode were constructed. For the first cell, two layers of GF were used as the separator (**Figure. 5.5a**). We designed another cell by placing the CP between two GF separators instead of onto the Na anode (**Figure 5.5b**). However, the electrochemical performance of the cell with a CP sandwiched between the two GF separators had no significant difference compared to the cell with only two GF separator, exhibiting both the short-circuit effect at very close ISCCs and a relatively low discharge capacity. These results indicate that the protective role of the CP is not simply originated from itself but a synergy effect when it is combined with Na anode.
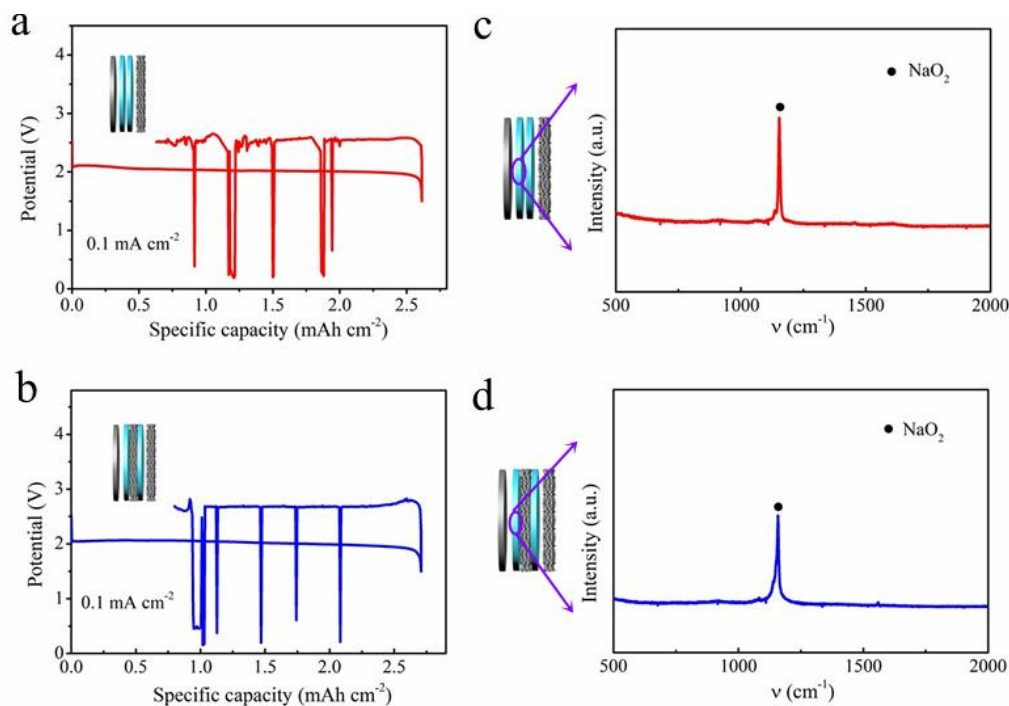
Figure 5.5 (a, b) Schematic diagram of Na-O₂ cells with different separators and corresponding charge/discharge curve at a current density of 0.1 mA cm⁻²; (c, d) Raman spectra of GF next to the Na anode after the cell fully discharged at 0.1 mA cm⁻².

We anticipate the answer to this puzzle can be related to the nature of the inner reaction mechanism of Na-O₂ batteries. The discharge process of Na-O₂ batteries that produces superoxide mostly involves a solution-based route, where the first step is the formation of a dissolvable O_2^- anion or HO_2 via an electrochemical reduction of O_2 gas, followed by a precipitation step to form NaO_2 as the final discharge product. To address the origin of the limited Coulombic efficiency in Na-O₂ cells, which is another limiting factor for the cycling performance of the battery, we examined the cell separator after the full discharge at 0.1 mA cm⁻². As shown in **Figure S5.11a** and **b**, cubic NaO_2 with a diameter of 10µm can be observed on the cell separator, which is indisputable evidence for the solution-mediated mechanism of NaO_2 formation.[32] The O_2^- produced during the discharge process dissolves into the electrolyte, and nucleation occurs once its concentration reaches the supersaturation threshold. The precipitated NaO_2 on the separator can be detected by XRD (**Figure S5.11c**), which indicate a considerable amount of NaO_2 precipitate on the separator. Based on the presented evidence, it is reasonable to assume that a high

concentration of O_2^- exists around the separator, and the O_2^- radicals likely migrates towards the Na anode due to the dual effect of an ion concentration gradient and electric field.

Na-O_2 cells with different separators were further constructed in order to examine the efficiency of the separator in blocking the migration of O_2^- from the cathode to anode (**Figure 5.5c** and **d**). The thickness of the separator in both cells was increased compared to the cell with only one layer of GF (**Figure 5.2a**). However, the O_2^- crossover cannot be totally inhibited by increasing the thickness of separator, as the Raman signal of NaO_2 can still be detected on the second layer of GF (next to the Na electrode) after the cell fully discharged at 0.1 mA cm^{-2}. As the low compact nature of SEI layer formed on the Na surface is insufficient to completely block the diffusion of O_2^-, and thus the chemical reduction of O_2^- at the Na surface is highly probable. Consequently, the migrated O_2^- cannot be recovered during the charge process which in turn result in capacity loss and limited Coulombic efficiency in Na-O_2 cells. This phenomenon is very similar to the well-known "shuttle-effect" observed in Li-S and Na-S batteries, where the dissolved polysulfide also migrate to the anode side.[52, 53] On the other hand, the formation of the reduced Na-containing products can be highly isolating to create polarization from the anode side, which results in Na degradation during the discharge process.

Those results on the Na-O_2 batteries with bare Na is in good agreement with previous reports, in which the Coulombic efficiencies of Na-O_2 batteries are much lower than 100%.[46, 54-56] It has been shown that the limited charge efficiency is partially related to the irreversible decomposition of the cell electrolyte, even in the relatively stable ether solvent. By the introduction of the CP on the Na anode, no side product was detected in both XRD pattern and Raman spectrum of the discharged cathode from the Na-O_2 cell in our study (**Figure 5.2b** and **S5.4**). Moreover, no obvious evidence of a charging plateau from parasitic reactions was observed, even when the electrode recharged back to 4.5V. The reappearance of the clean carbon fiber surface further confirms that no discharge product left on the fully charged cathode (**Figure S5.12**), in agreement with the XRD results for the charged electrode (**Figure S5.5b**). Therefore, it can be concluded based on all the presented evidence that the observed limited Coulombic efficiency in this work can be

related to the crossover of O_2^- from the cathode to anode. In the case of the Na-O_2 cell with bare Na, the side reactions induced by O_2^- crossover results in the formation of side products. The built up of side products can impede the Na^+ transportation, increase the polarization of the Na-O_2 battery and trigger the cut-off voltage of the cycling test. Therefore, the gradual accumulation of side products on the Na anode is responsible for the premature ending of the discharge process in Na-O_2 batteries with bare Na anode, leading to a relatively low discharge capacity and poor cycling performance.
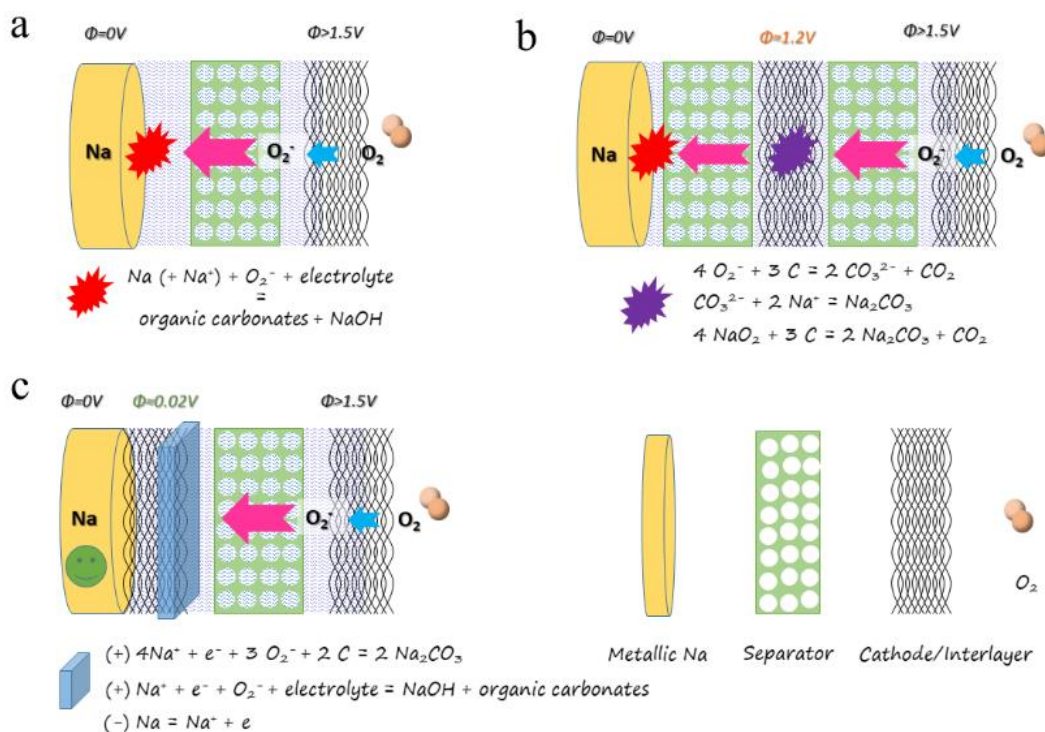
Figure 5.6 Illustration of reaction mechanisms in different Na-O_2 cell configurations. (a) The cell with one GF separator, (b) the cell with CP sandwiched between two GFs, and (c) the cell with CP on the Na anode.

Further comparison of the cells with different separator thicknesses indicates that the discharge capacity of the cell slightly improves by increasing the thickness (**Figure S5.13**), which can be ascribed to the suppression of the side reactions on Na surface caused by O_2^- crossover. However, this does not mean a thicker separator yields better electrochemical performance. As shown in **Figure S5.13**, the internal resistance of the cell also increases with increasing separator thickness, leading to a gradual decrease in the cell energy

efficiency. At the same time, the achievable charge capacity before voltage drop was slightly increased for both cells compared to the cell with one GF layer, indicating that the short-circuiting issue can only be delayed rather than completely solved by increasing the separator thickness. By comparing the electrochemical performance of the cells with four different configurations, it is easier to find that only the Na-O$_2$ cell with CP electrically connected with Na metal can effectively prevent the short-circuiting issue and exhibit reversible discharge/charge processes at different current densities.

Determining why the CP at the anode side strongly stops the migration of O$_2^-$ toward the surface of Na anode will be crucial to the future design of battery configurations. We attribute this phenomenon to the different sodium (electro)chemical potential of the CP either self-standing or attached to a Na anode. To determine this difference, we assembled the CP/Na and Na+CP/Na cells and their open circuit potentials are found to be around 1.2 V and 0.02 V, respectively. To give a clear picture on the protective effect of CP towards Na anode, the composition of the film-like products on the CP was further characterized by XPS and EDX techniques. The XPS spectra of C, O and S elements in both discharged and charged states of CP interlayer are shown in **Figure S5.14**, and all XPS spectra were calibrated by the standard position of the C-C bond at 284.8 eV. In the C1s spectrum, the existence of C-O, C=O and COO- species on the CP may originate from the decomposition of DEGDME solvent (**Figure S5.14** and **b**). **Figure S5.14c** and **d** shows the featured peaks of Na$_2$CO$_3$ and NaOH at 531.8 and 532.8 eV, respectively. Meanwhile, according to previous report, the S 2p 3/2 peak at 168.6 eV is likely from the –SO$_2$– fragment after the decomposition of TFSI$^-$ anion.[57] Therefore, the composition of products on the CP mainly contains NaOH, Na$_2$CO$_3$, sulfur oxide species and carboxylic/carbonyl species (**Figure S5.14e** and **f**). More interestingly, no composition difference can be observed at discharge and charge states, which can be further confirmed by the results obtained from EDX line scan on the CP. As shown in **Figure S5.15**, the Na and O elements follows the same changing trend along the distance, which is different to that of the C element. Also, the ratio of the O and C elements on the CP keeps the same (~3) at both discharge and charge states. Taking into consideration that the Na$_2$CO$_3$, NaOH and other products have formed on CP at the side facing air electrode (**Figure S5.9c**), the following electrochemical reactions are proposed to occur:

$$(+) \quad 4Na^+ + e^- + 3O_2^- + 2C \rightarrow Na_2CO_3 \tag{1}$$

$$(+) \quad Na^+ + e^- + O_2^- + electrolyte \rightarrow NaOH + organic\ carbonates \tag{2}$$

$$(-) \quad Na = Na^+ + e^- \tag{3}$$
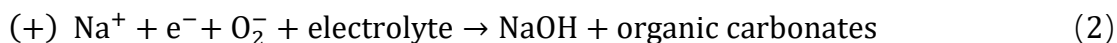
The attaching of CP onto Na results in a much lower electrochemical potential to provide high potential polarization as the driving force (enhanced kinetics) of the electrochemical reaction based on the Butler-Volmer equation. As a result, these side reactions occur at the CP and produce side products at the CP instead of on the Na surface due to diffusion control, so that less decomposition products will be formed on the Na surface.

Except for the issue of O_2 and O_2^- crossover discussed above, researchers have also verified the generation of reactive species, singlet oxygen ($^1O_2$), during charging process in Li- and Na-O_2 batteries recently.[58, 59] The $^1O_2$ is formed during both discharge and charge process, charging to higher voltage (>3.3V) yields significantly more $^1O_2$ in the Na-O_2 batteries. More importantly, the authors pointed out that the parasitic chemistry in the Na-O_2 cathode in closely related to the formation of $^1O_2$ since the extent of side reactions follows the occurrence of $^1O_2$. Thus, there is possibility that the $^1O_2$ produced during charge process as well as oxygen gas dissolved during both discharge and charge processes also may migrate to the anode side and induce parasitic reactions on the Na surface. Moreover, compared with O_2, the highly reactive $^1O_2$ may induce more serious side reactions.

In the Na-O_2 cells with protected Na, the CP is sandwiched between the Na foil and separator, and thus CP electrically connected with the Na metal to form a protected anode. In fact, the protected Na is equal to a shorted cell, and Na^+ can immediately intercalate into the CP and persists in the sodiated state when liquid electrolyte was added. Janek and co-workers have reported that the sodiated carbon paper can react chemically with oxygen to form sodium superoxide. [29] Thus, instead of migrates across the CP and trigger electrolyte decomposition on the Na anode, the migrated O_2 from the cathode side during charging (and discharging) will probably react with sodiated carbon (CP) to form NaO_2, and then electrochemical reactions involving NaO_2 occurs on the CP following the proposed reaction routes in eq. (1)-(3). Therefore, the application of CP on the Na surface not only

can alleviate the side reactions induced by O_2^- crossover, but also somewhat inhibit the detrimental effect of O_2 (and/or $^1O_2$) crossover on the Na anode. As a result, the charge overpotential is significantly reduced and the capacity of the Na-O_2 batteries are boosted due to the reduced accumulation of side product on the Na anode. Instead, the CP merely placed between two GFs may only slightly block the diffusion of O_2^- by the following chemical reactions:

$$4O_2^- + 3C = 2CO_3^{2-} + CO_2 \tag{4}$$

$$CO_3^{2-} + 2Na^+ = Na_2CO_3 \tag{5}$$

$$4NaO_2 + 3C = 2Na_2CO_3 + CO_2 \tag{6}$$

The sluggish rates of the chemical reactions and porous nature of CP make this chemical blocking effect highly inefficient compared to the above electrochemical protection routes. The overall mechanism is depicted in **Figure 5.6**.

5.3.4 Discussion on the dual critical roles of CP for Na-O_2 batteries

A full explanation for the effectiveness of the CP of Na-O_2 batteries can be elucidated in **Figure 5.7a**. In the Na-O_2 cells with protected Na anode, the function of the CP is beyond that of a simple physical barrier to protect the Na electrode. In the presence of CP, the side reactions involving the O_2 ($^1O_2$) and O_2^- will preferentially occur on the CP surface by kinetics, which is determined by the cell configuration and the pseudo-equal potential of CP and metallic Na. Thus, the CP acts as a protective layer to alleviate Na degradation during the discharge process and decrease the influence of the metallic Na electrode as a determining factor for the cell discharge capacity. On the other hand, electrons are available on the surface of the conductive CP during Na deposition compared with a non-conductive GF separator. Thus, the CP also plays a role of a 3D current collector, which can decrease the local concentration of current and suppress dendrite growth effectively. Therefore, application of a protected Na with electrically connected Na and CP can thoroughly prevent the short-circuiting issue, while the issue remains when replacing conductive CP with a nonconductive GF.

When the conductive CP is sandwiched between two GFs in the Na-O$_2$ cell, most O$_2$ and O$_2^-$ will still migrate across the CP and trigger electrolyte decomposition on the Na anode, similar to the case of Na-O$_2$ cells without a conductive CP on the Na anode (**Figure 5.7b**). One possible explanation is that a high reduction potential is needed for electrolyte decomposition in the presence of oxidative species (O$_2$ and O$_2^-$). Therefore, the key to the success of this approach is that the conductive CP should be coated directly on the Na metal, making sure that the electrode potential on the CP and metallic Na is the same. This finding is helpful for explaining the fact that the anode experiences more decomposition reactions than the cathode, and the crossover of contaminants from the cathode to the anode makes side reactions more aggravated in Na-O$_2$ battery system than traditional Na-ion batteries.
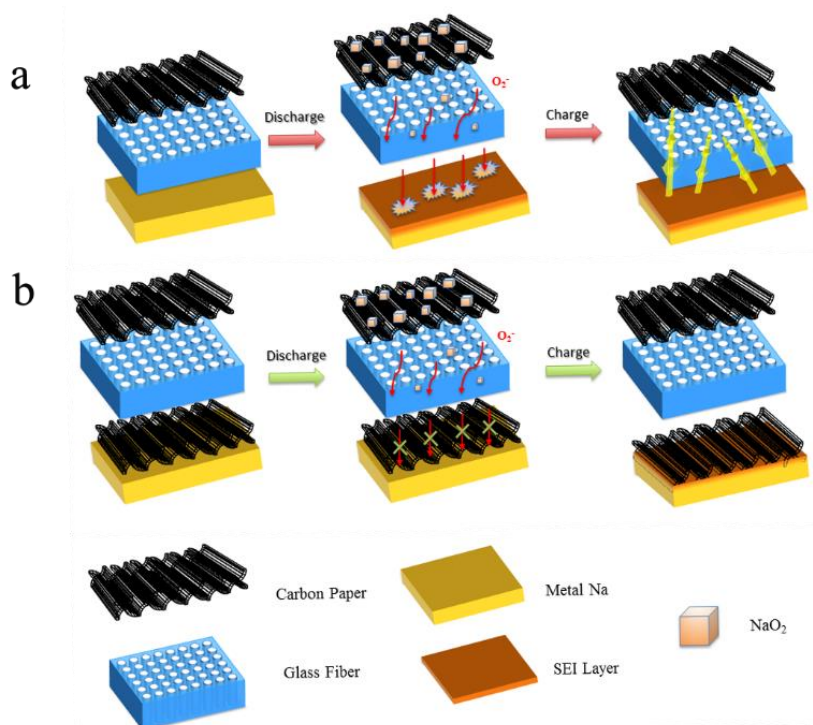
Figure 5.7 Schematic illustration of the discharge and charge process of Na-O$_2$ batteries with (a) bare Na and (b) protected Na anode.

The major focus of this study has been the effect of O$_2$ and O$_2^-$ crossover towards the metallic Na in Na-O$_2$ batteries and emphasize the important role that the Na anode plays in cell performance. However, the effectiveness of CP in alleviating the side reactions

induced by contaminant crossover on the Na anode is not yet totally sufficient. The CP is a porous structure and it cannot fully block the diffusion of O_2 and O_2^- from the cathode to the Na surface. Therefore, the porous structure of CP still allows a small amount of O_2 and superoxide ions to migrate and reach the Na surface, which also lead to the side reactions. Moreover, conductive CP acts as a sacrificial protective interlayer on the negative electrode, and the conductive surface of the CP will be gradually covered by the side products. Thus, the Na corrosion caused by contaminant crossover can only be alleviated, but not fully eliminated during the long cycling process of cells with CP protected Na. Therefore, effective strategies to restrict the O_2 and O_2^- crossover towards anode will need to be further developed in the future studies, which will hopefully result in significant improvement in the cycling performance of Na-O_2 batteries.

5.4 Conclusion

In this chapter, we report a novel design of Na-O_2 battery using electrically connected CP and Na metal as a protected Na anode. The CP demonstrates great effectiveness in addressing the fatal issue of cell short-circuiting by altering the growth and penetration of Na dendrite into dense Na deposition. We show additionally the evidence that the electrolyte decomposition on the Na anode in the presence of O_2 and O_2^- crossover can be the dominating cause of limited discharge capacity and poor cycling properties of Na-O_2 batteries. The electrochemical potential of the CP gains a pseudo-equal potential when in contact with Na metal, and the side reactions induced by O_2 and O_2^- crossover preferentially occur on the CP instead of Na surface. The Na corrosion can be alleviated to some extent compared with the cells with bare Na, and a satisfying cycling performance up to 65 cycles with a low charge overpotential can be achieved, which is three times than that of a cell without a CP interlayer. These results emphasize the important role of Na anode in determining the overall cell performance, and the experience obtained from this work also provides a new avenue for achieving safe and high-performance Na-O_2 batteries and other metal-air batteries.

5.5 Acknowledgments

5.6 Reference

1. Cheng, F.; Chen, J., Chemical Society Reviews 2012, 41, (6), 2172-2192.

2. Bruce, P. G.; Freunberger, S. A.; Hardwick, L. J.; Tarascon, J.-M., Nat Mater 2012, 11, (1), 19-29.

3. Landa-Medrano, I.; Li, C.; Ortiz-Vitoriano, N.; Ruiz de Larramendi, I.; Carrasco, J.; Rojo, T., The Journal of Physical Chemistry Letters 2016, 7, (7), 1161-1166.

4. Bing, S.; Shuangqiang, C.; Hao, L.; Guoxiu, W., *Advanced Functional Materials* 2015, 25, (28), 4436-4444.

5. Sharon, D.; Hirshberg, D.; Afri, M.; Frimer, A. A.; Noked, M.; Aurbach, D., *Journal of Solid State Electrochemistry* 2017, 21, (7), 1861-1878.

6. Lee, D. U.; Xu, P.; Cano, Z. P.; Kashkooli, A. G.; Park, M. G.; Chen, Z., *Journal of Materials Chemistry A* 2016, 4, (19), 7107-7134.

7. Sun, B.; Huang, X.; Chen, S.; Munroe, P.; Wang, G., *Nano Letters* 2014, 14, (6), 3145-3152.

8. Sun, B.; Guo, L.; Ju, Y.; Munroe, P.; Wang, E.; Peng, Z.; Wang, G., *Nano Energy* 2016, 28, 486-494.

9. Yoo, E.; Zhou, H., *ACS Nano* 2011, 5, (4), 3020-3026.

10. McCloskey, B. D.; Garcia, J. M.; Luntz, A. C., *The Journal of Physical Chemistry Letters* 2014, 5, (7), 1230-1235.

11. Hartmann, P.; Bender, C. L.; Vračar, M.; Dürr, A. K.; Garsuch, A.; Janek, J.; Adelhelm, P., *Nat Mater* 2013, 12, (3), 228-232.

12. Zhang, Y.; Li, X.; Zhang, M.; Liao, S.; Dong, P.; Xiao, J.; Zhang, Y.; Zeng, X., *Ceramics International* 2017, 43, (16), 14082-14089.

13. Ren, X.; Lau, K. C.; Yu, M.; Bi, X.; Kreidler, E.; Curtiss, L. A.; Wu, Y., *ACS Applied Materials & Interfaces* 2014, 6, (21), 19299-19307.

14. Yadegari, H.; Li, Y.; Banis, M. N.; Li, X.; Wang, B.; Sun, Q.; Li, R.; Sham, T.-K.; Cui, X.; Sun, X., *Energy & Environmental Science* 2014, 7, (11), 3747-3757.

15. Bender, C. L.; Hartmann, P.; Vračar, M.; Adelhelm, P.; Janek, J., *Advanced Energy Materials* 2014, 4, (12), 1301863.

16. Sun, B.; Kretschmer, K.; Xie, X.; Munroe, P.; Peng, Z.; Wang, G., *Advanced Materials* 2017, 29, (48), 1606816.

17. Yadegari, H.; Franko, C. J.; Banis, M. N.; Sun, Q.; Li, R.; Goward, G. R.; Sun, X., *The Journal of Physical Chemistry Letters* 2017, 8, (19), 4794-4800.

18. Li, Y.; Yadegari, H.; Li, X.; Banis, M. N.; Li, R.; Sun, X., *Chemical Communications* 2013, 49, (100), 11731-11733.

19. Xia, C.; Black, R.; Fernandes, R.; Adams, B.; Nazar, L. F., *Nat Chem* 2015, 7, (6), 496-501.

20. Zhao, N.; Guo, X., *The Journal of Physical Chemistry C* 2015, 119, (45), 25319-25326.

21. Sun, Q.; Lin, X.; Yadegari, H.; Xiao, W.; Zhao, Y.; Adair, K. R.; Li, R.; Sun, X., *Journal of Materials Chemistry A* 2018, 6, (4), 1473-1484.

22. Sun, Q.; Yadegari, H.; Banis, M. N.; Liu, J.; Xiao, B.; Li, X.; Langford, C.; Li, R.; Sun, X., *The Journal of Physical Chemistry C* 2015, 119, (24), 13433-13441.

23. Zhao, N.; Li, C.; Guo, X., *Physical Chemistry Chemical Physics* 2014, 16, (29), 15646-15652.

24. Bi, X.; Ren, X.; Huang, Z.; Yu, M.; Kreidler, E.; Wu, Y., *Chemical Communications* 2015, 51, (36), 7665-7668.

25. Medenbach, L.; Bender, C. L.; Haas, R.; Mogwitz, B.; Pompe, C.; Adelhelm, P.; Schröder, D.; Janek, J., *Energy Technology* 2017, 5, (12), 2265-2274.

26. Hartmann, P.; Bender, C. L.; Sann, J.; Durr, A. K.; Jansen, M.; Janek, J.; Adelhelm, P., *Physical Chemistry Chemical Physics* 2013, 15, (28), 11661-11672.

27. Pinedo, R.; Weber, D. A.; Bergner, B.; Schröder, D.; Adelhelm, P.; Janek, J., *The Journal of Physical Chemistry C* 2016, 120, (16), 8472-8481.

28. Schröder, D.; Bender, C. L.; Pinedo, R.; Bartuli, W.; Schwab, M. G.; Tomović, Ž.; Janek, J., *Energy Technology* 2017, 5, (8), 1242-1249.

29. Bender, C. L.; Jache, B.; Adelhelm, P.; Janek, J., *Journal of Materials Chemistry A* 2015, 3, (41), 20633-20641.

30. Yadegari, H.; Sun, Q.; Sun, X., *Advanced Materials* 2016, 28, (33), 7065-7093.

31. Xia, C.; Fernandes, R.; Cho, F. H.; Sudhakar, N.; Buonacorsi, B.; Walker, S.; Xu, M.; Baugh, J.; Nazar, L. F., *Journal of the American Chemical Society* 2016, 138, (35), 11219-11226.

32. Liu, T.; Kim, G.; Casford, M. T. L.; Grey, C. P., *The Journal of Physical Chemistry Letters* 2016, 7, (23), 4841-4846.

33. Hartmann, P.; Heinemann, M.; Bender, C. L.; Graf, K.; Baumann, R.-P.; Adelhelm, P.; Heiliger, C.; Janek, J., *The Journal of Physical Chemistry C* 2015, 119, (40), 22778-22786.

34. Assary, R. S.; Lu, J.; Du, P.; Luo , X.; Zhang, X.; Ren, Y.; Curtiss, L. A.; Amine, K., *ChemSusChem* 2013, 6, (1), 51-55.

35. Shui, J.-L.; Okasinski, J. S.; Kenesei, P.; Dobbs, H. A.; Zhao, D.; Almer, J. D.; Liu, D.-J., *Nature Communications* 2013, 4, 2255.

36. Bergner, B. J.; Busche, M. R.; Pinedo, R.; Berkes, B. B.; Schröder, D.; Janek, J., *ACS Applied Materials & Interfaces* 2016, 8, (12), 7756-7765.

37. Yu, W.; Lau, K. C.; Lei, Y.; Liu, R.; Qin, L.; Yang, W.; Li, B.; Curtiss, L. A.; Zhai, D.; Kang, F., *ACS Appl Mater Interfaces* 2017, 9, (37), 31871-31878.

38. Sun, Q.; Yadegari, H.; Banis, M. N.; Liu, J.; Xiao, B.; Wang, B.; Lawes, S.; Li, X.; Li, R.; Sun, X., *Nano Energy* 2015, 12, 698-708.

39. Sun, Q.; Liu, J.; Li, X.; Wang, B.; Yadegari, H.; Lushington, A.; Banis, M. N.; Zhao, Y.; Xiao, W.; Chen, N.; Wang, J.; Sham, T.-K.; Sun, X., *Advanced Functional Materials* 2017, 27, (16), 1606662.

40. Morasch, R.; Kwabi, D. G.; Tulodziecki, M.; Risch, M.; Zhang, S.; Shao-Horn, Y., *ACS Appl Mater Interfaces* 2017, 9, (5), 4374-4381.

41. Zhang, G. Q.; Zheng, J. P.; Liang, R.; Zhang, C.; Wang, B.; Hendrickson, M.; Plichta, E. J., *Journal of The Electrochemical Society* 2010, 157, (8), A953-A956.

42. Tran, C.; Yang, X.-Q.; Qu, D., *Journal of Power Sources* 2010, 195, (7), 2057-2063.

43. Liu, W.; Lin, D.; Pei, A.; Cui, Y., *Journal of the American Chemical Society* 2016, 138, (47), 15443-15450.

44. Luo, W.; Zhang, Y.; Xu, S.; Dai, J.; Hitz, E.; Li, Y.; Yang, C.; Chen, C.; Liu, B.; Hu, L., *Nano Letters* 2017, 17, (6), 3792-3797.

45. Lin, D.; Zhao, J.; Sun, J.; Yao, H.; Liu, Y.; Yan, K.; Cui, Y., *Proceedings of the National Academy of Sciences* 2017, 114, (18), 4613-4618.

46. Landa-Medrano, I.; Pinedo, R.; Bi, X.; Ruiz de Larramendi, I.; Lezama, L.; Janek, J.; Amine, K.; Lu, J.; Rojo, T., *ACS Applied Materials & Interfaces* 2016, 8, (31), 20120-20127.

47. Lutz, L.; Corte, D. A. D.; Chen, Y.; Batuk, D.; Johnson, L. R.; Abakumov, A.; Yate, L.; Azaceta, E.; Bruce, P. G.; Tarascon, J.-M.; Grimaud, A., *Advanced Energy Materials* 2018, 8, (4), 1701581.

48. Zhuang, G. V.; Yang, H.; Blizanac, B.; Ross, P. N., *Electrochemical and Solid-State Letters* 2005, 8, (9), A441-A445.

49. Younesi, R.; Hahlin, M.; Roberts, M.; Edström, K., *Journal of Power Sources* 2013, 225, 40-45.

50. Lutz, L.; Alves Dalla Corte, D.; Tang, M.; Salager, E.; Deschamps, M.; Grimaud, A.; Johnson, L.; Bruce, P. G.; Tarascon, J.-M., *Chemistry of Materials* 2017, 29, (14), 6066-6075.

51. Seh, Z. W.; Sun, J.; Sun, Y.; Cui, Y., *ACS Central Science* 2015, 1, (8), 449-455.

52. Busche, M. R.; Adelhelm, P.; Sommer, H.; Schneider, H.; Leitner, K.; Janek, J., *Journal of Power Sources* 2014, 259, 289-299.

53. Bruce, P. G.; Freunberger, S. A.; Hardwick, L. J.; Tarascon, J.-M., *Nature Materials* 2011, 11, 19.

54. Elia, G. A.; Hasa, I.; Hassoun, J., *Electrochimica Acta* 2016, 191, 516-520.

55. Wu, F.; Xing, Y.; Lai, J.; Zhang, X.; Ye, Y.; Qian, J.; Li, L.; Chen, R., *Advanced Functional Materials* 2017, 27, (30), 1700632.

56. Bi, X.; Wang, R.; Ma, L.; Zhang, D.; Amine, K.; Lu, J., *Small Methods* 2017, 1, (7), 1700102.

57. Ren, X.; He, M.; Xiao, N.; McCulloch, W. D.; Wu, Y., *Advanced Energy Materials* 2017, 7, (1), n/a-n/a.

58. Lukas, S.; Nika, M.; Bettina, S.; Martin, W.; Christian, S.; M., B. S.; A., F. S., *Angewandte Chemie International Edition* 2017, 56, (49), 15728-15732.

59. Nika, M.; E., R. S.; D., M. B.; A., F. S., *Angewandte Chemie International Edition* 2018, 57, (19), 5529-5533.

5.7 Supporting information
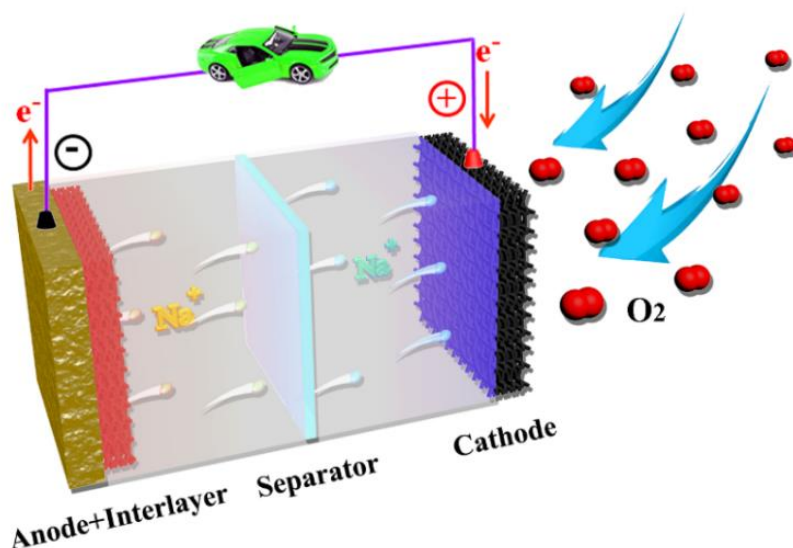
Figure S5.1 Schematic illustration of a novel Na-O$_2$ battery with protected Na anode using CP electrically connect with Na metal.
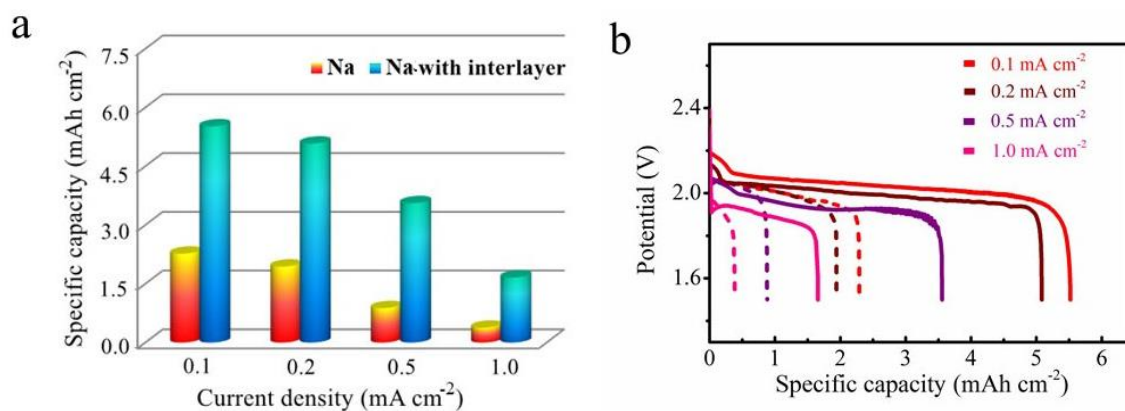
Figure S5.2 Comparison of the (a) initial discharge capacities and (b) initial discharge curves of Na-O$_2$ cells with bare Na and protected Na at different current densities, respectively; The solids lines are the discharge curves of cells with protected Na, and dashed lines represent the cells with bare Na.
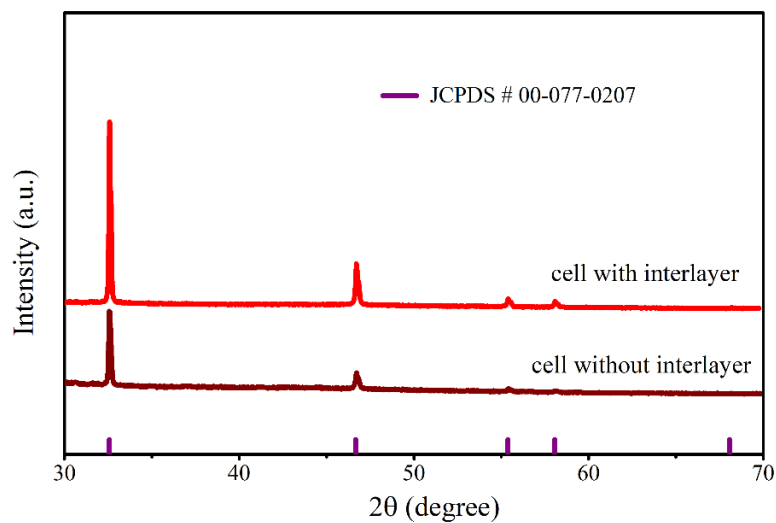
Figure S5.3 The comparative XRD patterns of fully discharged air electrodes obtained from Na-O_2 cells with bare Na and CP interlayer protected Na, respectively.
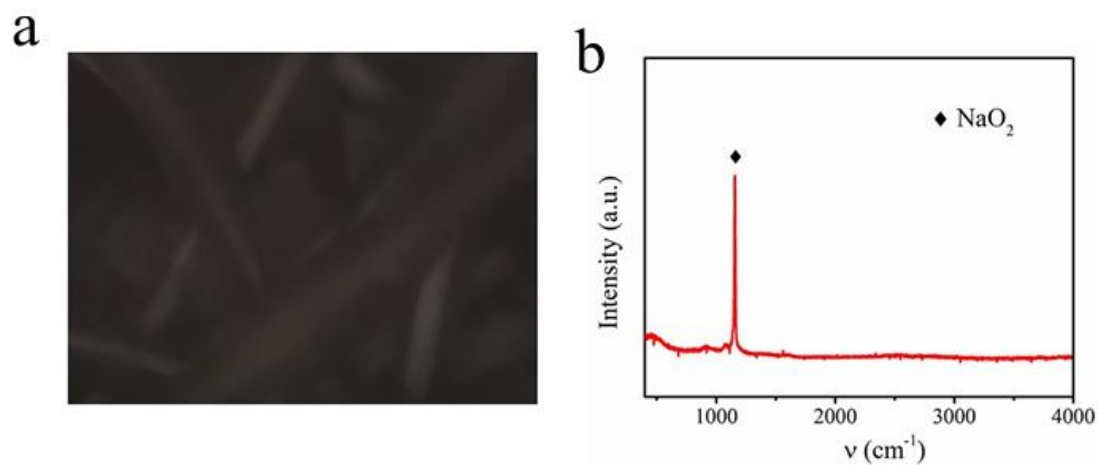
Figure S5.4 (a) The optical image of fully discharged cathode and (b) the Raman spectrum of cubic-shaped discharge products.
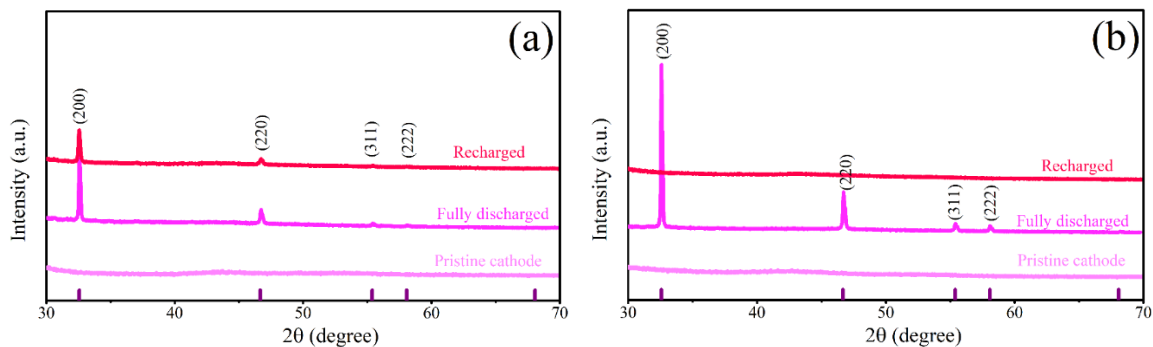
Figure S5.5 The XRD patterns of air electrodes in Na-O$_2$ cells with (a) bare Na and (b) protected Na at different electrochemical states. The current density of the Na-O$_2$ cells is 0.1 mA cm^{-2}.
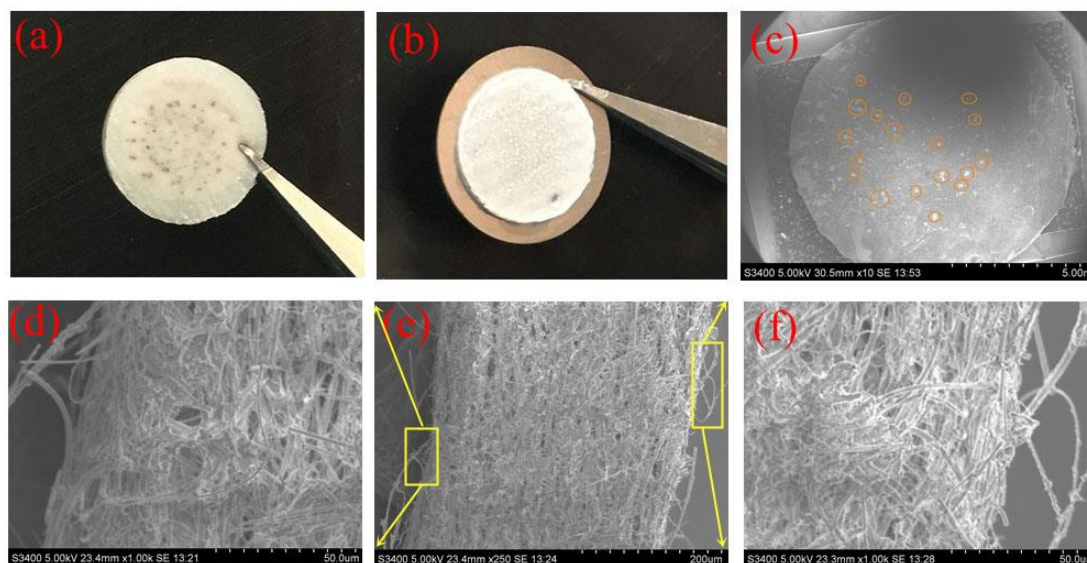
Figure S5.6 Digital camera and SEM images of (a) separator and (b, c) bulk Na anode after cell short circuit during the charge process. (d-f) The cross-sectional SEM images of separator after cell short circuit during the charge process. The current density of the failed Na-O$_2$ cell is 0.1 mA cm^{-2}, and charge capacity is about 0.35 mAh cm^{-2}.
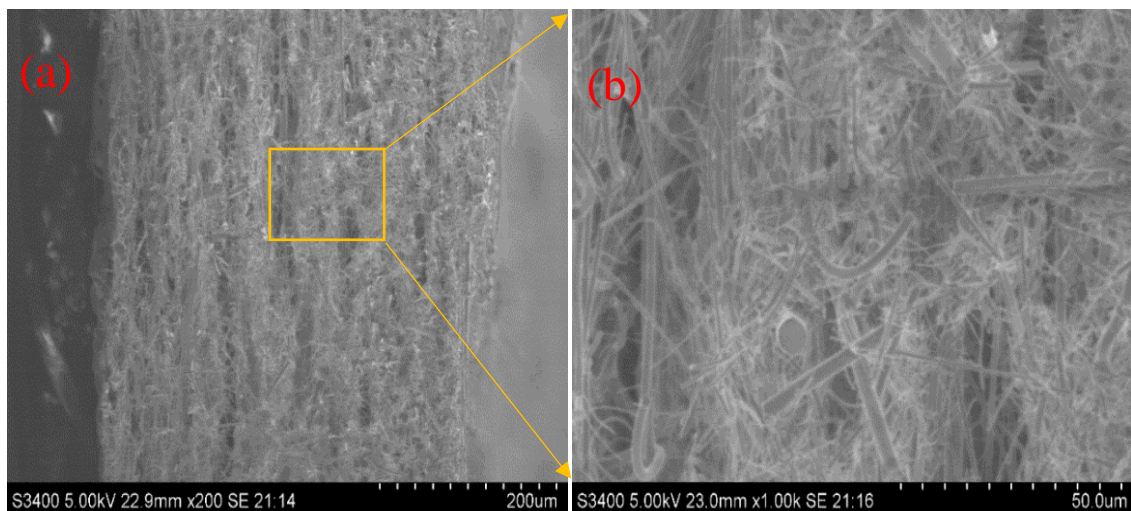
Figure S5.7 The cross-sectional SEM images of a pristine separator. The pristine separator exhibits a layered structure with obvious interlayer spacing.
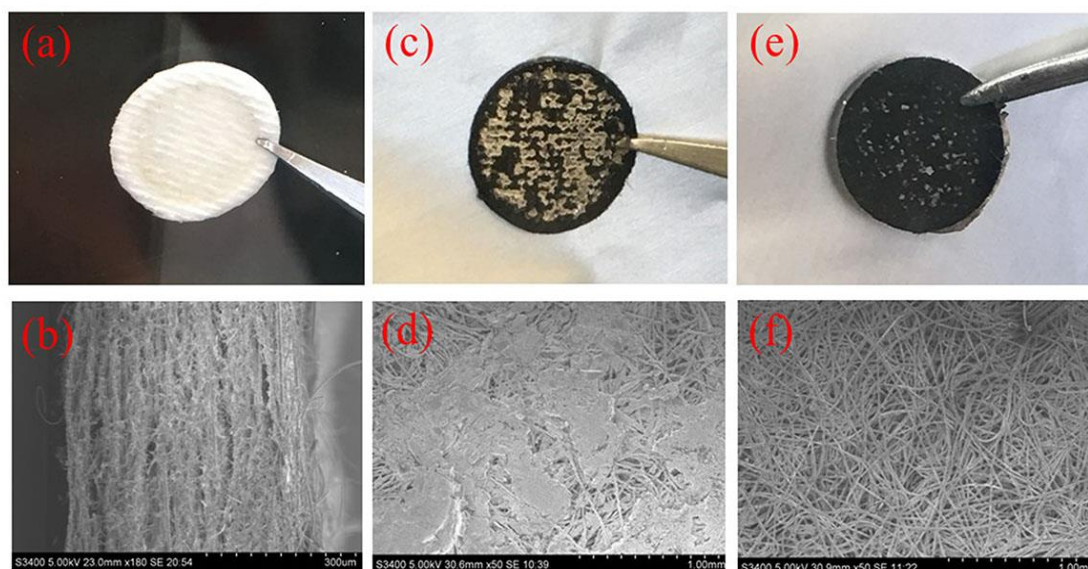
Figure S5.8 (a) Digital camera image and (b) cross-sectional SEM image of a separator after the cell with protected Na is fully charged at 0.1mA cm^{-2}. Digital camera image and top view SEM images of (c, d) bulk Na side and (e, f) separator side of the CP after the cell is fully charged at 0.1mA cm^{-2}.
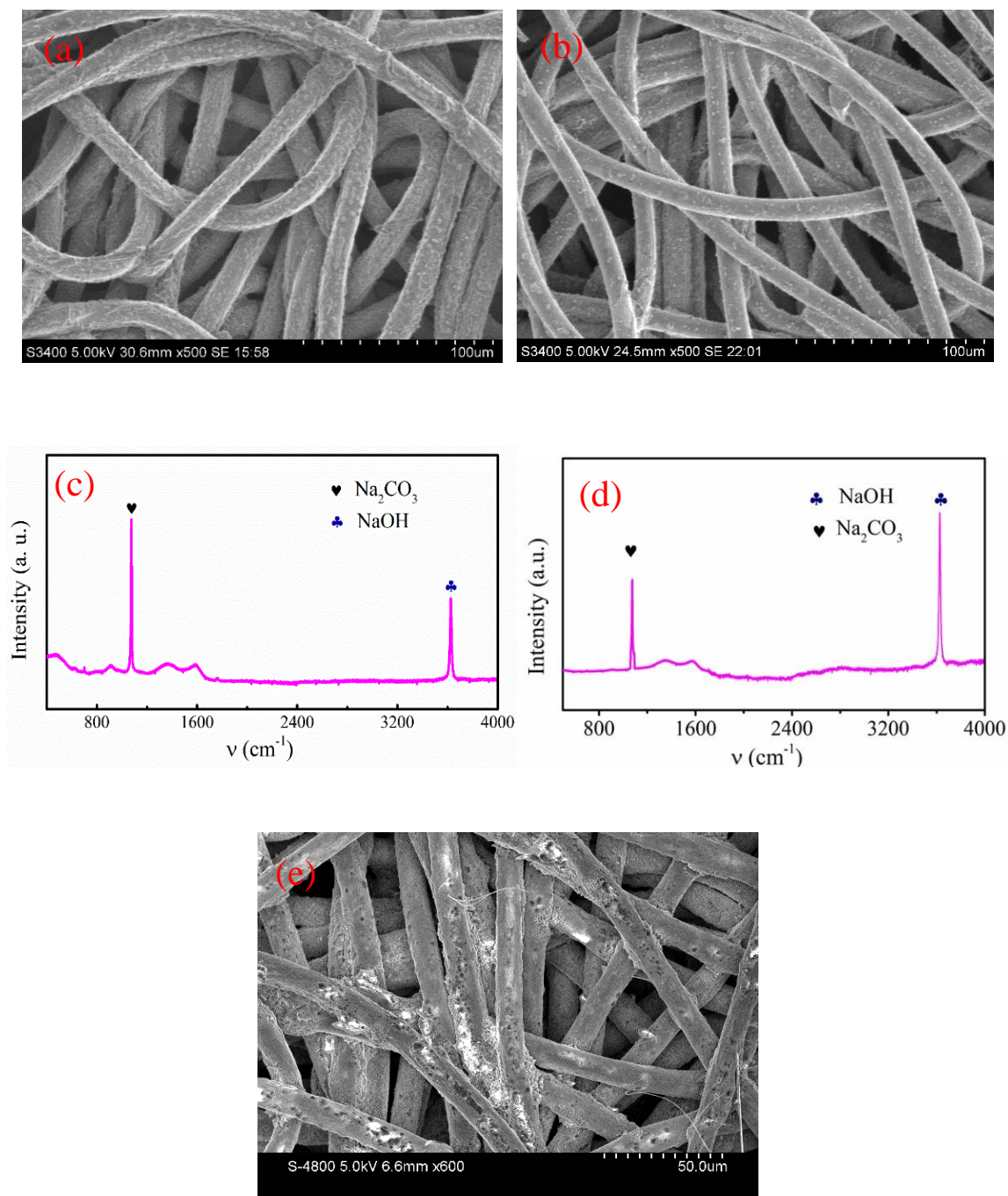
Figure S5.9 The SEM images of (a) separator/CP side and (b) CP/Na side of a CP after full discharge at 0.1 mA cm^{-2}. The Raman spectra of CP after the cell is (c) fully discharged and (d) recharged at 0.1 mA cm^{-2}. (e) The SEM image of separator/CP side of a CP after fully charged at 0.1 mA cm^{-2}.
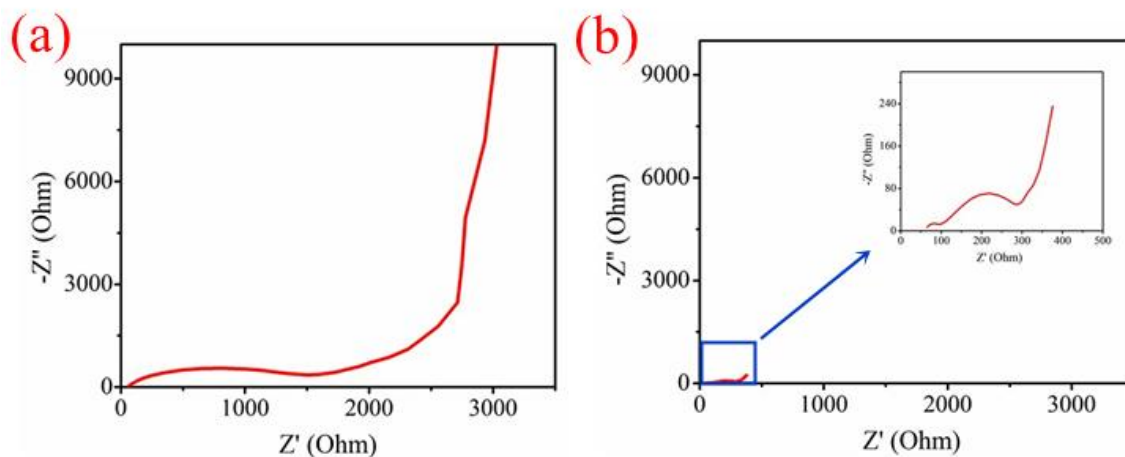
Figure S5.10 The EIS spectra of Na-O$_2$ cells with (a) bare Na and (b) CP interlayer protected Na at initial state.
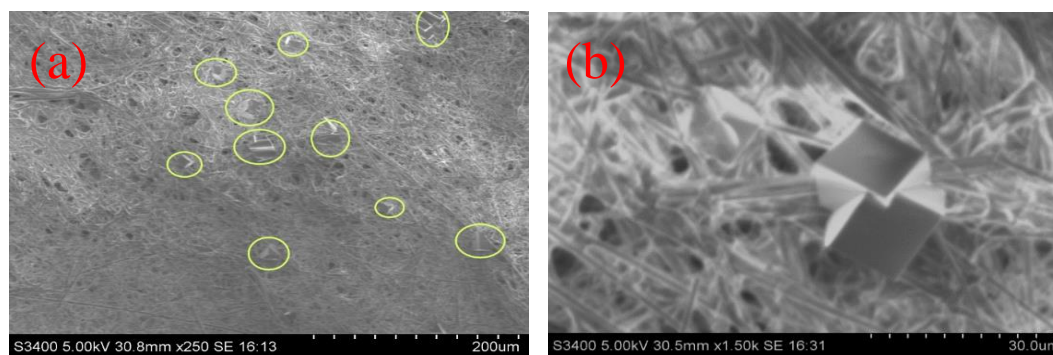
Figure S5.11 The SEM images (a, b) and XRD pattern (c) of separator obtained from a fully discharged Na-O$_2$ cell with bare Na. The current density is 0.1 mA cm^{-2}.
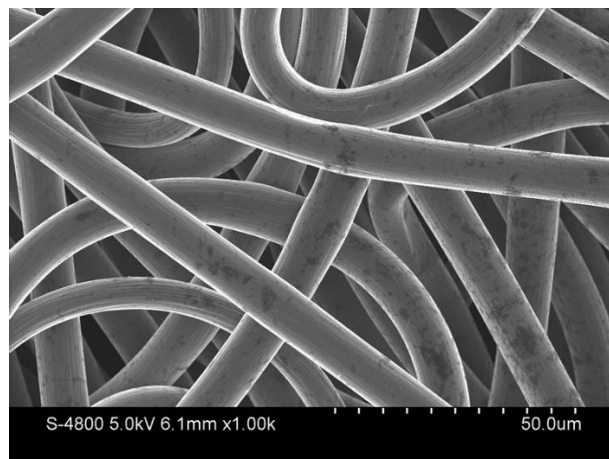
Figure S5.12 The SEM image of a fully charged cathode in a Na-O$_2$ cell with CP interlayer protected Na. The current density is 0.1 mA cm^{-2}.
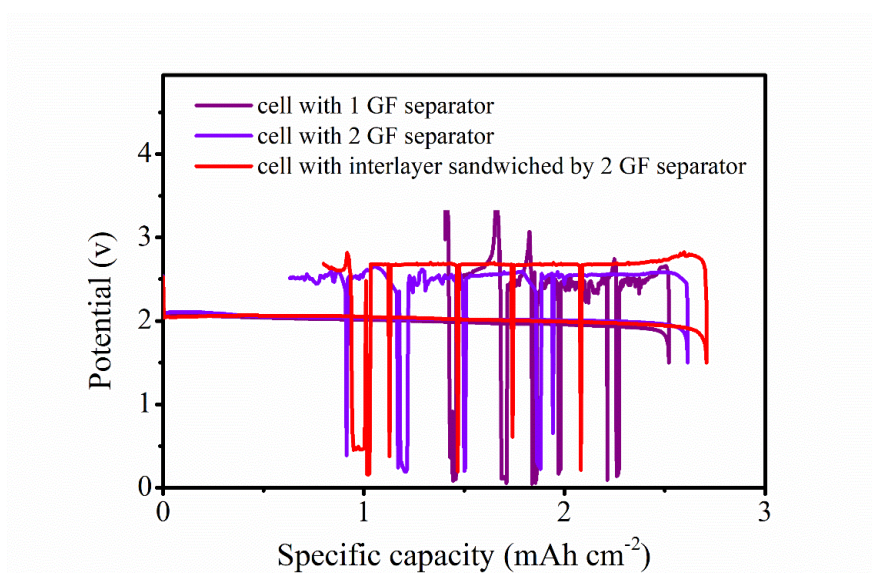
Figure S5.13. The charge/discharge curves of Na-O$_2$ batteries with three different cell configurations at the current density of 0.1 mA cm^{-2}.
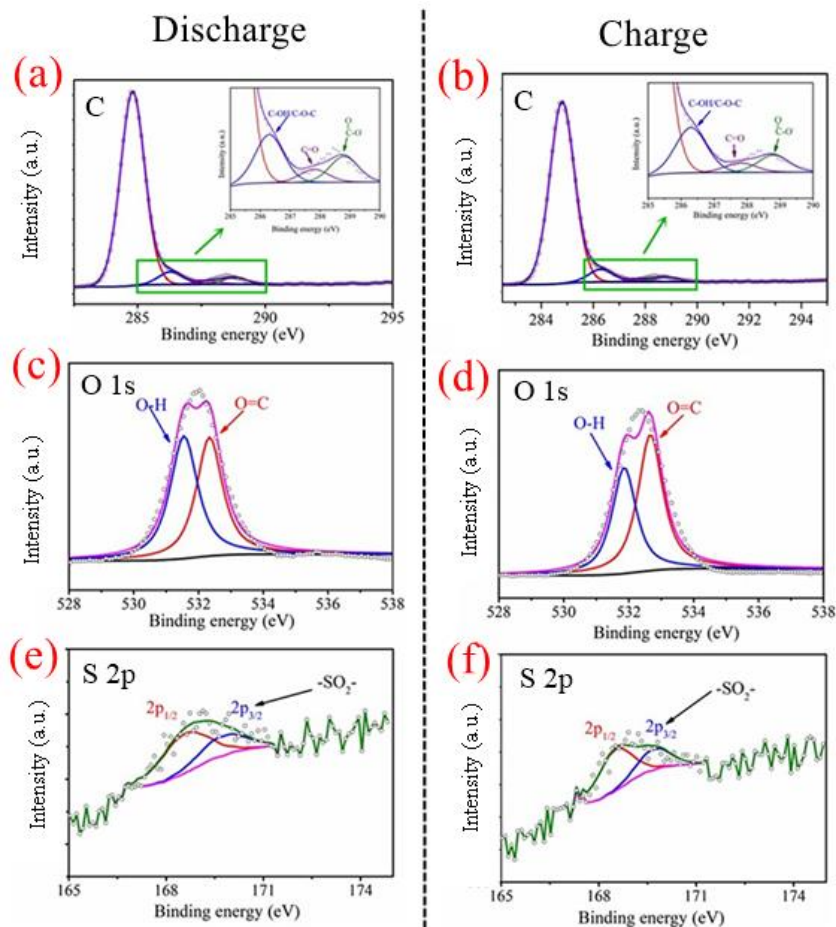
Figure S5.14. (a, b) C 1s, (c, d) O 1s, and (e, f) S 2p XPS spectra of the CP interlayer after discharge and charge back.
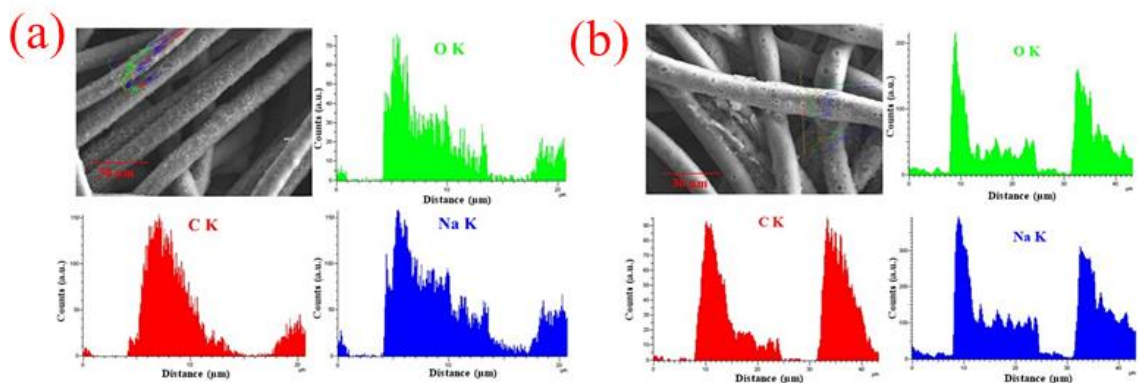
Figure S5.15 The EDS line scan of the CP interlayer at (a) discharge and (b) charge states, respectively.

Chapter 6

6 O_2/O_2^- crossover- and dendrite-free hybrid solid-state Na-O_2 batteries

Na metal anode plays an important role in determining the overall performance of Na-O_2 batteries, in which Na metal degradation caused by O_2/O_2^- crossover and uncontrollable Na dendrite growth often result in the premature cell death. In the last chapter, carbon paper (CP) protected Na anode was introduced to improve the electrochemical performance of Na-O_2 batteries. Although the Na dendrite growth can be completely suppressed, the Na anode degradation induced by O_2/O_2^- crossover can only be alleviated rather than fully eliminated during the long-term cell cycling, which inevitably attenuate the cycle life of Na-O_2 batteries.

Addressing these issues comprehensively, in this chapter, we successfully developed a hybrid solid-state (HSS) Na-O_2 battery based on solid-state electrolyte (SSE) and a protected Na anode. The dense structure of SSE effectively suppressed the O_2/O_2^- crossover, thus mitigating the Na degradation and improving the cell reversibility. Solid electrolyte interphase (SEI) formation on the Na anode in relation to the O_2/O_2^- crossover was further revealed. Additionally, 3D protection layer on Na anode facilitated uniform Na deposition within the conductive matrix. Consequently, the fabricated HSS Na-O_2 battery demonstrated stable cycling for over 160 cycles at 0.2 mA cm^{-2} under the shallow cycling mode. The results evidently emphasized the critical role of Na anode protection, and the importance of O_2/O_2^- blockage for achieving safe and high-performance Na-O_2 batteries.

6.1   Introduction

Owing to the appealingly high theoretical energy density, Li-O$_2$ batteries have been considered as a promising alternative to the state-of-the-art Li-ion batteries.[1-7] However, most Li-O$_2$ batteries generate insulating Li$_2$O$_2$ as the main discharge product, which is a plague on high charging overpotential and thus result in low round-trip energy efficiency.[8-10] Comparatively, Na-O$_2$ batteries are more favourable for large-scale implementations in terms of high energy efficiency and reversibility.[11-13] In addition, the low cost and abundance of Na on earth promise a long-term future for Na-O$_2$ batteries in a wide range of application.[14, 15]

Nevertheless, several technical bottlenecks are still limiting the cycle life of Na-O$_2$ batteries. Especially, O$_2$ crossover from the air electrode to the Na anode is detrimental for Na-O$_2$ batteries.[16-20] Parasitic reactions and continuous consumption of the metallic Na anodes due to O$_2$ crossover are one of the main causes of Na-O$_2$ battery failure.[21, 22] Another source of detrimental side reactions on Na metal is induced by the O$_2^-$ migration in superoxide-based Na-O$_2$ batteries because of the solution-mediated path for NaO$_2$ formation.[23-27] In fact, the O$_2^-$ radical is an aggressive species, which is prone to attack electrophilic sites. The effect of O$_2^-$ radicals on promoting parasitic reactions on Na metal anode is profound despite of the relatively low concentration.[28, 29] The presence of O$_2^-$ also causes severe decompositions of electrolyte solvents, sodium salts, binders, and air electrodes in superoxide-based Na-O$_2$ batteries.[30-37] However, studies towards understanding the O$_2$/O$_2^-$ crossover effect on the nature of solid electrolyte interphase (SEI) layer and overall Na-O$_2$ cell performance is scarce.

Blocking O$_2$/O$_2^-$ crossover is of primary importance for enhancing the electrochemical performance of Na-O$_2$ batteries. In traditional liquid electrolyte (LE)-based Na-O$_2$ cells with porous separators, the dissolved O$_2$/O$_2^-$ can diffuse freely from the cathode to the anode. A physical barrier is required to retard the migration of O$_2$/O$_2^-$. Inspired by the aqueous Na-air batteries, in which ceramic separators are widely used to prevent the undesirable "cross-talk" of an aqueous electrolyte and organic electrolyte,[38, 39] NASICON-type solid-state electrolyte (SSE) can be an ideal candidate to block the O$_2$/O$_2^-$ crossover for Na-O$_2$ batteries. However, the implementation of Na metal anodes in Na-O$_2$ batteries

encounters the Na dendrite formation problem.[40, 41] The inhomogeneous current distribution at the Na/NASICON SSE interface inevitably initiates rapid Na dendrite growth along the grain boundaries.[42] The penetration of Na dendrites through the SSE in (hybrid) solid-state Na-O_2 batteries leads to initial short circuit and safety concerns, especially for aqueous Na-O_2 batteries. While it is still a big challenge to enable both reversible plating/stripping of dendrite-free Na anodes and O_2/O_2^- blockage simply with the NASICON SSE pellet, the combination of SSE together with a protected Na anode could be a promising strategy to achieve high-efficiency and long-life Na-O_2 batteries.
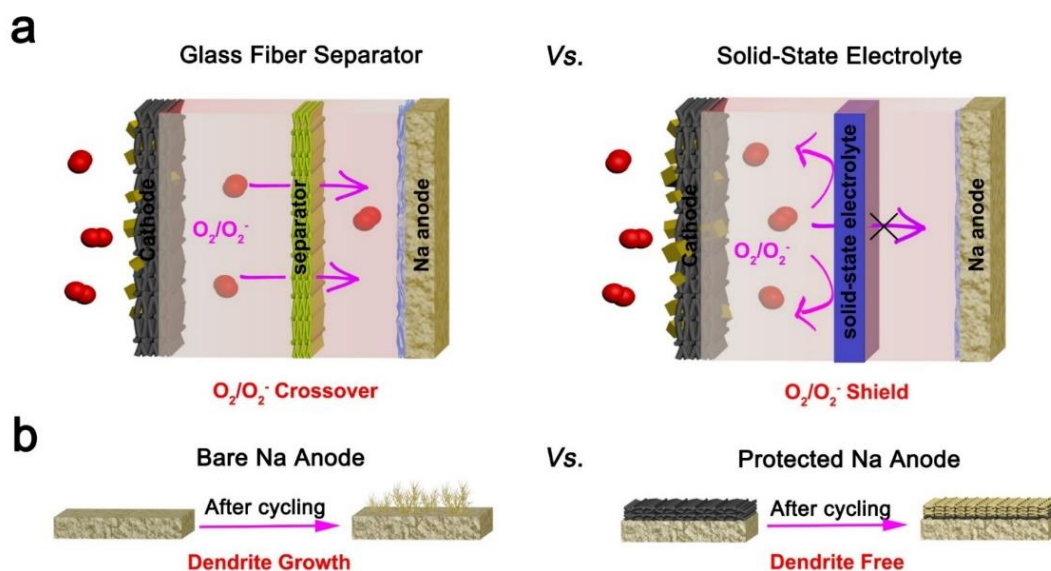
Figure 6.1 Schematic illustrating the effects of (a) O_2/O_2^- crossover prevention by solid-state electrolyte and (b) dendrite-free Na deposition by anode protection for high performance HSS Na-O_2 batteries.

In this work, we successfully demonstrate a high-performance hybrid solid-state (HSS) Na-O_2 battery with effective O_2/O_2^- crossover prevention and dendrite-free Na metal. Unlike the Na-O_2 batteries with LE and porous glass fiber (GF) separator, the dense structure of NASICON SSE is Na^+ conductive but impermeable to O_2/O_2^-, effectively avoiding Na metal corrosion and enhancing the reversible capacity. Furthermore, CP can be used not only as the air electrode directly but also as the versatile dendrite-free protector for the Na metal anode (**Figure 6.1**). The additional CP between SSE and Na metal anode facilitates dendrite-free deposition of Na within the 3D framework. Owing to the combined

advantages of SSE and CP modification, the developed HSS Na-O_2 cell delivered high discharge capacities with excellent Coulombic efficiency as well as stable cycling performance.

6.2 Experimental section

Preparation of solid-state electrolyte. The solid-state electrolyte $Na_{3.25}Zr_2Si_{2.25}P_{0.75}O_{12}$ was synthesized via a sol-gel method. Stoichiometric amounts of tetraethyl orthosilicate ($Si(OC_2H_5)_4$, TEOS) (Sigma-Aldrich, 98%) and Zirconium (IV) propoxide solution ($Zr(OC_4H_9)_4$) (Sigma-Aldrich, 99.99%) were sequentially dissolved in ethanol. Then, acetic acid and de-ionized water were added into the mixture dropwise, and the mixture sol was kept at 67°C under vigorous stirring for 10 h. Then, the sodium nitrate (Sigma-Aldrich, 99.0%) and ammonium dihydrogen phosphate (Prolabo, 99.9%) were, respectively, dissolved in water and the solution were consequently added into the hot mixture of silica and zirconia. In the next step, the solution was slowly evaporated at 67°C to produce the precursor powder with stirring, which was then heated at 500°C for 1h under O_2 atmosphere to burn out the organics. After this, the obtained powder was annealing at 1050°C for 10h and then uniaxially pressed into pellets, which were sintered at 1300°C for 12 h in air atmosphere.

Battery assembly and electrochemical measurements. The electrochemical performance of Na-O_2 batteries was evaculated with Swagelok-type cells. The HSS Na-O_2 batteries were assembled with CP protected Na anode, $Na_{3.25}Zr_2Si_{2.25}P_{0.75}O_{12}$ SSE, CP cathode and ether electrolyte. The CP cathode and Na metal foil were cut into circular pieces with a geometric surface area of 0.7125 cm^{-2}. The electrolyte was 0.5 M sodium trifluoromethanesulfonate ($NaSO_3CF_3$, Aldrich) dissolved in diethylene glycol dimethyl ether (DEGDME, reagent grade $\geq$ 98%, Aldrich). Minor amount of LE (2 µl) was added on the Na anode to mitigate the poor SSE/Na interfacial contact, and at the same time, facilitate the ion conduction during the cell cycling process. While on the cathode side, 30 µl LE was added to facilitate the formation of NaO_2 through solution-mediated path. The cells were operated under static O_2 with the pressure of 1.0 atm in a homemade testing box, and each cell was stabilized for 30 minutes at room temperature before electrochemical tests. The galvanostatic discharge-charge tests were carried out using Arbin BT-2000 battery testing system at

room temperature. The electrochemical analysis of Na symmetric cells was performed using CR2032 coin-type cells. The electrolyte preparation and battery assembly were carried out in an argon-filled glovebox with the oxygen and moisture levels below 0.1 ppm. Noted that the DEGDME was dried over freshly activated molecular sieves (4 Å, Aldrich) for at least one month. $NaSO_3CF_3$ was dried in a vacuum at 80°C for 3 days before use.

Material characterization. The X-ray powder diffraction (XRD) patterns were performed on the Bruker D8 X-ray diffractometer equipped with Cu-Kα (λ=1.5406Å) radiation. The morphology of the discharged cathodes were characterized by Hitachi S-4800 field emission scanning electron microscope (FE-SEM), and the morphological studies of the CP interlayer were performed using a Hitachi 3400N environmental SEM. The Raman spectra were collected on a HORIBA Scientific LabRAM Raman spectrometer equipped with a 532.03 nm laser. In this study, the disassembly of the Na-O$_2$ batteries was carried out in an Ar-filled glovebox. X-ray photoemission spectra (XPS) was carried out by a Kratos Axis Ultra Al-α spectrometer operated at 14 kV. The ionic conductivity of the $Na_{3.25}Zr_2Si_{2.25}P_{0.75}O_{12}$ pellet was measured through EIS using Au film sputtered on both sides of the pellet as blocking electrodes, and the EIS was performed over a frequency range of 1 MHz to 100 mHz with a 50 mV perturbation amplitude. Noted that the discharged cathodes were washed with fresh DEGDME to remove any residual $NaSO_3CF_3$ salt, and then rigorously dried in the vacuum chamber before SEM, XRD and Raman measurements. The dried samples were sealed into a leak-tight homemade sample holders to prevent the exposure of air during sample testing.

6.3 Results and discussion

Figure 6.2a schematically illustrates the configuration of the designed HSS Na-O$_2$ battery. Commercial CP was used as the cathode; NASICON-type $Na_{3.25}Zr_2Si_{2.25}P_{0.75}O_{12}$ pellet serves as the electrolyte and separator; and another layer of LE-infiltrated CP was placed on the Na metal for a dendrite-free anode. Here, $Na_{3.25}Zr_2Si_{2.25}P_{0.75}O_{12}$ was chosen in this work because of its high ionic conductivity, wide electrochemical stability window, as well as good stability against Na metal (**Figure S6.1-S6.2**). $Na_{3.25}Zr_2Si_{2.25}P_{0.75}O_{12}$ powder was synthesized by a modified sol-gel synthesis-combustion method and subsequently sintered and polished into thin SSE pellets.[43] The structure of $Na_{3.25}Zr_2Si_{2.25}P_{0.75}O_{12}$ SSE is shown

in **Figure 6.2b**. XRD pattern of the synthesized $Na_{3.25}Zr_2Si_{2.25}P_{0.75}O_{12}$ confirmed its desired phase (**Figure S6.3**).[44]
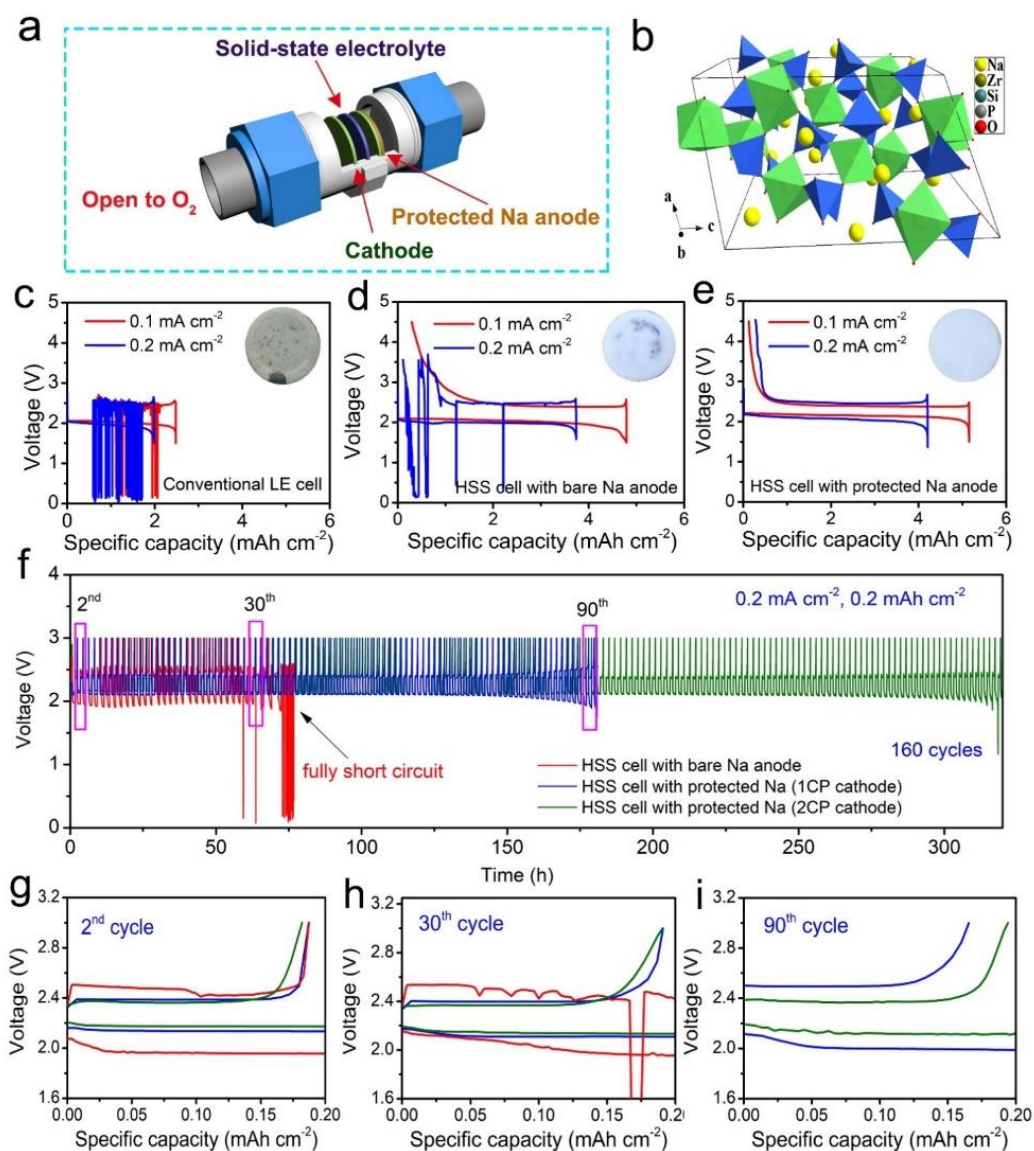
Figure 6.2 (a) Schematic illustration of a Swagelok-type Na-O$_2$ cell with SSE and CP protected Na anode. (b) The crystal structure of $Na_{3.25}Zr_2Si_{2.25}P_{0.75}O_{12}$ SSE. The discharge/charge curves of (c) conventional Na-O$_2$ batteries using LE, (d) HSS cells using SSE, (e) HSS cells using SSE and CP protected Na anode at current densities of 0.1 and 0.2 mA cm^{-2}; insets are corresponding optical images of separator or SSE collected after fully recharged at 0.2 mA cm^{-2}; (f) Cycling performance of HSS Na-O$_2$ batteries with or without CP protection on Na anode at 0.2 mA cm^{-2} with a limited capacity of 0.2 mAh cm^{-}

^{2}; (g-i) charge/discharge voltage profiles at the 2nd, 30th and 90th cycles (profile colors are as labeled in (f)).

As a proof of concept, the electrochemical performance of the proposed HSS Na-O$_2$ cells with SSE and CP protected Na anode was tested in a potential range of 1.5-4.5V. Meanwhile, Na-O$_2$ cells using conventional LE with GF separator as well as HSS Na-O$_2$ cells using bare Na anode were assembled for comparison. As shown in **Figure 6.2c**, the conventional LE cells with GF separator delivered low initial discharge capacities of 2.48 and 1.98 mAh cm^{-2} at 0.1 and 0.2mA cm^{-2}, respectively. The worst thing was that the LE Na-O$_2$ cells failed to be recharged due to Na dendrites induced short-circuit.[21, 45] Na dendrite dead spots were clearly observed in optical image of the GF separator collected after cell failure (insert in **Figure 6.2c**). Noticeably, replacing the GF separator with dense SSE significantly increased the initial discharge capacities of the Na-O$_2$ cells to 4.8 and 3.7 mAh cm^{-2} at 0.1 and 0.2 mA cm^{-2}, respectively (**Figure 6.2d**). Upon recharging, the HSS Na-O$_2$ cell with bare Na anode can be charged at 0.1 mA cm^{-2} with an adequate Coulombic efficiency of 93.8 %. However, the HSS Na-O$_2$ cell with bare Na anode still encountered short-circuit at a current density of 0.2 mA cm^{-2} because of the accelerated Na dendrite growth during charging (insert in **Figure 6.2d**). The implementation of SSE enhanced the electrochemical performance of Na-O$_2$ cells to some extend but not yet to the practical level. Efforts to further address the Na dendrite formation issue in HSS Na-O$_2$ batteries are required.

Taking the advantage of CP as a 3D electronic conductive matrix to accommodate Na deposition, HSS Na-O$_2$ cells utilizing SSE and CP protected Na anode demonstrated significantly improved electrochemical performance. High initial discharge capacities of 5.15 and 4.21 mAh cm^{-2} were delivered at 0.1 and 0.2 mA cm^{-2}, respectively, which were more than twice of the LE cell (**Figure 6.2e**). Moreover, the introduction of SSE can significantly decrease the reversible charge capacity loss and thus high Coulombic efficiencies (CEs) of 97.6 and 93.5% can be achieved at 0.1 and 0.2 mA cm^{-2}, respectively. It should be noted that these CEs are higher than that of the LE cells with protected Na anode in our previous report.[24] The SSE obviously played important roles in enhancing the discharge capacities and improving the reversibility of the Na-O$_2$ cells. Moreover, after

disassembling the fully recharged cell, the surface of the SSE remained unchanged without observable dark dendrite spots (insert in **Figure 6.2e**). The LE infiltrated soft CP layer can compensate the roughness of SSE/Na interface and facilitate even ion flux; and the 3D CP matrix provided buffer for accommodating dendrite-free Na deposition (**Figure S6.4**).[24] The effectiveness of Na anode protection in preventing the dendrites induced short circuit was also demonstrated by the extended cycle life and stable voltage profiles of Na symmetric cells (**Figure S6.5-6.6**). Noted that similar initial spike of potential during the charge process can be clearly observed for three types of Na-O$_2$ cells, despite of the distinct discharge/charge behaviors (**Figure 6.2c-e**). The initial increase of charge overpotential can be correlated to the formation of carbonate-based side products at the outshell shell of the NaO$_2$ cubes due to the instability of organic electrolyte, which acts as an initial barrier for the reversible decomposition of NaO$_2$.[46, 47]

To further validate the synergistic effect of SSE and protected Na anode, long term cycling performance of LE and HSS Na-O$_2$ cells were compared at 0.2 mA cm^{-2} with a cut-off capacity of 0.2 mAh cm^{-2} (**Figure 6.2f**). Using one layer of CP (1CP) as cathode, the HSS Na-O$_2$ cell with protected Na anode maintained stable cycling for over 90 cycles with a high CE, whereas the charge voltage of the HSS Na-O$_2$ cell with bare Na encountered sudden drops due to the dendrite penetration and failed to cycle beyond 35 times. The Na dendrite growth problem was even more severe in LE cell, which soon experienced dendrite caused short-circuit at the 19th cycle (**Figure S6.7**). The CP modification on Na anode played an effective role in preventing the cell short circuit and extending the cycle life of HSS Na-O$_2$ cells. In addition, the conductive CP modification on Na anode significantly reduced the discharge/charge overpotential of the Na-O$_2$ cell (**Figure 6.2g-h**). The discharge/charge voltage profile of the LE Na-O$_2$ cell was subjected to continuously enlarging polarization, presumably, due to Na degradation by O$_2$/O$_2^-$ crossover (**Figure S6.7**).[24] In contrast, the voltage profiles of the HSS Na-O$_2$ batteries with CP protected Na anode remained stable over the cycling duration (**Figure 6.2f**), indicating unchanged internal cell resistance.

In addition to the dendrite-induced short-circuit and Na anode degradation, insufficient cathode can be another limiting factor for the Na-O$_2$ cycle life. To further clarify the origin

failure for the HSS Na-O$_2$ cell with the protected Na anode, another cell with extra cathode loading [two layers of CP (2CP) instead of 1CP as the cathode] was tested. Interestingly, we found that the cell with the 2CP cathode significantly extended the cycle life to over 160 cycles with stable performance (**Figure 6.2f**), compared with 90 cycles for the cell with the 1CP cathode. Evidently, it was the cathode (CP) rather than the anode (protected Na) that limited the cycle life of Na-O$_2$ batteries. By investigating the morphological changes of the CP cathode at different cycles, it can be clearly observed that the surface of the air electrode was gradually covered by side products upon cycling (**Figure S6.8**). We can conclude that the gradual shielding of active sites by accumulated side products can be the intermediate cause of the increased discharge-charge overpotentials after 70 cycles and the limited cycle life of the Na-O$_2$ cell with the 1CP cathode (**Figure 6.2f-i**). Presumably, the decomposition of the ether electrolyte against superoxide and the reaction between the CP cathode and reactive discharge product(s) led to the formation of side products. Note that the constructed HSS Na-O$_2$ cells exhibit one of the best electrochemical performances among all the superoxide-based Na-O$_2$ batteries that use the same CP cathode (**Table S6.1**). It can be expected that the cycle life of HSS Na-O$_2$ cells with the protected Na anode can further achieve even longer cycle life using an advanced air electrode.

The chemical composition and morphology of the discharge product at the cathode of the HSS Na-O$_2$ cell were characterized at the fully discharged state at 0.1 mA cm^{-2}. As shown in **Figure S6.9**, the discharge product of HSS Na-O$_2$ cell was typical cubic-shaped NaO$_2$, based on SEM, XRD and Raman characterizations. The morphological evolution of the discharge product (NaO$_2$) in the HSS Na-O$_2$ cells was further explored at different discharge capacities, as shown in **Figure S6.10**. A few NaO$_2$ cubes and many discreet nuclei were observed on the carbon fiber surface at low discharge capacity of 0.2 mAh cm^{-2} (**Figure S6.10a** and **b**). When the cell was discharged to 0.5 mAh cm^{-2}, the discreet nuclei evolved into cubic-shaped particles, and at the same time, new NaO$_2$ nuclei precipitate on the surface of carbon fiber. This process proceeded with increasing discharge capacity, and thus increasing the size and the density of the NaO$_2$ cubes (**Figure S6.10c** and **d**). At a large discharge capacity of 3 mAh cm^{-2}, the neighboring NaO$_2$ cubes merged and gradually covered up the carbon fiber surface (**Figure S6.10e**). The oxygen reduction reaction of the

HSS Na-O$_2$ cell terminates when the pores on the oxygen side of the air electrode was fully blocked, which is known as the pore-clogging effect (**Figure S6.10f**).
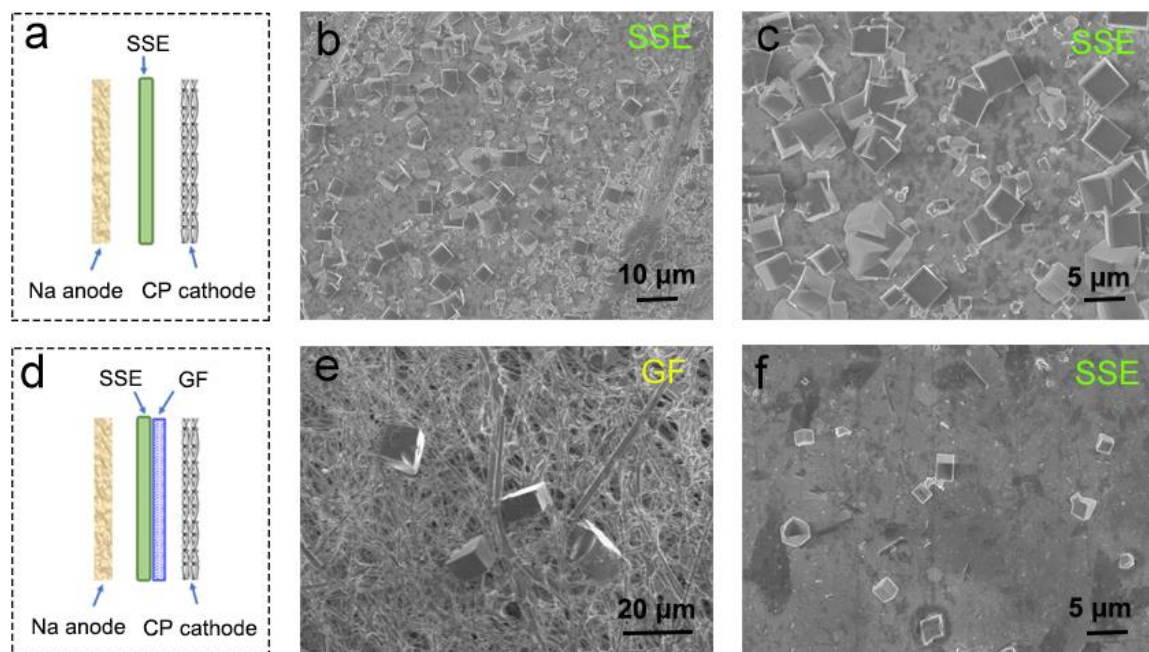
Figure 6.3 (a) The schematic diagram of HSS Na-O$_2$ cell with SSE and (b and c) corresponding SEM images of the SSE surface (cathode side) after discharging for 50 h at 0.1 mA cm^{-2}. (d) The schematic diagram of the HSS Na-O$_2$ cell with SSE and additional GF separator; corresponding SEM images of (e) GF and (f) SSE after discharging for 50h at 0.1 mA cm^{-2}.

The solution-based mechanism for the formation of NaO$_2$ in Na-O$_2$ batteries have been widely accepted, and it has been reported that the Na metal in the cell environment directly or indirectly contributed to the migration of O$_2^-$ from the cathode to the anode.[23] To demonstrate the effect of SSE in blocking the crossover of O$_2^-$, the morphological characterization of the SSE in different cell configurations was conducted (**Figure 6.3**). The SSE pellet has a dense structure without obvious pores (**Figure S6.11**). After the HSS Na-O$_2$ cell was discharged for 50 h at 0.1 mA cm^{-2}, numerous NaO$_2$ cubes sized approximately 1-5 μm were deposit on the SSE surface towards the air electrode (**Figure 6.3b-c** and **Figure S6.12**). The randomly distributed indentations were due to the attachment of carbon fibers on the SSE (**Figure 6.3b**). Since electrochemical reactions

require access to both Na^+ ions and electrons, the electrochemical formation of NaO_2 would not occur on the insulating GF separator. With an additional piece of GF separator placed between SSE and cathode (**Figure 6.3d**), we can distinguish the diffusion products from the reaction products. Corresponding SEM images of the GF separator and the SSE obtained at the fully discharged state are shown in **Figure 6.3e, f** and **Figure S6.13**. Interestingly, crystalline NaO_2 were observed on the surface of both the GF and the SSE. These NaO_2 on SSE were diffusion products from the CP cathode. The GF separator and LE are obviously permeable to dissolved O_2^- intermediate, leading to O_2^- crossover.

Taking a closer look into the NaO_2 products at different locations, their morphologies were significantly different. The NaO_2 cubes on the GF separator were as large as 20 μm, while a few discrete NaO_2 cubes with a much smaller size (~2 μm) was observed on SSE, which also differed from the NaO_2 cubes observed on the SSE without GF separation. This can be explained by the concentration difference of the O_2^-–Na^+ species in the organic electrolyte as well as the rate of nucleation and diffusion of $(O_2^-$–$Na^+)_n$ onto SSE versus GF separator. When the CP cathode was in direct contact with the SSE in the HSS Na-O_2 cell (**Figure 6.3a**), the concentration of the soluble O_2^-–Na^+ could quickly build up on the SSE surface as the dense structure of SSE terminated the passage of the O_2^- species, while the interface with CP was still accessible to electrons. The high nucleation rate led to a high concentration of NaO_2 nuclei at the SSE/CP interface, where the NaO_2 nuclei grew larger in size upon increasing discharge capacities. In another cell configuration with an extra GF layer, the O_2^- concentration at the cathode side of GF separator presciently reached saturation and initiated nucleation of NaO_2 on the GF. Subsequently, the soluble O_2^- anions diffused across the GF layer under dual effects of ion concentration gradient and electric field. Therefore, the NaO_2 nucleation kinetics on the GF was low; at the same time, continuous growth of NaO_2 particulates occurred preferentially at the existing NaO_2 nuclei. The resulting NaO_2 particles on the GF were thus scattered and large in size. On the other hand, the precipitation of NaO_2 on the GF separator still diluted the amount of NaO_2 accumulation on the SSE. This explains the observation of less NaO_2 cubes with smaller size on the SSE compared with that of the HSS Na-O_2 cell in **Figure 6.3c**. Noted that NaO_2 cubes cannot be observed on the SSE surface towards the negative electrode due to the shielding effect of SSE towards O_2^- crossover.
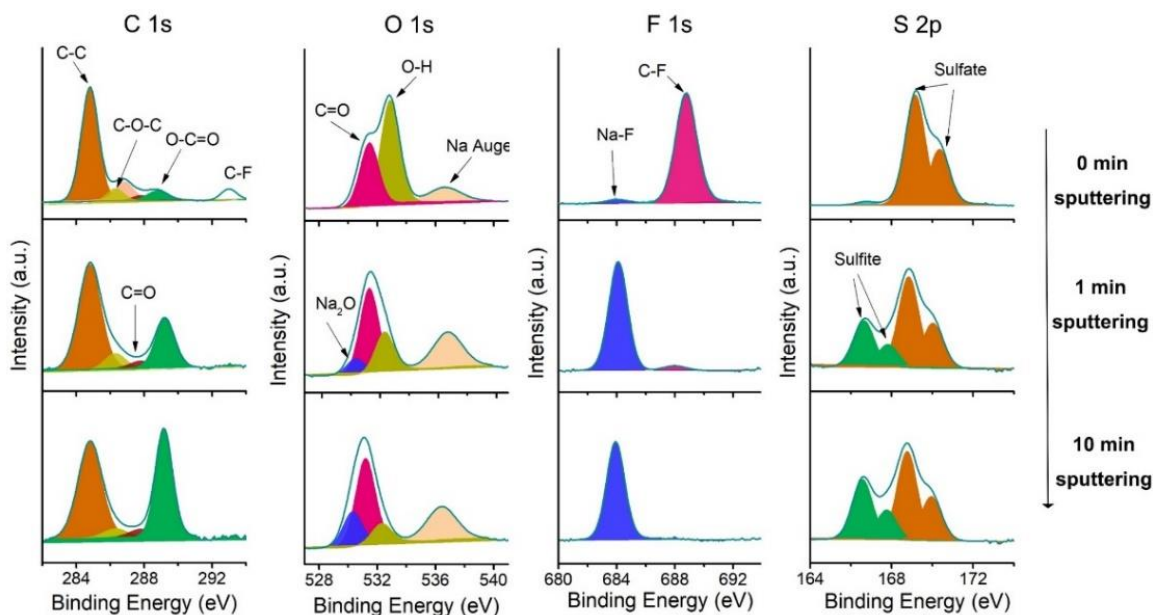
Figure 6.4 XPS characterization of the Na anode SEI layer formed in the LE Na-O$_2$ cell in the presence of O$_2$/O$_2^-$ crossover.

In addition to the O$_2^-$ crossover suppressing characteristic of the SSE, its chemical stability against the highly reactive NaO$_2$ is also very important for high performance HSS Na-O$_2$ batteries. While the apparent accumulation of NaO$_2$ on the SSE readily proofed their stability with each other, XRD and Raman characterizations were also conducted before and after the full recharge of the HSS Na-O$_2$ cells at 0.1 mA cm^{-2} to confirm. The Na$_{3.25}$Zr$_2$Si$_{2.25}$P$_{0.75}$O$_{12}$ phase was well maintained after recharging, indicating the excellent chemical stability of the SSE towards the highly oxidative NaO$_2$ (**Figure S6.14**).

However, as a strong oxidant, O$_2^-$ can easily react with Na anode, resulting in continuous O$_2^-$ crossover and serious Na degradation [23]. To systematically elucidating the O$_2$/O$_2^-$ crossover-induced Na degradation mechanism, X-ray photoelectron spectroscopy (XPS) analyses with depth profiling were conducted on Na metal anode. The LE Na-O$_2$ cell with porous separator was disassembled after discharging for 12 h at 0.1 mA cm^{-2} to examine the SEI compositions on the Na anode surface. **Figure 6.4** shows the XPS spectra of C 1s, O 1s, S 2p and F 1s. At 0 min of sputtering, the peaks at 284.8, 286.7 and 288.8 eV in the C 1s spectrum can be assigned to the presence of C-C/C-H, C-O and O-C=O, respectively, as a result of DEGDME solvent decomposition.[48] At the same time, the O 1s spectrum

shows the characteristic peaks of Na_2CO_3 and NaOH at 531.3 and 532.8 eV, respectively.[21] The F 1s feature at 688.7 eV (C-F) and the S $2p_{3/2}$ peak at 168.6 eV (SO_4^{2-}) were likely resulted from the decomposition of the $NaSO_3CF_3$ salt. Combining these information, we can deduce that the top surface of the anode SEI film mainly composed of inorganic (NaOH, Na_2CO_3, and Na_2SO_4) and organic (RCOONa, CF_x et. al) components for the discharged LE Na-O_2 cell. After 1 min of sputtering, the O, F, and S peaks corresponding to inorganic Na_2O (530.9 eV), NaF (683.8 eV), and Na_2SO_3 (166.6 and 167.7 eV) emerged, and remained distinct after 10 min of sputtering. Meanwhile, the O-C=O peak corresponding to the organic reduction product ROCOONa became stronger after 10 min of sputtering, suggesting a higher content in the depth . Overall, the SEI layer composed of both organic and inorganic components across the depth from the top surface to the interior, with a changing composition. Notably, Na_2CO_3 contributed to a large proportion across the depth of SEI layer; the NaOH component also penetrated throughout the SEI layer but showed a reducing amount towards the interior.
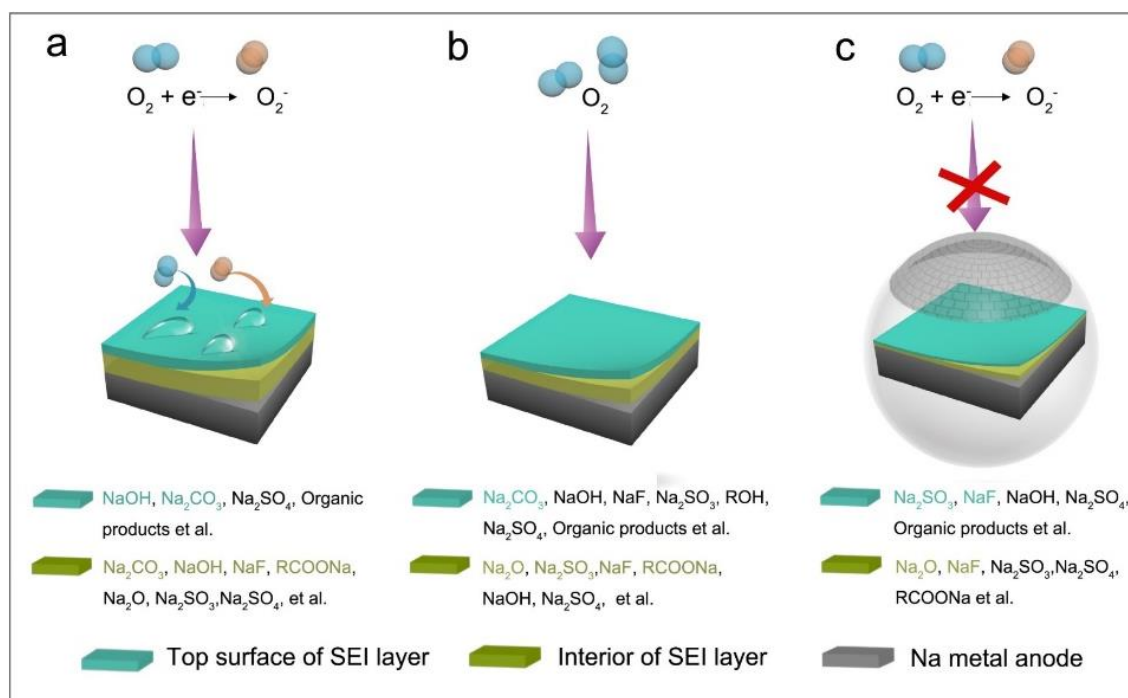
Figure 6.5 Schematic illustration of the SEI formation on the Na metal surface in the presence of (a) O_2/O_2^- crossover, (b) O_2 crossover and (c) in the absence of O_2/O_2^- crossover.

To distinguish between the effects of O_2 versus O_2^- crossovers, another LE Na-O_2 cell was rested in an O_2 atmosphere for 12 h without discharging. In this case, NaO_2 was not generated, so the SEI formation on the Na anode surface was mainly affected by O_2 crossover in the absent of O_2^-. As shown in **Figure S6.15**, the evolution of RCOONa, Na_2O, NaF, NaOH, and sulfate compositions in the SEI were consistent with those in the SEI of the discharged LE Na-O_2 cell. The SEI also contained both the organic and inorganic components. However, the relative concentration of NaOH and Na_2CO_3 on the top surface of the SEI layers varied in two cases. In the presence of both O_2 and O_2^- crossover, the NaOH component rather than Na_2CO_3 dominated the superficial SEI; however, the Na_2CO_3 component was more pronounced in the case of only O_2 crossover. Additionally, different from the case of the discharged SEI in which the NaF and sulfite were not observable at 0 min of sputtering, characteristic XPS peaks for sulfite and NaF species were clearly observed on the top SEI surface when formed at rest with O_2, indicating a relative thinner top SEI surface.

In fact, the anode SEI layer of the HSS Na-O_2 cell was distinct from the LE cell when the O_2/O_2^- crossover was inhibited (**Figure S6.16**). At 0 minute of sputtering, the peak corresponding to NaF was observed as well as the peaks for sulfite species. After sputtering for 1 and 10 min, the peaks for NaOH and Na_2CO_3 essentially faded, while the Na_2O and NaF peaks became the dominating feature in the interior SEI. The interior SEI composition was particularly favorable as protective inorganic SEI layer for Na anode. In addition, the weaker peak intensities of the S 2p and F 1s spectra may indicate less decomposition of $NaSO_3CF_3$ in the HSS Na-O_2 cell compared with that in LE Na-O_2 cell.

By comparison, with or without O_2 and/or O_2^- crossovers made a significant difference in the Na anode SEI formation in Na-O_2 battery system (**Figure 6.5**). Like Li- and K-O_2 batteries, the crossover of O_2 in the Na-O_2 batteries also contributes to the decomposition of electrolyte and the subsequent formation of NaOH and Na_2CO_3 on the Na anode. Compared to O_2, the highly reactive O_2^- can induce intensified side reactions, causing of not only corrosion of the Na metal anode but also severe decomposition of the electrolyte. As an evidence, the SO_4^{2-} species on the top surface of the SEI layer may be resulted from the further oxidation of SO_3^{2-} by the migrated O_2/O_2^-, while some SO_3^{2-} still remained in

the interior SEI. Moreover, the presence of organic products throughout the anode SEI layer in the LE Na-O$_2$ cell can lead to a loose SEI structure (**Figure 6.5a** and **b**), which is permeable to O$_2$/O$_2^-$ and electrolyte. Hence, electrolyte decomposition and SEI layer growth could occur continuously. The consequently increase of cell internal resistance can deteriorate the cell performance. We postulate that the restricted performance and the premature cell death of LE Na-O$_2$ cells arise from the crossover of O$_2$/O$_2^-$. However, by implementing the SSE, the O$_2$/O$_2^-$ crossover can be inhibited along with the formation of an inorganic NaF protective layer (**Figure 6.5c** and **S6.15**). This could be a reason for the stable charge/discharge overpotential of HSS Na-O$_2$ cell when cathode was sufficient (**Figure 6.2f**). Therefore, controlling the O$_2$/O$_2^-$ crossover to the Na anode surface by a highly stable SSE can be an effective strategy for achieving good performance of superoxide-based Na-O$_2$ batteries.

6.4 Conclusion

In summary, we successfully constructed a HSS Na-O$_2$ battery free of Na dendrites and oxygen species crossover by coupling a NASICON SSE and a protected Na anode. The SSE functions as a shield to the O$_2$/O$_2^-$ migrations and eliminates detrimental side reactions on the Na anode surface. The carbon paper modified Na anode complementarily addressed the Na dendrite growth issues. Moreover, the SEI formation on Na anode in relation to O$_2$/O$_2^-$ crossover is systematically analyzed by XPS with depth profile, revealing a favorable NaF-rich inorganic SEI enabled by the SSE shielding of O$_2$/O$_2^-$. Although more future work will be needed to make Na-O$_2$ battery system commercially viable, the results presented here provide valuable guidance for fabricating advanced Na-O$_2$ batteries with longer lifespans and better cycling performance.

6.5 Acknowledgments

6.6   Reference

1. Peng, Z.; Freunberger, S. A.; Chen, Y.; Bruce, P. G., *Science* **2012,** 337, (6094), 563-566.

2. Lu, J.; Lei, Y.; Lau, K. C.; Luo, X.; Du, P.; Wen, J.; Assary, R. S.; Das, U.; Miller, D. J.; Elam, J. W.; Albishri, H. M.; El-Hady, D. A.; Sun, Y.-K.; Curtiss, L. A.; Amine, K., *Nature Communications* **2013,** 4, 2383.

3. Khajehbashi, S. M. B.; Li, J.; Wang, M.; Xu, L.; Zhao, K.; Wei, Q.; Shi, C.; Tang, C.; Huang, L.; Wang, Z.; Mai, L., *Energy Technology* **2017,** 5, (4), 568-579.

4. Jian, Z.; Liu, P.; Li, F.; He, P.; Guo, X.; Chen, M.; Zhou, H., *Angewandte Chemie International Edition* **2014,** 53, (2), 442-446.

5. Wang, Y.-J.; Fang, B.; Zhang, D.; Li, A.; Wilkinson, D. P.; Ignaszak, A.; Zhang, L.; Zhang, J., *Electrochemical Energy Reviews* **2018,** 1, (1), 1-34.

6. Bruce, P. G.; Freunberger, S. A.; Hardwick, L. J.; Tarascon, J.-M., *Nat Mater* **2012,** 11, (1), 19-29.

7. Wei, Q.; Tan, S.; Liu, X.; Yan, M.; Wang, F.; Li, Q.; An, Q.; Sun, R.; Zhao, K.; Wu, H.; Mai, L., *Advanced Functional Materials* **2015,** 25, (12), 1773-1779.

8. Yadegari, H.; Norouzi Banis, M.; Lushington, A.; Sun, Q.; Li, R.; Sham, T.-K.; Sun, X., *Energy & Environmental Science* **2017,** 10, (1), 286-295.

9. Zhao, C.; Yu, C.; Banis, M. N.; Sun, Q.; Zhang, M.; Li, X.; Liu, Y.; Zhao, Y.; Huang, H.; Li, S.; Han, X.; Xiao, B.; Song, Z.; Li, R.; Qiu, J.; Sun, X., *Nano Energy* **2017,** 34, 399-407.

10. Zhang, Y.; Li, X.; Zhang, M.; Liao, S.; Dong, P.; Xiao, J.; Zhang, Y.; Zeng, X., *Ceramics International* **2017,** 43, (16), 14082-14089.

11. Hartmann, P.; Bender, C. L.; Vračar, M.; Dürr, A. K.; Garsuch, A.; Janek, J.; Adelhelm, P., *Nat Mater* **2013,** 12, (3), 228-232.

12. Bing, S.; Katja, K.; Xiuqiang, X.; Paul, M.; Zhangquan, P.; Guoxiu, W., *Advanced Materials* **2017,** 29, (48), 1606816.

13. Bender, C. L.; Hartmann, P.; Vračar, M.; Adelhelm, P.; Janek, J., *Advanced Energy Materials* **2014,** 4, (12), 1301863.

14. Yadegari, H.; Sun, Q.; Sun, X., *Advanced Materials* **2016,** 28, (33), 7065-7093.

15. Yadegari, H.; Sun, X., *Accounts of Chemical Research* **2018,** 51, (6), 1532-1540.

16. Assary, R. S.; Lu, J.; Du, P.; Luo , X.; Zhang, X.; Ren, Y.; Curtiss, L. A.; Amine, K., *ChemSusChem* **2013,** 6, (1), 51-55.

17. Shui, J.-L.; Okasinski, J. S.; Kenesei, P.; Dobbs, H. A.; Zhao, D.; Almer, J. D.; Liu, D.-J., **2013,** 4, 2255.

18. Ren, X.; Lau, K. C.; Yu, M.; Bi, X.; Kreidler, E.; Curtiss, L. A.; Wu, Y., *ACS Applied Materials & Interfaces* **2014,** 6, (21), 19299-19307.

19. Marinaro, M.; Balasubramanian, P.; Gucciardi, E.; Theil, S.; Jörissen, L.; Wohlfahrt-Mehrens, M., *ChemSusChem* **2015,** 8, (18), 3139-3145.

20. Kraytsberg, A.; Ein-Eli, Y., *J Power Sources* **2011,** 196.

21. Bi, X.; Ren, X.; Huang, Z.; Yu, M.; Kreidler, E.; Wu, Y., *Chemical Communications* **2015,** 51, (36), 7665-7668.

22. Wu, S.; Qiao, Y.; Jiang, K.; He, Y.; Guo, S.; Zhou, H., *Advanced Functional Materials* **2018,** 28, (13), 1706374.

23. Liu, C.; Carboni, M.; Brant, W. R.; Pan, R.; Hedman, J.; Zhu, J.; Gustafsson, T.; Younesi, R., *ACS Applied Materials & Interfaces* **2018**, 10-13534-13541.

24. Xiaoting, L.; Qian, S.; Hossein, Y.; Xiaofei, Y.; Yang, Z.; Changhong, W.; Jianneng, L.; Alicia, K.; Ruying, L.; Xueliang, S., *Advanced Functional Materials* 2018, (28), 1801904.

25. Xia, C.; Black, R.; Fernandes, R.; Adams, B.; Nazar, L. F., *Nat Chem* **2015,** 7, (6), 496-501.

26. Xia, C.; Fernandes, R.; Cho, F. H.; Sudhakar, N.; Buonacorsi, B.; Walker, S.; Xu, M.; Baugh, J.; Nazar, L. F., *Journal of the American Chemical Society* **2016,** 138, (35), 11219-11226.

27. Ma, S.; McKee, W. C.; Wang, J.; Guo, L.; Jansen, M.; Xu, Y.; Peng, Z., M *Physical Chemistry Chemical Physics* **2017,** 19, (19), 12375-12383.

28. Lee, H.; Lee, D. J.; Lee, J.-N.; Song, J.; Lee, Y.; Ryou, M.-H.; Park, J.-K.; Lee, Y. M., *Electrochimica Acta* **2014,** 123, 419-425.

29. Li, N.; Xu, D.; Bao, D.; Ma, J.; Zhang, X., *Chinese Journal of Catalysis* **2016,** 37, (7), 1172-1179.

30. Zhao, N.; Guo, X., *The Journal of Physical Chemistry C* **2015,** 119, (45), 25319-25326.

31. Kim, J.; Lim, H.-D.; Gwon, H.; Kang, K., *Physical Chemistry Chemical Physics* **2013,** 15, (10), 3623-3629.

32. Hartmann, P.; Bender, C. L.; Sann, J.; Durr, A. K.; Jansen, M.; Janek, J.; Adelhelm, P., *Physical Chemistry Chemical Physics* **2013,** 15, (28), 11661-11672.

33. Sun, Q.; Lin, X.; Yadegari, H.; Xiao, W.; Zhao, Y.; Adair, K. R.; Li, R.; Sun, X., *Journal of Materials Chemistry A* **2018,** 6, (4), 1473-1484.

34. Yadegari, H.; Franko, C. J.; Banis, M. N.; Sun, Q.; Li, R.; Goward, G. R.; Sun, X., *The Journal of Physical Chemistry Letters* **2017,** 8, (19), 4794-4800.

35. Yadegari, H.; Norouzi Banis, M.; Lin, X.; Koo, A.; Li, R.; Sun, X., *Chemistry of Materials* **2018,** 30, (15), 5156-5160.

36. Black, R.; Shyamsunder, A.; Adeli, P.; Kundu, D.; Murphy, G. K.; Nazar, L. F., *ChemSusChem* **2016,** 9, (14), 1795-1803.

37. chuanchao, S.; Fengjiao, Y.; Yuping, W.; Zhangquan, P.; Yuhui, C., *Angewandte Chemie* 2018, 57, 9906-9910.

38. Cheon, J. Y.; Kim, K.; Sa, Y. J.; Sahgong, S. H.; Hong, Y.; Woo, J.; Yim, S.-D.; Jeong, H. Y.; Kim, Y.; Joo, S. H., *Advanced Energy Materials* **2016,** 6, (7), 1501794.

39. Khan, Z.; Senthilkumar, B.; Park, S. O.; Park, S.; Yang, J.; Lee, J. H.; Song, H.-K.; Kim, Y.; Kwak, S. K.; Ko, H., *Journal of Materials Chemistry A* **2017,** 5, (5), 2037-2044.

40. Ma, J. L.; Yin, Y. B.; Liu, T.; Zhang, X. B.; Yan, J. M.; Jiang, Q., *Advanced Functional Materials* **2018,** 28, (13), 1703931.

41. Bing, S.; Peng, L.; Jinqiang, Z.; Dan, W.; Paul, M.; Chengyin, W.; L., N. P. H.; Guoxiu, W., *Advanced Materials* 2018, (30), 1801334.

42. Zhou, W.; Li, Y.; Xin, S.; Goodenough, J. B., *ACS Central Science* **2017,** 3, (1), 52-57.

43. Park, H.; Jung, K.; Nezafati, M.; Kim, C.-S.; Kang, B., *ACS Applied Materials & Interfaces* **2016,** 8, (41), 27814-27824.

44. Wu, Y.; Qiu, X.; Liang, F.; Zhang, Q.; Koo, A.; Dai, Y.; Lei, Y.; Sun, X., *Applied Catalysis B: Environmental* **2019,** 241, 407-414.

45. Medenbach, L.; Bender, C. L.; Haas, R.; Mogwitz, B.; Pompe, C.; Adelhelm, P.; Schröder, D.; Janek, J., *Energy Technology* **2017,** 5, (12), 2265-2274.

46. Sun, Q.; Liu, J.; Xiao, B.; Wang, B.; Banis, M.; Yadegari, H.; Adair, K. R.; Li, R.; Sun, X., *Advanced Functional Materials* 2019, 1808332.

47. N. Banis, M.; Yadegari, H.; Sun, Q.; Regier, T.; Boyko, T.; Zhou, J.; Yiu, Y. M.; Li, R.; Hu, Y.; Sham, T. K.; Sun, X., *Energy & Environmental Science* **2018**, 11, 2073-2077

48. Lutz, L.; Alves Dalla Corte, D.; Tang, M.; Salager, E.; Deschamps, M.; Grimaud, A.; Johnson, L.; Bruce, P. G.; Tarascon, J.-M., *Chemistry of Materials* **2017,** 29, (14), 6066-6075.

6.7   Supporting information
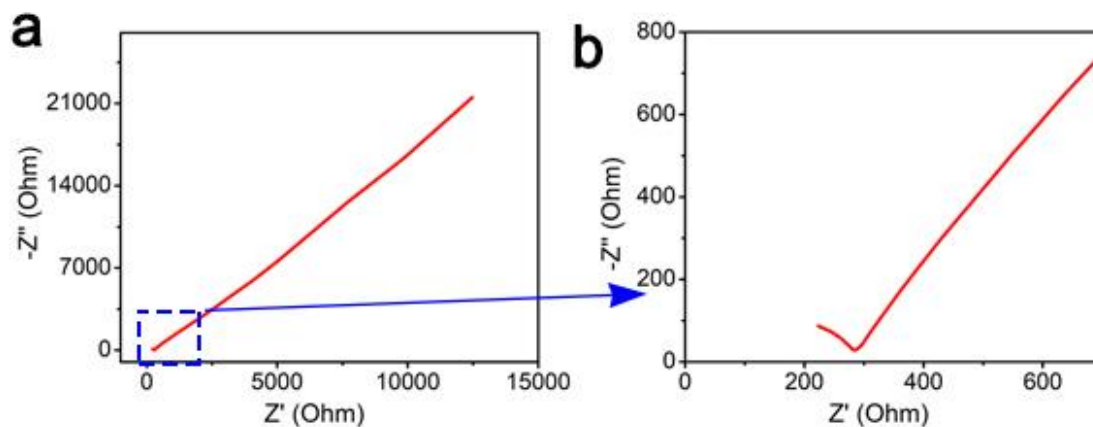
Figure   S6.1   Electrochemical   impedance   spectrum   of   the   NASICON-type $Na_{3.25}Zr_2Si_{2.25}P_{0.75}O_{12}$ solid-state   electrolyte.   The   ionic   conductivity   of   solid-state electrolyte was calculated as 1.5×10^{-3} S cm^{-1} at room temperature.
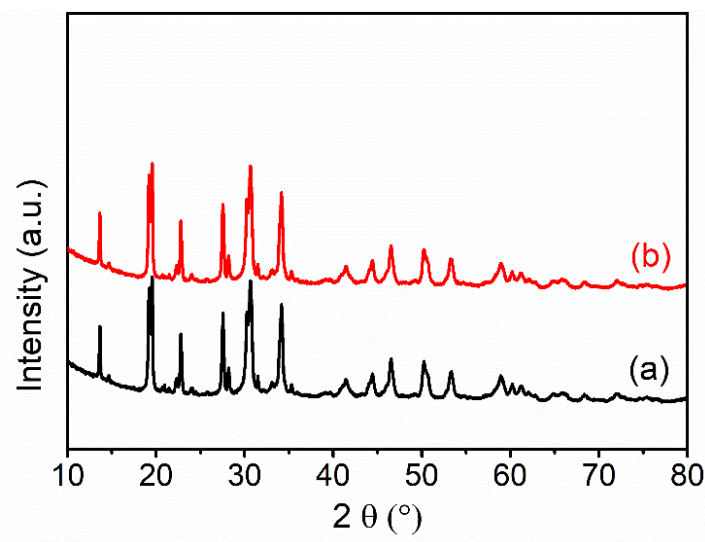
Figure S6.2 The XRD patterns of $Na_{3.25}Zr_2Si_{2.25}P_{0.75}O_{12}$ powder (a) before and (b) after contacting with Na foil for 3 months.
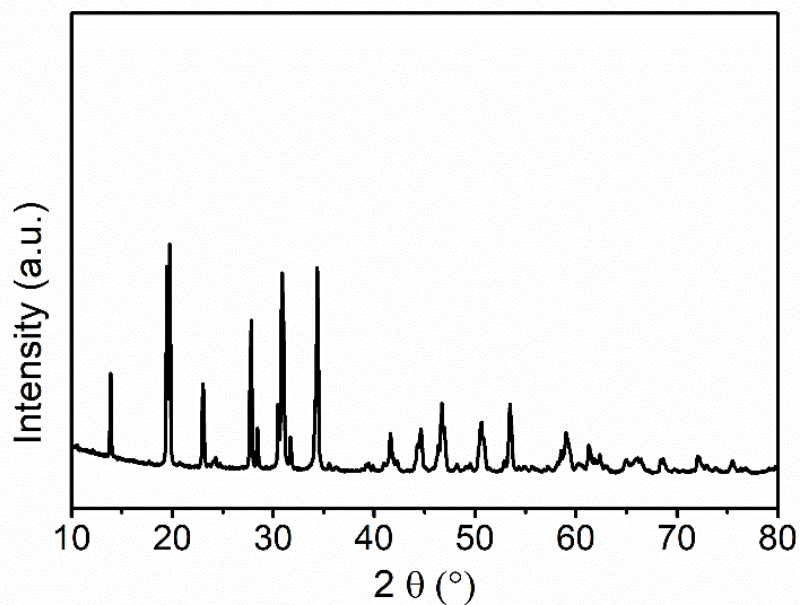
Figure S6.3 The XRD pattern of the $Na_{3.25}Zr_2Si_{2.25}P_{0.75}O_{12}$ solid-state electrolyte pellet.
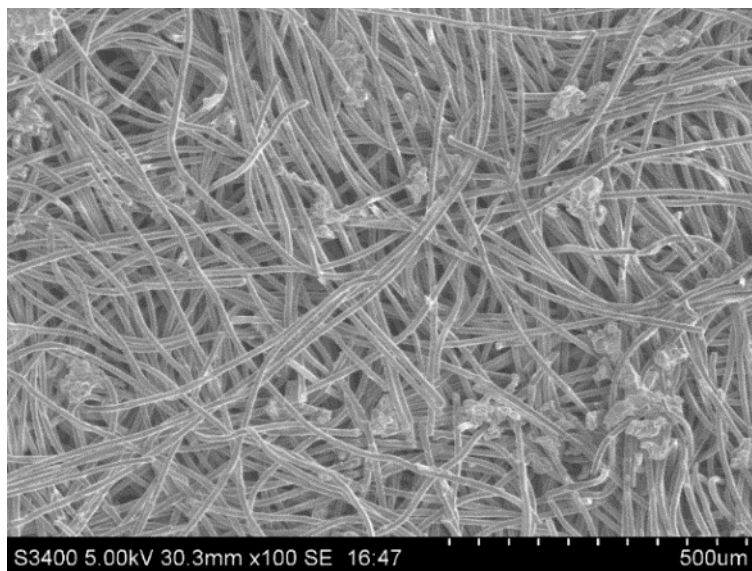
Figure S6.4 SEM image of the CP interlayer obtained from the HSS Na-O$_2$ cell after plating at 0.2 mA cm^{-2}.
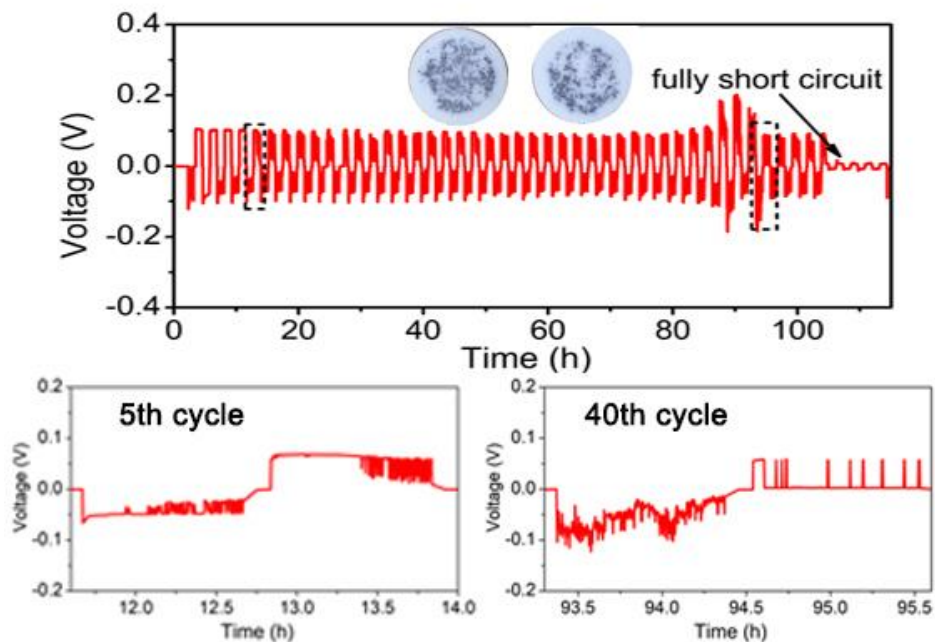
Figure S6.5 The cycling stability of the Na/NASICON/Na symmetric cell with trace amount of liquid electrolyte on the Na/SSE interface (0.2 mA cm^{-2}, 0.2 mAh cm^{-2}). Insets are the optical images of the two sides of the SSE after cycling.
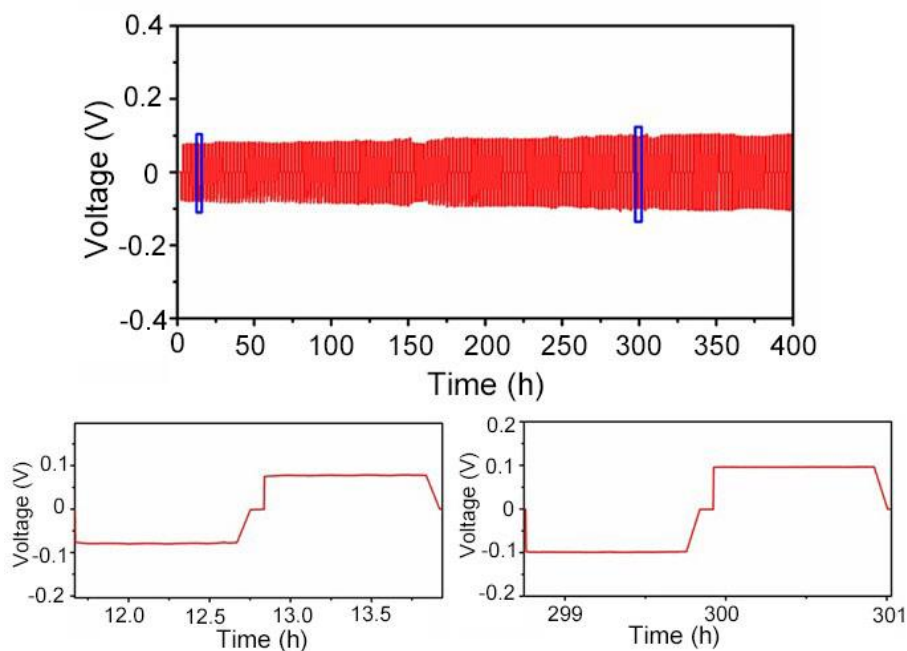
Figure S6.6 The cycling stability of the Na/NASICON/Na symmetric cell with protected Na anode (0.2 mA cm^{-2}, 0.2 mAh cm^{-2}).
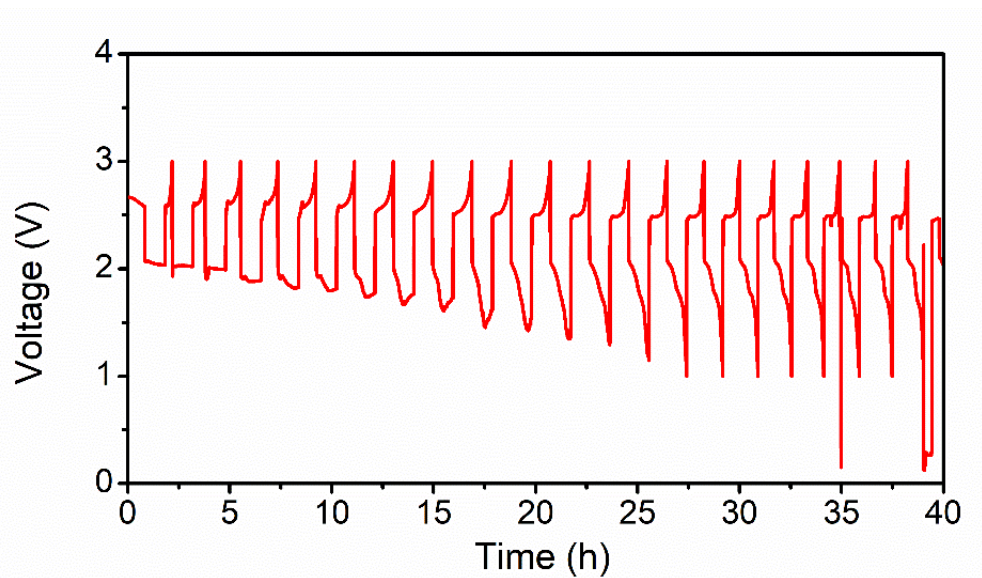
Figure S6.7 The cycling performance of the LE Na-O$_2$ cell at 0.2 mA cm^{-2} with a limited capacity of 0.2 mAh cm^{-2}.
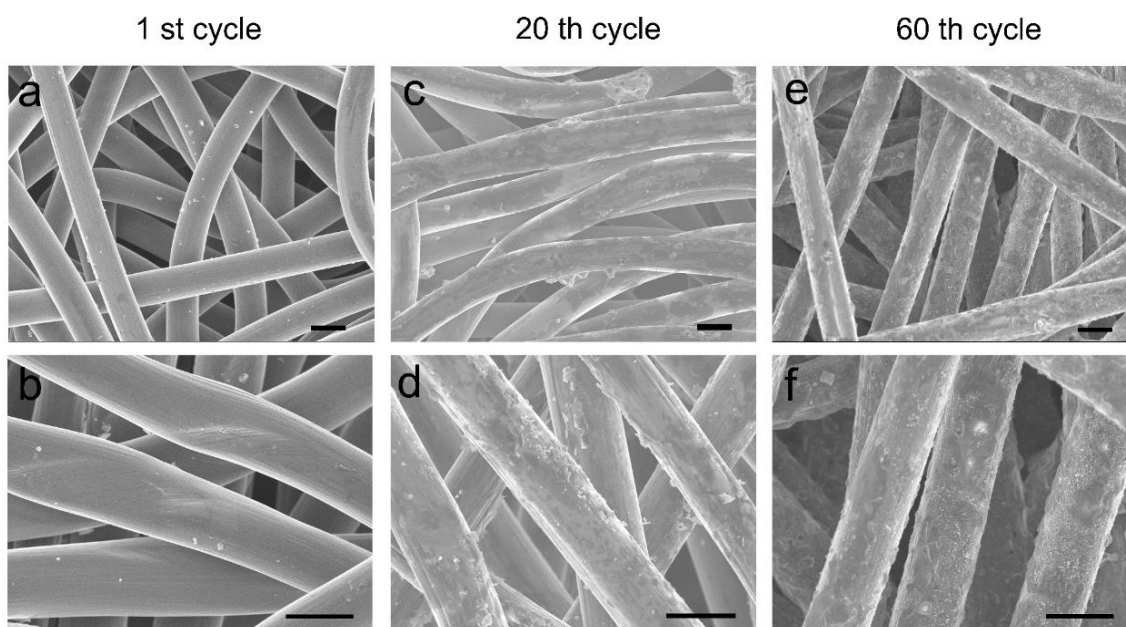
Figure S6.8 The SEM images of the CP cathodes at different magnifications after (a, b) 1st, (c, d) 20th and (e, f) 60th cycles at 0.2 mA cm^{-2} with a cutoff capacity of 0.2 mAh cm^{-2} (the scale bars in a-f represent 10 µm).
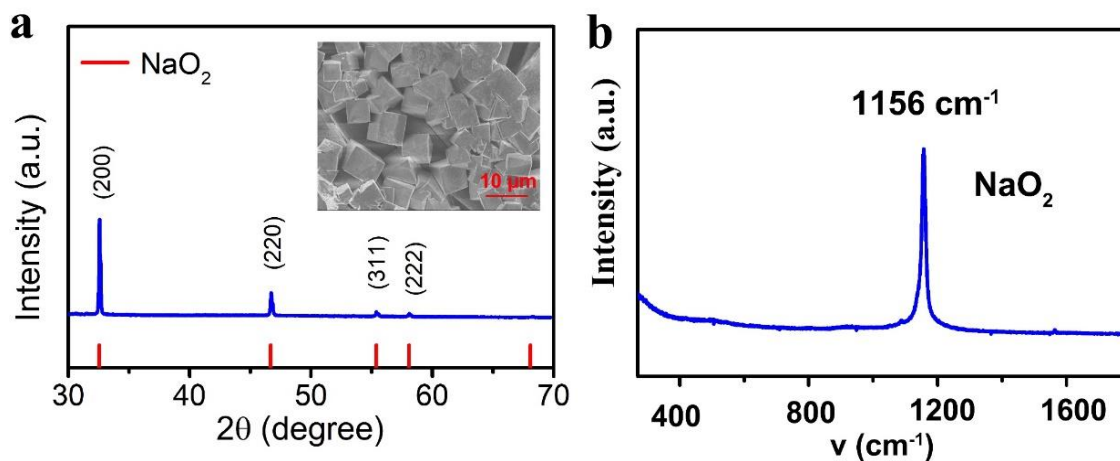
Figure S6.9 (a) The XRD pattern and (b) Raman spectrum of the discharged CP cathode obtained from a fully discharged HSS Na-O$_2$ cells at 0.1 mA cm^{-2} (insert in (a) is the SEM image of the discharged CP cathode).
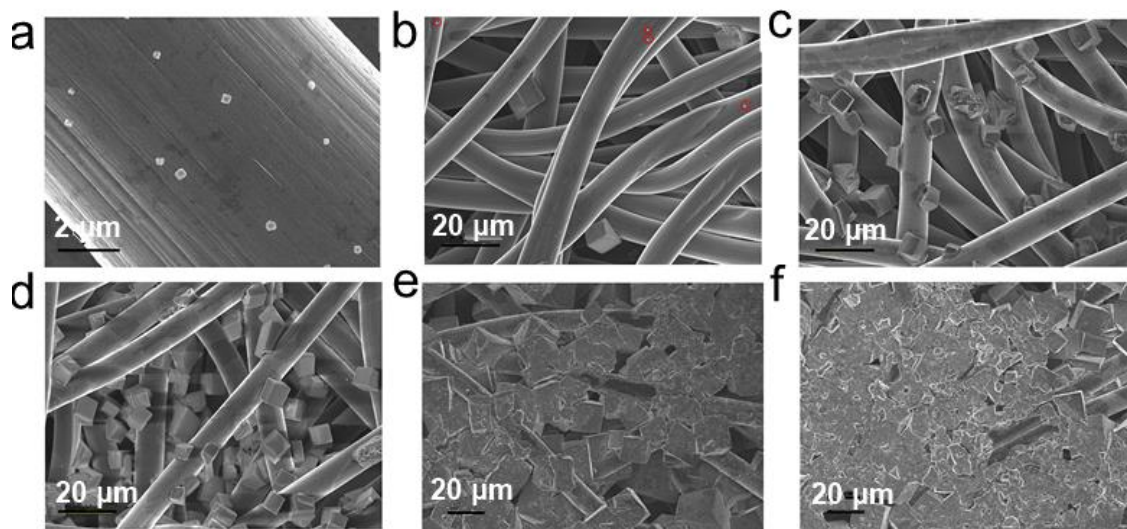
Figure S6.10 The SEM morphological evolutions of the discharge product (NaO$_2$) in the HSS Na-O$_2$ cells at 0.1 mA cm^{-2} with a discharge capacities of (a, b) 0.2 mAh cm^{-2}, (c) 0.5 mAh cm^{-2}, (d) 1.5 mAh cm^{-2}, (e) 3 mAh cm^{-2}, and (f) 5.2 mAh cm^{-2} (full discharge).
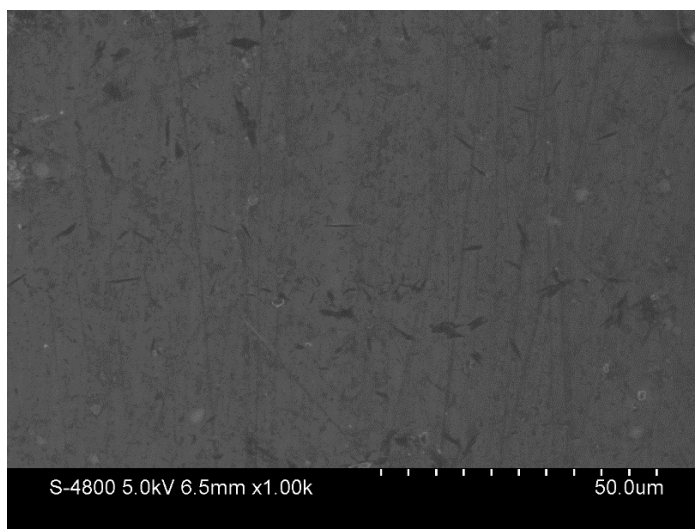
Figure S6.11 The SEM image of the pristine SSE surface.
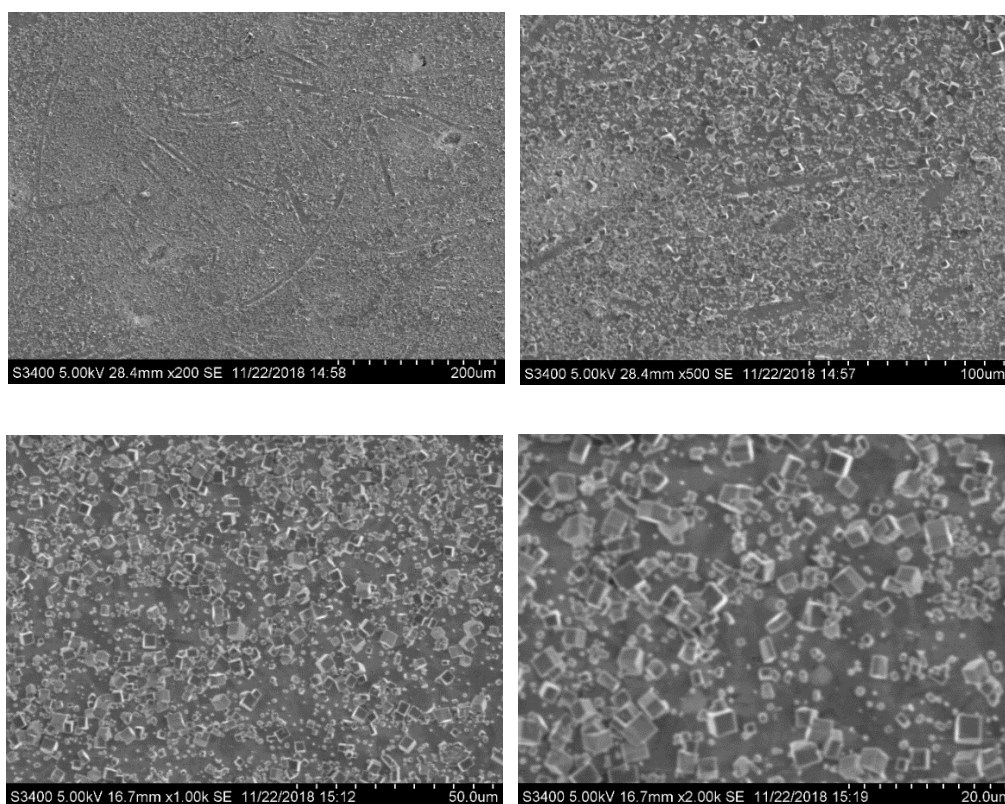
Figure S6.12 The SEM images of SSE surface (cathode side) obtained from discharged HSS Na-O$_2$ battery.
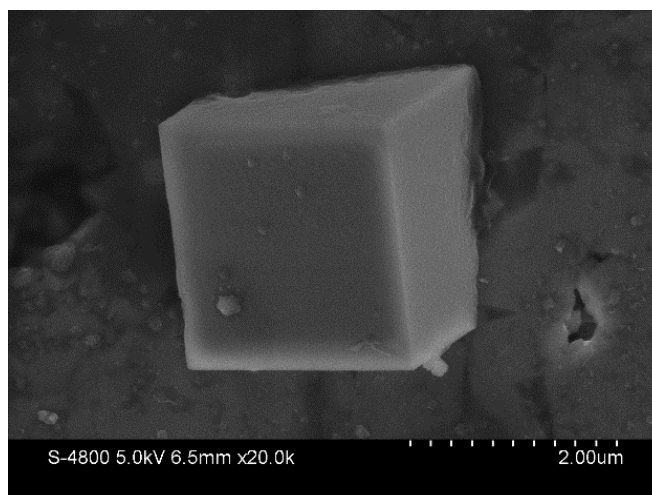
Figure 6.13 The SEM image of SSE surface obtained from discharged HSS Na-O$_2$ battery that using both SSE and GF.
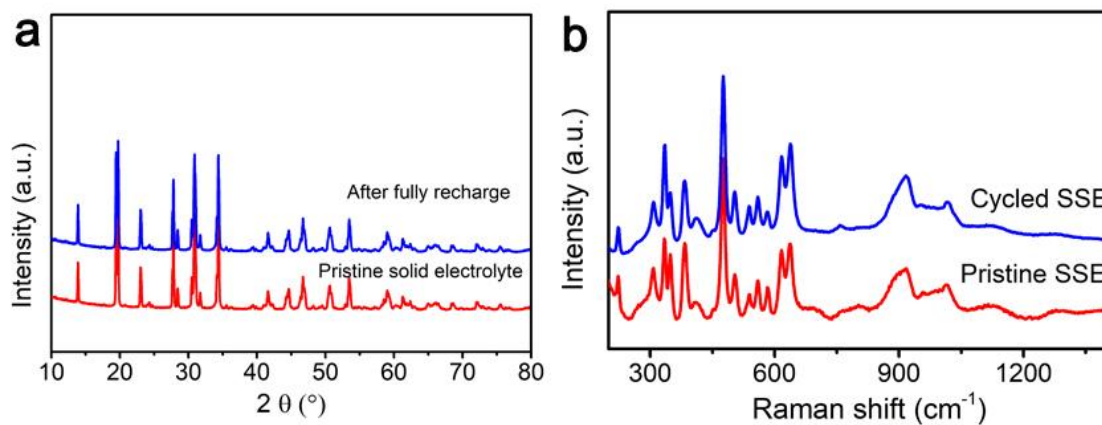
Figure S6.14 The (a) XRD patterns and (b) Raman spectra of solid electrolyte before and after the HSS Na-O$_2$ cell fully recharge at 0.1 mA cm^{-2}.
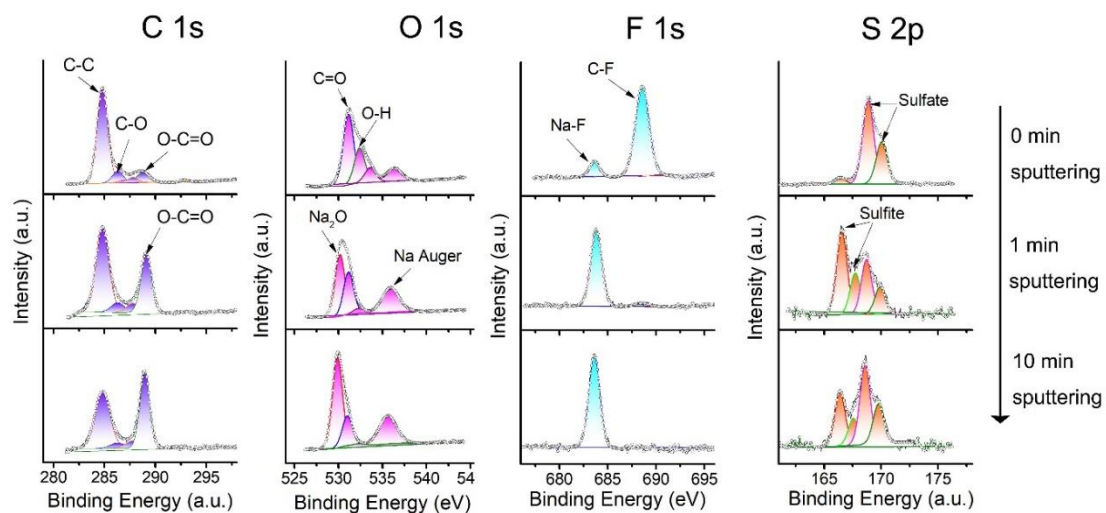
Figure S6.15 XPS characterization of the Na anode SEI layer formed in the LE Na-O₂ cell in the presence of O₂ crossover.
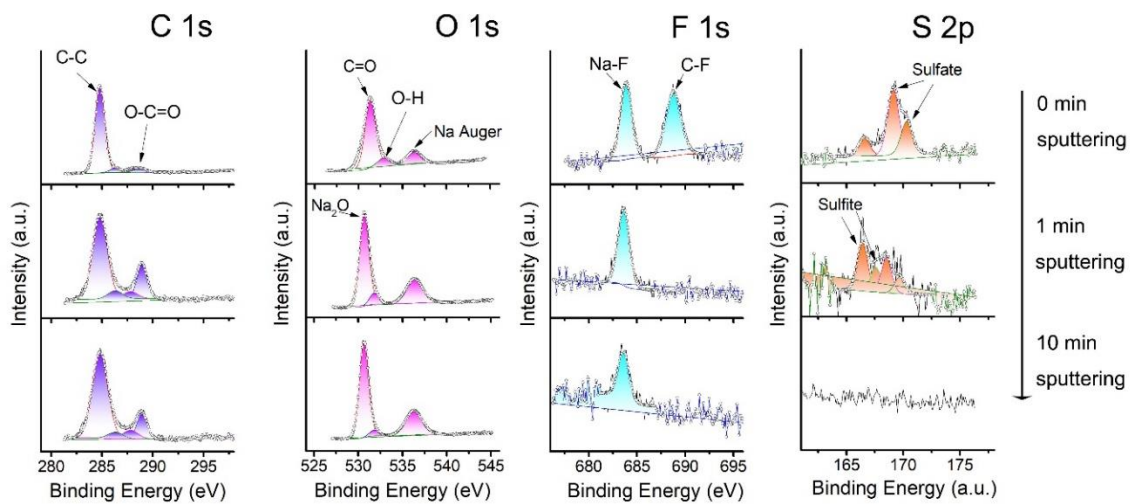
Figure S6.16 XPS characterization of the Na anode SEI layer formed in the HSS Na-O₂ cell in the absence of O₂/O₂⁻ crossover.

Table S6.1 Performance comparisons of HSS Na-O$_2$ batteries with recent works during the first cycle.

Cathode material	Current density (mA cm^{-2})	Discharge/charge capacity (mAh cm^{-2})	Year	Journal	Ref.
CP	0.1	5.15/5.02	2019	This work	-
	0.2	4.21/3.93			
CP	0.12	3.3	2013	Nature Materials	2013, 12, 228-232
	0.2	~1.45			
CP	0.12	~2.38/Short circuit	2017	Energy Technology	2017, 5, 2265-2274
CP	0.2	~3.08/2.8	2013	Phys. Chem. Chem. Phys.	2013, 15, 11661-11672
CP	0.1	5.52	2018	Adv. Funct. Mater.	2018, 28, 1801904
	0.2	5.08			

Chapter 7

7   Probing the blind point of the protected anodes in Na-O$_2$ batteries: Their failure mechanism against superoxide crossover and resolving strategy

Na-O$_2$ cell failure due to uncontrollable Na dendrite growth and Na corrosion has been systematically studied in the last two chapters. Although it is nature to expect the Na protection methodologies that are already found to be profound in Na-metal batteries (NMBs) should also bring significant improvement on the cycling performance of Na-O$_2$ batteries, there is yet few studies detailing the behavior of sodium protection (layer) in superoxide-based Na-O$_2$ batteries. Considering the distinct cell configuration, working principle and operating environment of two battery systems, the feasibility of artificial protected Na anode in Na-O$_2$ batteries needs further investigation.

In this chapter, we first report that the chemical instability of Na anode protective layer against superoxide can be fatal for the Na-O$_2$ cell performance. Using the molecular layer deposited alucone coated Na anode (Na@alucone) as a typical example, we found that alucone layer is vulnerable to the superoxide attack and thus incapable of facilitating stable cycling of Na-O$_2$ cells, which is in sharp contrast to its stable performance in NMBs. By eliminating the superoxide crossover effect towards Na@alucone anode with a solid-state electrolyte, the alucone film retrieves its dendrite suppressing effect on Na anode. Consequently, a long life of over 325 cycles can be achieved for Na-O$_2$ batteries at 0.2 mA cm^{-2} under shallow cycling mode. These results indicate that the further studies on Na-O$_2$ batteries should take serious consideration on the chemical stability of protected Na anode against superoxide radicals, and the lessons learn from this work can provide important guidance for other battery systems with soluble intermediates formation during operation.

---

*A version of this chapter is to be submitted.

7.1   Introduction

Growing environmental concerns and continuously surging demand for energy have stimulated extensive interests in exploring advanced energy storage systems. In the past few decades, the success of Li-ion batteries (LIBs) in portable electronics have greatly innovated our modern lifestyle. However, this battery system is still limited by its low energy density, and the development of next-generation electric vehicles obliges scientific and technological breakthroughs beyond LIBs. Na-O_2 batteries are appealing for their ultrahigh theoretical energy density, which is 6-9 folds higher than that of conventional LIBs.[1-3] Additionally, the high round-trip energy efficiency, as well as the nature abundance and low-cost of sodium resources make Na-O_2 batteries promising for large-scale application.[4, 5] However, the daunting challenges, such as low capacity and poor cycle life relevant to the metallic Na anode, should be well addressed before the realization of practical Na-O_2 batteries.[6-10]

Na dendrite growth is one of the major reasons for the premature failure of Na-O_2 batteries.[11-13] The growth of Na dendrite during repetitive cycling can penetrate through the separator, causing the cell short circuit and even safety concerns.[14-16] In order to address the dendrite formation problem, some Na metal protection strategies can be transferable from the NMBs.[15-20] One effective approach to suppress the dendrite formation is increasing the effective electrode surface area to dissipate the current density.[21-23] This can be realized by introducing 3D conductive interlayer on Na metal anode. As reported in our previous work, the presence of carbon paper (CP) interlayer can facilitate dendrite-free Na deposition within its conductive matrix, and the reversibility and cycle life of Na-O_2 batteries can be significantly improved.[21] Surface engineering is another typical approach to stabilize the artificial solid electrolyte interphase (SEI) layer and suppress Na dendrite growth.[24, 25] For example, Zhou and coworkers built an inorganic NaF-rich protective layer on Na anode by adding a sacrificial electrolyte additive, which can strength the interface to effectively inhibit the dendrite propagation in Na-O_2 batteries.[26]

However, the chemistry in Na-O_2 batteries is quite different from that in conventional NMBs. Uniquely, the solution-mediated path for the formation of NaO_2 result in the presence of superoxide radical in the electrolyte during Na-O_2 cell operation. As the

superoxide crossover has been reported to play an important role in the electrochemical behavior of Na metal anode,[21, 27, 28] the effectiveness of the reported Na protection layers should also be reinvestigated in the Na-O_2 battery system. To the best knowledge, the effect of superoxide crossover in Na-O_2 batteries on the Na anode protection layer remain unclear.

Here, we for the first time investigate the cycling stability of organic film protected Na anode in Na-O_2 batteries. For example, the molecular layer deposited alucone film has been demonstrated with successful Na metal anode enhancement in NMBs, but we found that the organic layer is actually vulnerable to the superoxide attack and consequently fails to suppress Na dendrites. With solid-state electrolyte (SSE) as a physical shield to eliminate the corrosion of superoxide towards the alucone layer, the dendrite suppressing effect of Na@alucone anode can be retrieved. As a result, the Na-O_2 cell show stable cycling performance for 325 cycles at 0.2 mA cm^{-2} under shallow cycling mode, which is much better than the cells solely with Na@alucone anode or SSE due to their synergistic positive effects. Future studies should also take serious consideration on the stability of Na protection layer against superoxide radicals, and Na protection strategy we developed holds great promise for realizing practical Na-O_2 batteries.

7.2   Experimental section

Preparation of alucone and polyurea protected Na anodes. Fresh Na foils with the diameter of 3/8 inch were prepared in the argon-filled glovebox using a homemade press machine. Molecular layer deposited (MLD) alucone and polyurea coating on Na metal anode was carried out with Gemstar-8 MLD system, which directly connected with Ar-filled glove box. The alucone thin film was deposit on as-prepared Na metal with two half reactions between trimethylaluminum (TMA) and ethylene glycol (EG) at 90℃. Firstly, Na anode is exposed to TMA, and CH_4 is released as the byproducts. In the next step, the resulting surface react with pulsed EG precursor, and again release CH_4 as a product. The MLD alucone process use 0.01s/40s/0.01s/70s TMA pulse/purge/EG pulse/purge sequence. The MLD polyurea was performed on fresh Na foil by alternatively introducing ethylenediamine (ED) and phenylene diisocyanate (PDIC) as the precursors at 90℃. A complete MLD polyurea cycle was described as ED pulse/purge/PDIC pulse/purge for

period of 0.1s/30s/1s/50s. In this thesis, 50 MLD alucone and 50 MLD polyurea cycle coatings were carried out on Na foils, which denoted as Na@alucone and Na@polyurea, respectively.

Battery assembly and electrochemical measurements. The electrochemical performance of Na-O$_2$ batteries was evaluated with Swagelok-type cells. The cells were assembled in an argon-filled glove box, which has been described in details in our previous work.[29] The liquid electrolyte (LE)-based Na-O$_2$ batteries were fabricated with Na or Na@Alucone anode, glass fiber separator, CP cathode and ether-based electrolyte. The CP and Na metal foil were cut into disks with an area of 0.7125 cm^{-2}. The electrolyte was 1 M sodium trifluoromethanesulfonate (NaSO$_3$CF$_3$, Aldrich) dissolved in diethylene glycol dimethyl ether (DEGDME, reagent grade ≥ 98%, Aldrich). The SSE-based Na-O$_2$ batteries were assembled via the same procedures, where the SSE was sandwiched between the Na@alucone anode and the CP cathode. The cells were operated under static O$_2$ with a pressure of 1.0 atm in a homemade testing box. Each cell was stabilized for 1h at room temperature before electrochemical tests. The galvanostatic discharge-charge tests were carried out using Arbin BT-2000 battery testing system at room temperature. The electrolyte preparation and battery assembly were carried out in an Ar-filled glovebox with the oxygen and moisture levels below 0.1 ppm. DEGDME was dried using freshly activated molecular sieves (4 Å, Aldrich) for at least one month, and NaSO$_3$CF$_3$ was dried in a vacuum at 80°C for one week before use.

Material characterization. The X-ray powder diffraction (XRD) patterns were collected using the Bruker D8 X-ray diffractometer equipped with Cu-Kα (λ =1.5406Å) radiation. The morphology of the cathodes after discharge were characterized by Hitachi S-4800 field emission scanning electron microscope (FE-SEM) at an acceleration voltage of 5 kV. The morphological studies of the GF were performed using a Hitachi 3400N environmental SEM. The Raman spectra were collected on a HORIBA Scientific LabRAM Raman spectrometer equipped with a 532.03 nm laser. In this study, the disassembly of the Na-O$_2$ batteries was carried out in an ultra-pure Ar-filled glovebox. The discharged cathodes were washed with DEGDME to remove any residual NaSO$_3$CF$_3$ salt and dried thoroughly in a vacuum chamber before SEM, XRD and Raman measurements. The specimens were

sealed in a leak-tight homemade sample holder to prevent exposure to air during analyses of XRD and Raman.

7.3   Results and discussion

The alucone thin film was deposit on fresh Na metal via molecular layer deposition (MLD). Typical MLD alucone process is shown in **Figure S7.1** with alternative pulses of trimethylaluminum (TMA) and ethylene glycol (EG) at 90°C, following our previous work with 50 MLD cycles.[30] The successful coating of alucone layer on Na foil was confirmed by time-of-flight secondary ion mass spectrometry (ToF-SIMS). As shown in **Figure S7.2a** and **b**, characteristic secondary ions from alucone film, such as Al^-, C_2Al^-, and C_2OAl^-, were detected with strong signals at the top surface of the sample. The depth-profiles was established by etching a selected area (400×300 µm) on the Na@alucone electrode, which was subject to continuous Cs^+ sputtering (**Figure S7.2c**). After sputtering for 200 s, the signal from alucone showed a large decrease. The 3D images constructed from SIMS intensity and the etching depth show uniform spacial distribution of the alucone fium on Na metal surface (**Figure S7.2d**). The thickness of the alucone layer can be estimated to be 20 nm based on the growth rate of alucone on Na metal, which is consistent with the estimation based on sputtering rate (~0.1 nm s^{-1}).[30]

The cycling stability of Na@alucone anode was evacuated in Na-O_2 batteries in the presence of superoxide crossover. **Figure 7.1a** shows the discharge-charge profiles of conventional Na-O_2 cells with bare Na anode, and the charging process is interrupted by the dendrite short-circuiting. This result is consistent with the previous reports.[6, 21, 28] Even under the shallow cycling mode by limiting the discharge capacity to 0.2 mAh cm^{-2} at 0.2 mA cm^{-2}, the dendrite penetration induced potential drop also can be observed from 9th cycle (**Figure 7.1b**). As for the cell with Na@alucone anode, stable discharge plateau at ~2.0V with the formation of micrometer-sized NaO_2 cubes as the only discharge product indicated normal electrochemistry of Na-O_2 batteries using Na@alucone anode (**Figure S7.3**). However, unlike the success in NMBs,[30] the Na@alucone anode exhibit no obvious improvement over the bare Na anode in terms of electrochemical performance. Slight increase of discharge capacities was observed, while dendrite-induced short circuit was just delayed rather than completely inhibited after introducing alucone protective layer on Na

metal (**Figure 7.1c**). As shown in **Figure 7.1d**, stable discharge/charge cycling was maintained for only 14 cycles.
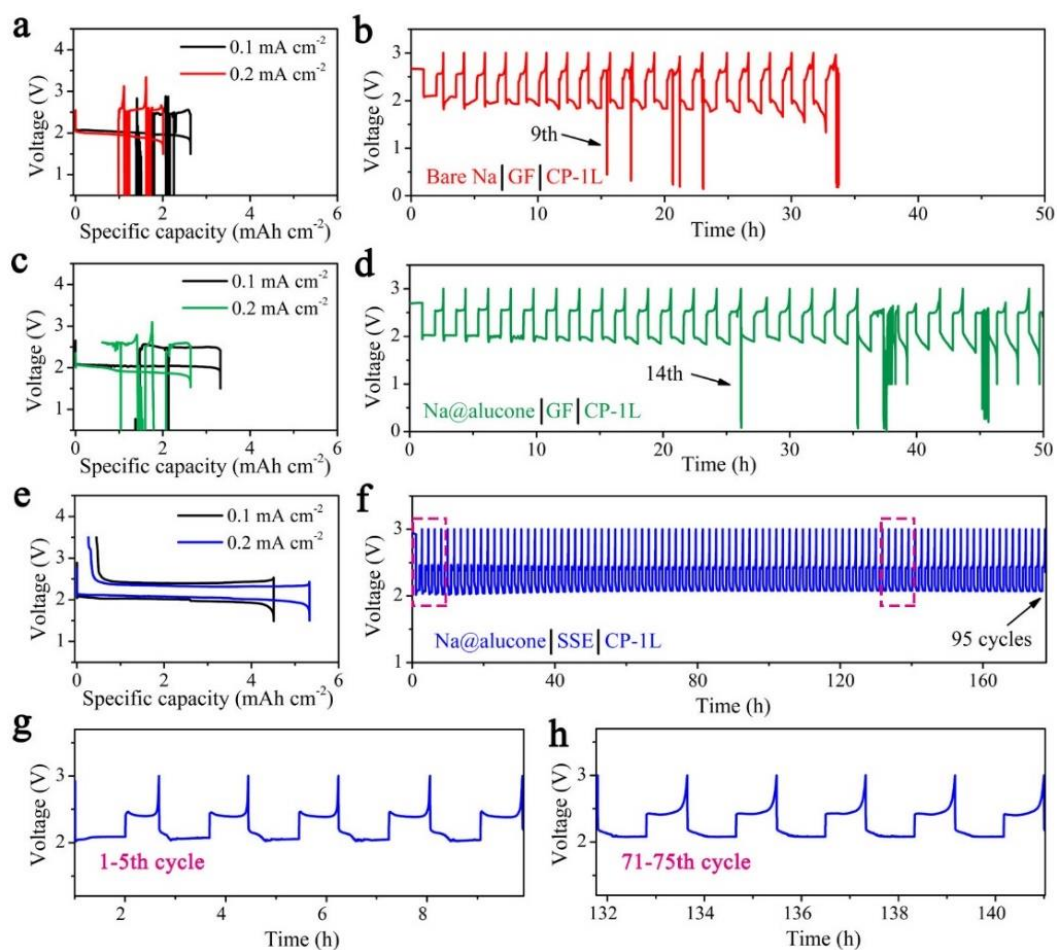
Figure 7.1 The discharge/charge profiles and cycling performance of Na-O$_2$ batteries with different cell configurations: (a, b) Na-O$_2$ cells with GF separator and bare Na anode, (c, d) Na-O$_2$ cells with GF separator and Na@alucone anode, and (e, f) HSS Na-O$_2$ cells with SSE and Na@alucone anode. (g, h) Enlarged discharge/charge profiles of the HSS Na-O$_2$ cell at selected cycles.

The Na@alucone anode facilitate long-term cycling of NMBs, while Na-O$_2$ cells with Na@alucone still suffered from Na dendrites induced short circuit. The distinct striping/plating behaviors of Na@alucone anode in NMBs and Na-O$_2$ cells can be possibly related to the different working chemistries of the two battery systems. To verify the effects of migrated superoxide to alucone protective layer efficiency in suppressing the dendrite

growth, hybrid solid state (HSS) Na-O$_2$ cell was constructed. By replacing the porous glass fiber (GF) separator with dense NASICON-type SSE, the superoxide crossover from the cathode to the anode was eliminated. Interestingly, the HSS Na-O$_2$ batteries delivered high discharge capacities of 5.33 and 4.51 mAh cm^{-2} at the current densities of 0.1 and 0.2 mA cm^{-2}, respectively (**Figure 7.1e**). The discharge capacities were much higher than that of the cells using GF separator and Na@alucone anode in **Figure 7.1c**. Since the air electrode of two cell configurations were the same, the lower discharge capacity of Na-O$_2$ batteries with GF was attributed to the corrosion of Na@alucone anode by superoxide crossover.

Interestingly, in addition to the significant increase in discharge capacities, the HSS Na-O$_2$ cells with Na@alucone anode can be fully recharged without dendrite-induced short circuit, and the corresponding Coulombic efficiencies are as high as 95.1 and 90.14% at 0.1 and 0.2 mA cm^{-2}, respectively. Additionally, significant improved cycling stability of HSS Na-O$_2$ cells can be achieved with a long cycle life of over 95 cycles, as shown in **Figure 7.1f-h**. It is believed that the SSEs are more effective in inhibiting dendrite penetration compared with porous GF separator. However, long-term plating/stripping of dendrite-free Na anode with the pure SSE pellet is still a challenge since the Na dendrite tends to grow through grain boundaries and interconnected pores in the SSE.[31] As shown in **Figure S7.4**, HSS Na-O$_2$ cells based on SSE and bare Na anode still suffered from the short-circuiting issue and failed to cycle beyond 40 cycles under the same experimental conditions. The optical images of the cycled SSE clearly display "dark spots" on the surface, which can be reasonably assigned as Na dendrite and were found to penetrate across the SSE pellet after cell failure (**Figure S7.5**). Therefore, the employment of SSE partially contributed to the long-term cycling of HSS Na-O$_2$ batteries in **Figure 7.1f**, and the integration of SSE with Na@alucone anode was crucial to simultaneously address short circuit and superoxide-related anode degradation. It is worth noting that the slightly higher discharge/charge overpotential in the initial cycles may attributed to the sodiation of alucone layer with the formation of new solid electrolyte interphase (SEI) layer. Benefiting from the formation of this new protective layer, flat voltage profiles during both discharge and charge can be well retained during the subsequent cycles without obvious increase in discharge/charge overpotentials.
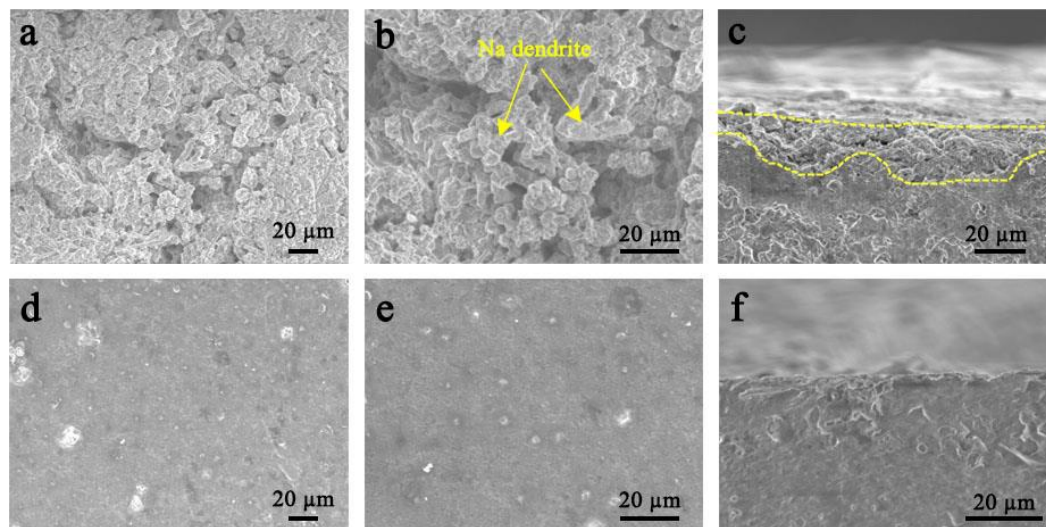
Figure 7.2 (a, b) Top-view and (c) cross-sectional view SEM images of the Na@alucone anode obtained from cycled Na-O$_2$ cell with GF separator; the distance between two dotted yellow lines in (c) shows the thickness of porous Na. (d, e) Top-view and (f) cross-sectional view SEM images of the Na@alucone anode obtained from cycled Na-O$_2$ cell with SSE.

Collecting the Na@alucone anodes from the Na-O$_2$ batteries with GF and SSE after cycling, their different morphologies gave hints to their distinct electrochemical behaviors. Both Na-O$_2$ cells were cycled at 0.2 mA cm^{-2} with a cutoff capacity of 0.2 mAh cm^{-2}. From the SEM images shown in **Figure S7.6**, the uncycled Na@alucone anode exhibited clean and relatively smooth surface. After cycling in the Na-O$_2$ cell with GF separator, the Na@alucone show a cracked surface with inhomogeneous Na deposition on the bulk Na electrode(**Figure S7.7**). At the same time, Na dendrites of approximately 10-20 µm can be clearly observed on the cycled Na@alucone electrode (**Figure 7.2a**, **b**). The corresponding cross-sectional view clearly show that the top surface of original bulk Na has transformed to the high-surface-area porous structure (**Figure 7.2c**). The formation of porous layer indicate the destruction of protective alucone film on Na metal anode. This porous layer was permeable to superoxide that continuously corroded the Na anode, leading to low Coulombic efficiency. Continuous electrolyte decomposition and active Na consumption were unavoided. The optical and SEM images of GF separator are shown in **Figure S7.8**, the presence of dendritic spots on the GF surface on the side facing the CP cathode further verified the dendrite penetration issue. In sharp contrast, as shown in **Figure 7.2d, e** and

Figure S7.9, a relatively smooth surface without dendritic Na or unfavorable porous layer can be observed on the cycled Na@alucone electrode after introducing SSE. The unchanged SSE surface had no sign of Na dendrites growth (**Figure S7.10**). Meanwhile, the cross-sectional view of the Na@alucone displayed a negligible gap between plated Na and bulk Na (**Figure 7.2f**). The results indicated that with the shielding effect of SSE against superoxide crossover restore the dendrite suppressing function of alucone on Na metal anode.
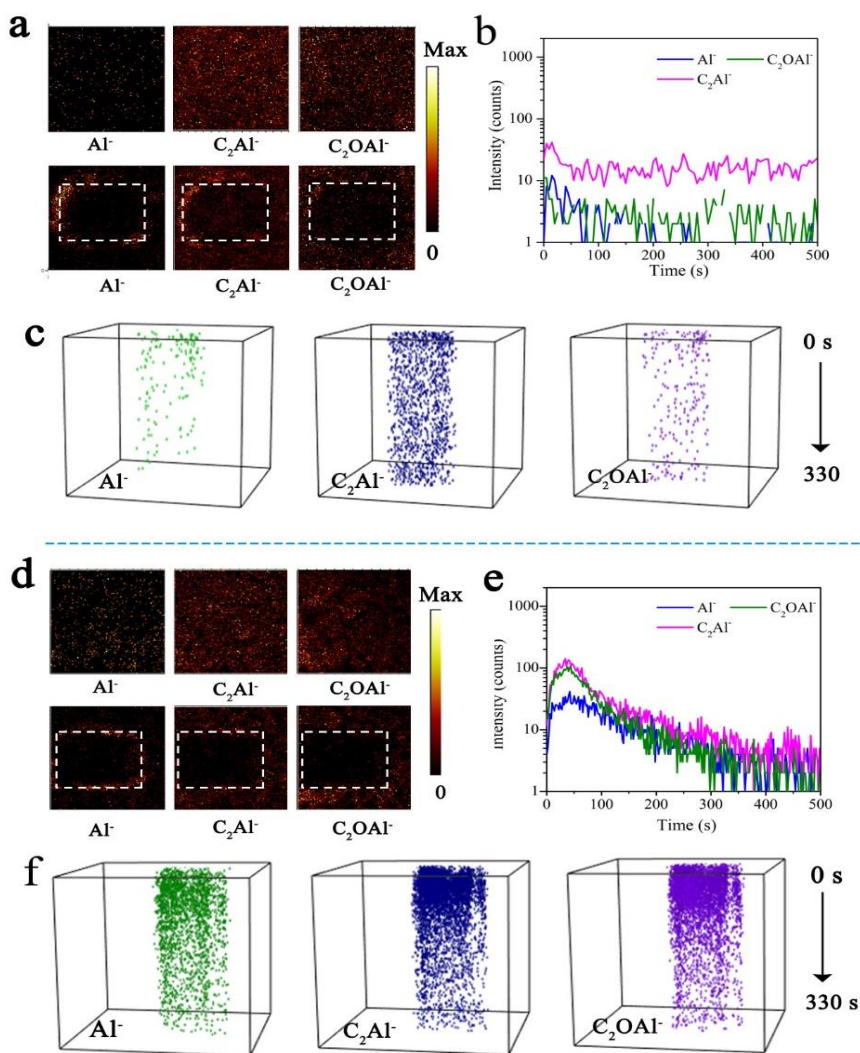
Figure 7.3 (a, b) TOF-SIMS depth profiles and chemical ion images of the Al^-, C_2Al^-, and C_2OAl^- species for the cycled Na@alucone anode obtained from Na-O_2 cell with GF. (c) The corresponding 3D view images of the variation of SIMS intensity with the etching depth. (d, e) TOF-SIMS depth profiles and chemical ion images of the Al^-, C_2Al^-, and

C_2OAl^- species for the cycled Na@alucone anode obtained from Na-O_2 cell with SSE. (f) The corresponding 3D view images of the variation of SIMS intensity with the etching depth.

ToF-SIMS analyses were conducted on the cycled Na@alucone anodes with or without exposure to superoxide crossover to further understand the interfacial change of the Na@alucone anodes. It should be noted that electrolyte decomposition cannot be avoided on the anode surface with formation of various organic and inorganic species including Na_2CO_3, NaF, NaOH, RONa, ROONa, et al..[32] To have a clear picture on the changes of alucone film, only the variation of Al-containing secondary ions that exclusively generated from the alucone film were analyzed. **Figure 7.3a** illustrate the ToF-SIMS chemical mappings of secondary ions of interest on Na@alucone electrode after cycling in the presence of superoxide crossover. Surprisingly, although the secondary ion fragments from alucone still can be detected on the surface of Na@alucone anode, the intensity of those species significantly decreased after cycling. For example, compared with the pristine sample in **Figure S7.2**, the signals of C_2Al^- decreased dramatically from 200 to 40 counts, while the signals of Al^- and C_2OAl^- become negligible. From the **Figure 7.3b** and **c**, the alucone protective layer was not visible on the electrode surface, which suggested the breakdown of the alucone film during cycling. However, the sputtering depth should not be mistaken as the thickness of the SEI layer. Considering serious electrolyte decomposition on the electrode surface due to malfunction of the alucone layer in protecting Na anode when exposed to superoxide crossover, stable SEI layer cannot be formed. Continuous electrolyte decomposition occurs during cell operation, resulting in the increase in internal cell resistance and cell performance decay.

In contrast, after cycling in the absence of superoxide crossover, the Na@alucone anode still showed strong signals of secondary ions from alucone (C_2Al^-, $COAl^-$, and C_2OAl^-) on the outer most surface (**Figure 7.3d-f**). By consecutive Cs^+ sputtering for 500s, an area with a depth of ~50 nm was removed to obtain the depth profiles and 3D view images of various fragments (**Figure 7.3e** and **f**). The signals of secondary ions from alucone remain distinct from the top surface to the interior of the electrode, despite of slight decrease of intensity compared with pristine sample, suggesting preservation of the robust alucone film

after cycling. Noticeably, the sodiated alucone layer has a thickness of ~25 nm (considering the sputtering rate of 0.1 nm s^{-1}), which is thicker than the alucone film before cycling. This observation suggests a newly formed SEI layer on the Na@alucone electrode during cycling process, which is consistent with the electrochemical behavior of HSS Na-O$_2$ cell in **Figure 7.1f**.
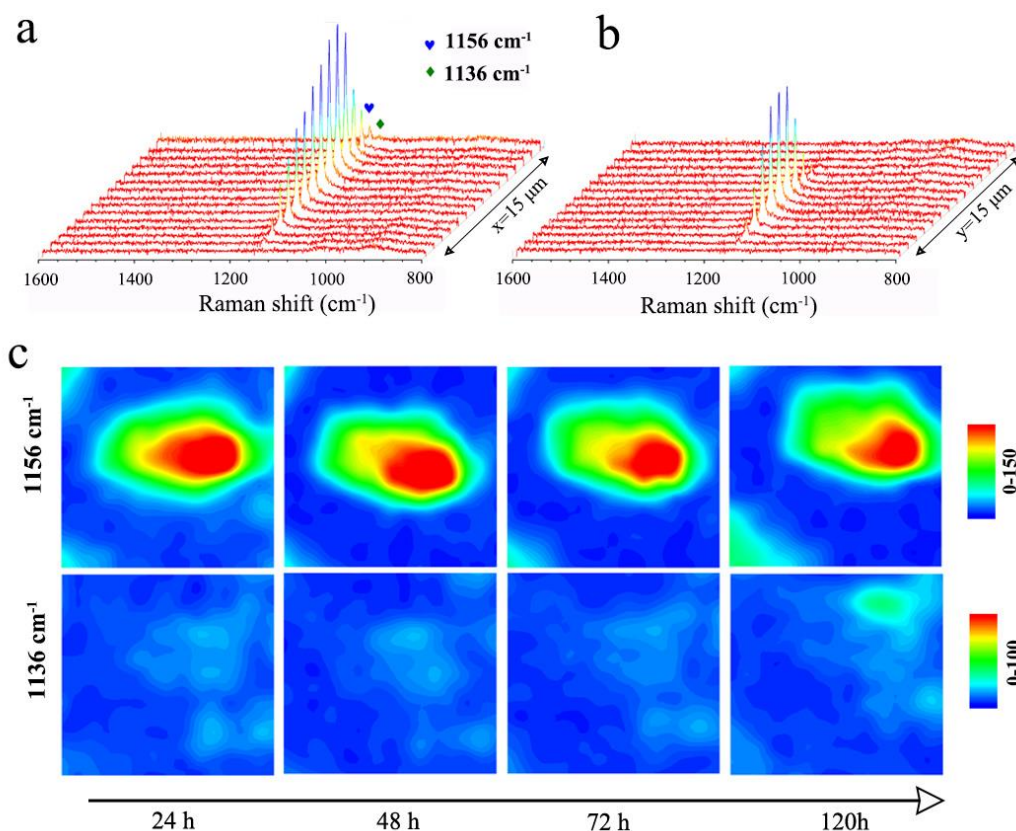

Figure 7.4 (a, b) Raman spectra recorded over a liner scan on a typical NaO$_2$ cube after resting for 24 h. (c) chemical maps at various frequencies reproduced from Raman spectra recorded from a NaO$_2$ cube on the SSE at different time intervals.

Although the electrochemical reversibility of Na@alucone anode in the Na-O$_2$ batteries can be significantly improved by incorporating SSE, the chemical stability of SSE against the highly reactive NaO$_2$ also can not be neglected. As the SSE was in direct contact with the CP cathode, and the accomulation of NaO$_2$ cubes on the SSE surface is inevitable due to the growth of NaO$_2$ through solution-mediated mechanism.[32] The possible reactions between SSE and NaO$_2$ not only can decrease the reversible charge capacity due to the

consumption of NaO_2, but also result in the increase of internal cell resistance as a result of side products formation. Here, we employ *in-situ* Raman imaging technique to monitor the chemical changes of NaO_2 cube when in contacting with the SSE. The SSE was collected from a discharged HSS Na-O_2 cell. The distribution of NaO_2 cubes on the SSE can be clearly observed via Raman and SEM microscope (**Figure S7.11**). As shown in **Figure S7.12**, a NaO_2 cube was linearly scanned, and the Raman spectra were collected in an area of 15 µm × 15 µm for 15 points in each X and Y directions. **Figure 7.4a** and **b** show the Raman spectra collected from two vertical liner scan on the NaO_2 cube after a period of 24 h. The characteristic Raman peak located at 1156 cm^{-1} was related to the O-O stretching mode in NaO_2, and weak Raman peak at 1136 cm^{-1} corresponded to $Na_2O_2 \cdot 2H_2O$. The obtained spectra were converted into 2D mapping images using the chemical maps at frequencies of 1136 and 1156 cm^{-1} (**Figure 7.4c**). As clearly evidenced in **Figure 7.4c**, the intensity of the NaO_2 chemical maps showed a slightly decreasing trend over time, along with a slight increase in $Na_2O_2 \cdot 2H_2O$ intensity. This phenomenon can be attribute to the transformation of NaO_2 to $Na_2O_2 \cdot 2H_2O$ in the presence of residual electrolyte solvent or air leakage of the Raman cell.[33-35] However, it is notable that the absence of other obvious side products (even after 168 h) and the preservation of the original shape of NaO_2 particle again verified the excellent chemical stability of NASICON-type SSE with NaO_2 (**Figure S7.13**, **S7.14**).

After addressing the anode issues and ruling out the possible effects of SSE, the limited cycle life of HSS Na-O_2 cell in **Figure 7.1f** may indicate a degradation effect related to the cathode.[32] Therefore, HSS Na-O_2 cells with extra cathode loading were assembled in order to extend the Na-O_2 cell life time, and at the same time, to investigate the durability of Na@alucone anode during long-term cycling process. Here, extra cathode loading was realized by simply increasing the number of CP cathode, and the cathodes with 2, 3, 4, and 5 CP are named as CP-2L, CP-3L, CP-4L and CP-5L, respectively. The electrochemical performance of HSS Na-O_2 batteries with different cathodes were investigated at 0.2 mA cm^{-2} with a cutoff capacity of 0.2 mAh cm^{-2}. It can be seen from **Figure S7.15** and **Figure 7.5** that the cycle life of HSS Na-O_2 cells increased with increasing cathode loading. The HSS Na-O_2 cells with CP-2L, CP-3L and CP-4L cathodes exhibited stable cycling for over 175, 238, and 292 cycles, respectively. When the Na@alucone anode was coupled with

CP-5L cathode in the HSS Na-O$_2$ cell, the cell delivered highly stable discharge/charge performance for over 325 cycles (**Figure 7.5b-e**), which was almost 3.4 times longer life time than that of the CP-1L cathode in **Figure 7.1f**.
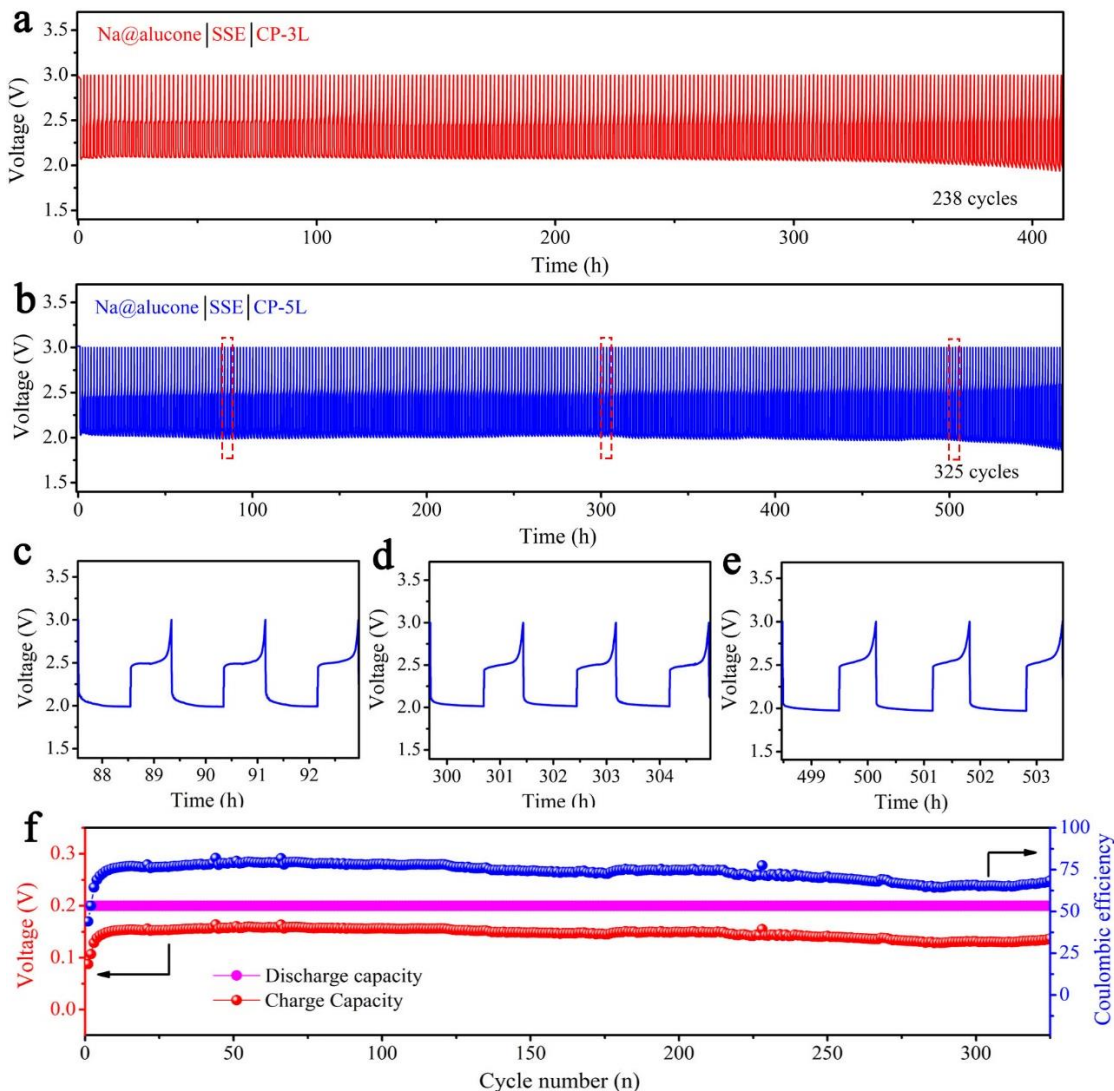
Figure 7.5 Cycling performance of HSS Na-O$_2$ cells with (a) CP-3L cathode and (b) CP-5L cathode; (c-e) selected discharge/charge profiles of HSS Na-O$_2$ cell with CP-5L cathode; (f) cycling performance and Coulombic efficiency of HSS Na-O$_2$ cell with CP-5L cathode.

The long cycle life of HSS Na-O$_2$ cell with CP-5L cathode reflected good stripping/plating stability of Na@alucone anode after integrating with SSE (~565 h). The increase of cathode

loading was accompanied with increase in number of active sites for electrochemical reactions, which contributed to the enhancement of cell life under the shallow cycling mode. However, the more active sites and longer cycling time, the greater chance of O_2^- attack occurrence. Additionally, the parasitic reactions involving NaO_2, $^1O_2$ and electrolyte may induce the degradation of air electrodes. Coverage of active sites by the insulating side products thus results in the decrease of Coulombic efficiency along cycling (**Figure 7.5f**). All these factors contributed to the nonlinear correlation between cycle life of HSS Na-O_2 batteries and the number of layers of CP cathode. Another important aspect to note is that the cathode thickness increased with increasing the CP layers. Therefore, the increase of Na^+/O_2^- diffusion distance and the diffusion kinetic limits of O_2 in the organic electrolyte explained the slight increase in discharge/charge overpotential of the cell using CP-5L cathode, compared with that of the cell with CP-3L cathode (**Figure S7.14**).
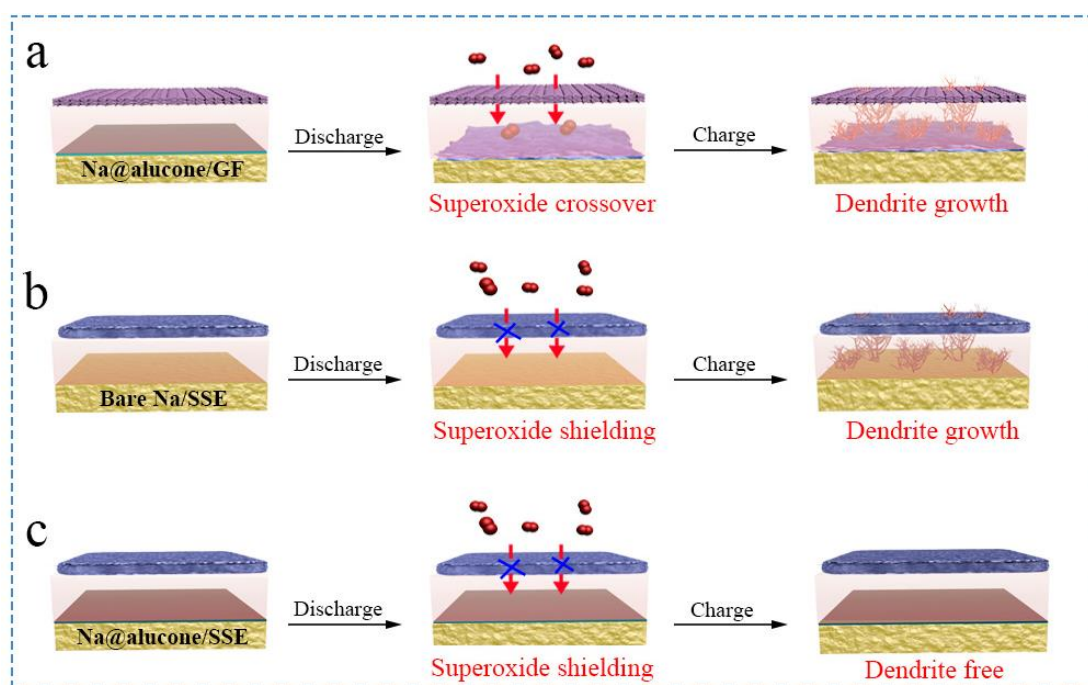
Figure 7.6 Schematic illustration of Na stripping/plating behaviors in Na-O_2 batteries with different configurations.

To further verify the failure mechanism of organic thin film protected Na metal anode in Na-O_2 batteries, the electrochemical behavior of Na-O_2 cells using another organic protective layer coated Na anode (Na@polyurea) was investigated. As consistent with the

results of Na@alucone, the Na@polyurea anode in Na-O$_2$ cells showed minimal improvement over bare Na anode when using GF separator (**Figure S7.17**). The Na@polyurea anode demonstrated significant improvement in cycling stability when SSE was used to eliminate the superoxide crossover. Those results are identical to that of the cells using Na@alucone anode in **Figure 7.1**. Schematic diagram of Na striping/plating behaviors in different Na-O$_2$ cell configurations are illustrated in **Figure 7.6**. For Na-O$_2$ batteries, the vulnerability of organic and organic-inorganic protective films to superoxide should taken into serious consideration for Na metal anode. Insufficient Na anode protection will lead to continuous corrosion of the Na metal anode and the growth of Na dendrite. The Na degradation issue in Na-O$_2$ batteries is much more complicated than that in NMBs, especially when superoxide intermediates is involved. The dissolved superoxide radicals is an aggressive species, which prone to attack electrophilic sites and induce various side reactions in Na-O$_2$ batteries.[27, 34, 35] Thus, the chemical/electrochemical reduction of organic electrolyte on Na anode can be further aggravated in the presence of superoxide crossover, and the build up of parasitic products on the Na anode could result in blockage of the Na$^+$ migration and soaring internal resistance.[31] Therefore, except for Na-O$_2$ battery system, the properties of metal protective layer in other batteries that involve the solution redox, such as Li-O$_2$, Li-S and Na-S, may also need taken special consideration.

7.4   Conclusion

In summary, we have for the first time investigated the effect of superoxide crossover on the protection layer of Na metal anode and correlation to the electrochemical performance of Na-O$_2$ batteries. The unique superoxide ions dissolution in electrolyte for Na-O$_2$ batteries play a critical role in the electrochemical behavior. Taking alucone protective layer on Na anode in Na-O$_2$ batteries as an example, we found that the alucone layer suffer from decomposition under attacks of reactive superoxide radical. After eliminating superoxide crossover effect towards Na@alucone anode with a chemical-stable SSE layer, the organic alucone coating retrieved its Na dendrite suppressing effect and maintained high reversible charge capacity for Na-O$_2$ batteries. In addition, the cell life can be significantly improved with extra cathode loading, which guaranteed sufficient active sites for reversible reactions. The synergistic combination of Na@alucone anode, SSE, and

efficient cathode contributed to a high-performance rechargeable HSS Na-O$_2$ battery. Long cycle life of 325 cycles at 0.2 mA cm^{-2} with a limited capacity of 0.2 mAh cm^{-2} was demonstrated. The stability of Na protection layer and the issues involving the high reactive superoxide radicals should be considered seriously in Na-O$_2$ batteries. It is believed that our results provide important guidance for improve the cycling stability of Na anode, as well as the realization of next-generation high energy density Na-O$_2$ batteries.

7.5 Acknowledgments

7.6 Reference

1. Hartmann, P.; Bender, C. L.; Vračar, M.; Dürr, A. K.; Garsuch, A.; Janek, J.; Adelhelm, P., *Nat Mater* 2013, 12, (3), 228-232.

2. Yadegari, H.; Sun, X., *Accounts of Chemical Research* 2018, 51, (6), 1532-1540.

3. Bi, X.; Wang, R.; Amine, K.; Lu, J., *Small Methods* 2019, (3), 1800247.

4. Yadegari, H.; Sun, Q.; Sun, X., *Advanced Materials* 2016, 28, (33), 7065-7093.

5. Das, S. K.; Lau, S.; Archer, L. A., *Journal of Materials Chemistry A* 2014, 2, (32), 12623-12629.

6. Medenbach, L.; Bender, C. L.; Haas, R.; Mogwitz, B.; Pompe, C.; Adelhelm, P.; Schröder, D.; Janek, J., *Energy Technology* 2017, 5, (12), 2265-2274.

7. Ma, J.-l.; Meng, F.-l.; Yu, Y.; Liu, D.-p.; Yan, J.-m.; Zhang, Y.; Zhang, X.-b.; Jiang, Q., *Nature Chemistry* 2019, 11, (1), 64-70.

8. Ma, J. L.; Yin, Y. B.; Liu, T.; Zhang, X. B.; Yan, J. M.; Jiang, Q., *Advanced Functional Materials* 2018, 28, (13), 1703931.

9. Yang, H.; Sun, J.; Wang, H.; Liang, J.; Li, H., *Chemical Communications* 2018, 54, (32), 4057-4060.

10. Sun, B.; Pompe, C.; Dongmo, S.; Zhang, J.; Kretschmer, K.; Schröder, D.; Janek, J.; Wang, G., *Advanced Materials Technologies* 2018, 3, (9), 1800110.

11. Lin, X.; Sun, Q.; Doyle Davis, K.; Li, R.; Sun, X., *Carbon Energy* 2019, (1) 141-164.

12. Luo, W.; Lin, C.-F.; Zhao, O.; Noked, M.; Zhang, Y.; Rubloff, G. W.; Hu, L., *Advanced Energy Materials* 2017, 7, (2), 1601526.

13. Shen, F.; Luo, W.; Dai, J.; Yao, Y.; Zhu, M.; Hitz, E.; Tang, Y.; Chen, Y.; Sprenkle, V. L.; Li, X.; Hu, L., *Advanced Energy Materials* 2016, 6, (14), 1600377.

14. Zhao, Y.; Yang, X.; Kuo, L. Y.; Kaghazchi, P.; Sun, Q.; Liang, J.; Wang, B.; Lushington, A.; Li, R.; Zhang, H.; Sun, X., *Small* 2018, (14), 1703717.

15. Zhao, Y.; Adair, K. R.; Sun, X., *Energy & Environmental Science* 2018, 11, (10), 2673-2695.

16. Zheng, X.; Bommier, C.; Luo, W.; Jiang, L.; Hao, Y.; Huang, Y., *Energy Storage Materials* 2019, 16, 6-23.

17. Lee, B.; Paek, E.; Mitlin, D.; Lee, S. W., *Chemical Reviews* 2019, 119, (8), 5416-5460.

18. Luo, W.; Zhang, Y.; Xu, S.; Dai, J.; Hitz, E.; Li, Y.; Yang, C.; Chen, C.; Liu, B.; Hu, L., *Nano Letters* 2017, 17, (6), 3792-3797.

19. Wang, H.; Wang, C.; Matios, E.; Li, W., *Nano Letters* 2017, 17, (11), 6808-6815.

20. Zhao, S.; Qin, B.; Chan, K.-Y.; Li, C.-Y. V.; Li, F., *Batteries & Supercaps* 2019, (2), 725.

21. Xiaoting, L.; Qian, S.; Hossein, Y.; Xiaofei, Y.; Yang, Z.; Changhong, W.; Jianneng, L.; Alicia, K.; Ruying, L.; Xueliang, S., *Advanced Functional Materials* 2018, (28), 1801904.

22. Bing, S.; Peng, L.; Jinqiang, Z.; Dan, W.; Paul, M.; Chengyin, W.; L., N. P. H.; Guoxiu, W., *Advanced Materials* 2018, 1801334.

23. Wang, A.; Hu, X.; Tang, H.; Zhang, C.; Liu, S.; Yang, Y.-W.; Yang, Q.-H.; Luo, J., *Angewandte Chemie* 2017, 129, (39), 12083-12088.

24. Zhao, Y.; Liang, J.; Sun, Q.; Goncharova, Lyudmila V.; Wang, J.; Wang, C.; Adair, K. R.; Li, X.; Zhao, F.; Sun, Y.; Li, R.; Sun, X., *Journal of Materials Chemistry A* 2019, 7, (8), 4119-4125.

25. Kim, Y.-J.; Lee, H.; Noh, H.; Lee, J.; Kim, S.; Ryou, M.-H.; Lee, Y. M.; Kim, H.-T., *ACS Applied Materials & Interfaces* 2017, 9, (7), 6000-6006.

26. Wu, S.; Qiao, Y.; Jiang, K.; He, Y.; Guo, S.; Zhou, H., *Advanced Functional Materials* 2018, 28, (13), 1706374.

27. Liu, C.; Carboni, M.; Brant, W. R.; Pan, R.; Hedman, J.; Zhu, J.; Gustafsson, T.; Younesi, R., *ACS Applied Materials & Interfaces* 2018.

28. Bi, X.; Ren, X.; Huang, Z.; Yu, M.; Kreidler, E.; Wu, Y., *Chemical Communications* 2015, 51, (36), 7665-7668.

29. Sun, Q.; Yadegari, H.; Banis, M. N.; Liu, J.; Xiao, B.; Li, X.; Langford, C.; Li, R.; Sun, X., *The Journal of Physical Chemistry C* 2015, 119, (24), 13433-13441.

30. Zhao, Y.; Goncharova, L. V.; Zhang, Q.; Kaghazchi, P.; Sun, Q.; Lushington, A.; Wang, B.; Li, R.; Sun, X., *Nano Letters* 2017, 17, (9), 5653-5659.

31. Zhou, W.; Li, Y.; Xin, S.; Goodenough, J. B., *ACS Central Science* 2017, 3, (1), 52-57.

32. Lin, X.; Sun, F.; Sun, Q.; Wang, S.; Luo, J.; Zhao, C.; Yang, X.; Zhao, Y.; Wang, C.; Li, R.; Sun, X., *Chemistry of Materials* 2019, 31, (21), 9024-9031.

33. Kim, J.; Park, H.; Lee, B.; Seong, W. M.; Lim, H.-D.; Bae, Y.; Kim, H.; Kim, W. K.; Ryu, K. H.; Kang, K., *Nature Communications* 2016, 7, 10670.

34. Ortiz-Vitoriano, N.; Batcho, T. P.; Kwabi, D. G.; Han, B.; Pour, N.; Yao, K. P. C.; Thompson, C. V.; Shao-Horn, Y., *The Journal of Physical Chemistry Letters* 2015, 6, (13), 2636-2643.
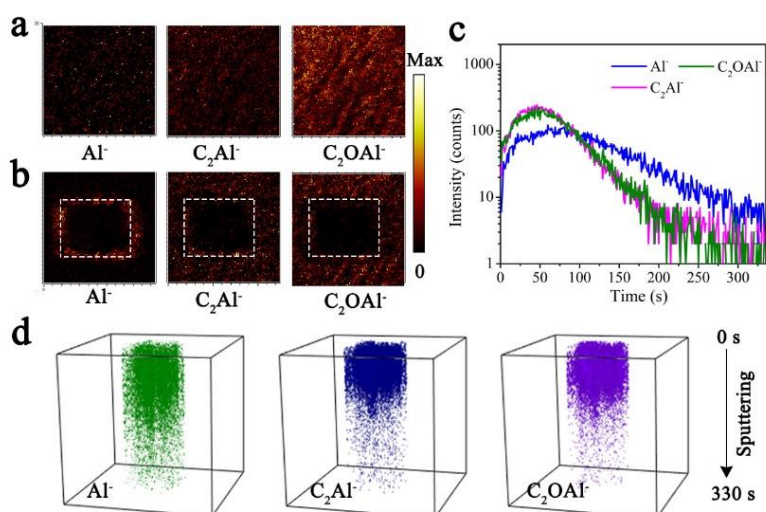
35. Yadegari, H.; Norouzi Banis, M.; Lin, X.; Koo, A.; Li, R.; Sun, X., *Chemistry of Materials* 2018, 30, (15), 5156-5160.

36. Sun, Q.; Liu, J.; Xiao, B.; Wang, B.; Banis, M.; Yadegari, H.; Adair, K. R.; Li, R.; Sun, X., *Advanced Functional Materials* 2019, 1808332.
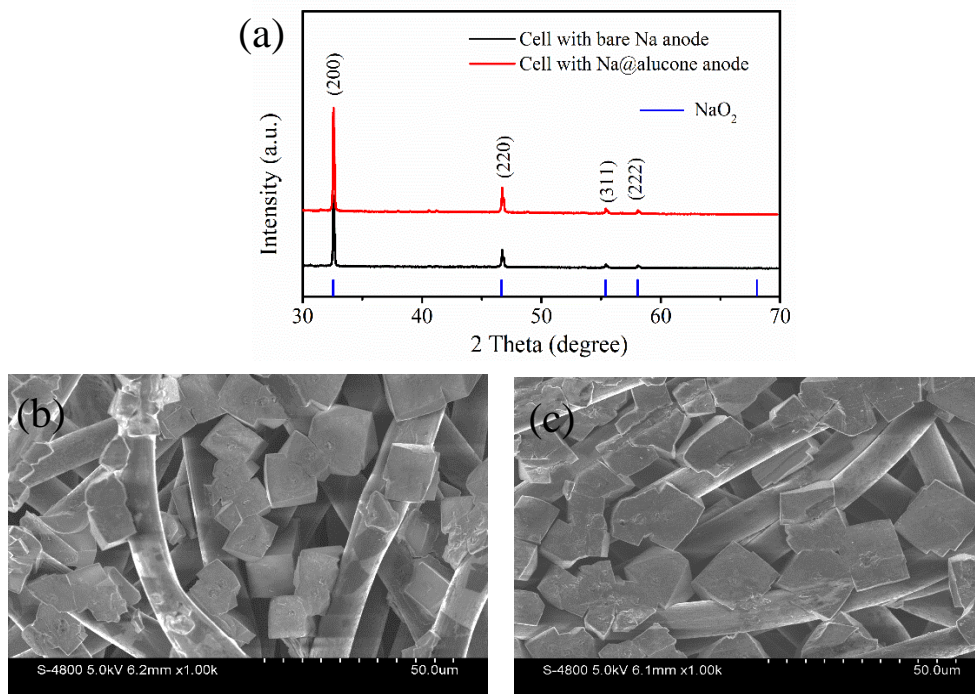
7.7 Supporting information
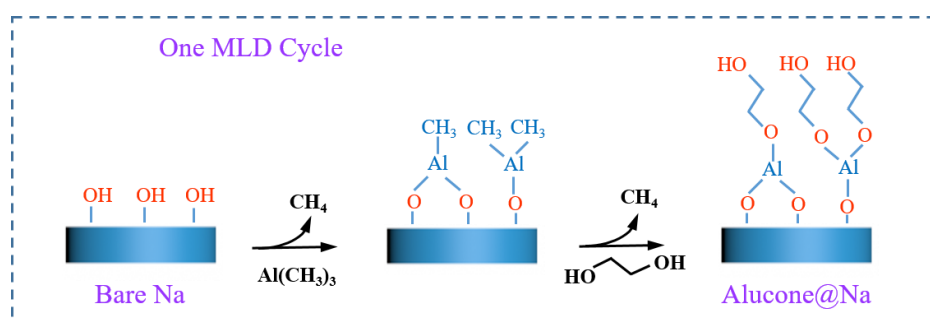
Figure S7.1 The typical MLD alucone coating process on Na foil.


Figure S7.2 The TOF-SIMS secondary ion images of Na@alucome before (a) and after (b) Cs^+ consecutive sputtering for 370 s. (c) Depth profile of various secondary ion species

obtained by sputtering. d) The 3D view images of the sputtered volume corresponding to the depth profiles in (c).


Figure S7.3 (a) The XRD spectrum of discharged CP cathode obtained from the Na-O_2 cell using bare Na anode and Na@alucone anode. The SEM images of discharged CP cathode obtained from the Na-O_2 cell using (b) bare Na anode and (c) Na@alucone anode.
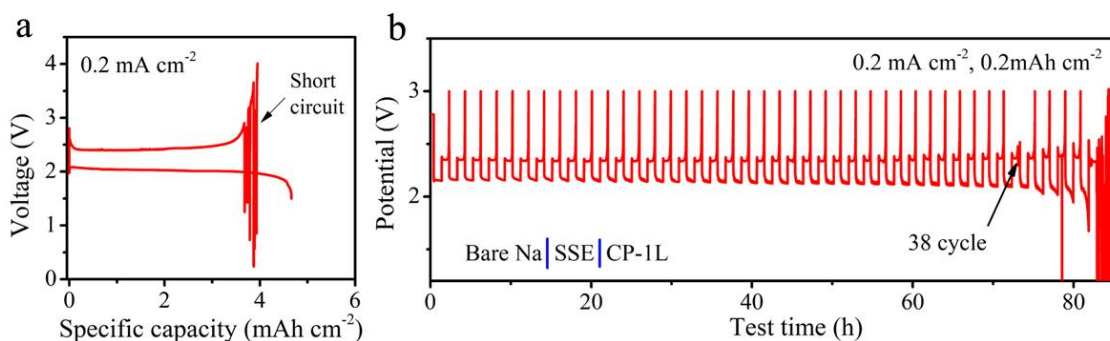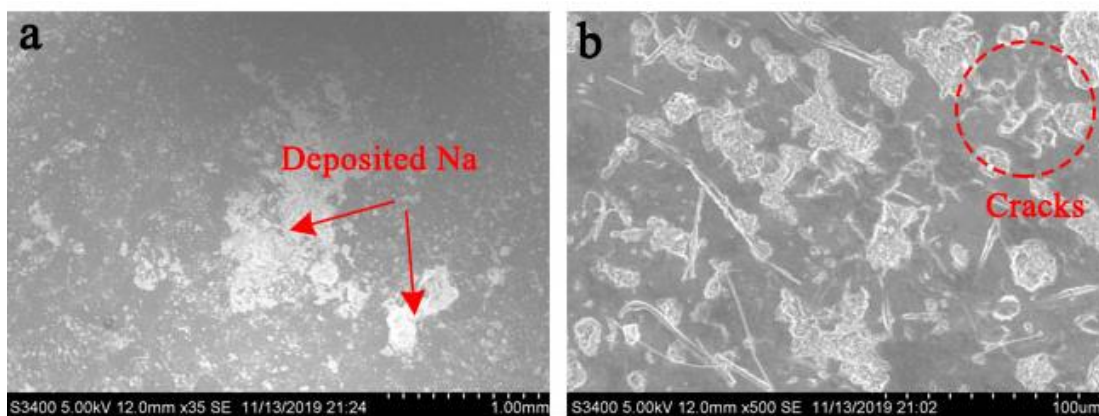

Figure S7.4. (a) The discharge-charge curves of Na-O_2 batteries with SSE and bare Na anode at 0.2 mA cm^{-2}, (b) The cycling performance of Na-O_2 batteries with SSE and bare Na at 0.2 mA cm^{-2} with a limited discharge capacity of 0.2 mA cm^{-2}.
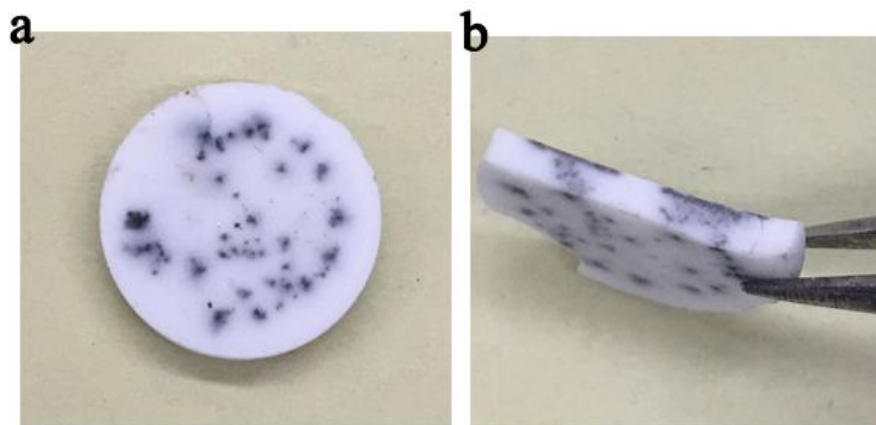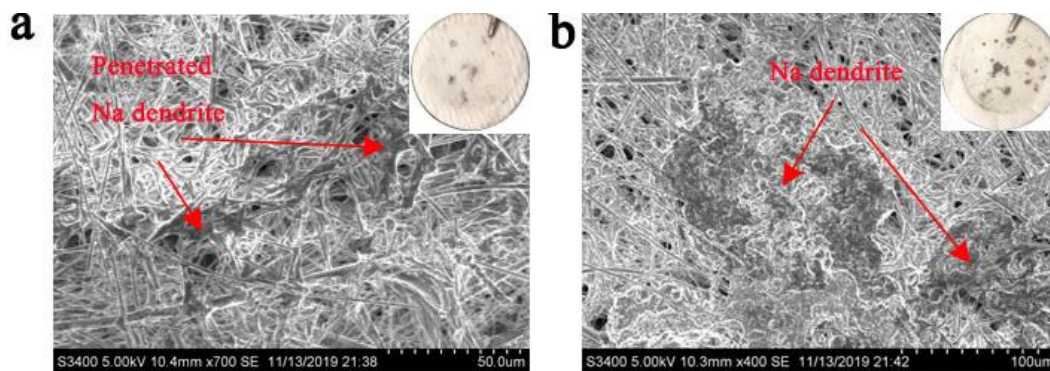
Figure S7.5 Digital photographs of the cycled SSE.
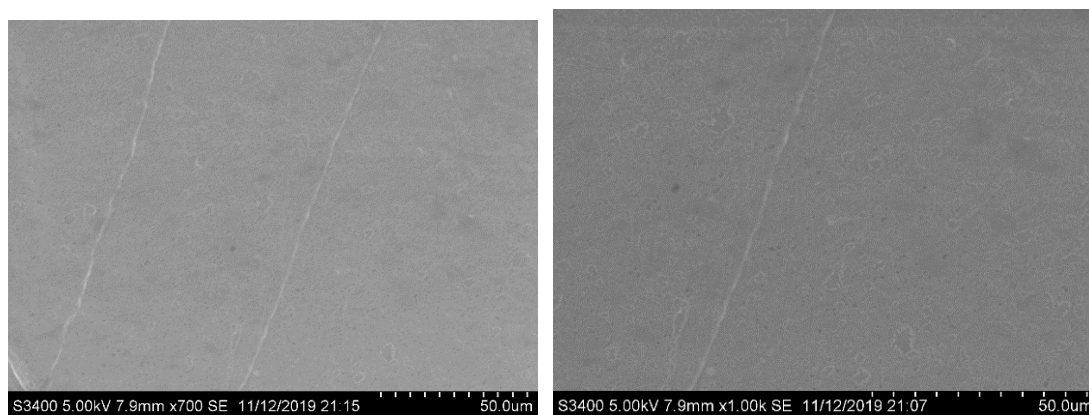
Figure S7.6 The surface morphology of the pristine Na@alucone anode.

Figure S7.7 The SEM images of cycled Na@alucone electrode that obtained from Na-O$_2$ battery using GF separator.

Figure S7.8 The optical and SEM images of GF separator obtained from cycled Na-O$_2$ cell.
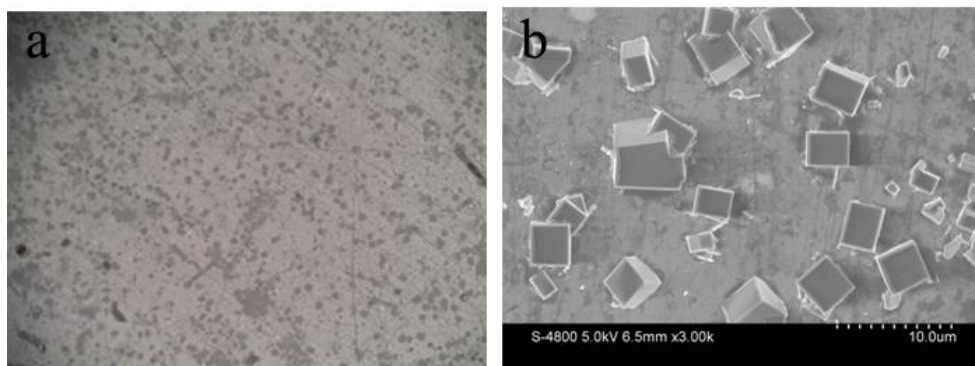

Figure S7.9 The SEM images of cycled Na@alucone electrode that obtained from Na-O$_2$ battery using SSE.
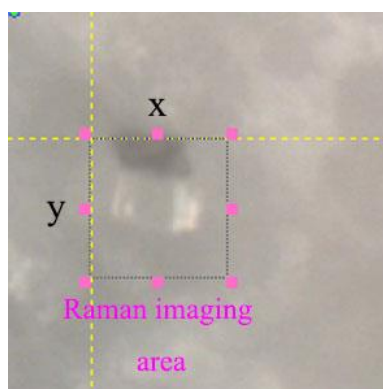

Figure S7.10 The optical image of SSE that obtained from HSS Na-O$_2$ battery with Na@alucone anode after cycling for 80h at 0.2 mA cm^{-2} with a cutoff capacity of 0.2 mAh cm^{-2}.
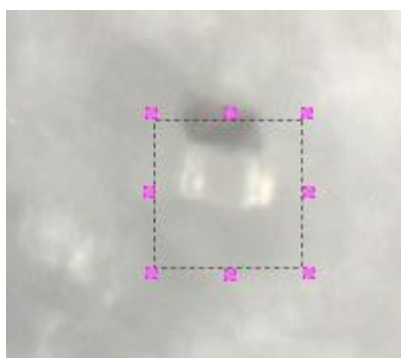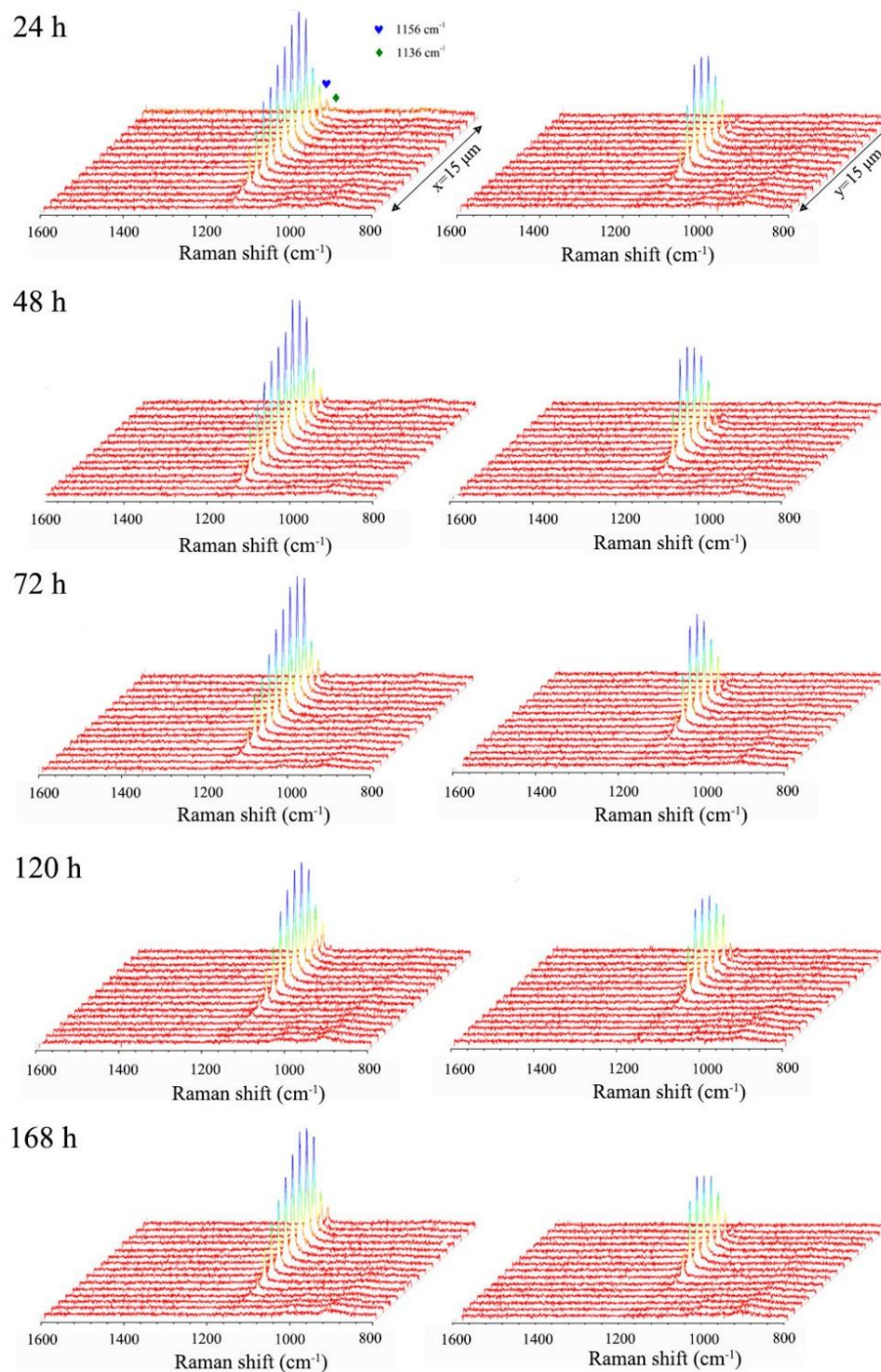
Figure S7.11 The optical image of SSE obtained from (a) Raman microscope and (b) SEM image of SSE.

Figure S7.12 A typical optical image of NaO_2 cube obtained from the Raman microscope.

Figure S7.13 The optical Raman image of NaO_2 cube after 7 days (168 h).

Figure S7.14 Raman spectra recorded over linear scans on a typical NaO_2 cube at different time intervals.
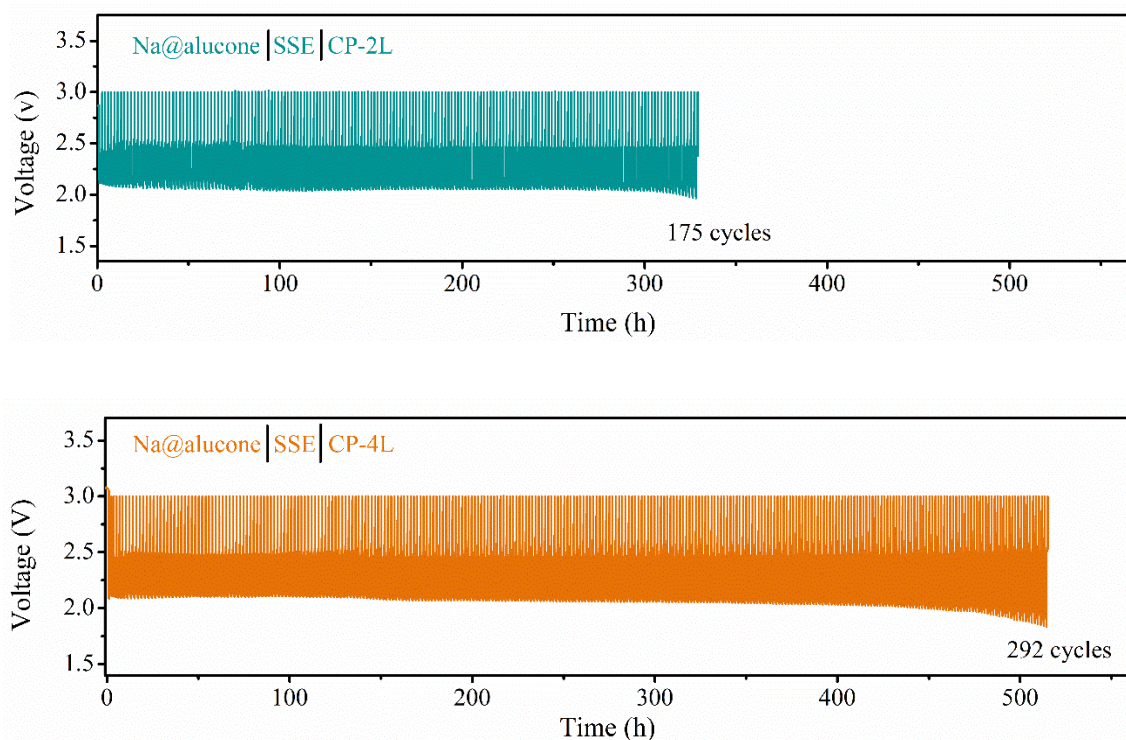
Figure S7.15 The cycling performance of HSS Na-O₂ batteries with CP-2L and CP-4L cathodes.
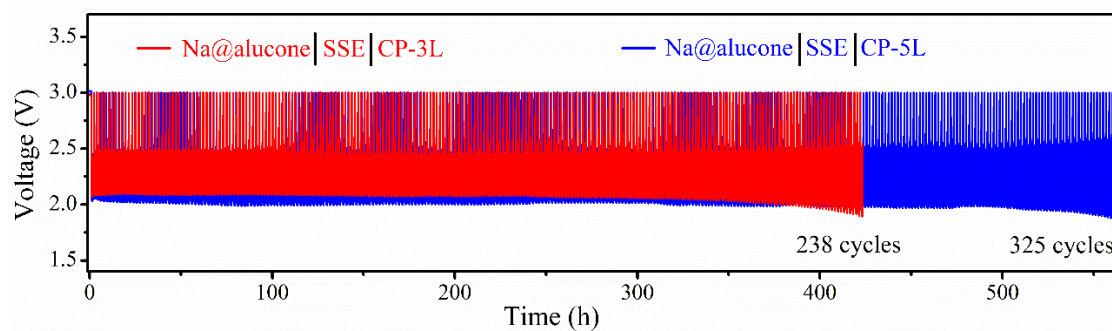
Figure S7.16 The cycling performance of HSS Na-O₂ batteries with CP-3L and CP-5L cathodes.
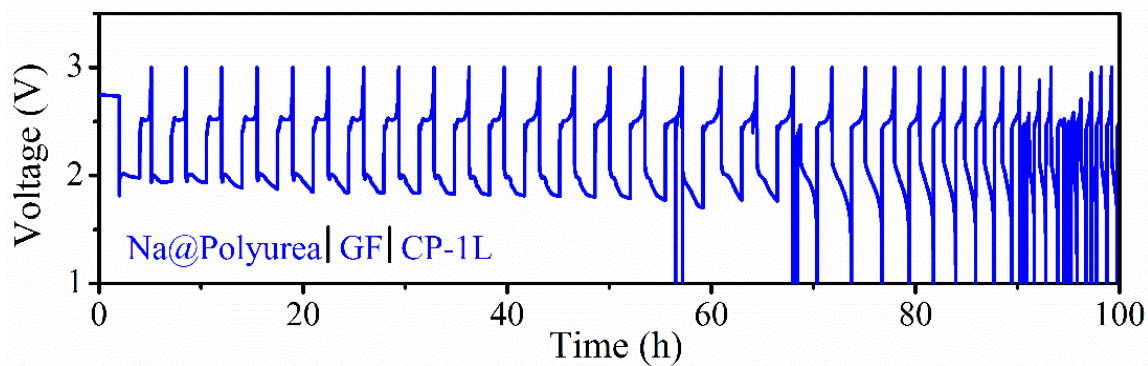
Figure S7.17 The electrochemical performance of Na-O_2 cell with Na@Polyurea anode and GF separator at 0.2 mA cm^{-2} with a cutoff capacity of 0.2 mAh cm^{-2}.

Figure S7.18 The electrochemical performance of Na-O_2 cell with Na@Polyurea anode and SSE at 0.2 mA cm^{-2} with a cutoff capacity of 0.2 mAh cm^{-2}.

Chapter 8

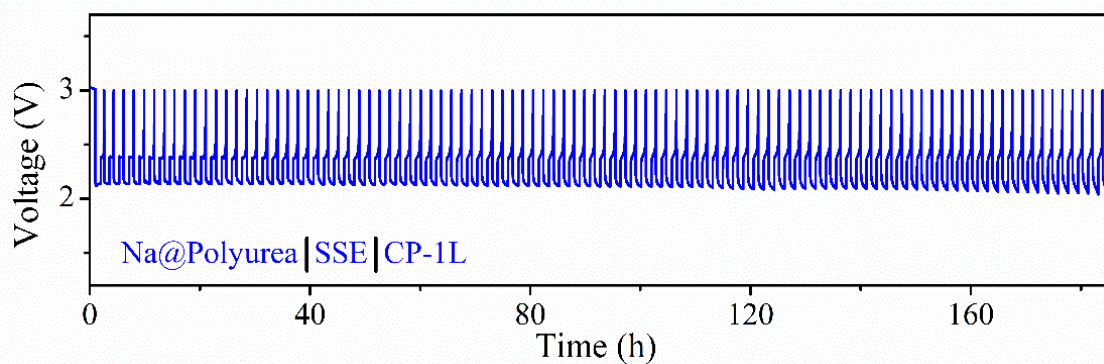# 8 Flame-resistant, dendrite-free and O_2/O_2^--impermeable composite electrolyte for quasi-solid-state Na-O$_2$ batteries

Besides the poor cycle life of Na-O$_2$ batteries, the safety concerns associated with Na dendrite growth and the adoption of flammable organic liquid electrolyte (LE) in conventional Na-O$_2$ batteries also greatly hamper the practical application of Na-O$_2$ batteries.

In this chapter, a novel composite electrolyte using the inorganic 3D porous solid-state electrolyte (PSSE) framework infused with gel polymer electrolyte (GPE) was fabricated. The composite electrolyte was first introduced in Na-O$_2$ batteries to overcome the safety issue and enhance the electrochemical performance. The prepared PSSE/GPE composite electrolyte can synergistically integrate merits from both the inorganic SSE and GPE, exhibiting low flammability, high ionic conductivity, stable electrode/electrolyte interface, and high mechanical strength to suppress the Na dendrite penetration. As a result, excellent electrochemical performance is demonstrated beyond the conventional LE-based Na-O$_2$ batteries under the same conditions. Also, the constructed quasi-solid-state (QSS) Na-O$_2$ batteries exhibited high reversibility and long cycle life of 130 cycles at 0.2 mA cm^{-2} with a cutoff capacity of 0.2 mAh cm^{-2}. It is important to note that the elongated cycling life also benefits from the crucial role of the PSSE/GPE composite electrolyte in alleviating Na corrosion by blocking O_2/O_2^- crossover. It is expected that the present study can shed light on the future study on developing practical Na-O$_2$ batteries.

---

*A version of this manuscript is in preparation.

8.1   Introduction

Great progress has been achieved in researching Li-ion batteries in the past two decades, however their limited energy density still hardly satisfies the requirement of emerging electric vehicles and large-scale energy storage devices.[1] New battery chemistries that beyond Li-ion batteries have been urgently targeted,[2-4] and Na-O_2 batteries have captured extensive attention due to their attractive features such as high theoretical energy density, high energy efficiency and clean chemistry.[5, 6] Despite the high attractiveness of Na-O_2 batteries, their widespread application is currently hampered due to the challenges associated with the uncontrollable Na dendrite growth and the adoption of flammable organic electrolyte in this open battery system, causing safety concerns and unsatisfactory cycling performance.[7-10]

Liquid electrolytes (LEs) combined with porous separators are widely used in Na-O_2 because LEs offer the benefits of high ionic conductivity and excellent wetting of the electrode material at room temperature.[11-14] However, safety hazards continuously arise from the leakage and flammability of organic LEs,[15] especially for open Na-O_2 battery system. Besides, nonuniform deposition of sodium in the LEs during the cell charging process will cause the formation of Na dendrite, which will trigger the risk of internal short circuits or even battery explosions.[10, 16-19] Furthermore, the LEs are incapable of blocking the crossover of oxygen species (O_2/O_2^-) from the cathode to the anode. The resultant Na corrosion has been reported to yield the formation of insulating side products that gradually cover the Na anode surface, causing premature death of Na-O_2 batteries.[5, 7] It is thereby vital to seek new alternatives to organic LEs.

Solid inorganic electrolytes have been considered as promising candidates to overcome the drawbacks of LEs. NASICON-type solid-state electrolytes (SSEs) are capable of outperforming the LEs in terms of battery safety due to their non-flammable nature, as well as their good mechanical strength that enables SSEs to restrain Na dendrite penetration. Nonetheless, although oxygen species (O_2/O_2^-) crossover can also be efficiently blocked by introducing dense SSE pellets into Na-O_2 batteries, the rigidity of inorganic SSEs usually causes contacting problems between the electrolyte and Na electrode.[20, 21] Fortunately, gel-polymer electrolytes (GPEs) can improve the interfacial contact matter

because of its flexibility, and at the same time, solve the liquid solvent leakage problem by encapsulating liquid components in polymer matrices.[22-24] However, most GPEs have inferior mechanical strength and fails to suppress dendrite penetration.[25, 26] To overcome the disadvantages of the NASICON SSE and GPE, such as high interfacial resistance and poor mechanical strength, a composite electrolyte integrating the benefits from different components and addressing the drawbacks of each would be a promising strategy for the development of safe Na-O$_2$ batteres with satisfying electrochemical performance. To the best of our knowledge, the NZSPO and GPE composite electrolyte has never been introduced in Na-O$_2$ battery system.

In this work, a novel composite solid electrolyte based on a PSSE host and GPE filler was successfully designed for constructing quasi-solid-state (QSS) Na-O$_2$ batteries. The PSSE/GPE composite electrolyte can not only inherit the advantages of favorable flame resistance and excellent dendrite impermeability from PSSE framework, but also achieve high ionic conductivity and excellent interfacial contact resulting from the infusion of GPE. Subsequently, the Na symmetric cell based on the PSSE/GPE composite electrolyte stably runs for over 900 h at a current density of 0.2 mA cm^{-2}. Additionally, the introduction of this composite electrolyte avoids the leakage, volatility caused by the adoption of organic LEs in Na-O$_2$ batteries and prevents oxygen species from corroding Na metal anode. The assembled QSS Na-O$_2$ batteries exhibit a long cycle life of 130 cycles at 0.2 mA cm^{-2} with a cutoff capacity of 0.2 mAh cm^{-2}.

8.2   Experimental section

Preparation of PSSE pellets: Firstly, the Na$_{3.25}$Zr$_2$Si$_{2.25}$P$_{0.75}$O$_{12}$ SSE was prepared in air by sol-gel method. Stoichiometric amounts of tetraethyl orthosilicate (Si(OC$_2$H$_5$)$_4$, 98%) and Zirconium (IV) propoxide solution (Zr(OC$_4$H$_9$)$_4$, 99.99%) were sequentially dissolved in 500 mL ethanol. Then, acetic acid and de-ionized water were added to adjust the pH. The mixture sol was kept at 67°C under vigorous stirring for 12 h. Next, the sodium nitrate (Sigma-Aldrich, 99.0%) and ammonium dihydrogen phosphate (Prolabo, 99.9%) were dissolved in distilled water, respectively, and then consecutively added into the hot mixture of silica and zirconia. In the next step, the solution was slowly evaporated at 67°C to get the precursor powder, which was then heated at 500°C for 1h under an O$_2$ atmosphere to

burn out the organics. The obtained powder was hand grounded and then annealed at 1050°C for 10h in an air atmosphere to get the $Na_{3.25}Zr_2Si_{2.25}P_{0.75}O_{12}$ SSE powder. The PSSE framework was prepared via template-assisted calcination method. The as-prepared $Na_{3.25}Zr_2Si_{2.25}P_{0.75}O_{12}$ SSE was mixed with poly(methyl methacrylate) PMMA at a weight ratio of 7:3, and then uniaxially pressed into pellets. The PSSE pellets were achieved after calcinating at 1300°C for 12 h in an air atmosphere.

Preparation of the PSSE/GPE composite electrolyte: The GPE solution was first prepared by adding 2g of PEO and 2 mL of the liquid electrolyte (1M $NaClO_4$ in Tetraethylene glycol dimethyl ether) into 20 mL of acetonitrile, and then vigorously stirred at room temperature overnight. Then, the viscous solution was infused into the PSSE pellets using a vacuum pump, which were then naturally dried in the air. This process was repeated several times to ensure the pores in the PSSE pellets are fully filled. After the PSSE/GPE was obtained, the GPE membrane was prepared by a solution-casting method. The viscous GPE solution was cast onto a clean glass plate and naturally dried in the air to remove the acetonitrile solvent, yielding a PEO membrane with a thickness of about 500 µm.

Battery assembly and electrochemical performance characterization: The cycling stability of Na symmetric cells with the PSSE/GPE or GPE membrane was performed using CR2032 coin-type cells. The electrochemical performance of $Na-O_2$ batteries was evaculated with Swagelok-type cells. The QSS $Na-O_2$ batteries were assembled with Na metal anode, PSSE/GPE or GPE electrolyte, and CP cathode. The CP cathode and Na metal foil were cut into circular pieces with a diameter of 3/8 inch. Both Na symmetric cells and $Na-O_2$ cells were assembled in a Ar-filled glovebox with the oxygen and moisture levels below 0.1 ppm. The $Na-O_2$ batteries were operated under static O_2 with the pressure of 1.0 atm in a homemade testing box, and each cell was stabilized for 1h before testing. The galvanostatic discharge/charge tests were carried out using the Arbin BT-2000 battery testing system. It is noteworthy that the PSSE/GPE and GPE were dried under a vacuum to remove the moisture and residual acetrontile solvent before transfering into the glove box to assemble the batteries.

Materials characterization: The X-ray powder diffraction (XRD) patterns were performed via Bruker D8 X-ray diffractometer equipped with Cu-Kα (λ=1.5406Å) radiation. The morphologies of CP cathodes were characterized by Hitachi S-4800 field-emission scanning electron microscope (FE-SEM), and the morphological studies of the PSSE/GPE and GPE electrolytes were performed using a Hitachi 3400N environmental SEM. The ionic conductivity of the PSSE/GPE composite electrolyte was measured using electrochemical impedance spectroscopy (EIS) in the frequency range of 10 Hz to 100 k Hz. In this study, the disassembly of the Na-O_2 batteries was carried out in an ultra pure argon-filled glovebox. The discharged cathodes were washed with fresh TEGDME to remove any residual $NaClO_4$ salt, and then vacuum dried before SEM and XRD measurements. Additionally, the as-prepared samples were sealed into leak-tight homemade sample holders to prevent the exposure of air during sample testing.

8.3   Results and discussion
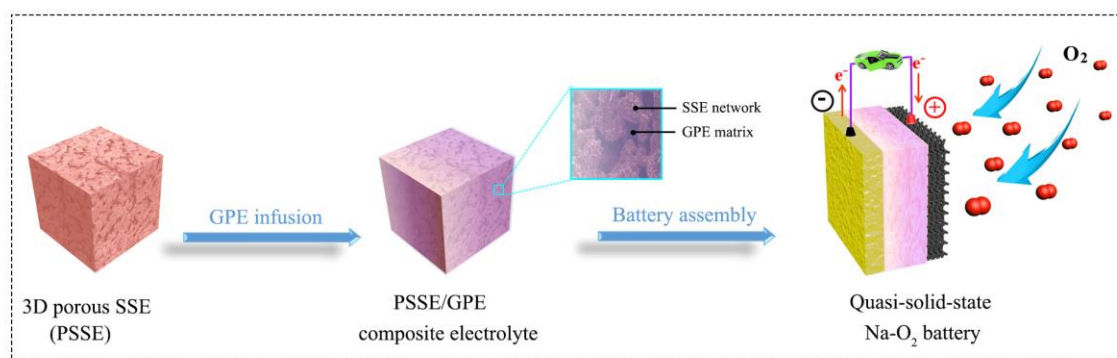
Figure 8.1 A schematic for the preparation process of the PSSE/GPE composite electrolyte for QSS Na-O_2 batteries.

The schematic diagram for the preparation of the PSSE/GPE composite electrolyte is shown in **Figure 8.1**. Firstly, the mixture of $Na_{3.25}Zr_2Si_{2.25}P_{0.75}O_{12}$ SSE powder and poly(methyl methacrylate) (PMMA) spheres with a weight ratio of 7:3 was pressed into pellets, and then sintered in the air to obtain the PSSE framework. During this process, the PMMA spheres (**Figure S8.1**) were added as the sacrificial porogens to create the pores in the PSSE pellets. In the next step, polyethylene oxide (PEO)-based GPE solution was infused into the PSSE framework using a vacuum pump, followed by naturally drying in

the air to evaporate the acetonitrile solvent. Among various polymer candidates, the PEO is chosen in this work due to its relatively high electrochemical stability below 4.0V, which match well with the electrochemical window (1.0-3.0 V) of Na-O$_2$ batteries. It is worth mentioning that the infusion process was repeated for several times to ensure the pores within the PSSE pellets are fully filled. In comparison, the GPE membrane was also prepared using the solution-casting method. While before the as-prepared electrolytes were transferred into the glovebox for battery assembly, a further vacuum drying procedure was conducted at room temperature in order to remove the moisture and residual acetonitrile solvent.
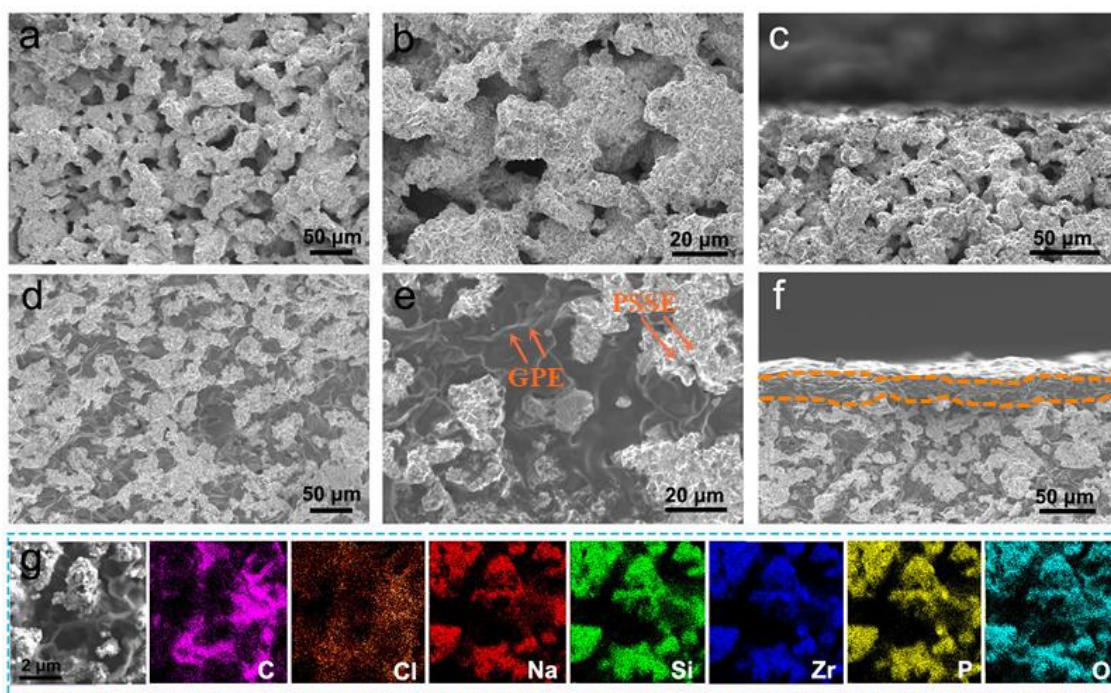
Figure 8.2 Cross-sectional SEM images of (a-c) PSSE, and (d-f) PSSE/GPE composite electrolyte at different magnification; (g) SEM image and corresponding elemental mapping of PSSE/GPE composite electrolyte.

Unlike sulfide- and halide-type SSEs that are very sensitive to air and moisture, NASICON-type SSEs are chemically stable for processing in the air.[27,28] Even co-sintering with PMMA in the air does not change the crystalline structure of Na$_{3.25}$Zr$_2$Si$_{2.25}$P$_{0.75}$O$_{12}$, which is confirmed by the XRD pattern in **Figure S8.2**. The microstructure morphologies

of the PSSE framework are characterized by using scanning electron microscopy (SEM). As presented in **Figure 8.2a-c** and **S8.3**, the cross-section view SEM images show that the NZSPO crystal grains (0.5-2 µm) are interconnected to create a porous framework with high open porosity and abundant networks. The irregular pores within the PSSE are in the range of 20-50 µm and are also continuous, which is favorable for the subsequent GPE filling. After the infusion process, almost all the pores within the PSSE have been filled with GPE. Furthermore, high-magnification SEM image indicate that the PSSE are compactly coated and surrounded by GPE, suggesting an excellent contact and adhesion capability between the PSSE and GPE (**Figure 8.2d-f** and **S8.4**). The energy dispersive spectroscopy (EDS) elementary mapping of composite electrolyte demonstrates the distribution of elemental Cl, C, Na, Si, Zr, P and O, further confirming the successful infusion of $NaClO_4$-containing PEO GPE into PSSE networks (**Figure 8.2f**). Interestingly, the GPE not only fills the inner space of the PSSE, the flooded GPE also forms a film (~ 25 µm) that comformally coated on the surface of the PSSE skeleton. The formation of this thin GPE layer can compensates for the interfacial roughness of PSSE and ensures intimate contact between the PSSE/GPE composite electrolyte and Na metal anode, facilitating an evenly distributed Na^+ flux at the interface. Moreover, the good compatibility between PSSE and GPE results in a dense structure of the composite electrolyte, which is presumbly capable of preventing O_2/O_2^- migration to the Na anode and thus prevents Na metal from O_2/O_2^- corrosion.[29]

Since the flame-retardant properties of the electrolyte is crucial for the safety of the Na-O_2 batteries, the combustion test for the electrolyte membranes was conducted. For the conventional 2400 Celgard separator saturated with electrolyte that is used in conventional Na-O_2 batteries, as shown in **Figure 8.3a-c**, the separator showed a big flame when it was ignited. Following the generation of the large flame, the Celgard separator completely extinguishes and shrinks within a short period of time. Although the GPE electrolyte did not catch fire immediately when lit, the destruction of the electrolyte cannot be avoided. In sharp contrast, the PSSE/GPE demonstrated a much lower flammability, and the fire can be quenched spontaneously after several seconds (**Figure 8.3d-f**). Moreover, the composite electrolyte can keep it's original shape and size due to the presence of the PSSE framework, indicating perfect flame retarding ability under harsh condition. The structural stability of

the composite electrolyte keeps the Na anode and cathode separated when the accident took place, guaranteeing higher safety performance compared to the conventional Celgard separator and GPE membrane.
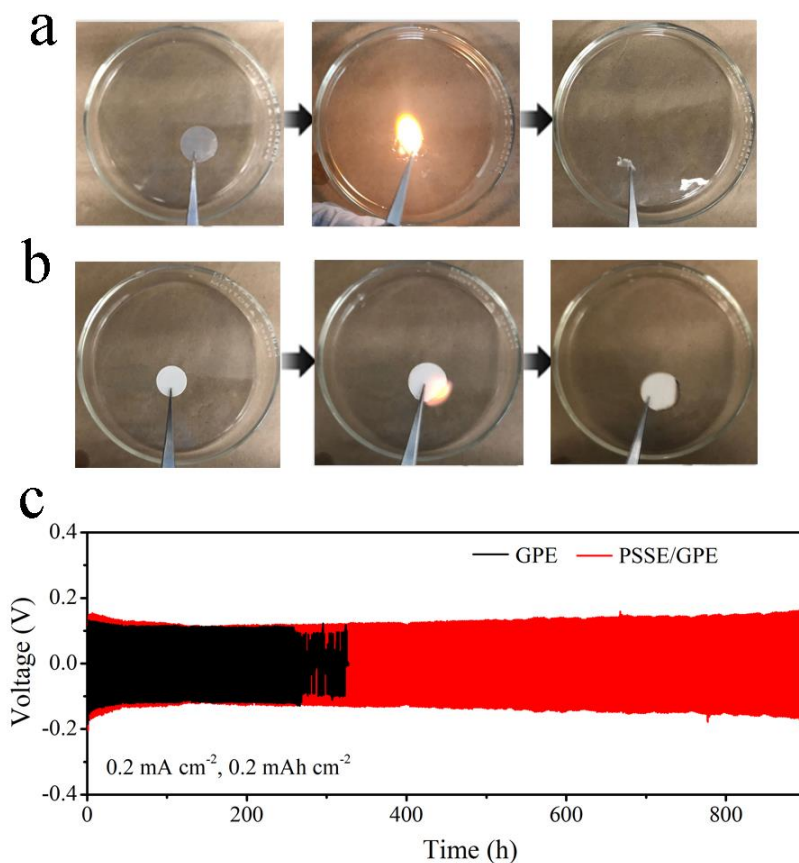
Figure 8.3 Combustion of (a) 2400 Celgard separator saturated with ether-based liquid electrolyte and (b) PSSE/GPE quasi-solid-state electrolyte; (c) cycling performance of Na symmetric cells with GPE membrane and PSSE/GPE quasi-solid-state electrolyte at 0.2 mA cm^{-2}, respectively.

The ionic conductivity of the composite electrolyte was measured through electrochemical impedance spectroscopy (EIS) measurement and is determined to be 1.4×10^{-3} S cm^{-1} (**Figure S8.5**). Such a high ionic conductivity of the PSSP/GPE composite electrolyte is comparable to that of a liquid electrolyte that enables fast Na$^+$ transportation during the discharge and charging process. To provide an in-depth insight of the PSSE/GPE composite electrolyte, the galvanostatic cycling stability of Na symmetric cells with the PSSE/GPE composite electrolyte was investigated. Upon cycling, Na was

electrochemically stripped and plated between the two elelctrodes at 0.2 mA cm^{-2} with a deposition capacity of 0.2 mAh cm^{-2} (**Figure 8.3g**). In comparison, the cell using GPE was also tested under same experimental conditions. Notably, the voltage of the cell using the PSSE/GPE electrolyte is satbilized at ~ 0.18V with slight increase of overpotential during the long cycle of 900 h. After 300h cycles, no obvious Na dendrite can be observed on the Na metal, as verified by the SEM images in **Figure S8.6**. While the Na/GPE/Na cell short circuit after only 280 due to the penetration of Na dendrites. As observed by SEM, Na dendrites and dead Na appeared on the surface of the Na anode **(Figure S8.7)**. It is important to highlight that the cycling stability of the Na symmetric cell using PSSE/GPE composite electrolyte is also superior to that of the Na/SSE/Na cell, in which the poor Na/SSE interfacial contact result in the nonuniform Na$^+$ distribution and subsequent Na dendrite growth along the grain boundaries of NZSPO particles.[7, 20] These results indicated that the penetration of Na dendrites can be efficiently mitigated by employing the PSSE/GPE composite electrolyte, which is derived from not only the high mechanical strength of the composite electrolyte, but also the good interfacial contact between the composite electrolyte and Na electrodes.
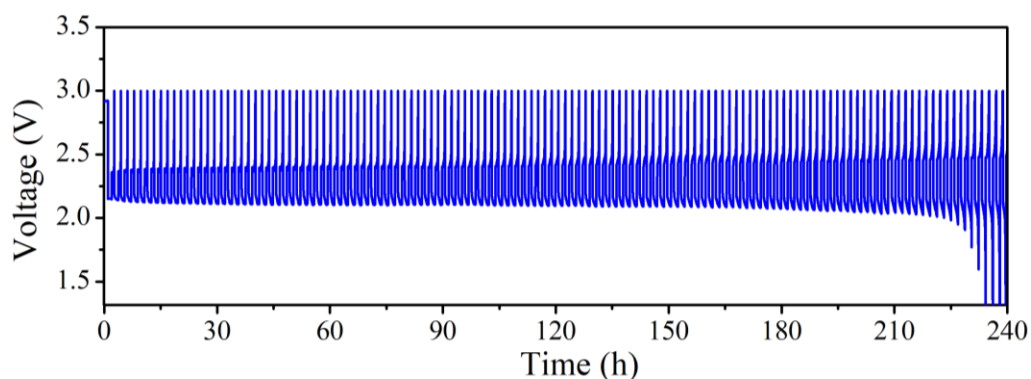
Figure 8.4 The cycling stability of QSS Na-O$_2$ battery at 0.2 mA cm^{-2} with a cutoff capacity of 0.2 mAh cm^{-2}.

Na-O$_2$ batteries are designed as an open system with O$_2$ as the active material; O$_2$ crossover has been reported to have a significant effect on the operational stability of conventional Na-O$_2$ batteries. To demonstrate the applicability of the PSSE/PEO composite electrolyte for the development of Na-O$_2$ batteries, the PSSE/PEO composite electrolyte is further

combined with a Na metal anode and carbon paper (CP) cathode to assemble the full cells. As shown in **Figure S8.8**, the fabricated QSS Na-O$_2$ battery delivered a high initial discharge capacity of 4.22 mAh cm^{-2} at the current density of 0.2 mA cm^{-2}. More importantly, the cells can be fully recharged without short circuits compared to those observed in conventional Na-O$_2$ batteries with Celgard separators.[30] Moreover, the PSSE/GPE-based Na-O$_2$ battery exhibits comparable discharge and charge plateau voltages to that of LE-based battery, agreeing well with the EIS results.[31] The major discharge product of the Na-O$_2$ batteries was identified as micrometer-sized NaO$_2$ cubes (**Figure S8.9**). After completing the recharging process, the NaO$_2$ can be decomposed, evidenced from the disappearance of NaO$_2$ cubes in the CP cathode. This indicatesg the excellent reversibility of the generation and decomposition of NaO$_2$ (**Figure S8.10**). This is consistent with the reaction mechanism that is reported in liquid-based Na-O$_2$ batteries.[32] The cyclability of QSS Na-O$_2$ batteries was further characterized at 0.2 mA cm^{-2} with a cutoff capacity of 0.2 mAh cm^{-2}. The battery exhibits an extended cycle life of 130 cycles without obvious discharge/charge overpotential increasees in the initial 80 cycles(**Figure 8.4**). This phenomenon indicate the constent internal cell resistance due to the elimination of Na corrosion by migrated oxygen species.
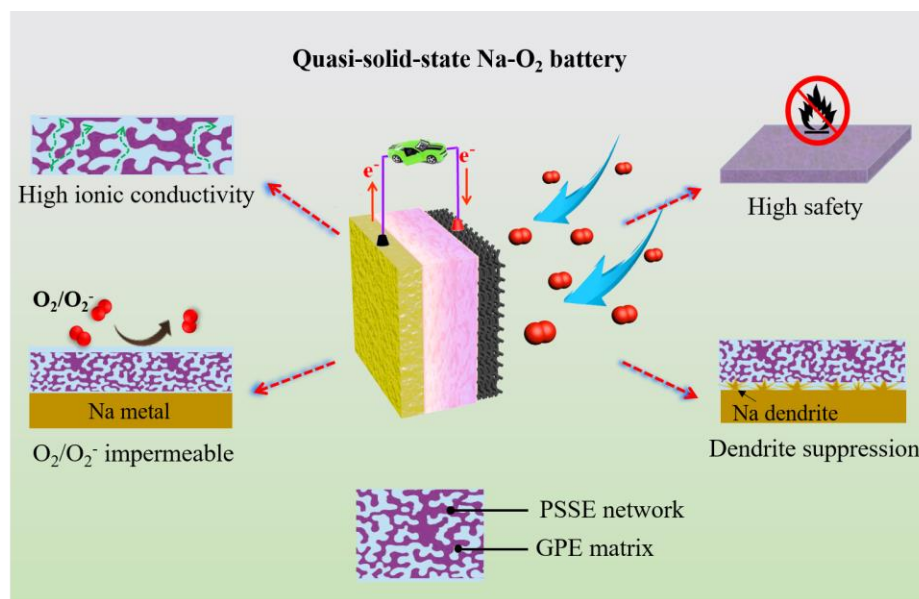
Figure 8.5 Schematic diagram of PSSE/GPE composite electrolyte-based QSS Na-O$_2$ battery.

Understanding the origin of the superiority of PSSE/PEO composite electrolyte in Na-O$_2$ batteries is pivitol for designing novel Na-O$_2$ batteries with further improved performance. As mentioned, the conventional Na-O$_2$ batteries suffer from premature cell death due to the Na dendrite penetration through the separator and the Na corrosion as a result on O$_2$ migration. The PSSE/PEO composite electrolyte is composed of connected PSSE reinforcement scaffold and GPE matrix. On one hand, the NZSPO framework enables composite electrolytes with high mechanical rigidity to suppress Na dendrite growth without internal cell short circuiting. On the other hand, the liquid electrolyte phase that is incorporated into the PEO matrix endows the composite electrolyte with high ionic conductivity. At the same time, the soft PEO layer on the composite electrolyte surface can adopt the volume changes of the Na electrode during the repeated striping/plating process, which is beneficial for maintaining an intimate interfacial contact and smooth ion transportation. In addition, the composite electrolyte with a compact structure possesses strong resistibility towards O$_2$ crossover corrosion of the Na metal anode. All those merits of the composite electrolyte may contribute to the high cycling stability of QSS Na-O$_2$ battery (**Figure 8.5**). While it should be mentioned that efforts on Li-O$_2$ batteries screening have identified that the PEO is relatively stable against the oxidative species at low voltages ($\leq$ 3V),[33] which additionally contributed to the long life of Na-O$_2$ batteries in this study. Additionally, the high flame-resistant ability enables composite electrolytes promising practical applications in Na-O$_2$ batteries in the future.

8.4 Conclusion

In conclusion, a novel composite electrolyte consisting of a 3D NASICON framework and GPE matrix have been successfully designed for high-performance Na-O$_2$ batteries. The PSSE skeleton in composite electrolytes acts as a mechanical barrier to prevent Na dendrite penetration and flame attacks. With the infusion of the GPE matrix, the composite electrolyte manifests high ionic conductivity and offers a stable interface between composite electrolytes and electrodes. Benefiting from the above-mentioned merits, the PSSE/GPE composite electrolyte shows a steady performance in the Na symmetric cell. More importantly, the composite electrolyte can hold back the O$_2$ crossover to the reactive Na metal anode, enabling the achievement of QSS Na-O$_2$ batteries with high discharge

capacities and stable cycle life for more than 130 cycles. This work provides an appealing strategy for the development of high-safety solid-state Na-O$_2$ batteries.

8.5 Acknowledgments

8.6 Reference

1. Lin, X.; Li, P.; Shao, L.; Shui, M.; Wang, D.; Long, N.; Ren, Y.; Shu, J., Journal of Power Sources 2015, 278, 546-554.

2. Yang, X.; Gao, X.; Sun, Q.; Jand, S. P.; Yu, Y.; Zhao, Y.; Li, X.; Adair, K.; Kuo, L.-Y.; Rohrer, J.; Liang, J.; Lin, X.; Banis, M. N.; Hu, Y.; Zhang, H.; Li, X.; Li, R.; Zhang, H.; Kaghazchi, P.; Sham, T.-K.; Sun, X., Advanced Materials 2019, 31, (25), 1901220.

3. Zhao, C.; Yu, C.; Liu, S.; Yang, J.; Fan, X.; Huang, H.; Qiu, J., Advanced Functional Materials 2015, 25, (44), 6913-6920.

4. Zeng, X.; You, C.; Leng, L.; Dang, D.; Qiao, X.; Li, X.; Li, Y.; Liao, S.; Adzic, R. R., Journal of Materials Chemistry A 2015, 3, (21), 11224-11231.

5. Xiaoting, L.; Qian, S.; Hossein, Y.; Xiaofei, Y.; Yang, Z.; Changhong, W.; Jianneng, L.; Alicia, K.; Ruying, L.; Xueliang, S., Advanced Functional Materials 0, (0), 1801904.

6. Yadegari, H.; Sun, Q.; Sun, X., Advanced Materials 2016, 28, (33), 7065-7093.

7. Lin, X.; Sun, F.; Sun, Q.; Wang, S.; Luo, J.; Zhao, C.; Yang, X.; Zhao, Y.; Wang, C.; Li, R.; Sun, X., Chemistry of Materials 2019, 31, (21), 9024-9031.

8. Bi, X.; Ren, X.; Huang, Z.; Yu, M.; Kreidler, E.; Wu, Y., Chemical Communications 2015, 51, (36), 7665-7668.

9. Bing, S.; Peng, L.; Jinqiang, Z.; Dan, W.; Paul, M.; Chengyin, W.; L., N. P. H.; Guoxiu, W., Advanced Materials 0, (0), 1801334.

10. Medenbach, L.; Bender, C. L.; Haas, R.; Mogwitz, B.; Pompe, C.; Adelhelm, P.; Schröder, D.; Janek, J., Energy Technology 2017, 5, (12), 2265-2274.

11. Xia, C.; Black, R.; Fernandes, R.; Adams, B.; Nazar, L. F., Nat Chem 2015, 7, (6), 496-501.

12. Hartmann, P.; Bender, C. L.; Vračar, M.; Dürr, A. K.; Garsuch, A.; Janek, J.; Adelhelm, P., Nat Mater 2013, 12, (3), 228-232.

13. Ha, T. A.; Fdz De Anastro, A.; Ortiz-Vitoriano, N.; Fang, J.; MacFarlane, D. R.; Forsyth, M.; Mecerreyes, D.; Howlett, P. C.; Pozo-Gonzalo, C., The Journal of Physical Chemistry Letters 2019, 10, (22), 7050-7055.

14. Ortiz-Vitoriano, N.; Monterrubio, I.; Garcia-Quintana, L.; López del Amo, J. M.; Chen, F.; Rojo, T.; Howlett, P. C.; Forsyth, M.; Pozo-Gonzalo, C., ACS Energy Letters 2020, 5, (3), 903-909.

15. Li, X.; Liang, J.; Yang, X.; Adair, K. R.; Wang, C.; Zhao, F.; Sun, X., Energy & Environmental Science 2020.

16. Lin, X.; Sun, Q.; Doyle Davis, K.; Li, R.; Sun, X., Carbon Energy n/a, (n/a).

17. Ma, J.-l.; Meng, F.-l.; Yu, Y.; Liu, D.-p.; Yan, J.-m.; Zhang, Y.; Zhang, X.-b.; Jiang, Q., Nature Chemistry 2019, 11, (1), 64-70.

18. Guo, X.; Sun, B.; Su, D.; Liu, X.; Liu, H.; Wang, Y.; Wang, G., Science Bulletin.

19. Sun, B.; Xiong, P.; Maitra, U.; Langsdorf, D.; Yan, K.; Wang, C.; Janek, J.; Schröder, D.; Wang, G., Advanced Materials n/a, (n/a), 1903891.

20. Zhou, W.; Li, Y.; Xin, S.; Goodenough, J. B., ACS Central Science 2017, 3, (1), 52-57.

21. Yu, X.; Xue, L.; Goodenough, J. B.; Manthiram, A., ACS Materials Letters 2019, 1, (1), 132-138.

22. Zhao, C.; Liang, J.; Zhao, Y.; Luo, J.; Sun, Q.; Liu, Y.; Lin, X.; Yang, X.; Huang, H.; Zhang, L.; Zhao, S.; Lu, S.; Sun, X., Journal of Materials Chemistry A 2019, 7, (43), 24947-24952.

23. Zou, X.; Lu, Q.; Zhong, Y.; Liao, K.; Zhou, W.; Shao, Z., Flexible, Small 2018, 14, (34), 1801798.

24. Liu, M.; Zhou, D.; He, Y.-B.; Fu, Y.; Qin, X.; Miao, C.; Du, H.; Li, B.; Yang, Q.-H.; Lin, Z.; Zhao, T. S.; Kang, F., Nano Energy 2016, 22, 278-289.

25. Yang, T.; Shu, C.; Zheng, R.; Li, M.; Hou, Z.; Hei, P.; Zhang, Q.; Mei, D.; Long, J., ACS Sustainable Chemistry & Engineering 2019, 7, (20), 17362-17371.

26. Chen, G.; Zhang, F.; Zhou, Z.; Li, J.; Tang, Y., Advanced Energy Materials 2018, 8, (25), 1801219.

27. Song, S.; Duong, H. M.; Korsunsky, A. M.; Hu, N.; Lu, L., Scientific Reports 2016, 6, (1), 32330.

28. Chen, S.; Wu, C.; Shen, L.; Zhu, C.; Huang, Y.; Xi, K.; Maier, J.; Yu, Y., Advanced Materials 2017, 29, (48), 1700431.

29. Ansari, Y.; Virwani, K.; Yahyazadeh, S.; Thompson, L. E.; Lofano, E.; Fong, A.; Miller, R. D.; La, Y.-H., Advanced Energy Materials 0, (0), 1802603.

30. Lin, X.; Sun, Q.; Yadegari, H.; Yang, X.; Zhao, Y.; Wang, C.; Liang, J.; Koo, A.; Li, R.; Sun, X., Advanced Functional Materials 2018, 28, (35), 1801904.

31. Zhao, N.; Li, C.; Guo, X., Physical Chemistry Chemical Physics 2014, 16, (29), 15646-15652.

32. Ortiz-Vitoriano, N.; Batcho, T. P.; Kwabi, D. G.; Han, B.; Pour, N.; Yao, K. P. C.; Thompson, C. V.; Shao-Horn, Y., The Journal of Physical Chemistry Letters 2015, 6, (13), 2636-2643.

33. Amanchukwu, C. V.; Harding, J. R.; Shao-Horn, Y.; Hammond, P. T., Chemistry of Materials 2015, 27, (2), 550-561.
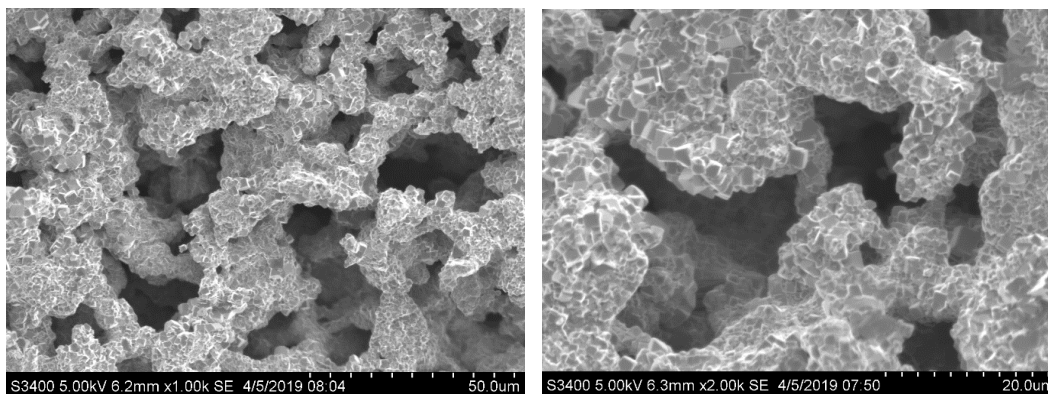
8.7   Supporting information
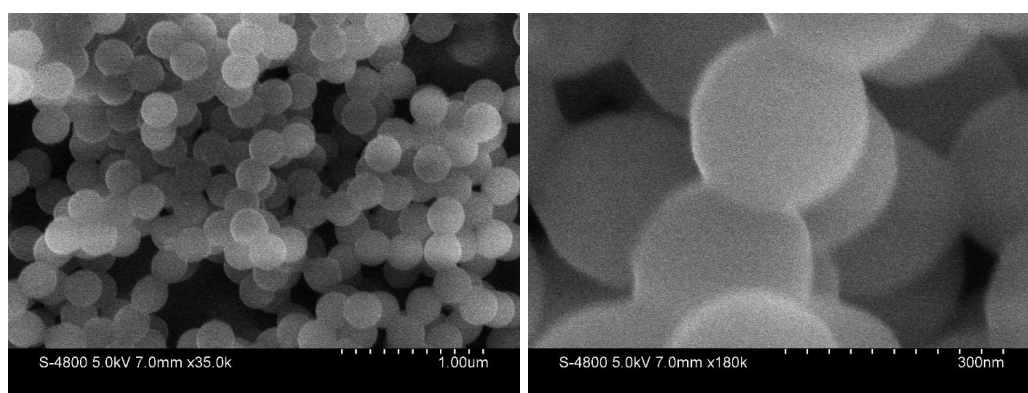
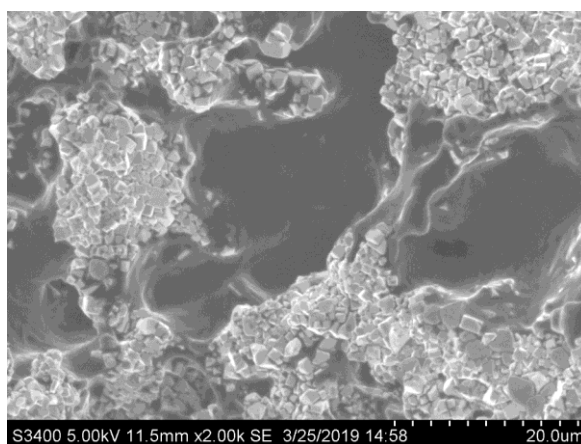**Figure S8.1**. The SEM images of the PMMA spheres at different magnifications.
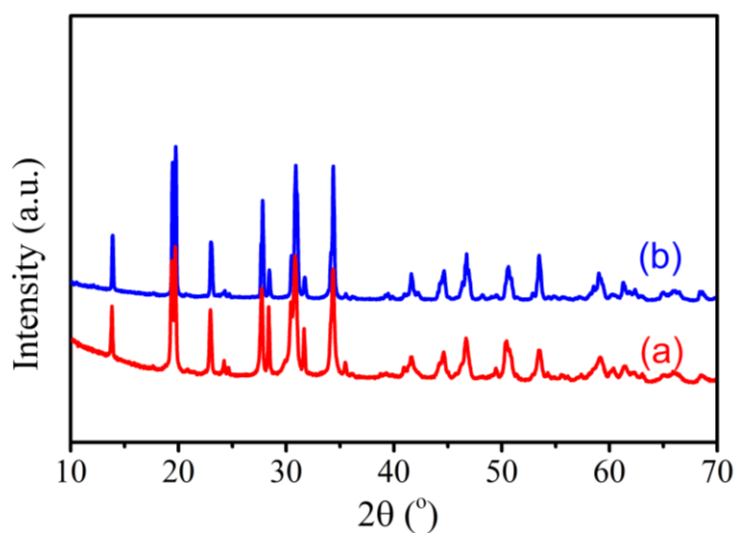
Figure S8.2. The XRD patterns of (a) dense SSE and (b) as-prepared PSSE framework.
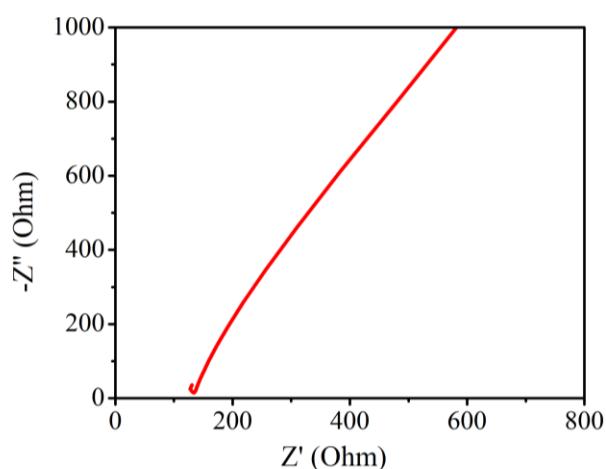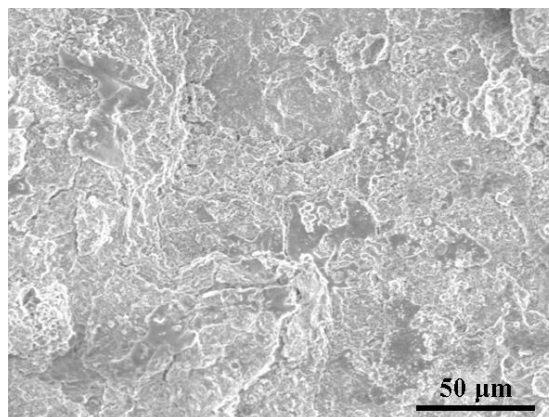
Figure S8.3. The cross-sectional SEM images of PSSE at different magnifications.
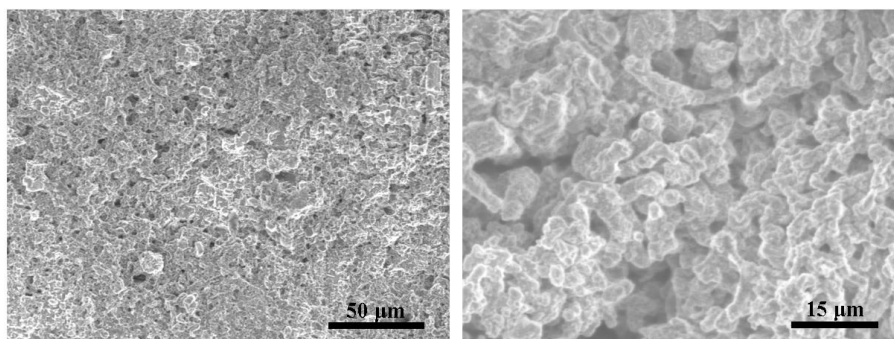

**Figure S8.4.** The cross-sectional SEM image of composite electrolyte.

Figure S8.5. Nyquist plots of the composite electrolyte with the cell structure of stainless steel (SS)/composite electrolyte/SS.
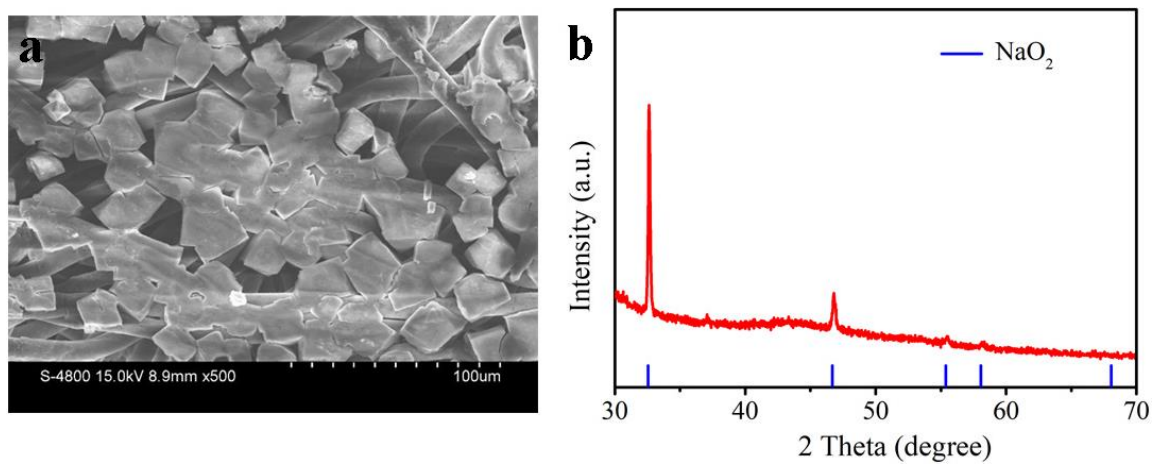
Figure S8.6. The SEM image of Na electrode that obtained from cycled Na symmetric cell assembled with PSSE/GPE composite electrolyte.
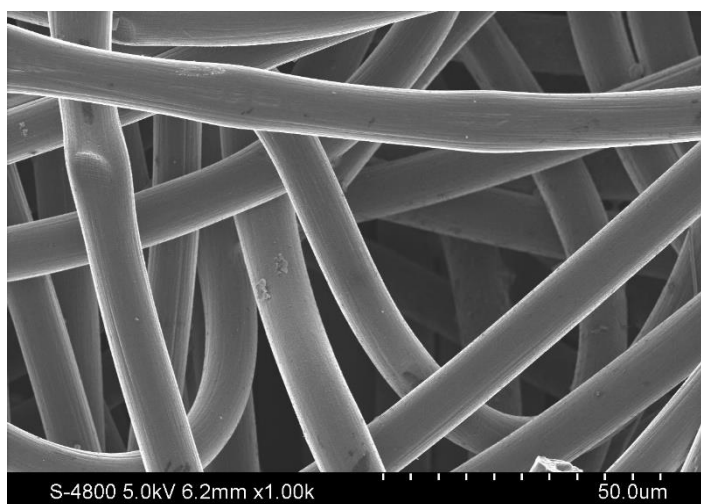

Figure S8.7. The SEM image of Na electrode that obtained from cycled Na symmetric cell that assembled with GPE electrolyte.
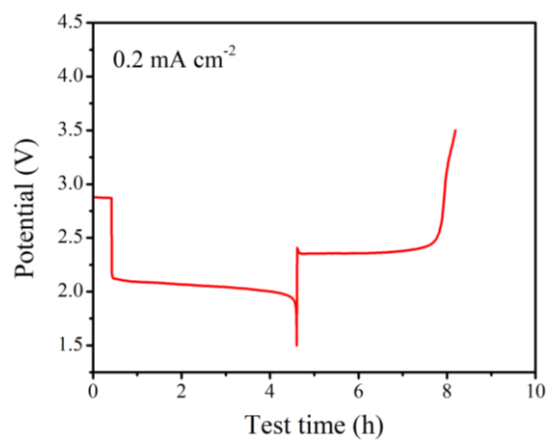
Figure 8.8. The discharge/charge behavior of QSS Na-O$_2$ battery at the current density of 0.2 mA cm^{-2}.

Figure S8.9. The (a) SEM image and (b) XRD pattern of discharged CP cathode.

Figure S8.10. The SEM image of recharged CP cathode.

Chapter 9

9   Conclusion and future perspective

This chapter summarizes conclusions and contributions of this thesis, as well as personal statements and suggestions for future work.

9.1 Conclusion

The development of next-generation electric vehicles and large-scale energy storage systems requires new chemistries beyond state-of-the-art lithium ion batteries. Among various new battery technologies, such as Li-S and metal-oxygen batteries, superoxide-based Na-O$_2$ batteries have attracted an extensive amount of attention due to their ultra-high theoretical energy density, high energy efficiency, and the abundance of sodium. Although great efforts have been devoted in developing advanced electrodes, the low achievable discharge capacities and poor cycling performance are still hindering the practical application of Na-O$_2$ batteries. Currently, the main challenges of superoxide-based Na-O$_2$ batteries can be summarized as: 1) pore clogging and insufficient O$_2$ transportation within the air electrode; 2) the uncontrollable Na dendrite growth; 3) Na degradation caused by O$_2$/O$_2^-$ crossover.

This thesis work mainly focuses on improving the electrochemical performance of Na-O$_2$ batteries via rational design of cell configurations. A series of experimental designs were carried out in this study to fabricate novel air electrode and stabilize Na metal anodes for Na-O$_2$ batteries. Different physical and electrochemical characterizations were conducted to determine the relationship of physical/chemical properties of the as-prepared electrodes and Na-O$_2$ cell performance. Furthermore, the underlying mechanisms of materials/electrodes and their electrochemical reactions were explored, such as the relationship between air electrodes structure and spatial distribution of NaO$_2$; the O$_2$/O$_2^-$ crossover effect on the nature of solid electrolyte interphase (SEI) layer; the chemical changes of NaO$_2$ in contacting with NASICON-type solid-state electrolyte (SSE); etc. In summary, this thesis focused on the design of the Na-O$_2$ cell components and mainly works on four parts: air electrode fabrication, Na anode protection, physical/electrochemical characterization, and the understanding of underlying mechanisms. The detailed study gained a better understanding on the importance of electrodes design in Na-O$_2$ cell performance, and it is believed that these novel designs and analysis bring new insights of Na-O$_2$ batteries in their future applications.

Firstly, freestanding "O$_2$ breathable" air electrodes for Na-O$_2$ batteries were fabricated using 3D printing technique. The designed air electrode provides separated pathways for

O_2, Na^+ and electron transport. The built-in open pores can facilitate O_2 access into the interior cathode, preventing pore clogging and premature cease of discharge process. At the same time, the electrolyte is accommodated among the rGO sheets and the electrons are conducted via the conductive rGO framework, which is beneficial for the fast mass/electron transportation within the air electrodes. The high discharge capacities and unprecedentedly stable cycling performance of Na-O_2 batteries with 3D printed air electrodes clearly elucidates the importance of the structural design of the air electrodes for realizing high-performance Na-O_2 batteries.

Novel Na-O_2 batteries using electrically connected carbon paper (CP) and Na metal as protected Na anodes were constructed. In this study, the O_2^- crossover issue was first revealed, which contributed to the detrimental Na corrosion and limited Coulombic efficiency. The study further demonstrated that the adoption of CP protected Na anode can completely inhibit the cell short-circuiting by preventing the Na dendrite growth. At the same time, the CP on the Na anode also acts as a protective layer to alleviate the Na degradation induced by O_2/O_2^- crossover, and the exact mechanisms underlying the protective effect of CP were elucidated. These results indicate that the Na anode greatly affects the overall performance of Na-O_2 batteries and thus should be attracting further research attention in the future studies.

Following above work, O_2/O_2^- crossover- and dendrite-free hybrid solid-state (HSS) Na-O_2 batteries based on solid-state electrolytes (SSEs) and protected Na anode were successfully developed. Stable operation for over 160 cycles at 0.2 mA cm^{-2} using commercial CP cathode is a breakthrough for superoxide-based Na-O_2 batteries. The study demonstrated that the dense SSE function acts as a physical shield to block the O_2/O_2^- migration to the Na anode and thus, eliminates Na metal corrosion. Further, the nature of the SEI layer on the Na anode in relation to O_2/O_2^- crossovers was systematically analyzed by X-ray photoelectron spectroscopic (XPS) with depth profile in this study, demonstrating the importance of O_2/O_2^- blockage for safe and high-performance Na-O_2 batteries.

The electrochemical behavior of alucone protected Na anode (Na@alucone) was studied in Na-O_2 batteries. It was found that the alucone protective layer decomposes under

superoxide radical attacks and consequently fails to suppress the Na dendrite growth, in sharp contrast to its stable cycling in NMBs. With SSE as a physical shield to eliminate the corrosion of superoxide towards the alucone layer, the dendrite suppressing effect of Na@alucone anode can be retrieved. As a result, the synergistic effect of SSE and Na@alucone enables Na-O_2 batteries stably runs for over 325 cycles at 0.2 mA cm^{-2} under shallow cycling mode. Furthermore, the cathode loading in relation to the life time of Na-O_2 batteries was systematically investigated. For the first time, we revealed that the chemical instability of the Na protection layer against superoxide can be highly fatal for the Na-O_2 cell performance, and the issues involving the highly reactive O_2^- radicals should be considered seriously in future studies of the Na-O_2 battery system.

To address the safety issues of conventional Na-O_2 batteries related to Na dendrite growth and the adoption of flammable organic electrolytes, a quasi-solid-state Na-O_2 battery based on composite electrolyte was reported. The composite electrolyte was fabricated by infusing poly(ethylene oxide)-based gel polymer electrolyte into the 3D NASICON SSE structure. The hybrid electrolyte exhibits an unprecedented combination of mechanical strength, ionic conductivity, and effective suppression of Na dendrite growth. Further, the developed composite electrolyte exhibits a low flammability and high-temperature stability, and the O_2/O_2^- crossover towards the Na anode can be blocked in Na-O_2 batteries with this composite electrolyte. To the best of our knowledge, we are the first to construct quasi-solid-state Na-O_2 batteries, and a long cycle life of can be achieved at 0.2 mA cm^{-2} under shallow cycling mode.

9.2   Contributions to this field

1. 3D printing of freestanding "O_2 breathable" air electrode for Na-O_2 batteries. In this thesis, for the first time, we demonstrate the successful employment of 3D printing technique to construct freestanding "O_2 breathable" air electrodes for Na-O_2 batteries (***Chemistry of Materials***, 2020, 32, 7, 3018-3027). The structure of the air electrodes can be optimized by adjusting the printing parameters, contributing to enhanced discharge capacities and cycling stability of Na-O_2 batteries. This study may open the new window to develop advanced air electrodes for the high-energy-density Na-O_2 batteries.

2. Confirming the superoxide crossover issue in superoxide-based Na-O$_2$ batteries. In this thesis, for the first time, we demonstrate that the O$_2^-$ intermediate can migrate from the cathode to the anode, which not only results in the loss of reversible charge capacity but also contributes to the severe Na corrosion during the Na-O$_2$ cell operation. Further, the CP interlayer protected Na anode has been used to alleviate the Na corrosion, leading to enhanced cycling stability of Na-O$_2$ batteries (*Advanced Functional Materials*, 2018, 28, 1801904). This study revealed that the Na degradation is partially responsible for the performance decay of Na-O$_2$ batteries, emphasizing the importance of Na protection in achieving high-performance Na-O$_2$ batteries in the future studies.

3. O$_2$/O$_2^-$ crossover- and dendrite-free hybrid solid-state Na-O$_2$ batteries. In this thesis, hybrid solid-state Na-O$_2$ batteries are first constructed with NASICON SSEs as a shield to block the O$_2$/O$_2^-$ crossover, and excellent cycling stability of Na-O$_2$ batteries was achieved. Further, for the first time, the effect of O$_2$/O$_2^-$ crossover relating to the properties of the SEI layer on the Na metal anode was revealed (*Chemistry of Materials*, 2019, 31, 9024-9031).

4. Deep understanding on the failure mechanism of the protective layer on the Na metal anode. In this thesis, we report for the first time that the chemical instability of the Na anode protective layer against superoxide intermediate can be fatal to the Na-O$_2$ cell performance; and a universal strategy was proposed to achieve high-performance Na-O$_2$ batteries. Further, the failure mechanism of the Na@alucone anode in Na-O$_2$ batteries was confirmed by using SEM and ToF-SIMS characterizations. The results obtained in this study indicate that the issues involving O$_2^-$ radicals should be considered seriously, which provide important guidance for the future study of Na-O$_2$ battery systems.

Overall, in this thesis, we first fabricated the "O$_2$ breathable" air electrodes for Na-O$_2$ batteries using 3D printing technique. The detrimental effect of O$_2^-$ crossover towards Na metal anode, as well as the Na-O$_2$ cell performance was also demonstrated, for the first time. More importantly, the underlying degradation mechanisms of Na-O$_2$ cell performance was revealed, and effective strategies to address the challenges of Na-O$_2$ batteries were proposed. The results of this thesis can provide important guidance for the further development of Na-O$_2$ batteries.

9.3   Perspectives

Compared with LIBs with limited energy densities, development of Na-O$_2$ batteries is an important direction on the road of high-energy-density batteries. Significant progress has been made in exploring the cell chemistry and designing advanced electrodes for Na-O$_2$ batteries. However, Na-O$_2$ battery technology is still at an immature stage, and there are still significant challenges that need to be addressed before practical application. Herein, we propose potential directions and perspectives for this field:

1. Better fundamental understanding on the Na-O$_2$ battery system is needed. So far, the electrochemistry of Na-O$_2$ battery system is still elusive and controversial, and a more detailed fundamental understanding is needed. Different discharge products and conflict results have been reported by different groups, while the determining factors that govern the reaction paths in Na-O$_2$ batteries are still unclear. Meanwhile, it is generally recognized that parasitic reactions at the anode, cathode, and electrolyte should be responsible for the Na-O$_2$ cell failure. Although the detailed mechanisms of these reactions have been investigated separately, the possible synergistic effect between these side reactions remain poorly understood. Moreover, it is still unclear if the growth mechanism of Na dendrites in Na-O$_2$ batteries is identical to that of Na-ion battery systems because of the distinct cell configuration and working principle. Lastly, the understanding of the decomposition of insulating NaO$_2$ cubes at a low voltage is far from complete, and more research is needed in future studies.

2. Advanced *in-situ* characterization techniques are urgently needed. Ex-situ analysis on the highly reactive discharge products and Na metal anode in Na-O$_2$ batteries is generally affected by the contaminants from the surrounding environment during the sample preparation process. Therefore, the *in-situ* characterization techniques are required. For example, synchrotron radiation-related techniques are good candidates for the study of electrochemical reactions during the Na-O$_2$ cell operation, which helps to have an accurate understanding on the electrochemistry of Na-O$_2$ batteries. Other analysis techniques, such as in-situ SEM, in-situ TEM, and in-situ XRD, can also help to have a comprehensive understanding on the Na-O$_2$ battery chemistry. Currently, few studies have focused on the mechanisms study on the Na degradation and Na dendrite growth in the presence of O$_2^-$

crossover. In-situ X-ray tomography and cryo-based techniques are ideal techniques to obtain the morphology and composition evolution of the Na anode (and SEI layer) in the Na-O$_2$ batteries.

3. Development of highly efficient air electrode. The physicochemical properties of the cathode materials are crucial for the Na-O$_2$ cell performance. Although various air electrodes have been developed, very few designs have realized the full utilization of the air electrode structure due to the pore clogging as a result of insufficient O$_2$ transportation within the air electrode. Air electrodes with a hierarchical porous structure and enough O$_2$ transport channels are highly desired, which enables continuous O$_2$ transportation and discharge product accomodation during the discharge process. Secondly, carbonaceous cathode corrosion at high voltages is still a major problem that decays the cell performance. Protection strategies such as surface coating on the air electrode with a highly conductive and stable material can help boost the chemical stability of the carbon cathode. Thirdly, the attachement of a catalyst on the cathode is effective in facilitating peroxides oxidation with a low charge overpotential. However, the possible parasitic reactions promoted by the catalyst should not be neglected when screening a suitable catalyst in Na-O$_2$ batteries. Lastly, advanced binder-free air electrodes should be developed to mitigate the binder-related side reactions under the attack of O$_2^-$ radicals.

4. Stabilization of the Na metal anode. With a deeper understanding on the Na-O$_2$ batteries, an increasing number of researchers have moved towards the Na metal anode protection. To achieve high-performance Na-O$_2$ batteries, the effective utilization of Na metal anode is crucial. However, the Na protection methodologies that are already found to be profound in NIBs may not be applicable in Na-O$_2$ batteries due to its unique reaction mechanisms. Surface modification with polymer thin films is a promising strategy to suppress the Na dendrite growth in NIBs, while the stability of the protective layer against the O$_2^-$ should be considered seriously. Furthermore, introducing a physical barrier, such as SSE or engineered membrane/separator, is a good choice to block the O$_2$/O$_2^-$ migration and alleviate Na corrosion. It is important to underline that the chemical stability of the physical barrier against O$_2^-$ and the interface stability between the SSE and Na metal should also be taken into consideration.

In conclusion, Na-O$_2$ batteries have attracted enormous attention as promising energy storage systems for future electric vehicles and hybrid electric vehicles. Although significant progress has been achieved in exploring the cell chemistry of Na-O$_2$ battery system, many fundamental and engineering challenges remain. Additionally, much efforts have been devoted to designing advanced air electrodes in order to increase the cell capacity, while the Na anode related issues (Na dendrite growth, Na corrosion) has been overlooked and needs pay more attention in the future studies. In-depth studies on the underlying electrochemistry of Na-O$_2$ batteries via various in-situ/in-operando characterization techniques are needed. The binder-free air electrodes with hierarchical porous structure and efficient O$_2$ transport pathways can facilitate the ORR/OER kinetics and improve the air electrode utilization. For the metallic Na anode, coating a chemical stable artificial layer on the Na anode surface or introducing an O$_2^-$ ionic shield should enable stable Na cycling in Na-O$_2$ batteries by suppressing Na dendrite growth and avoiding Na corrosion that related to O$_2$/O$_2^-$ crossover. We believe that, with more and more efforts being devoted, the practical application of Na-O$_2$ batteries can be expected in the foreseen future.

Appendices

Appendix A: Permission from John Wiley and Sons for Published Article on *Carbon Energy*

Carbon Energy journal Copyright Policy:

(https://onlinelibrary.wiley.com/terms-and-conditions)

Published papers:

Xiaoting Lin, Qian Sun, Kieran Doyle Davis, Ruying Li, *Xueliang Sun*, The application of carbon materials in nonaqueous Na-O_2 batteries, *Carbon Energy,* 2019; 1: 141-164.

Appendix B: Permission from American Chemical Society (ACS) for Published Article on *Chemistry of Materials*.

Published papers:

Xiaoting Lin, Jiwei Wang, Xuejie Gao, Sizhe Wang, Qian Sun, Jing Luo, Changtai Zhao, Yang Zhao, Xiaofei Yang, Changhong Wang, Ruying Li, ***Xueliang Sun***, 3D Printing of "O_2 Breathable" Air Electrodes for High-Capacity and Long-Life Na-O_2 batteries, ***Chemistry of Materials***, 2020, 32, 7, 3018-3027.

Appendix C: Permission from John Wiley and Sons for Published Article on *Advanced Functional Materials*

Published papers:

Xiaoting Lin, Qian Sun, Hossein Yadegari, Xiaofei Yang, Yang Zhao, Changhong Wang, Jianneng Liang, Alicia Koo, Ruying Li, *Xueliang Sun*, On the cycling performance of Na-O$_2$ cells: Revealing the Impact of the Superoxide Crossover toward the Metallic Na Electrode, *Advanced Functional Materials*, 2018, 28, 1801904.

Appendix D: Permission from American Chemical Society (ACS) for Published Article on *Chemistry of Materials*.

Published papers:

Xiaoting Lin, Fei Sun, Qian Sun, Sizhe Wang, Jing Luo, Changtai Zhao, Xiaofei Yang, Yang Zhao, Changhong Wang, Ruying Li, ***Xueliang Sun***, O_2/O_2^- Crossover- and Dendrite-Free Hybrid-Solid-State Na-O_2 batteries, ***Chemistry of Materials***, 2019, 31, 9024-9031.

Curriculum Vitae

Name:	Xiaoting Lin
Post-secondary Education and Degrees:	Liaocheng University Liaocheng, Shandong, China 2008-2012 B.A. Ningbo University Ningbo, Zhejiang, China 2013-2016 M.A. The University of Western Ontario London, Ontario, Canada 2016-2020 Ph.D.
Honours and Awards:	China Scholarship Council (CSC) Scholarship 2016-2020 National Scholarship for Graduate Students of China 2013
Related Work Experience	Research Assistant The University of Western Ontario 2016-2020

Publications:

Publications: (A) Peer-reviewed Journal Papers and Book Chapters Based on This Thesis (First Author)

1. *Xiaoting Lin*, Qian Sun, Kieran Doyle Davis, Ruying Li, Xueliang Sun, The application of carbon materials in nonaqueous Na-O$_2$ batteries, *Carbon Energy*, 2019, 1: 141-164.

2. *Xiaoting Lin*, Jiwei Wang, Xuejie Gao, Sizhe Wang, Qian Sun, Jing Luo, Changtai Zhao, Yang Zhao, Xiaofei Yang, Changhong Wang, Ruying Li, Xueliang Sun, 3D printing of freestanding "O$_2$ breathable" air electrodes for high-capacity and long-life Na-O$_2$ batteries, *Chemistry of Materials*, 2020, 32, 7, 3018-3027.

3. *Xiaoting Lin*, Qian Sun, Hossein Yadegari, Xiaofei Yang, Yang Zhao, Changhong Wang, Jianneng Liang, Alicia Koo, Ruying Li, Xueliang Sun, On the cycling performance of Na-O_2 cells: Revealing the impact of the superoxide crossover toward the metallic Na electrode, *Advanced Functional Materials*, 2018, 28, 1801904.

4. *Xiaoting Lin*, Fei Sun, Qian Sun, Sizhe Wang, Jing Luo, Changtai Zhao, Xiaofei Yang, Yang Zhao, Changhong Wang, Ruying Li, Xueliang Sun, O_2/O_2^- crossover- and dendrite-free hybrid solid-state Na-O_2 batteries, *Chemistry of Materials*, 2019, 31, 9024-9031.

5. *Xiaoting Lin*, Yipeng Sun, Qian Sun, Yang Zhao, Jing Luo, Changtai Zhao, Xiaofei Yang, Changhong Wang, Hanyu Huo, Ruying Li, Xueliang Sun, Probing blind point of the protected Na anodes in Na-O_2 batteries: Their failure mechanism against superoxide crossover and resolving strategy. To be submitted.

6. *Xiaoting Lin*, Changtai Zhao, Qian Sun, Xiaofei Yang, Jing Luo, Fei Sun, Jianneng Liang, Changhong Wang, Ruying Li, Xueliang Sun, Flame-resistant, dendrite- and O_2/O_2^--impermeable composite electrolyte for quasi-solid-state Na-O_2 batteries. In preparation.

7. *Xiaoting Lin*, Keegan R. Adair, Xueliang Sun, carbon nanomaterials for Na-O_2 batteries, 2017, book chapter in "**Carbon Nanomaterials for electrochemical energy technologies**"

8. *Xiaoting Lin*, Keegan R. Adair, Xueliang Sun, carbon nanomaterials for Li-O_2 batteries, 2017, book chapter in "**Carbon Nanomaterials for electrochemical energy technologies**"

(B) Peer-reviewed Journal Papers Related to This Thesis (Co-author)

9. Qian Sun, *Xiaoting Lin*, Hossein Yadegari, Wei Xiao, Yang Zhao, Keegan R. Adair, Ruying Li, Xueliang Sun, Aligning the binder effect on sodium-air batteries, *Journal of Materials Chemistry A*, 2018, 6, 1473-1484.

10. Hossein Yadegari, Mohammad Norouzi Banis, *Xiaoting Lin*, Alicia Koo, Ruying Li, Xueliang Sun, Revealing the chemical mechanism of NaO_2 decomposition by in situ Raman imaging, *Chemistry of Materials*, 2018, 30, 15, 5156-5160.

11. Xiaofei Yang, Ying Yu, *Xiaoting Lin*, Jianneng Liang, Keegan Adair, Yang Zhao, Changhong Wang, Xia Li, Qian Sun, Hongzhang Zhang, Xianfeng Li, Ruying Li, Huamin Zhang, Xueliang Sun, Multi-functional nanowall arrays with unrestricted Li^+ transport channels and an integrated conductive network for high-areal-capacity Li-S batteries, *Journal of Materials Chemistry A*, 2018, 6, 22958.

12. Yang Zhao, Xiaofei Yang, Qian Sun, Xuejie Gao, *Xiaoting Lin*, Changhong Wang, Feipeng Zhao, Yipeng Sun, Keegan R. Adair, Ruying Li, Mei Cai, Xueliang Sun, Dendrite-free and minimum volume change of Li metal anode achieved by three-dimensional artificial interlayers, *Energy Storage Materials*, 2018, 15, 415-421.

13. Changhong Wang, Qian Sun, Yulong Liu, Yang Zhao, Xia Li, *Xiaoting Lin*, Mohammad Norouzi Banis, Minsi Li, Weihan Li, Keegan R. Adair, Dawei Wang, Jianneng Liang, Ruying Li, Li Zhang, Rong Yang, Shigang Lu, Xueliang Sun, Boosting the performance of lithium batteries with solid-liquid hybrid electrolytes: Interfacial properties and effects of liquid electrolytes, *Nano Energy*, 2018, 48, 35-43.

14. Changtai Zhao, Chang Yu, Shaofeng Li, Wei Guo, Yang Zhao, Qiang Dong, *Xiaoting Lin*, Zhongxin Song, Xinyi Tan, Changhong Wang, Matthew Zheng, Xueliang Sun, Jieshan Qiu, Ultrahigh-capacity and long-life lithium metal batteries enabled by engineering carbon nanofiber-stabilized graphene aerogel film host, *Small*, 2018, 14, 1803310.

15. Changhong Wang, Yang Zhao, Qian Sun, Xia Li, Yulong Liu, Jianwen Liang, Xiaona Li, *Xiaoting Lin*, Ruying Li, Keegan R. Adair, Li Zhang, Rong Yang, Shigang Lu, Xueliang Sun, Stabilizing interface between $Li_{10}SnP_2S_{12}$ and Li metal by molecular layer deposition, *Nano Energy*, 2018, 53, 168-174.

16. Changtai Zhao, Jianneng Liang, Qian Sun, Jing Luo, Yulong Liu, *Xiaoting Lin*, Yang Zhao, Hossein Yadegari, Mohammad Norouzi Banis, Ruying Li, Huan Huang, Li Zhang, Rong Yang, Shigang Lu, Xueliang Sun, Ultralong-life quasi-solid-state Li-O_2

batteries enabled by coupling advanced air electrode design with Li metal anode protection, *Small Methods*, 2019, 3, 1800437.

17. Xiaofei Yang, Qian Sun, Changtai Zhao, Xuejie Gao, Keegan R. Adair, Yang Zhao, Jing Luo, *Xiaoting Lin*, Jianneng Liang, Huan Huang, Li Zhang, Shigang Lu, Xueliang Sun, Self-healing electrostatic shield enabling uniform lithium deposition in all-solid-state lithium batteries, *Energy Storage Materials*, 2019, 22, 194-199.

18. Changtai Zhao, Jianneng Liang, Yang Zhao, Jing Luo, Qian Sun, Yulong Liu, *Xiaoting Lin*, Xiaofei Yang, Huan Huang, Li Zhang, Shanqian Zhao, Shigang Lu, Xueliang Sun, Engineering a "nanonet"-reinforced polymer electrolyte for long-life Li-O$_2$ batteries, *Journal of Materials Chemistry A*, 2019, 7, 24947.

19. Xiaofei Yang, Xuejie Gao, Qian Sun, Sara Panahian Jand, Ying Yu, Yang Zhao, Xia Li, Keegan R. Adair, Liang-Yin Kuo, Jochen Rohrer Jianneng Liang, *Xiaoting Lin*, Mohammad Norouzi Banis, Yongfeng Hu, Hongzhang Zhang, Xianfeng Li, Ruying Li, Huamin Zhang, Payam Kaghazchi, Tsun-Kong Sham, Xueliang Sun, Promoting the transformation of Li$_2$S$_2$ to Li$_2$S: Significantly increasing utilization of active materials for high-sulfur-loading Li-S batteries, *Advanced Materials*, 2019, 31, 1901220.

20. Xiaofei Yang, Qian Sun, Changtai Zhao, Xuejie Gao, Keegan R. Adair, Yulong Liu, Jing Luo, *Xiaoting Lin*, Jianneng Liang, Huan Huang, Li Zhang, Rong Yang, Shigang Lu, Ruying Li, Xueliang Sun, High-areal-capacity all-solid-state lithium batteries enabled by rational design of fast ion transport channels n vertically aligned composite polymer electrodes, *Nano Energy*, 2019, 61, 567-575.

21. Changhong Wang, Keegan R. Adair, Jianwen Liang, Xiaona Li, Yipeng Sun, Xia Li, Jiwei Wang, Qian Sun, Feipeng Zhao, *Xiaoting Lin*, Ruying Li, Huan Huang, Li Zhang, Rong Yang, Shigang Lu, Xueliang Sun, *Advanced Functional materials*, 2019, 29, 1900392.

22. Hanyu Huo, Yue Chen, Ning Zhao, *Xiaoting Lin*, Jing Luo, Xiaofei Yang, Yulong Liu, Xiangxin Guo, Xueliang Sun, In-situ formed Li$_2$CO$_3$-free garnet/Li interface by rapid acid treatment for dendrite-free solid-state batteries, *Nano Energy*, 2019, 61, 119-125.

23. Changhong Wang, Xia Li, Yang Zhao, Mohammad N. Banis, Jianwen Liang, Xiaona Li, Yipeng Sun, Keegan R. Adair, Qian Sun, Yulong Liu, Feipeng Zhao, Sixu Deng, **Xiaoting Lin**, Ruying Li, Yongfeng Hu, Tsun-Kong Sham, Huan Huang, Li Zhang, Rong Yang, Shigang Lu, Xueliang Sun, Manipulating interfacial nanostructure to achieve high-performance all-solid-state lithium-ion batteries, *Small Methods*, 2019, 3, 1900261.

24. Sizhe Wang, Haiyuan Chen, Jiaxuan Liao, Qian Sun, Feipeng Zhao, Jing Luo, *Xiaoting Lin*, Xiaobin Niu, Mengqiang Wu, Ruying Li, Xueliang Sun, Efficient trapping and catalytic conversion of polysulfides by VS_4 nanosites for Li-S batteries, *ACS Energy Letters*, 2019, 4, 3, 755-762.

25. Yipeng Sun, Yang Zhao, Jiwei Wang, Jianneng Liang, Changhong Wang, Qian Sun, *Xiaoting Lin*, Keegan R. Adair, Jing Luo, Dawei wang, Ruying Li, Mei Cai, Tsun-Kong Sham, Xueliang Sun, A novel organic "polyurea" thin film for ultralong-life lithium-metal anode via molecular-layer deposition, *Advanced Materials*, 2019, 31, 1806541.

26. Xiaofei Yang, Xuejie Gao, Changtai Zhao, Qian Sun, Yang Zhao, Keegan R. Adair, Jing Luo, *Xiaoting Lin*, Jianneng Liang, Huan Huang, Li Zhang, Shigang Lu, Ruying Li, Xueliang Sun, Suppressed dendrite formation realized by selective Li deposition in all-solid-state lithium batteries, *Energy Storage Materials*, 2020, 27, 198-204.

27. Changhong Wang, Jianneng Liang, Sooyeon Hwang, Xiaona Li, Yang Zhao, Keegan R. Adair, Changtai Zhao, Xia Li, Sixu Deng, *Xiaoting Lin*, Xiaofei Yang, Ruying Li, Huan Huang, Li Zhang, Shigang Lu, Dong Su, Xueliang Sun, Unveiling the critical role of interfacial ionic conductivity in all-solid-state lithium batteries, *Nano Energy*, 2020, 72, 104686.

28. Jianneng Liang, Yipeng Sun, Yang Zhao, Qian Sun, Jing Luo, Feipeng Zhao, *Xiaoting Lin*, Xia Li, Ruying Li, Li Zhang, Shigang Lu, Huan Huang, Xueliang Sun, Engineering the conductive carbon/PEO interface to stabilize solid polymer electrolytes for all-solid-state high voltage $LiCoO_2$ batteries, *Journal of Materials Chemistry A*, 2020, 8, 2769-2776.

29. Hanyu Huo, Xiaona Li, Yipeng Sun, **Xiaoting Lin**, Kieran Doyle-Davis, Jianwen Liang, Xuejie Gao, Ruying Li, Huan Huang, Xiangxin Guo, Xueliang Sun, Li_2CO_3 effects: New insignts into polymer/garnet electrolytes for dendrite-free solid lithium batteries, Nano Energy, 2020, 104836.

30. Hanyu Huo, Jianneng Liang, Ning Zhao, Xiaona Li, **Xiaoting Lin**, Yang Zhao, Keegan Adair, Ruying Li, Xiangxin Guo, Xueliang Sun, Dynamics of the garnet/Lli interface for dendrite-free solid-state batteries, *ACS Energy Letters*, 2020, 5, 7, 2156-2164.

31. Changtai Zhao, Jianwen Liang, Xiaona Li, Nathaniel Holmes, Changhong Wang, Jian Wang, Feipeng Zhao, Shaofeng Li, Qian Sun, Xiaofei Yang, Jianneng Liang, **Xiaoting Lin**, Weihan Li, Shangqian Zhao, Huan Huang, Li Zhang, Shigang Lu, Xueliang Sun, *Nano Energy*, 2020, 105036.

(C) Previous Publications Before Join UWO

32. *Xiaoting Lin*, Shangshu Qian, Haoxiang Yu, Lei Yan, Peng Li, Yaoyao Wu, Nengbing Long, Miao Shui, Jie Shu, Advanced $BaLi_2Ti_6O_{14}$ anode fabricated via lithium site substitution by magnesium, *ACS sustainable Chemistry & Engineering*, 2016, 4, 4859-4867.

33. *Xiaoting Lin*, Peng Li, Lianyi Shao, Miao Shui, Dongjie Wang, Nengbing Long, Yuanlong Ren, Jie Shu, Lithium barium titanate: A stable lithium storage material for lithium-ion batteries, *Journal of Power Sources*, 2015, 278, 546-554.

34. *Xiaoting Lin*, Pengfei Wang, Peng Li, Haoxiang Yu, Shangshu Qian, Miao Shui, Dongjie Wang, Nengbing Long, Jie Shu, Improved the lithium storage capability of $BaLi_2Ti_6O_{14}$ by electroless silver coating, *Electrochimica Acta*, 2015, 186, 24-33.

35. *Xiaoting Lin*, Peng li, Pengfei Wang, Haoxiang Yu, Shangshu Qian, Miao Shui, Xi Zheng, Nengbing Long, Jie Shu, $SrLi_2Ti_6O_{14}$: A probable host material for high performance lithium storage, *Electrochimica Acta*, 2015, 180, 831-844.

36. *Xiaoting Lin*, Peng Li, Lianyi Shao, Xi Zheng, Miao Shui, Nengbing Long, Dongjie Wang, Jie Shu, CNT-enhanced electrochemical property and sodium storage

mechanism of $Pb(NO_3)_2$ as anode material for Na-ion batteries, ***Electrochimica Acta***, 2015, 169, 382-394.

37. ***Xiaoting Lin***, Jie Shu, Kaiqiang Wu, Lianyi Shao, Peng Li, Miao Shui, Dongjie Wang, Nengbing Long, Yuanlong Ren, Improved electrochemical property of $Pb(NO_3)_2$ by carbon black, graphene and carbon nanotube, ***Electrochimica Acta***, 2014, 137, 767-773.

38. ***Xiaoting Lin***, Rui Ma, Lianyi Shao, Miao Shui, Kaiqiang Wu, Dongjie Wang, Nengbing Long, Yuanlong Ren, Jie Shu, In-situ X-ray diffraction study on the structural evolution of oxidized fluorophosphates as anode materials for lithium-ion batteries, ***Ceramics International***, 2014, 40, 9107-9120.

39. ***Xiaoting Lin***, Kaiqiang Wu, Lianyi Shao, Miao Shui, Dongjie Wang, Nengbing Long, Yuanlong Ren, Jie Hsu, In situ growth of coiled carbon nanotubes on $LiFePO_4$ as high-performance lithium storage material, ***Journal of Electroanalytical Chemistry***, 2014, 726, 71-76.

40. ***Xiaoting Lin***, Kaiqiang Wu, Lianyi Shao, Miao Shui, Xinxin Jiang, Dongjie Wang, Nengbing Long, Yuanlong Ren, Jie Shu, Facile preparation of $Cr_2O_3@Ag_2O$ composite as high-performance lithium storage material, ***Journal of Alloys and Compounds***, 2014, 598, 68-72.

41. Minghe Luo[+], ***Xiaoting Lin***[+], Hua Lan, Haoxiang Yu, Lai Yan, Shangshu Qian, Nengbing Long, Miao Shui, Jie Shu, Lithiation-delithiation kinetics of $BaLi_2Ti_6O_{14}$ anode in high-performance secondary Li-ion batteries, ***Journal of Electroanalytical Chemistry***, 2017, 786, 86-93.

42. Peng Li, Shangshu Qian, Haoxiang Yu, Lei Yan, ***Xiaoting Lin***, Ke Yang, Nengbing Long, Miao Shui, Jie Shu, $PbLi_2Ti_6O_{14}$: A novel high-rate long-life anode material for rechargeable lithium-ion batteries, ***Journal of Power Sources***, 2016, 330, 45-54.

43. Shangshu Qian, Haoxiang Yu, Lei Yan, Peng Li, ***Xiaoting Lin***, Yanyu Zhang, Nengbing Long, Miao Shui, Jie Shu, $Sr_{0.95}In_{0.05}Li_2Ti_6O_{14}$: A high performance lithium host material, ***Journal of Power Sources***, 2016, 322, 68-76.

44. Lei Yan, Haoxiang Yu, Shangshu Qian, Peng Li, *Xiaoting Lin*, Nengbing Long, Ruifeng Zhang, Miao Shui, Jie Shu, Enhanced lithium storage performance of $Li_5Cr_9Ti_4O_{24}$ anode by nitrogen and sulfur dual-doped carbon coating, *Electrochimica Acta*, 2016, 213, 217-224.

45. Shangshu Qian, Haoxiang Yu, Lei Yan, Peng Li, *Xiaoting Lin*, Yaoyao Wu, Nengbing Long, Miao Shui, Jie Shu, Complex titanates $Sr_{1-x}Pb_xLi_2Ti_6O_{14}$ ($0 \leq x \leq 1$) as anode materials for high-performance lithium-ion batteries, *Electrochimica Acta*, 2016, 212, 950-957.

46. Haoxiang Yu, Shangshu Qian, Lei Yan, Peng Li, *Xiaoting Lin*, Minghe Luo, Nengbing Long, Miao Shui, Jie Shu, Observation of the lithium storage behavior in $LiCrTiO_4$ via in-situ and ex-situ techniques, *Electrochimica Acta*, 2016, 212, 84-94.

47. Lei Yan, Haoxiang Yu, Shangshu Qian, Peng Li, *Xiaoting Lin*, Yaoyao Wu, Nengbing Long, Miao Shui, Jie Shu, Novel spinel $Li_5Cr_9Ti_4O_{24}$ anode: Its electrochemical property and lithium storage process, *Electrochimica Acta*, 2016, 209, 17-24.

48. Pengfei Wang, Shangshu Qian, Tingfeng Yi, Haoxiang Yu, Lei Yan, Peng Li, *Xiaoting Lin*, Miao Shui, Jie Shu, Effect of sodium-site doping on enhancing the lithium storage performance of sodium lithium titanate, *ACS Applied Materials & Interfaces*, 2016, 8, 16, 10302-10314.

49. Youren Dong, Shangshu Qian, Lianyi Shao, Haoxiang Yu, Lei Yan, Peng Li, *Xiaoting Lin*, Nengbing Long, Miao Shui, Jie Shu, Evaluation of the electrochemical behavior and structural reversibility of $Li_{3-x}Na_xV_2(PO_4)_3/C$ ($0 \leq x \leq 3$) as anode materials for Na-ion batteries, *Ceramics International*, 2016, 42, 9, 10943-10950.

50. Pengfei Wang, Lianyi Shao, Shangshu Qian, Tingfeng Yi, Haoxiang Yu, Lei Yan, Peng Li, *Xiaoting Lin*, Miao Shui, Jie Shu, $Li_{3-x}Na_xV_2(PO_4)_3$ ($0 \leq x \leq 3$): Possible anode materials for rechargeable lithium-ion batteries, *Electrochimica Acta*, 2016, 200, 1-11.

51. Mengmeng Lao, Shangshu Qian, Haoxiang Yu, Lei Yan, Peng Li, *Xiaoting Lin*, Nengbing Long, Miao Shui, Jie Shu, Enhanced electrochemical properties of Mg^{2+} doped $Li_2Na_2Ti_6O_{14}$ anode material for lithium-ion batteries, *Electrochimica Acta*, 2016, 196, 642-652.

52. Haoxiang Yu, Shangshu Qian, Lei Yan, Peng Li, *Xiaoting Lin*, Minghe Luo, Nengbing Long, Miao Shui, Jie Shu, Morphological, electrochemical and in-situ XRD study of $LiNi_{0.6}Co_{0.2}Mn_{0.1}Al_{0.1}O_2$ as high potential cathode material for rechargeable lithium-ion batteries, *Journal of Alloys and Compounds*, 2016, 667, 58-64.

53. Shangshu Qian, Haoxiang Yu, Lei Yan, Peng Li, *Xiaoting Lin*, Ying Bai, Songjing Wang, Nengbing Long, Miao Shui, Jie Shu, Ag enhanced electrochemical performance for $Na_2Li_2Ti_6O_{14}$ anode in rechargeable lithium-ion batteries, *Ceramics International*, 2016, 42, 6, 6874-6882.

54. Pengfei Wang, Peng Li, Tingfeng Yi, Haoxiang Yu, *Xiaoting Lin*, Shangshu Qian, Yanrong Zhu, Miao Shui, Jie Shu, In-situ X-ray diffraction study on the structural reversibility of lithium nickel cobalt oxide in a broad electrochemical window of 1.35–4.3V, *Electrochimica Acta*, 2016, 190, 248-257.

55. Peng Li, Pengfei Wang, Shangshu Qian, Haoxiang Yu, *Xiaoting Lin*, Miao Shui, Xi Zheng, Nengbing Long, Jie Shu, Synthesis of $Na_2Ti_6O_{13}$ nanorods as possible anode materials for rechargeable lithium ion batteries, *Electrochimica Acta*, 2016, 187, 46-54.

56. Pengfei Wang, Peng Li, Tingfeng Yi, *Xiaoting Lin*, Haoxiang Yu, Yanrong Zhu, Shangshu Qian, Miao Shui, Jie Shu, Enhanced lithium storage capability of sodium lithium titanate via lithium-site doping, *Journal of Power Sources*, 2015, 297, 283-294.

57. Pengfei Wang, Peng Li, Tingfeng Yi, *Xiaoting Lin*, Yanrong Zhu, Lianyi Shao, Miao Shui, Nengbing Long, Jie Shu, Improved lithium storage performance of lithium sodium titanate anode by titanium site substitution with aluminum, *Journal of Power Sources*, 2015, 293, 33-41.

58. Peng Li, Pengfei Wang, Xi Zheng, Haoxiang Yu, Shangshu Qian, Miao Shui, **Xiaoting Lin**, Nengbing Long, Jie Shu, Enhanced sodium storage property of copper nitrate hydrate by carbon nanotube, *Journal of Electroanalytical Chemistry*, 2015, 755, 92-99.

59. Jie Shu, Kaiqiang Wu, Pengfei Wang, Peng Li, *Xiaoting Lin*, Lianyi Shao, Miao Shui, Nengbing Long, Dongjie Wang, Lithiation and delithiation behavior of sodium lithium titanate anode, *Electrochimica Acta*, 2015, 173, 595-606.

60. Peng Li, Rui Ma, *Xiaoting Lin*, Lianyi Shao, Kaiqiang Wu, Miao Shui, Nengbing Long, Jie Shu, Impact of H_2O exposure on the structure and electrochemical performance of $LiVPO_4F$ cathode material, *Journal of Alloys and compounds*, 2015, 637, 20-19.

61. Peng Li, Kaiqiang Wu, Pengfei Wang, *Xiaoting Lin*, Haoxiang Yu, Miao Shui, Xi Zheng, Nengbing Long, Jie Shu, Preparation, electrochemical characterization and in-situ kinetic observation of $Na_2Li_2Ti_6O_{14}$ as anode material for lithium ion batteries, *Ceramics Internationals*, 2015, 41, 10, 14508-14516.

62. Mengmeng Lao, Peng Li, Pengfei Wang, Xi Zheng, Weijian Wu, Miao Shui, *Xiaoting Lin*, Nengbing Long, Jie Shu, Advanced electrochemical performance of $Li_{1.95}Al_{0.05}Na_2Ti_6O_{14}$ anode material for lithium ion batteries, *Electrochimica Acta*, 2015, 176, 694-704.

63. Peng Li, *Xiaoting Lin*, Lianyi Shao, Miao Shui, Dongjie Wang, Nengbing Long, Jie Shu, $PbSbO_2Cl@C$ nanocomposite as lithium storage material for secondary lithium-ion batteries, *Journal of Electroanalytical Chemistry*, 2015, 747, 39-44.

64. Mengmeng lao, Peng Li, *Xiaoting Lin*, Lianyi Shao, Miao Shui, Nengbing Long, Dongjie Wang, Jie Shu, Enhanced lithium storage property of Na-doped $Li_2Na_2Ti_6O_{14}$ anode materials for secondary lithium-ion batteries, *RSC Advance*, 2015, 5, 41999-42008.

65. Jinli Mao, Lianyi Shao, Peng Li, *Xiaoting Lin*, Miao Shui, Nengbing Long, Jie Shu, Comparison of phase composition, morphology and electrochemical property for $Li_{3-x}Na_xV_2(PO4)_3$ (x=0.5, 1.5 and 2.0) as lithium storage cathode materials, *Electrochimica Acta*, 2015, 173, 96-104.

66. Peng Li, Pengfei Wang, Haoxiang Yu, *Xiaoting Lin*, Lianyi Shao, Miao Shui, Nengbing Long, Jie Shu, Carbothermal synthesis of $LiVPO_4F$ and its structural change in a broad potential range observed by in-situ X-ray diffraction, *Ceramics International*, 2015, 41, 9, 10766-10774.

67. Lianyi Shao, Jie Shu, Yuanhao Tang, Peng Li, *Xiaoting Lin*, Miao Shui, Nengbing Long, Deyu Wang, Phase diagram and electrochemical behavior of lithium sodium vanadium phosphates cathode materials for lithium ion batteries, *Ceramics International*, 2015, 41, 3, 5164-5171.

68. Mengmeng Lao, *Xiaoting Lin*, Peng Li, Lianyi Shao, Kaiqiang Wu, Miao Shui, Nengbing Long, Yuanlong Ren, Jie Shu, Preparation and electrochemical characterization of $Li_{2+x}Na_{2-x}Ti_6O_{14}$ ($0 \leq x \leq 0.2$) as anode materials for lithium-ion batteries, *Ceramics International*, 2015, 41, 2, 2900-2907.

69. Songjing Wang, Peng Li, Lianyi Shao, Kaiqiang Wu, *Xiaoting Lin*, Miao Shui, Nengbing Long, Dongjie Wang, Jie Shu, Preparation of spinel $LiNi_{0.5}Mn_{1.5}O_4$ and Cr-doped $LiNi_{0.5}Mn_{1.5}O_4$ cathode materials by tartaric acid assisted sol–gel method, *Ceramics International*, 2015, 41, 1, 1347-1353.

70. Pengfei Wang, Peng Li, Tingfeng Yi, *Xiaoting Lin*, Yanrong Zhu, Lianyi Shao, Miao Shui, Nengbing Long, Jie Shu, Fabrication and electrochemical properties of $CuCrO_2$ anode obtained by a sol–gel method, *Ceramics International*, 2015, 41, 5, 6668-6675.

71. Kaiqiang Wu, Jie Shu, *Xiaoting Lin*, Lianyi Shao, Mengmeng Lao, Miao Shui, Peng Li, Nengbing Long, Dongjie Wang, Enhanced electrochemical performance of sodium lithium titanate by coating various carbons, *Journal of Power Sources*, 2014, 272, 25, 283-290.

72. Lianyi Shao, Jie Shu, Mengmeng Lao, *Xiaoting Lin*, Kaiqiang Wu, Miao Shui, Peng Li, Nengbing Long, Yuanlong Ren, Hydroxylamine hydrochloride: A novel anode material for high capacity lithium-ion batteries, *Journal of Power Sources*, 2014, 171, 39-44.

73. Xi Zheng, Kaiqiang Wu, Jinli Mao, Xinxin Jiang, Lianyi Shao, *Xiaoting Lin*, Peng Li, Miao Shui, Jie Shu, Improved electrochemical property of copper nitrate hydrate by multi-wall carbon nanotube, *Electrochimica Acta*, 2014, 147, 765-772.

74. Kaiqiang Wu, Jie Shu, *Xiaoting Lin*, Lianyi Shao, Peng Li, Miao Shui, Mengmeng Lao, Nengbing Long, Dongjie Wang, Phase composition and electrochemical performance

of sodium lithium titanates as anode materials for lithium rechargeable batteries, *Journal of Power Sources*, 2015, 275, 419-428.

75. Jie Shu, Kaiqiang Wu, Lianyi Shao, *Xiaoting Lin*, Peng Li, Miao Shui, Dongjie Wang, Nengbing Long, Yuanlong Ren, Nano/microstructure ammonium cerium nitrate tetrahydrate/carbon nanotube as high-performance lithium storage material, *Journal of Power Sources*, 2015, 275, 458-467.

76. Rui Ma, Jie Shu, Lianyi Shao, *Xiaoting Lin*, Kaiqiang Wu, Miao Shui, Peng Li, Nengbing Long, Yuanlong Ran, Determination of lithium ion diffusion behaviors in tsavorite LiVPO$_4$F by galvanostatic intermittent titration technique, *Ceramics International*, 2014, 40, 9, 15113-15119.

77. Peng Li, Jie Hsu, Lianyi Shao, *Xiaoting Lin*, Kaiqiang Wu, Miao Shui, Dongjie Wang, Nengbing Long, Yuanlong Ren, Comparison of morphology and electrochemical behavior between PbSbO$_2$Cl and PbCl$_2$/Sb$_4$O$_5$C$_{l2}$, Journal of *Electroanalytical Chemistry*, 2014, 731, 128-132.

78. Mengmeng Lao, Jie Shu, Lianyi Shao, *Xiaoting Lin*, Kaiqiang Wu, Miao Shui, Peng Li, Nengbing Long, Yuanlong Ren, Enhanced electrochemical performance of Ag-coated CuCr$_2$O$_4$ as anode material for lithium-ion batteries, *Ceramics International*, 2014, 40, 8, 11899-11904.

79. Lianyi Shao, Jie Shu, Kaiqiang Wu, *Xiaoting Lin*, Peng Li, Miao Shui, Dongjie Wang, Nengbing Long, Yuanlong Ren, Low pressure preparation of spherical Si@C@CNT@C anode material for lithium-ion batteries, *Journal of Electroanalytical Chemistry*, 2014, 727, 8-12.

80. Xinxin Jiang, Kaiqiang Wu, Lianyi Shao, Miao Shui, *Xiaoting Lin*, Mengmeng Lao, Nengbing Long, Yuanlong Ren, Jie Shu, Lithium storage mechanism in superior high capacity copper nitrate hydrate anode material, *Journal of Power Sources*, 2014, 260, 218-224.

81. Kaiqiang Wu, *Xiaoting Lin*, Lianyi Shao, Miao Shui, Nengbing Long, Yuanlong Ren, Jie Shu, Copper/carbon coated lithium sodium titanate as advanced anode material for lithium-ion batteries, *Journal of Power Sources*, 2014, 259, 177-182.

82. Lianyi Shao, Kaiqiang Wu, *Xiaoting Lin*, Miao Shui, Rui Ma, Dongjie Wang, Nengbing Long, Yuanlong Ren, Jie Shu, Sol–gel preparation of V_2O_5 sheets and their lithium storage behaviors studied by electrochemical and *in-situ* X-ray diffraction techniques, *Ceramics International*, 2014, 40, 6115-6125.

83. Tianhua Li, Lianyi Shao, *Xiaoting Lin*, Miao Shui, Kaiqiang Wu, Dongjie Wang, Nengbing Long, Yuanlong Ren, Jie Shu, High rate $Li_4Ti_5O_{12}$@C anode material fabricated by a facile carbon coating method, *Journal of Electroanalytical Chemistry*, 2014, 722-723, 54-59.

84. Kaiqiang Wu, Lianyi Shao, Xinxin Jiang, Miao Shui, Rui Ma, Mengmeng Lao, *Xiaoting Lin*, Dongjie Wang, Nengbing Long, Yuanlong Ren, Jie Shu, Facile preparation of $[Bi_6O_4](OH)_4(NO_3)_6 \cdot 4H_2O$, $[Bi_6O_4](OH)_4(NO_3)_6 \cdot H_2O$ and $[Bi_6O_4](OH)_4(NO_3)_6 \cdot H_2O$/C as novel high capacity anode materials for rechargeable lithium-ion batteries, *Journal of Power Sources*, 2014, 254, 88-97.

85. Lianyi Shao, Kaiqiang Wu, Xinxin Jiang, Miao Shui, Rui Ma, Mengmeng Lao, *Xiaoting Lin*, Dongjie Wang, Nengbing Long, Jie Shu, Preparation and characterization of basic carbonates as novel anode materials for lithium-ion batteries, *Ceramics International*, 2014, 40, 2, 3105-3116.

86. Lianyi Shao, Kaiqiang Wu, *Xiaoting Lin*, Miao Shui, Rui Ma, Dongjie wang, Nengbing Long, Yuanlong Ren, Jie Shu, Enhanced electrochemical performance of $CuCrO_2$ anode material by Ag_2O coating, *Journal of Electroanalytical Chemistry*, 2014, 717-718, 153-156.

87. Kaiqiang Wu, Dongjie Wang, *Xiaoting Lin*, Lianyi Shao, Miao Shui, Xinxin Jiang, Nengbing Long, Yuanlong Ren, Jie Shu, Comparative study of $Na_2Li_2Ti_6O_{14}$ prepared by different methods as advanced anode material for lithium-ion batteries, Journal of Electroanalytical Chemistry, *Journal of Electroanalytical Chemistry*, 2014, 717-718, 10-16.

88. Dongjie Wang, Kaiqiang Wu, Lianyi Shao, Miao Shui, Rui Ma, *Xiaoting Lin*, Nengbing Long, Yuanlong Ren, Jie Shu, Facile fabrication of $Pb(NO_3)_2$/C as advanced

anode material and its lithium storage mechanism, ***Electrochimica Acta***, 2014, 120, 110-1221.

(D) Conference Presentation and Abstract

1. ***Xiaoting Lin***, Xueliang Sun, Novel cell configurations for high-performance superoxide-based Na-O_2 batteries, CSME-CFDSC Congress 2019, London, Ontario, Canada. (Oral presentation)

2. ***Xiaoting Lin***, Xueliang Sun, O_2/O_2^- crossover- and dendrite-free hybrid solid-state Na-O_2 batteries, ECS 3rd annual research symposium, 2019, London, Ontario, Canada. (Oral presentation)

3. ***Xiaoting Lin***, Xueliang Sun, Na-O_2 batteries: steps towards reality, HEVPD&D CREATE AND EECOMOBILITY (ORF) ANNUAL CONFERENCE, 2019, Windsor, Ontario, Canada. (Oral presentation)

4. ***Xiaoting Lin***, Xueliang Sun, Sodium-oxygen batteries: materials design and chemical reactions, HEVPD&D CREATE AND EECOMOBILITY (ORF) ANNUAL CONFERENCE, 2018, Macmaster, Ontario, Canada. (Best poster for knowledge transfer award)